

# Advanced Control Functionalities for Smart-Transformers Integrating Hybrid MicroGrids

Justino Miguel Ferreira Rodrigues

June 2022

Scientific Supervision by

Supervisor: Carlos Coelho Leal Monteiro Moreira, PhD <sup>1</sup>

Co-supervisor: João Abel Peças Lopes, PhD <sup>2</sup>

<sup>1</sup> Assistant Professor at DEEC-FEUP/Senior researcher at CPES-INESC TEC

<sup>2</sup> Full Professor at DEEC-FEUP/Associate director of INESC TEC

**Contact Information:**

Justino Miguel Ferreira Rodrigues

Instituto de Engenharia de Sistemas e Computadores, Tecnologia e Ciência (INESC  
TEC)

Centre for Power and Energy Systems (CPES)

Rua Dr. Roberto Frias, s/n

4200-465 Porto

Portugal

Tel.: +351 222 094 000

Email: justino.m.f.rodrigues@gmail.com; justino.m.rodrigues@inesctec.pt

Justino Miguel Ferreira Rodrigues

*“Advanced Control Functionalities for Smart-Transformers Integrating Hybrid MicroGrids”*

Copyright © 2022 Justino Miguel Ferreira Rodrigues. All rights reserved.



*My apologies to family and friends for the time I deprived myself  
with them, a deep thank you to my supervisors for their  
invaluable guidance, and to INESC TEC in general for the  
support.*

*This page was intentionally left blank.*

*"Imagination will often carry us to worlds that never were.  
But without it we go nowhere."*

CARL SAGAN

*This page was intentionally left blank.*

# Abstract

In this thesis, a set of advanced control functionalities are proposed for Smart-Transformers integrating Hybrid Microgrids and Multi-Microgrids, aiming to enhance and consolidate the controllability of Hybrid Microgrids and Multi-Microgrids in face of the expected increasing penetration ratios of distributed energy resources. Based on research gaps identified in the literature, advanced control functionalities for power-frequency support, fault-ride-through provision and reconfiguration of distribution grid structures within a Hybrid Multi-Microgrids are proposed and demonstrated.

The power-frequency support control approach rely on droop-based controllers incorporated in the Smart-Transformer, aiming to modulate the electrical variables in the Hybrid Microgrid derived from the Smart-Transformer in order to obtain the power modulation in the Smart-Transformer following frequency disturbances in the upstream AC power system, by exploiting the power-voltage and power-frequency sensitivity of the Hybrid Microgrid. The fault-ride-through control approach for grid-following Smart-Transformers allows the provision of fault-ride-through even if the Smart-Transformer has no energy storage capacity, by exploiting the power-voltage and power-frequency sensitivities in the Smart-Transformer based Hybrid Microgrid. The fault-ride-through control strategy for grid-forming Smart-Transformer is based on a virtual impedance combined with the exploitation of the voltage drop in the output filter of the Smart-Transformer in order to enhance its current limitation capabilities. The fault-ride-through control strategy for grid-forming Smart-Transformers can sustain the islanding of wider Hybrid Multi-Microgrids after a fault disturbance, and operate in coordination with grid-following Smart-Transformers regarding the provision of fault-ride-through and power-frequency support. The proposed fault-ride-through control approach is exploited and validated considering balanced and unbalanced faults. At last, the communication-free grid reconfiguration mechanisms is also demonstrated, which enables the association of LV AC grids under the same MV AC grid in meshed configurations by resorting to the angular position and frequency measured from the MV AC grid.



# Resumo

Nesta dissertação são propostas funcionalidades avançadas para Transformadores Inteligentes em Micro-Redes Híbridas e Multi-Micro-redes Híbridas, com o objetivo de melhorar e consolidar a controlabilidade das Micro-Redes Híbridas e Multi-Micro-redes Híbridas face ao aumento esperado de integração de recursos de energia distribuídos. Com base em lacunas identificadas na literatura, são propostas e demonstradas funcionalidades de controlo avançadas para suporte de potência-frequência, sobrevivência a cavas de tensão e reconfiguração de redes de distribuição no seio de Multi-Micro-Redes Híbridas. A abordagem de controlo para suporte de potência-frequência baseia-se em controladores "*droop*" incorporados no Transformador Inteligente, que procuram modular as variáveis elétricas na Micro-Rede Híbrida do Transformador Inteligente, com o objetivo de modular a potência no Transformador Inteligente após a ocorrência de perturbações de frequência no sistema elétrico a montante, explorando as sensibilidades de potência-tensão e potência-frequência da Micro-Rede Híbrida. A abordagem de controlo para sobrevivência a cavas de tensão para Transformadores Inteligentes *grid-following* permite a sobrevivência a cavas de tensão mesmo quando o Transformador Inteligente não tem armazenamento de energia, ao explorar as sensibilidades de potência-tensão e potência-frequência da Micro-Rede Híbrida. A abordagem de controlo para sobrevivência a cavas de tensão para Transformadores Inteligentes *grid-forming* é baseada numa impedância virtual e na exploração da queda de tensão no filtro de saída do Transformador Inteligente para melhorar a capacidade de limitação de corrente. Este último suporta o ilhamento de Multi-Micro-Redes Híbridas em resposta a falhas na rede a montante, e operar em conjunto com Transformadores Inteligentes *grid-following* no que respeita à sobrevivência a cavas de tensão e suporte de potência-frequência. As abordagens de controlo para sobrevivência a cavas de tensão são exploradas e validadas face a cavas de tensão equilibradas e desequilibradas. É também demonstrado o mecanismo para a reconfiguração para redes de distribuição, não baseado em comunicações, que permite a operação em malha de redes de distribuição BT sob a mesma rede MT, com recurso a medições da rede MT.





# Contents

<b>Abstract</b>	<b>i</b>
<b>Resumo</b>	<b>iii</b>
<b>List of Figures</b>	<b>xi</b>
<b>List of Tables</b>	<b>xxi</b>
<b>Nomenclature</b>	<b>xxiii</b>
<b>1 Introduction</b>	<b>1</b>
1.1 Motivation and Background . . . . .	1
1.2 Objectives of the Thesis and Research Questions . . . . .	6
1.3 Structure of the Thesis . . . . .	7
1.4 Contributions of the Thesis . . . . .	8
<b>2 Microgrids and Smart-Transformer Development</b>	<b>9</b>
2.1 Historical Background . . . . .	9
2.1.1 From Solid-State Transformer to Smart-Transformer . . . . .	9
2.1.2 Microgrids . . . . .	10
2.1.2.1 AC and DC Microgrids . . . . .	11
2.1.2.2 Hybrid AC/DC Microgrids and the Role of Solid-State Transformers . . . . .	11
2.1.3 Multi-Microgrids . . . . .	13
2.2 Smart-Transformer: Architectures and Operation Modes . . . . .	13
2.2.1 Medium-Voltage Converter . . . . .	15
2.2.1.1 Pure Grid-Forming . . . . .	16
2.2.1.2 Non-pure Grid-Forming . . . . .	20
2.2.1.3 Grid-Following . . . . .	21

2.2.1.4	PLL-based Modified Current Control Methods . . . . .	23
2.2.2	Low-Voltage Converter . . . . .	24
2.2.3	Bidirectional Isolated DC-DC Converter . . . . .	25
2.3	Microgrids and Multi-Microgrids: Concepts and Architectures . . . . .	26
2.3.1	AC Microgrids . . . . .	26
2.3.2	DC Microgrids . . . . .	29
2.3.3	Hybrid AC/DC Microgrids . . . . .	30
2.3.3.1	Independent AC and DC Sub-Grids . . . . .	31
2.3.3.2	Meshed Hybrid AC/DC Microgrids . . . . .	33
2.3.4	Multi-Microgrids . . . . .	33
2.3.4.1	AC Multi-Microgrids . . . . .	34
2.3.4.2	DC Multi-Microgrids . . . . .	35
2.3.4.3	Hybrid Multi-Microgrids . . . . .	36
2.4	Advanced Functionalities for Hybrid Microgrids and Multi-Microgrids based on Smart-Transformers . . . . .	38
2.4.1	Voltage/Var Control in AC Grids . . . . .	38
2.4.2	Frequency Regulation and Support . . . . .	40
2.4.2.1	Using Energy Storage . . . . .	42
2.4.2.2	Using Frequency Regulation . . . . .	42
2.4.2.3	Using Voltage Regulation . . . . .	43
2.4.2.4	Frequency and Voltage Regulation Strategies from non- ST-based HMG . . . . .	43
2.4.3	Inertia Emulation . . . . .	44
2.4.4	Fault-Ride-Through Capabilities . . . . .	45
2.4.5	Islanding and Reconnection Capabilities on Meshed MG . . . . .	45
2.4.6	Other Capabilities and Applications . . . . .	47
2.4.6.1	Load Sensitive Identification . . . . .	47
2.4.6.2	Self-Healing and Black-Start . . . . .	47
2.5	Technical Challenges . . . . .	48
2.6	Final Considerations - Literature Gaps . . . . .	50
3	<b>Modeling Principles for Hybrid Microgrids</b>	<b>51</b>
3.1	Modeling and Simulation Approach . . . . .	52
3.2	Smart-Transformers: Power Converter Architectures and Control . . . . .	54
3.2.1	Medium-Voltage Power Converters . . . . .	55
3.2.1.1	Grid-Following Converter - Base Architecture and Control	55

3.2.1.2	Grid-Forming Converter - Base Architecture and Control	60
3.2.2	Isolated DC-DC Power Converters . . . . .	64
3.2.3	Local Energy Storage System and Supercapacitor Bank . . . . .	65
3.2.3.1	Local Energy Storage System . . . . .	66
3.2.3.2	Supercapacitor Bank (Grid-Following Smart-Transformer only) . . . . .	67
3.2.4	Low-Voltage Power Converters . . . . .	69
3.3	Test Distribution Grids: Architectures and Control . . . . .	72
3.3.1	Upstream AC Power System . . . . .	73
3.3.2	Hybrid AC/DC Microgrid based on ST . . . . .	75
3.3.2.1	Low Voltage AC grid in Radial Configuration . . . . .	75
3.3.2.2	Low Voltage DC grid . . . . .	79
3.3.3	MV DC grid based on a single ST . . . . .	82
3.3.4	Hybrid AC/DC Multi-Microgrid based on Smart-Transformers . . . . .	84
3.4	Final Remarks - Summary . . . . .	85
<b>4</b>	<b>Advanced Control Strategies for Smart-Transformers</b>	<b>87</b>
4.1	Power-Frequency Support . . . . .	88
4.1.1	Droop Controllers . . . . .	88
4.1.1.1	Active Power – Frequency . . . . .	90
4.1.1.2	LV Frequency – MV Frequency : $f_{LV}(f_{MV})$ . . . . .	92
4.1.1.3	LV AC voltage – MV Frequency : $VAC_{LV}(f_{MV})$ . . . . .	92
4.1.1.4	MV DC voltage – MV Frequency : $VDC_{MV}(f_{MV})$ . . . . .	92
4.1.2	Droop Controllers integration in the overall ST Control Architecture	93
4.2	Fault-Ride-Through Capabilities . . . . .	97
4.2.1	Fault-Ride-Through for Grid-following ST . . . . .	97
4.2.1.1	Dump Load . . . . .	98
4.2.1.2	Non-Isolated DC-DC Converter . . . . .	99
4.2.1.3	FRT Control Strategy . . . . .	100
4.2.1.4	Chain of Events induced by the FRT Control Strategy . . . . .	106
4.2.2	Fault-Ride-Through for Grid-forming ST . . . . .	108
4.2.2.1	Supplementary FRT Control Mechanisms . . . . .	112
4.2.2.2	Chain of Events induced by the FRT Control Strategy . . . . .	116
4.3	Reconfiguration Capabilities on Hybrid Multi-Microgrids . . . . .	117
4.4	Final Remarks - Summary . . . . .	120

<b>5</b>	<b>Providing Power-frequency Regulation from Smart-Transformer connected Hybrid Microgrids - Numerical Results</b>	<b>123</b>
5.1	Case Studies . . . . .	123
5.2	Simulation Results . . . . .	126
5.2.1	Grid-Following ST . . . . .	127
5.2.2	Grid-Forming ST . . . . .	130
5.3	Final Remarks - Summary . . . . .	136
<b>6</b>	<b>Validation of Advanced Control Strategies for Fault-Ride-Through and Grid Reconfiguration on Hybrid Multi-Microgrids</b>	<b>137</b>
6.1	Case Studies . . . . .	137
6.1.1	Case Studies 1, 2 and 3 . . . . .	138
6.1.2	Case Study 4 . . . . .	144
6.1.3	Case Study 5 . . . . .	147
6.2	Simulation Results . . . . .	148
6.2.1	Case Studies 1 and 2 . . . . .	148
6.2.2	Case Study 3 . . . . .	168
6.2.3	Case Study 4 . . . . .	182
6.2.4	Case Study 5 . . . . .	186
6.3	Final Remarks - Summary . . . . .	189
<b>7</b>	<b>Conclusions and Future Research</b>	<b>191</b>
7.1	Conclusions . . . . .	191
7.2	Future Research . . . . .	193
	<b>Appendices</b>	<b>195</b>
<b>A</b>	<b>Parametrization of Smart-Transformers, Hybrid Microgrids and Hybrid Multi-Microgrids</b>	<b>197</b>
A.1	Smart-Transformers . . . . .	197
A.2	Hybrid Microgrids and Hybrid Multi-Microgrids . . . . .	200
<b>B</b>	<b>Additional Results for Case Studies 1, 2 and 3 - Chapter 6</b>	<b>205</b>
B.1	Case Studies 1 and 2 . . . . .	205
B.2	Case Study 3 . . . . .	219
	<b>Publications</b>	<b>227</b>

<b>References</b>	<b>229</b>
<b>Index</b>	<b>249</b>



# List of Figures

1.1	Shares of net additions in power generating capacity, 2010-2020. . . . .	1
1.2	Germany annual PV capacity additions 2016-22 and average annual additions for 2023-25 (left), and monthly distributed PV additions in 2020 (right). . . . .	2
1.3	Electric car registrations and sales share in selected countries and regions, 2015-2020. PHEV = plug-in hybrid electric vehicle; BEV = battery electric vehicle. . . . .	3
2.1	SST prototype (1.2-MVA) for a 15kV 16.7Hz railway grid. . . . .	10
2.2	Seogeocho DC microgrid system network diagram. . . . .	12
2.3	Conceptual representation of a SST. . . . .	14
2.4	The classification of the SST architecture according to the number of power conversions and modularity. . . . .	15
2.5	Conceptual representation of a ST based on a three-stage topology. . . .	15
2.6	MV converter topologies: Three-level Neutral Point Clamped (a) Cascaded H-bridge (b) and Modular Multilevel (c). . . . .	16
2.7	Basic droop characteristics for grid-forming MV inverters. . . . .	17
2.8	Basic representation of the Power Synchronization Loop control. . . . .	18
2.9	Example of a Virtual Synchronous Machine control. . . . .	18
2.10	Block diagram of an example of a matching controller. . . . .	19
2.11	Block diagram of a virtual oscillator controller based on a Van der Pol oscillator. . . . .	20
2.12	Block diagram of a PLL-free Direct Power Control. . . . .	21
2.13	Droop-based Grid-forming control with PLL. . . . .	21
2.14	Example of a Voltage Oriented Control structure. . . . .	22
2.15	Example of a Voltage Field Oriented Control structure. . . . .	23
2.16	Example of a Virtual Flux Direct Power Control structure. . . . .	23

2.17	Example of a PLL-based Modified Current Control: Outer control loops for grid support. . . . .	24
2.18	Four-wire topologies for the LV converter stage: Three-level Neutral Point Clamped - classic (a), Three-level Neutral Point Clamped - T-type (b) and Half-bridge (c). . . . .	24
2.19	Topologies for the bidirectional isolated DC-DC converter stage: Dual-Active-Bridge (a), Series-Resonant (b) and Multiple-Active-Bridge (c). . . . .	25
2.20	Basic architecture of an AC microgrid. . . . .	26
2.21	Example of a hierarchical control of an AC MG: Primary, Secondary and Tertiary control. . . . .	27
2.22	Example of droop characteristics for AC MG: Active power - voltage droop (a) and Reactive power - frequency droop (b). . . . .	28
2.23	Example of droop characteristics for DC MG: Active power - DC voltage droop (left) and DC current - DC voltage droop (right). . . . .	30
2.24	HMG architecture classification for independent AC and DC sub-grids. . . . .	31
2.25	Proportional power sharing in HMG (a); Hybrid AC-DC droop with dead-zone (b) . . . . .	32
2.26	ST-based HMG . . . . .	33
2.27	Example of an AC MMG . . . . .	34
2.28	Example of a hierarchical control scheme for AC MMG . . . . .	35
2.29	Example of a DC MMG . . . . .	35
2.30	Example of a HMMG using ST . . . . .	36
2.31	Typical requirements for power factor variation range in relation to the voltage (left) and static power factor-voltage regulation as a function of the active power in the German grid code (right). . . . .	39
2.32	The active power reduction in case of over-frequency according to the German grid-code . . . . .	41
3.1	Equivalence between a detailed model of a SST and a model of a SST based on the DAM approach. . . . .	53
3.2	Overall structure of the modeled ST. . . . .	54
3.3	Block diagram of the MV Inverter of the grid-following ST - base architecture. . . . .	56
3.4	Block diagram of the MV Inverter of the grid-forming ST - base architecture. . . . .	61



3.5	Equivalence between $f(P)$ droop plus First-Order Low-pass Filter (right) and Swing Equation (left). . . . .	62
3.6	Control rule for $f(\Delta P_{MV})$ and $\Delta VAC_{MV}(Q_{MVg})$ droop controllers. . . .	62
3.7	Block diagram of the DC/DC converter stage. . . . .	64
3.8	Block diagram of the modeled local ESS. . . . .	66
3.9	Block diagram of the modeled supercapacitor bank. . . . .	68
3.10	Block diagram of the LV inverter of the ST - base architecture. . . . .	70
3.11	Base architecture for the modeled test grids. . . . .	73
3.12	Equivalent computational model for the Upstream AC power system. . .	74
3.13	One-line diagram of the IEEE European low voltage test feeder . . . . .	75
3.14	One-line diagram of the modeled LV AC sub-grid (right) based on the IEEE European low voltage test feeder (left). . . . .	77
3.15	Block diagram of the developed computational models for the controllable DER units in the LV AC grid. . . . .	78
3.16	Control rule for $P(VAC_{LV})$ and $P(f_{LV})$ droop controllers. . . . .	79
3.17	One-line diagram of the modeled LV DC sub-grid. . . . .	80
3.18	Block diagram of the developed computational models for the controllable DER units in the LV DC grid. . . . .	81
3.19	One-line diagram of the modeled MV DC sub-grid. . . . .	82
3.20	Block diagram of the developed computational models for the controllable DER units in the MV DC grid. . . . .	83
3.21	One-line diagram of the IEEE 15 Bus Radial System. . . . .	84
3.22	One-line diagram of the modeled HMMG. . . . .	85
4.1	Schematic of the advanced functionalities to be exploited by the ST for power-frequency support. . . . .	88
4.2	Control rule adopted by droop controllers for ST. . . . .	89
4.3	Block diagram of the MV Inverter of the grid-following ST including droop control functionalities for power-frequency support (highlighted). . .	94
4.4	Block diagram of the MV Inverter of the grid-forming ST including droop control functionalities for power-frequency support (highlighted). . .	95
4.5	Block diagram of the ST's LV Inverter including the droop control functionalities for power-frequency support (highlighted). . . . .	95
4.6	Reaction chain triggered in the grid-following ST and its derived grids following a frequency disturbance in the MV AC grid. Positive values for the active power correspond to consumed active power. . . . .	96

4.7	Reaction chain triggered in the grid-forming ST and its derived grids following a frequency disturbance in the MV AC grid. Positive values for the active power correspond to consumed active power. . . . .	96
4.8	Grid-following ST with no ESS available incorporating the additional FRT hardware requirements. . . . .	98
4.9	Computational model for the Dump-Load. . . . .	98
4.10	Computational model for the non-isolated bidirectional DC-DC converter. . . . .	100
4.11	Block diagram of the proposed Fault-Ride-Through control mechanism for grid-following ST. . . . .	101
4.12	Block diagram of the grid-following ST's MV inverter incorporating the proposed Fault-Ride-Through control mechanism. . . . .	103
4.13	Block diagram of the ST's LV inverter incorporating the $\Delta f_{FRT}$ signal. . . . .	105
4.14	Reaction chain triggered for a net load scenario in the ST-based hybrid AC/DC grid following a voltage disturbance in the MV AC grid. Positive values for the active power correspond to consumed active power. . . . .	107
4.15	Reaction chain triggered for a net generation scenario in the ST-based hybrid AC/DC grid following a voltage disturbance in the MV AC grid. Positive values for the active power correspond to consumed active power. . . . .	107
4.16	Block diagram of the proposed Fault-Ride-Through control mechanism for grid-forming ST. . . . .	108
4.17	Block diagram of the grid-forming ST's MV inverter incorporating the proposed Fault-Ride-Through control mechanism. . . . .	109
4.18	Reaction chain triggered in the grid-forming ST and its derived grids following a fault disturbance in the MV AC grid. Positive values for the active power correspond to consumed active power. . . . .	117
4.19	Conceptual representation of the proposed synchronization mechanism for the ST's LV inverter. . . . .	118
4.20	Block diagram of the ST's LV inverter incorporating the proposed synchronization mechanism. . . . .	118
5.1	Overview of the computational models adopted for the evaluation of the advanced control functionalities for power-frequency support using ST. . . . .	124
5.2	Over-frequency and under-frequency disturbances in the upstream AC power system for 10% and 20% load step-up and step-down variations in the upstream AC grid. . . . .	127

5.3	Frequency and voltage modulation in ST-based sub-grids following frequency disturbances in the upstream AC grid. . . . .	128
5.4	Active Power response in the ST's MV inverter following frequency disturbances in the upstream AC grid, discriminated by sub-grid contribution. . . . .	129
5.5	Active Power response in the ST's MV inverter following frequency disturbances in the upstream AC grid, discriminated by resource type contribution. . . . .	130
5.6	Active Power response in the local ESS in the absence of response in the ST-based sub-grids, following frequency disturbances in the upstream AC grid. . . . .	131
5.7	Active Power response in the ST's MV inverter following under-frequency disturbances in the upstream AC grid, discriminated by resource type. . . . .	132
5.8	Active Power response in the ST's MV inverter following over-frequency disturbances in the upstream AC grid, discriminated by resource type. . . . .	133
5.9	Frequency and Voltage modulation in ST-based sub-grids for 10% and 20% load step variation in the upstream AC grid. . . . .	134
5.10	Active Power response in the ST's MV inverter following frequency disturbances in the upstream AC grid, discriminated by resource type contribution. . . . .	135
6.1	Overview of the computational models adopted in case studies, 1, 2 and 3 for the evaluation of the advanced control functionalities for FRT provision. . . . .	139
6.2	Overview of the computational models adopted in case study 4 for the evaluation of the advanced control functionalities for FRT provision. . . . .	144
6.3	Overview of the computational models adopted in case study 5 for the evaluation of the grid reconfiguration mechanism. . . . .	147
6.4	Voltage disturbances observed at ST's MV inverter resulting from fault disturbances in the upstream AC power system, for several fault impedances with a time duration of 0.2 s. . . . .	149
6.5	Voltage disturbances observed at ST's MV inverter resulting from fault disturbances in the upstream AC power system, for several fault impedances with a time duration of 0.5 s. . . . .	149

6.6	Frequency disturbances observed at ST's MV inverter resulting from fault disturbances in the upstream AC power system, for several fault impedances with a time duration of 0.2 s and 0.5 s. . . . .	150
6.7	DC voltage in the ST-based MV DC grid for several fault impedances with a time duration of 0.5 s. . . . .	151
6.8	DC voltage in the ST-based LV DC grid for several fault impedances with a time duration of 0.5 s. . . . .	152
6.9	AC voltage in the ST-based LV AC grid for several fault impedances with a time duration of 0.5 s. . . . .	153
6.10	Frequency in the ST-based LV AC grid for several fault impedances with time duration of 0.5 s. . . . .	154
6.11	Active power in the ST-based MV DC grid for several fault impedances with a time duration of 0.5 s. . . . .	156
6.12	Active power in the ST-based LV DC grid for several fault impedances with a time duration of 0.5 s. . . . .	157
6.13	Active power in the ST-based LV AC grid for several fault impedances with a time duration of 0.5 s. . . . .	158
6.14	Active power in total non-controllable load in the ST-based hybrid grid for several fault impedances with a time duration of 0.5 s. . . . .	159
6.15	Active power in total PV generation in the ST-based hybrid grid for several fault impedances with a time duration of 0.5 s. . . . .	160
6.16	Active power in total EV chargers in the ST-based hybrid grid for several fault impedances with a time duration of 0.5 s. . . . .	161
6.17	Active power in total energy storage available in the ST-based hybrid grid for several fault impedances with a time duration of 0.5 s. . . . .	162
6.18	Case study 2 - Active power in the local ESS of the ST for several fault impedances with a time duration of 0.5 s. . . . .	163
6.19	Active power in the ST's MV inverter for several fault impedances with a time duration of 0.5 s. . . . .	164
6.20	RMS current in the ST's MV inverter for several fault impedances with a time duration of 0.5 s. . . . .	165
6.21	RMS current in the ST's MV inverter for several fault impedances with a time duration of 0.2 s. . . . .	166

6.22	Three-phase voltage and current waveforms in the ST MV inverter during fault surge: fault impedance of $0.02\Omega$ and time duration of 0.5 s. Black: phase-phase A-B voltage and phase A current; Red: phase-phase B-C voltage and phase B current; Green: phase-phase C-A voltage and phase C current. . . . .	167
6.23	Three-phase voltage and current waveforms in the ST MV inverter during fault clearance: fault impedance of $0.02\Omega$ and time duration of 0.5 s. Black: phase-phase A-B voltage and phase A current; Red: phase-phase B-C voltage and phase B current; Green: phase-phase C-A voltage and phase C current. . . . .	168
6.24	Frequency disturbances observed at ST's MV inverter resulting from fault disturbances in the upstream AC power system considering $Z_{eq1}$ . .	169
6.25	Frequency disturbances observed at ST's MV inverter resulting from fault disturbances in the upstream AC power system considering $Z_{eq2}$ . .	169
6.26	Voltage disturbances observed at ST's MV inverter resulting from fault disturbances in the upstream AC power system, considering $Z_{eq1}$ and fault impedances with a time duration of 0.2 s. . . . .	170
6.27	Voltage disturbances observed at ST's MV inverter resulting from fault disturbances in the upstream AC power system, considering $Z_{eq1}$ and fault impedances with a time duration of 0.5 s. . . . .	170
6.28	Voltage disturbances observed at ST's MV inverter resulting from fault disturbances in the upstream AC power system, considering $Z_{eq2}$ and fault impedances with a time duration of 0.2 s. . . . .	171
6.29	Voltage disturbances observed at ST's MV inverter resulting from fault disturbances in the upstream AC power system, considering $Z_{eq2}$ and fault impedances with a time duration of 0.5 s. . . . .	171
6.30	RMS current in the ST's MV inverter considering $Z_{eq1}$ and fault impedances with a time duration of 0.5 s. . . . .	173
6.31	RMS current in the ST's MV inverter considering $Z_{eq2}$ and fault impedances with a time duration of 0.5 s. . . . .	174
6.32	Active power and phase shift in the output LC filter of the ST's MV inverter, considering $Z_{eq1}$ and fault impedances with a time duration of 0.5 s. . . . .	176
6.33	Active power and phase shift in the output LC filter of the ST's MV inverter, considering $Z_{eq2}$ and fault impedances with a time duration of 0.5 s. . . . .	177

6.34	Reactive power and voltage drops (per phase) in the output LC filter of the ST's MV inverter considering $Z_{eq1}$ and fault impedances with a time duration of 0.5 s. . . . .	178
6.35	Reactive power and voltage drops (per phase) in the output LC filter of the ST's MV inverter considering $Z_{eq2}$ and fault impedances with a time duration of 0.5 s. . . . .	179
6.36	Three-phase current waveforms in the ST MV inverter for faults with impedance of $0.02\Omega$ and time duration of 0.5 s, considering $Z_{eq1}$ . Black: phase A current; Red: phase B current; Green: phase C current. . . . .	180
6.37	Three-phase current waveforms in the ST MV inverter for faults with impedance of $0.02\Omega$ and time duration of 0.5 s, considering $Z_{eq2}$ . Black: phase A current; Red: phase B current; Green: phase C current. . . . .	181
6.38	Voltage and frequency disturbances observed at HMMG side in the connection point with the upstream AC power system, resulting from fault disturbances in the upstream AC power system. HMMG islanding at time = 0.2 s . . . . .	182
6.39	Voltage and frequency disturbances observed at HMMG side in the connection point with the upstream AC power system, resulting from fault disturbances in the upstream AC power system. HMMG islanding at time = 0.5 s . . . . .	183
6.40	Active power profiles in the ST and remaining generation and loads integrating the HMMG for all types of fault disturbances. HMMG islanding at time = 0.2 s . . . . .	184
6.41	Active power profiles in the ST and remaining generation and loads integrating the HMMG for all types of fault disturbances. HMMG islanding at time = 0.5 s . . . . .	185
6.42	Reactive power profiles in the ST and remaining generation and loads integrating the HMMG for all types of fault disturbances. HMMG islanding at time = 0.2 s . . . . .	186
6.43	Reactive power profiles in the ST and remaining generation and loads integrating the HMMG for all types of fault disturbances. HMMG islanding at time = 0.5 s . . . . .	187
6.44	Active and Reactive power in the LFT and ST's LV inverter, and angular position difference between the voltages in the LV and MV AC grids, following the disconnection of the LFT. . . . .	188

6.45	Active and Reactive power in the LFT and ST's LV inverter, and angular position difference between the voltages in the LV and MV AC grids, following the pre-synchronization process and the effective reconnection of the LFT. . . . .	189
6.46	Three-phase voltage and currents in the LV inverter of the ST and in the LFT (secondary winding) following the reconnection of the LFT to the upstream AC power system. . . . .	189
B.1	Case study 2 - Active power in the local ESS of the ST for several fault impedances with a time duration of 0.2 s. . . . .	205
B.2	DC voltage in the ST-based MV DC grid for several fault impedances with a time duration of 0.2 s. . . . .	206
B.3	DC voltage in the ST-based LV DC grid for several fault impedances with a time duration of 0.2 s. . . . .	207
B.4	AC voltage in the ST-based LV AC grid for several fault impedances with a time duration of 0.2 s. . . . .	208
B.5	Frequency in the ST-based LV AC grid for several fault impedances with a time duration of 0.2 s. . . . .	209
B.6	Active power in the ST-based MV DC grid for several fault impedances with a time duration of 0.2 s. . . . .	210
B.7	Active power in the ST-based LV DC grid for several fault impedances with a time duration of 0.2 s. . . . .	211
B.8	Active power in the ST-based LV AC grid for several fault impedances with a time duration of 0.2 s. . . . .	212
B.9	Active power in total non-controllable load in the ST-based hybrid grid for several fault impedances with a time duration of 0.2 s. . . . .	213
B.10	Active power in total PV generation in the ST-based hybrid grid for several fault impedances with a time duration of 0.2 s. . . . .	214
B.11	Active power in total EV chargers in the ST-based hybrid grid for several fault impedances with a time duration of 0.2 s. . . . .	215
B.12	Active power in total energy storage capacity available in the ST-based hybrid grid for several fault impedances with a time duration of 0.2 s. . . . .	216
B.13	Active power in the ST's MV inverter for several fault impedances with a time duration of 0.2 s. . . . .	217



B.14	Three-phase voltage and current waveforms in the ST MV inverter for faults with impedance of $0.02\Omega$ and time duration of 0.2 s. Black: phase-phase A-B voltage and phase A current; Red: phase-phase B-C voltage and phase B current; Green: phase-phase C-A voltage and phase C current.	218
B.15	RMS current in the ST's MV inverter considering $Z_{eq1}$ and fault impedances with a time duration of 0.2 s. . . . .	219
B.16	RMS current in the ST's MV inverter considering $Z_{eq2}$ and fault impedances with a time duration of 0.2 s. . . . .	220
B.17	Active power and phase shift in the output LC filter of the ST's MV inverter, considering $Z_{eq1}$ and fault impedances with a time duration of 0.2 s. . . . .	221
B.18	Active power and phase shift in the output LC filter of the ST's MV inverter, considering $Z_{eq2}$ and fault impedances with a time duration of 0.2 s. . . . .	222
B.19	Reactive power and voltage drops (per phase) in the output LC filter of the ST's MV inverter considering $Z_{eq1}$ and fault impedances with a time duration of 0.2 s. . . . .	223
B.20	Reactive power and voltage drops (per phase) in the output LC filter of the ST's MV inverter considering $Z_{eq2}$ and fault impedances with a time duration of 0.2 s. . . . .	224
B.21	Three-phase current waveforms in the ST MV inverter for faults with impedance of $0.02\Omega$ and time duration of 0.2 s, considering $Z_{eq1}$ . Black: phase A current; Red: phase B current; Green: phase C current. . . . .	225
B.22	Three-phase current waveforms in the ST MV inverter for faults with impedance of $0.02\Omega$ and time duration of 0.2 s, considering $Z_{eq2}$ . Black: phase A current; Red: phase B current; Green: phase C current. . . . .	226



# List of Tables

5.1	Smart-Transformer: main parameters . . . . .	124
5.2	Upstream AC power system: main parameters . . . . .	125
5.3	Steady-state power and operation limits in the ST-based hybrid AC/DC grid . . . . .	125
6.1	Simulated fault disturbances: main parameters . . . . .	140
6.2	Equivalent impedance: main parameters . . . . .	140
6.3	Smart-Transformer: main parameters . . . . .	140
6.4	Upstream AC power system: main parameters . . . . .	140
6.5	Steady-state power and operation limits in the hybrid AC/DC grid based on the grid-following ST for case studies 1 and 2 . . . . .	141
6.6	Steady-state power and operation limits in the ST-based hybrid AC/DC grid for case study 3 . . . . .	142
6.7	Simulated fault disturbances: main parameters . . . . .	145
6.8	Steady-state power and operation limits in a single ST-based hybrid AC/DC grid for case study 4 . . . . .	145
6.9	Main characteristics of the HMMG considered for case study 4 . . . . .	146
6.10	MV/LV substation based on a low-frequency transformer: main parameters . . . . .	148
A.1	Smart-Transformer: general parameters . . . . .	197
A.2	Grid-Following MV inverter: Control parameters . . . . .	198
A.3	Grid-Forming MV inverter: Control parameters . . . . .	198
A.4	Hypothetical Supercapacitor Bank (not modeled) . . . . .	199
A.5	Grid-Forming LV inverter: Control parameters . . . . .	199
A.6	Upstream AC power system . . . . .	200
A.7	Base parameters for the simplified LV AC sub-grid: buses, lines and loads (per phase) . . . . .	200

A.8	Base parameters for the simplified LV AC sub-grid: DER units (per phase)	201
A.9	Base Simplified LV AC sub-grid: load-voltage and load-frequency sensitivity coefficients (per phase) . . . . .	201
A.10	Base Simplified LV AC sub-grid: droop controllers in DER units . . . . .	201
A.11	Base parameters for the LV DC sub-grid: buses, lines and loads . . . . .	202
A.12	Base parameters for the LV DC sub-grid: DER units . . . . .	202
A.13	Base Simplified LV DC sub-grid: droop controllers in DER units . . . . .	202
A.14	Base parameters for the MV DC sub-grid: buses, lines, loads and DER .	202
A.15	Base Simplified MV DC sub-grid: droop controllers in DER units . . . . .	202
A.16	Parameters for the HMMG . . . . .	203

## List of Abbreviations

*DAB* Dual-Active-Bridge.

*DAM* Dynamic Average Modeling.

*DER* Distributed Energy Resources.

*DG* Distributed Generation.

*DPC* Direct Power Control.

*ESS* Energy Storage System.

*EV* Electric Vehicle.

*FCL* Fault Current Limiter.

*FOC* Field Oriented Control.

*FRT* Fault-Ride-Through.

*HFT* High-Frequency Transformer.

*HMG* Hybrid AC/DC Microgrid.

*HMMG* Hybrid AC/DC Multi-Microgrid.

*LFT* Low-Frequency Transformer.

*LV* Low-Voltage.

*MG* Microgrid.

*MGCC* Microgrid Central Controller.

*MMG* Multi-Microgrid.

*MV* Medium-Voltage.

*PLL* Phase-Locked Loop.

*RES* Renewable Energy Sources.

*SST* Solid-State Transformer.

*ST* Smart-Transformer.

*VFDPC* Virtual Flux Direct Power Control.

*VFOC* Virtual Flux Oriented Control.

*VOC* Voltage Oriented Control.

## Nomenclature

$\delta_{MVf}$  Voltage phase shift in the ST's MV LC filter.

$\Delta P_d$  Active power variation generated by the  $P(f_{MV})$  droop controller.

$\Delta VAC_{LVd}$  Voltage variation generated in the LV AC grid by the  $VAC_{LV}(f_{MV})$  droop controller.

$\Delta VDC_{MVd}$  Voltage variation generated in the MV DC grid by the  $VDC_{MV}(f_{MV})$  droop controller.

$\Delta VDC_{LVsw}$  Voltage ripple in the LV DC bus associated to the LV inverter's switching.

$\Delta VDC_{MVsw}$  Voltage ripple in the MV DC bus associated to the MV inverter's switching.

$\Delta \omega_{LVd}$  Angular frequency variation in the LV AC grid generated by the  $f_{LV}(f_{MV})$  droop controller.

$C_{LVf}$  Capacitance of the LV coupling filter.

$C_{LV}$  Capacitance of the ST's LV DC bus.

$C_{MVf}$  Capacitance of the MV coupling filter.

$C_{MV}$  Capacitance of the ST's MV DC bus.

$C_{SC}$  Capacitance of the supercapacitor bank.

$d_{MV}^*$  External duty-cycle control of the non-isolated DC-DC converter coupling the MV DC grid to the ST's MV DC bus.

$d^*$  External duty-cycle control of the ST's isolated DC/DC converter.

$f_c$  Cut-off frequency of the coupling filter.

$f_0$  Nominal frequency of AC grids.

$f_{LV}$  Fundamental frequency in the LV AC grid interfaced by the ST.

$f_{MV}$  Fundamental frequency in the MV AC grid interfaced by the ST.

$f_{sw}$  Switching frequency of the power converters.

$H$  Inertia constant.

$I^{LV-0H}$  DC bus voltage ripple compensation for negative and zero sequence component and harmonics in LV AC grid.

$I^{MV-}$  DC bus voltage ripple compensation for negative sequence component in the MV AC grid.

$i_{a_{LV}}, i_{b_{LV}}, i_{c_{LV}}$  Phase AC currents in the ST's LV inverter.

$i_{a_{MV}}, i_{b_{MV}}, i_{c_{MV}}$  Phase AC currents in the ST's MV inverter.

$I_{ESSn}$  Nominal current of the local ESS.

$I_{ESS}^*$  Current reference for the ST's local ESS.

$I_{ESS}$  Outout current of the ST's local ESS.

$I_{FRT}$  Reference control signal for the FRT mechanism in grid-following ST.

$IAC_{LVn}$  Nominal three-phase AC current in the ST's LV inverter.

$IAC_{LV}^-$  Negative sequence component of the three-phase AC current in the ST's LV inverter.

$IAC_{LV}$  Three-phase AC current in the ST's LV inverter.

$IAC_{MVg}$  Three-Phase MV AC current after the ST's MV LC filter.

$IAC_{MVn}$  Nominal three-phase AC current in the ST's MV inverter.

$IAC_{MVp}$  Peak value of the nominal AC current of the ST's MV inverter.

$IAC_{MV}^-$  Negative sequence component of the three-phase AC current in the ST's MV inverter.

$IAC_{MV}$  Three-phase AC current in the ST's MV inverter.

$IDAB_{LV}$  DC current in the secondary stage of the isolated DC/DC converter.

$IDAB_{MV}$  DC current in the primary stage of the isolated DC/DC converter.

$IDC_{LVbus}$  DC current drawn by ST's LV DC bus.

$IDC_{LVcap}$  Current flowing to the capacitance  $C_{LV}$ .

$IDC_{LV}$  Current exchanged between the ST's LV inverter and the ST's LV DC bus.

$IDC_{MVbus}$  DC current drawn by ST's MV DC bus.

$IDC_{MVcap}$  Current flowing to the capacitance  $C_{MV}$ .

$IDC_{MVg}$  DC current in the MV DC grid.

$IDC_{MV}$  Current exchanged between the ST's MV inverter and the ST's MV DC bus.

$L_{LVf}$  Inductance of the LV coupling filter.

$L_{MVf}$  Inductance of the MV coupling filter.

$N$  Transformation ratio of the HFT in the isolated DC/DC converter.

$P_{DL}$  Active power in the dump-load.

$P_{ESS}^*$  Active power reference for the ST's local ESS.

$P_{ESS}$  Active power of the ST's local ESS.

$P_e$  Electrical active power.

$P_{LV}$  Active power in the ST's LV inverter.

$P_{MVn}$  Nominal active power of the ST's MV inverter.

$P_{MVsp}$  Active power set-point for the ST's MV inverter.

$P_{MV}$  Active power in the ST's MV inverter.

$P_m$  Mechanical active power.

$PAC_{LVg}$  Active power in the LV AC grid.

$PAC_{MVg}$  Active power measurement after the ST's MV LC filter.

$PDAB_{LV}$  Power output of the isolated DC/DC converter in the LV side.

$PDAB_{MV}$  Power output of the isolated DC/DC converter in the MV side.

$PDC_{LVg}$  Active power in the LV DC grid.

$PDC_{MVg}$  Active power in the MV DC grid.

$Q_{MVg}$  Reactive power measurement after the ST's MV LC filter.

$Q_{MVsp}$  Reactive power set-point for the ST's MV inverter.

$S_{MVn}$  Nominal apparent power for the ST's MV inverter.

$v_{ab_{MV}}, v_{bc_{MV}}, v_{ca_{MV}}$  Phase-phase AC voltages in the ST's MV inverter.

$v_{an_{LV}}, v_{bn_{LV}}, v_{cn_{LV}}$  Phase-neutral AC voltages in the ST's LV inverter.

$V_{SC}$  Voltage in the supercapacitor bank.

$VAC_{LVg}$  Three-phase AC voltage in the LV AC grid.

$VAC_{LVn}$  Nominal value for the AC voltage in the ST's LV inverter.

$VAC_{LV}$  Three-phase AC voltage in the ST's LV inverter.

$VAC_{MVg}$  Three-Phase MV AC voltage after the ST's MV LC filter.

$VAC_{MV}^+$  Positive sequence component of three-phase AC voltage in the ST's MV inverter.

$VAC_{MV}$  Three-Phase AC voltage in the ST's MV inverter.

$VDC_{LVg}$  DC voltage in the LV DC grid.

$VDC_{LVn}$  Nominal DC voltage for the ST's LV DC bus.

$VDC_{LV}$  DC voltage in the ST's LV DC bus.

$VDC_{MVg}$  DC voltage in the MV DC grid.

$VDC_{MVn}$  Nominal DC voltage for the ST's MV DC bus.



$VDC_{MV}$  DC voltage in the ST's MV DC bus.

$X_L$  Primary-referred leakage reactance of the isolated DC/DC converter.

$XC_{MVf}$  Capacitive reactance of the ST's MV LC filter at  $f_{MV}$ .

$XL_{MVf}$  Inductive reactance of the ST's MV LC filter at  $f_{MV}$ .

$Z_0$  Characteristic impedance of the coupling filter.

$Z_{MVg}$  Equivalent impedance of the MV DC grid.

$\omega_0$  Nominal angular frequency in AC grids.

$\omega_{LV}$  Angular frequency in LV AC grid.

$\phi$  Phase-shift between the square waveforms applied to the HFT.



# Chapter 1

## Introduction

### 1.1 Motivation and Background

The replacement of fossil fuels by cleaner energy sources has been receiving major attention in recent times in face of the increasing urgency in curbing anthropogenic climate change. Electric power systems, as important contributor for greenhouse gas emissions, are naturally relevant players in this emergency, with profound changes looming on the horizon. Renewable Energy Sources (RES) are expected to assume the main role in electricity generation, progressively displacing fossil-fuels still prominent in this role in many countries worldwide. The most recent data available clearly indicates that such revolution is taking place. Worldwide, wind and solar reached nearly 1.5 TW installed generation capacity in 2020 [1], generating roughly 2400 TWh of electric energy in 2020 alone [2], and accounted for 72% of the net additions in power generation capacity in 2020 (Figure 1.1) [3]. However, according to existing projections, wind and solar alone should account at least for 60% of electricity generation globally by 2050 [4, 5].

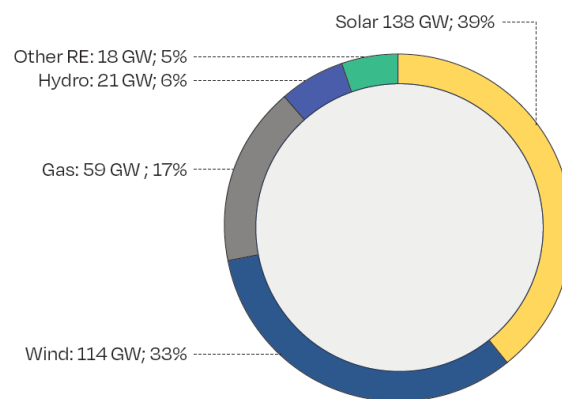


**Figure 1.1:** Shares of net additions in power generating capacity in 2020 [3].

Reflecting the more distributed nature of wind and solar energy resources, electricity generation is expected to become more distributed, contrasting with the reality of traditional power generation systems. Utility-scale renewable power plants, connected to the transmission grid due to its relatively high installed generation capacity (such as large wind farms, big PV and concentrating solar power plants, among others) should remain responsible for a major share of renewable energy generation, with many more projected or under construction [3, 6]. Still, besides such power plants being in average smaller and more distributed than large conventional power plants [7, 8], the vast majority of renewable generation power plants consist of relatively smaller generation units connected to the distribution grids [9]. Such smaller generation units connected to distribution grids are widely designated as Distributed Generation (DG), with millions of such units connected to Low-Voltage (LV) distribution grids. For example, residential PV generation units alone are expected to reach 100 million installations worldwide by 2024, representing one-quarter of total distributed solar PV capacity (which also includes commercial and industrial installations) [10]. Thus, small-scale DG units connected to Low-Voltage (LV) distribution grids are expected to play an important role (as exemplified in Figure 1.2 for Germany) in the overall energy paradigm changes taking place.

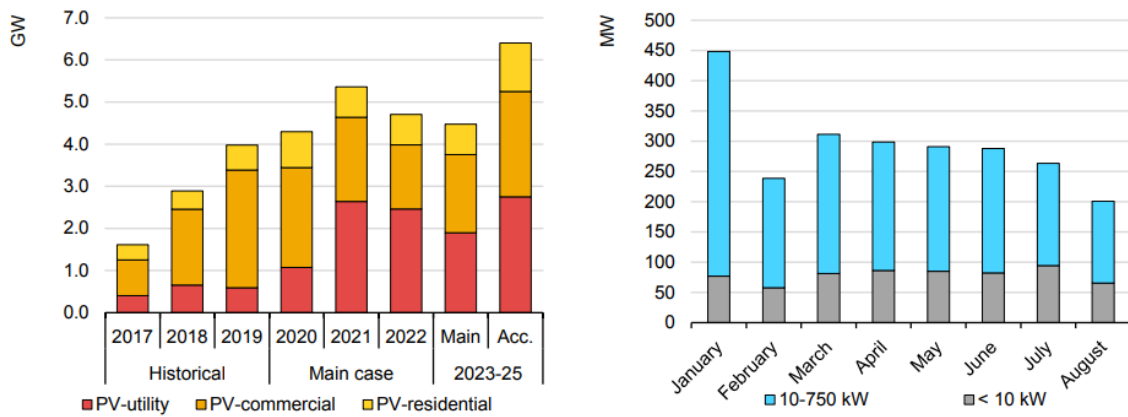


**Figure 1.2:** Germany annual PV capacity additions 2016-22 and average annual additions for 2023-25 (left), and monthly distributed PV additions in 2020 (right) [11].

Simultaneously, important changes are also expected in the energy consumption side. One of the major changes is the electrification of the transportation sector, with Electric Vehicles (EV) posed to represent an important share of the future load of the system. EV are starting to become mainstream with 10 million EV on the road worldwide in 2020, a number expected to increase to 145 million by 2030 [12]. Despite the pandemic-related decrease in car sales (16%), EV registrations increased by 41% in

2020, with around 3 million EV sold globally [12]. The figures for major EV markets are illustrated in Figure 1.3. Following the deployment of EV, private and public charging points (slow and fast) increased respectively to 9.5 million and 1.3 million worldwide in 2020, with around 200 million in total expected by 2030 [12].

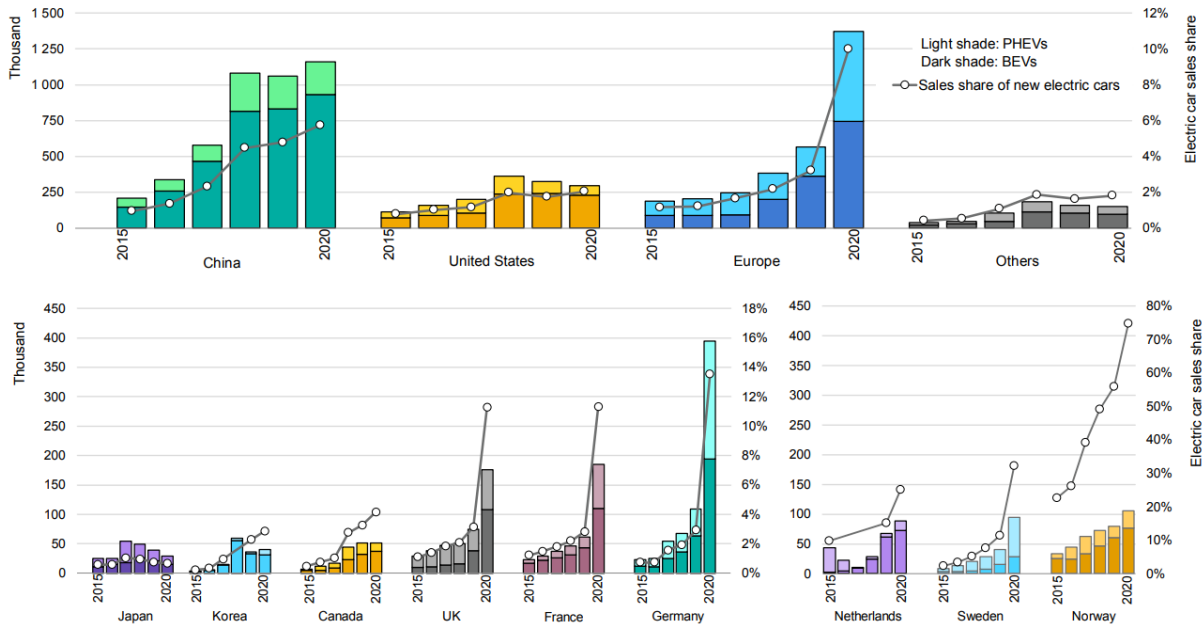


**Figure 1.3:** Electric car registrations and sales share in selected countries and regions, 2015-2020: PHEV = plug-in hybrid electric vehicle; BEV = battery electric vehicle [12].

Not less important is the expected proliferation of distributed Energy Storage Systems (ESS), given that ESS constitute a promising technical solution to address the variability of RES [13]. The deployment of distributed ESS is still lagging considerably behind the deployment of DG, but it has been accelerating in the most recent years, with 4.2 GWh in new deployments of residential storage worldwide in 2020 alone [14]. Globally, behind-the-meter ESS is expected to reach 57 GWh of new deployments worldwide by 2030 [15]. The European residential ESS cumulative market evolved from some 400 MWh in 2016 to roughly 3.7 GWh in 2020 [14, 16], being posed to reach above 27 GWh by 2030 [15].

These figures largely result from energy policies that have been adopted worldwide. In this matter, the European Union (EU) represents the most relevant case. EU had defined ambitious targets on a new 2030 Framework for climate and energy [17], whose overall objectives are:

- a 45% cut in greenhouse gas emissions compared to 1990 levels;
- at least a 32% share of renewable energy consumption;
- at least 32.5% in energy savings compared with the business-as-usual scenario.

However, a revision of the 2030 Framework for climate and energy was proposed by the European Commission in July 2021, where a 55% cut in greenhouse gas emissions compared to 1990 levels is targeted [18]. Many other initiatives within the EU could be mentioned. For example, Portugal have set ambitious targets to reach carbon neutrality until 2050, under the RNC2050 program [19]. Among the goals are the potential of nearly 100% penetration of renewable energy in the transportation sector, and about 12-13 GW of dispersed installed PV generation capacity.

The United States (US) has recently strengthened their commitment for a clean energy future. Adding to the existing measures, such as the favorable financial incentives through federal tax credits and the many states' renewable integration targets [20, 21], a plan for a 100% clean energy economy and net-zero emissions no later than 2050 was proposed in 2021, with a federal \$1.7 trillion investment over the next 10 years.

China has also defined ambitious targets for the energy transition, aiming to peak their carbon dioxide emissions before 2030 and achieve carbon neutrality by 2060 [22].

However, the increasing penetration of Distributed Energy Resources (DER) such as DG and EV is expected to amplify important adverse impacts in the electric power systems as they are today regarding operation and control, specially in distribution networks [23–25]. Adverse impacts related to voltage control and line congestion in distribution networks are among the most relevant. The need to overcome adverse impacts has been fostering the development of innovative architectures and control capabilities.

Concepts such as Microgrids (MG), Multi-Microgrids (MMG) and hybrid AC/DC distribution networks have been proposed in order to enable high penetration ratios of DG and EV in distribution networks, usually under the smart-grid concept umbrella [26–29]. Under these concepts, ESS may play an important role [30]. Moreover, more advanced configurations based on such concepts, such as the Hybrid AC/DC Microgrid concept (HMG)[31–34] and the more broader Hybrid AC/DC Multi-Microgrid concept (HMMG)[35–37], are gathering an increasing interest given their enhanced flexibility and resilience. In comparison with MG based on AC networks, MG based on hybrid AC/DC networks have a set of characteristics that make them more attractive to deal with increasing penetration ratios of DG, EV and ESS in distribution networks. Many RES technologies generate in DC and many loads are nowadays operated in DC through a AC/DC rectifier. In addition, DC/DC converters are more efficient, contributing to highlight an increasing interest in DC solutions.

It is worth to mention that the great potential in these domains have been enabled by correspondent advances in the power electronics domain. Power electronics has been fundamental for the widespread of DG itself and to enable the increasing number of control possibilities that characterize the aforementioned concepts [38–40]. Moreover, power electronic converters are necessary to interface AC and DC network subsystems forming the HMG, and may be present in the interface between the HMG and the upstream system.

But despite all the developments taking place, the existing solutions remain insufficient in many aspects to properly cope with the exponential increase in penetration ratios of DG, EV and ESS in distribution grids. The existing solutions do not offer a satisfactorily standardized and scalable platform capable to enable HMG and HMMG with a wide range of advanced control capabilities while providing galvanic insulation between different voltage levels and facilitating the integration of DC networks, HMG and HMMG with legacy AC distribution networks. Advanced control capabilities such as frequency–active power support to the upstream AC power system, voltage regulation, Fault-Ride-Through (FRT) and islanded operation capabilities are among the most relevant.

A relatively recent concept, evolving within the power electronics domain, has been gathering an increasing interest as a possible game changer – the Smart-Transformer (ST) concept. The ST offers the possibility to enhance power system resilience and controllability in the distribution grid domain, making use of the most recent developments in power electronics regarding costs and technical capabilities [41]. The ST is based on the Solid-State Transformer (SST) concept, where the traditional Low-Frequency Transformer (LFT) is replaced by a high-frequency transformer (HFT) interfaced with electronic power converters in both sides. The original application scope of the SST was to provide the desired galvanic isolation but with reduced size and weight. However, the ST concept focuses in advanced control, monitoring and observability capabilities to the distribution grids, with hardware advantages relegated to a secondary position [41]. The capacity to provide DC link connectivity and total decoupling between Medium-Voltage (MV) and LV networks in terms of voltage and frequency, endows the ST with unmatched flexibility and control capabilities. Besides providing galvanic isolation, the ST has the potential to provide voltage and frequency regulation, enable the development of hybrid AC/DC distribution networks, act as a front-end to provide FRT to its distribution networks, explore the MG concept and islanded operation both for MV and LV networks, among other possibilities. For that reason, the ST emerges as an interesting alternative to the current power electronic interface topologies due to its

greater potentialities. The ST potential is of such magnitude that it may well become the backbone of tomorrow's modern distribution grids [42]. As such, the ST is adopted as the key element in the scope of the work developed in this PhD thesis.

## 1.2 Objectives of the Thesis and Research Questions

Derived from the context presented in section 1.1, the overarching objective of this thesis is to identify and develop advanced control functionalities for ST enabling the consolidation of the HMG and HMMG concepts in face of increasing penetration ratios of DG, EV and ESS. Due to the wide range of the potentialities offered by the ST, it is not possible to address them all with the deserved detail in this thesis. Instead, this PhD thesis focuses in a set of selected topics related to the future role of HMG and HMMG in the electric power system of the future, being selected in accordance to its prospective coverage in the existing literature. Hence, considering the relevance of the ST to act as a key building block for the formation of HMG and HMMG, the main objectives of this PhD thesis can be stated as follows:

- Evaluation of the capability of HMG based on ST to provide power–frequency support functionalities to the upstream AC power system, by exploiting the flexibility available in the fleet of distributed resources located in the HMG.
- Evaluation of the incorporation of FRT capabilities in a ST with its MV inverter operating in grid-following mode, in order to improve immunity to fault disturbances within its HMG in events where energy storage capacity is insufficient or unavailable.
- Evaluation of the capability of the ST to sustain the islanded operation of a HMMG and sections of the legacy MV AC network, following fault disturbances in the upstream power system. This objective is tackled by exploiting the operation of the MV inverter of the ST in grid-forming mode, but incorporating FRT capabilities enabling the ST to remain connected during the fault disturbance and sustain the islanding procedure. The use of a single ST or the coordination of multiple ST in the formation of the islanded HMMG is investigated.
- Evaluate the role of ST in the reconfiguration of radial and meshed grid structures within a HMMG. A particular focus is given to the evaluation of communication-free strategies enabling the permutation between radial and meshed grid configurations formed by two or more LV AC grids derived from different distribution substations (based on ST and LFT).



From the presented objectives, the following research questions were formulated:

- Is the ST capable to provide frequency support to the upstream system, by exploiting the active power flexibility available in its HMG?
- Can a grid-following ST improve the immunity of its HMG against fault disturbances occurring in the upstream AC grid, even if no suitable energy storage capacity is available?
- Is the ST operating in grid-forming mode capable to provide FRT capabilities in face of fault disturbances in the upstream system, in order to allow the transition of HMMG or sections of the legacy MV network to islanded mode without interruption of supply?
- Is the ST capable to sustain the islanded operation of sections of an HMMG, alone or in coordination with other ST?
- Can the ST use communication-free control strategies to enable the reconfiguration between radial and meshed grid configurations within a HMMG?

### 1.3 Structure of the Thesis

A brief historical background and a review of the state-of-the-art of MG and ST are presented in Chapter 2. The most relevant concepts and architectures for MG, hybrid AC/DC networks and ST, advanced functionalities suitable for MG and MMG based on ST, and existing technical challenges are addressed in Chapter 2.

Chapters 3 and 4 present the adopted modeling approaches and developed control strategies for HMG, HMMG and ST. Chapter 3 is devoted to describe the computational modeling approach, hardware architectures and elementary control structures considered in the development of the simulation models for the HMG, HMMG and ST used in the various case studies addressed in this PHD thesis. Chapter 4 is focused on the description of the advanced control strategies developed for the operation of HMG and HMMG, namely for power-frequency control, FRT and islanded operation of HMG and HMMG.

Chapters 5 and 6 present the various case studies considered in this thesis and respective results. Chapter 5 presents the case studies and respective results related to the developed advanced control strategies for power-frequency support. Chapter 6 presents the case studies and respective results related to the developed FRT strategies for ST with its MV inverter operating in grid-following and grid-forming mode, and their ability to enable HMG and HMMG survival against fault disturbances in the upstream power system and subsequent islanding. It also presents a case

study and respective results demonstrating the developed functionalities enabling the reconfiguration of sections of LV AC sub-grids within an HMMG between radial and meshed configurations.

To conclude, Chapter 7 summarizes the findings of this thesis, answering the raised research questions. The research limitations identified and assumed in the presented work are also discussed. At last, the main contributions of this thesis for the state-of-the-art are highlighted, and future research topics are identified.

## 1.4 Contributions of the Thesis

The overall contribution of this thesis is the validation of HMG and HMMG based on ST as suitable solutions to address the expected increasing penetration of DG, EV and ESS in distribution networks in terms of improved resiliency, observability and controllability. More particularly, the following contributions for the literature must be highlighted:

- Reinforcement of the ST's potential as the backbone of future distribution grids. Based on the work presented in this thesis, it became clear that the ST offers a modular solution for the formation and integration of HMG and HMMG in legacy AC distribution grids.
- The capability of HMG based on ST to provide power–frequency regulation to the upstream AC system. It is shown that using the ST, even legacy LV AC networks without controllable resources can provide power-frequency regulation to the upstream AC system.
- It is shown that HMG and HMMG based on ST can withstand fault disturbances without disconnecting from the main power system until the fault clearance or an islanding procedure takes place. It is also demonstrated that ST can sustain HMMG and sections of the upstream AC MV network in the advent of an islanding procedure.
- It is shown that HMG based on ST can incorporate FRT strategies which can strongly mitigate the adverse impacts of fault disturbances in the upstream AC system even if no energy storage capacity is available for the ST.
- The ST capability to support the reconnection of its LV AC sub-grid with other LV AC grids in meshed configurations without interruption of supply, enabling multiple feeding points with obvious benefits regarding continuity of supply.

## Chapter 2

# Microgrids and Smart-Transformer Development

### 2.1 Historical Background

This section presents a brief historical review regarding the development and evolution of the Smart-Transformer (ST), Microgrid (MG) and Multi-Microgrid (MMG) concepts within the scope of active distribution grids.

#### 2.1.1 From Solid-State Transformer to Smart-Transformer

The first concept of a Solid-State-Transformer (SST) was based on thyristors and emerged in the late 1960s/early 1970s [43, 44]. Initially thought for distribution systems [44], its first serious consideration was for traction applications in the turn of the millennium [45]. At the time, the traditional low frequency traction transformers faced important limitations regarding volume and weight, which compromised its efficiency (typically around 90%) due to the required high power densities. Comparatively to the traditional low-frequency traction transformers, the SST could provide high reductions in volume and weight with improvements in efficiency.

Several companies sought to develop a functional single-phase (AC-DC) SST for traction applications, which resulted in several prototypes and even in a shunting locomotive equipped with a fully functional SST, field tested on the Swiss railways [46] (see Figure 2.1). However, no actual development of a SST reached industrial production. The use of a SST for traction applications could only be justified by gains in hardware (possible additional control functionalities play a very limited role), but

such gains are considerably reduced with the adoption of 50Hz distribution networks in traction systems, which is becoming the current standard [47].



**Figure 2.1:** SST prototype (1.2-MVA) for a 15kV 16.7Hz railway grid (adapted from [46]).

Nevertheless, the consideration of the SST to provide advanced control functionalities for distribution networks is experiencing a growing momentum since the beginning of the millennium [48]. The SST designed for this purpose started to be frequently designated as “Smart Transformer” (ST) [41, 47]. Important technical obstacles deterring the implementation of SST for distribution networks could be overcome with the emergence of the wide-bandgap Silicon-Carbide semiconductors [49, 50]. Industrial prototypes were already developed [51–53] and tested in real MV networks [52]. Although no industrial application in distribution networks exists so far, the development of a demonstration trial of ST within secondary substations on a real distribution grid is under way in the LV Engine project developed by SP Energy Networks [54].

### 2.1.2 Microgrids

The Microgrid (MG) concept, initially introduced in the early 2000s [55–57], was originally thought as a AC Low Voltage (LV) grid formed by a cluster of micro-sources, Energy Storage Systems (ESS) and loads, interfacing with the wider power system through a controllable circuit breaker or other types of controllable devices, but presenting itself to the power system as a single entity able to respond to central control signals [56]. Its purpose was to take advantage of new opportunities for on-site power generation (thermal and electric energy) enabled by new generation technologies (such as micro-turbines and fuel cells) in order to meet the growing customer’s needs regarding reliability, efficiency and power quality [57]. The MG has distinctive features such as the ability to operate in islanded mode or connected to the power grid, and the possibility to control and dispatch internally the available resources with partial or total

autonomy from the main power system [56]. Soon after, the MG concept was further developed in two consecutive European projects (*Microgrids* and *More Microgrids*) in the same decade (2003 - 2009) [58, 59]. Since then, the MG concept has been observing important developments, which occasionally originated distinct research paths. The most relevant developments are addressed in the following sub-sections.

#### 2.1.2.1 AC and DC Microgrids

In its initial developments, the application of the MG concept was focused on AC LV grids (AC MG) [56, 57], which resulted in several implementations worldwide [60]. The development of AC MG was a logical starting point given the existing experience with large AC grids, the dominance of AC loads, and the maturity of DC/AC power inverters [61].

However, the application of the MG concept to DC grids (DC MG) also emerged soon after [62], as it became notorious that DC distribution grids could offer important advantages comparatively to their AC counterpart [63]. Initially, DC MG were envisioned as a suitable solution to reduce costs and energy losses (as less power converter stages were required), and to improve the integration and control of Distributed Energy Resources (DER) which are DC by nature [62]. Other advantages were further identified. DC MG have no requirements regarding reactive power control, frequency control and synchronization in islanded mode. DC MG also enable considerable reductions in load losses given that an increasing share of the grid load is constituted by electronic devices which are DC by nature (enabling the removal of the AC/DC converter stage) [29, 61, 64, 65]. However, their deployment in the field have faced important obstacles due to factors such as the limited experience with DC grids, lack of proper standards for DC grids and the underdeveloped state of protection devices designed for DC grids [61]. Still, some field implementations of DC MG with promising results already exist [66, 67], such as the Seogeocho demonstration site (South Korea) illustrated in Figure 2.2 [66]. Other demonstration sites are also planned or in progress [68].

#### 2.1.2.2 Hybrid AC/DC Microgrids and the Role of Solid-State Transformers

The aggregation of AC and DC MG emerged as a solution to combine in a single MG the advantages of AC and DC technologies in order to facilitate the integration of a heterogeneous set of AC and DC DER [69, 70]. This approach gave birth to the Hybrid AC/DC Microgrids (HMG) concept.

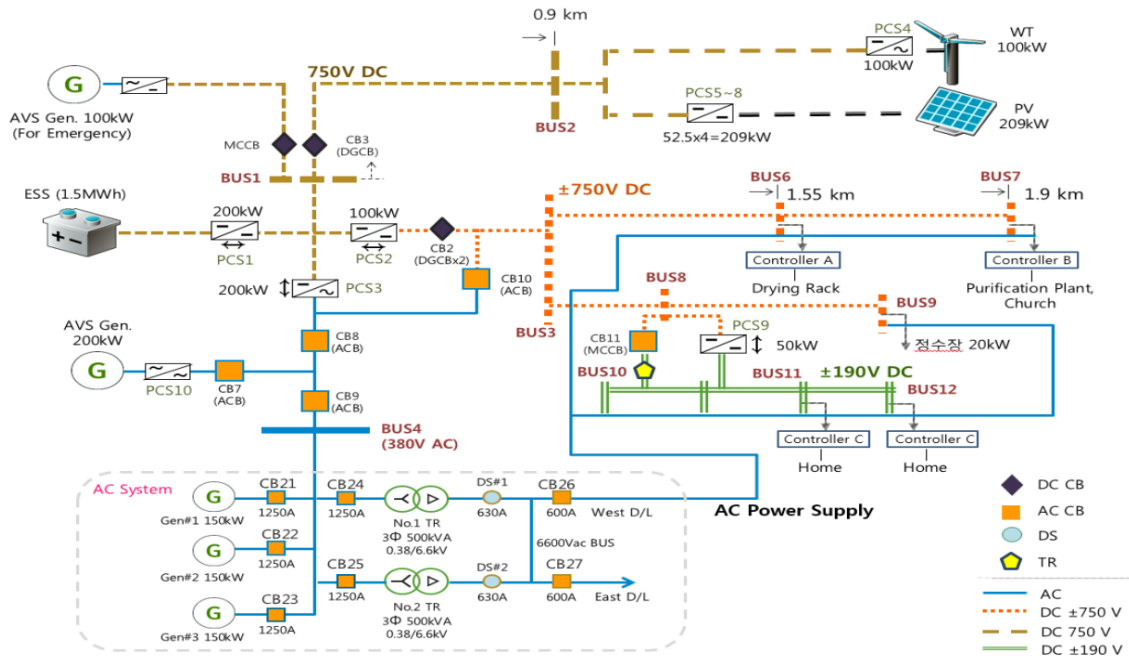


Figure 2.2: Seogeocho DC microgrid system network diagram (adapted from [66]).

However, it is important to distinguish between similar denominations found in the literature. In [32], the HMG denomination is applied to MG containing both AC/DC power sources and AC/DC loads, but this definition can overlap with the concepts of AC and DC MG mentioned in 2.1.2.1, since AC and DC loads and power sources can be connected respectively to both DC and AC MG through AC/DC power converters. Thus, a more suitable definition is adopted. Adding to the criteria proposed in [32], a HMG is a MG where there is at least one feeder, in both AC and DC zones, connecting at least two loads and/or DER, as assumed in [71]. Based on this consideration, the first true conceptualization of HMG emerged at the end of the 2000s [69, 70].

The initial architectures consisted on hierarchical integration of AC and DC zones in the same MG [69, 70], but further architectures were proposed in further research activities that took place in the following years [72–74]. However, a major development occurred with the proposal of HMG based on Solid-State Transformers (SST) in the early 2010s [75, 76]. The SST offers a modular and scalable solution capable to replace the conventional magnetic MV/LV transformer and the mechanical switches governing the connection of the HMG with the upstream power system, while providing total electrical and galvanic decoupling of the HMG from the upstream power system. It also allows the plug-and-play of distributed generation, energy storage and loads to the grid with no adverse effects on the upstream power system, enables the creation of a LV DC grid from its DC link, provides unmatched power quality to residential

users and industry customers, and enables greater control possibilities, all in one single device [75, 76]. There are several works focusing in the development of AC and DC MG based on SST [77–79], but given the existence of a DC/AC inverter in the SST itself, the HMG concept offers a better and more logical use of the potentialities offered by SST [75, 76].

Given its properties, the vision of the SST as an energy router between the HMG and the upstream power system has emerged [76]. As mentioned in section 2.1.1, the SST application oriented to the provision of advanced control functionalities to distribution power grids (which naturally includes HMG) has started to be frequently designated as “Smart Transformer” (ST) [41, 47]. Nevertheless, besides laboratory-scale demonstrators [80], no commercial implementation of HMG exists yet.

### 2.1.3 Multi-Microgrids

The Multi-Microgrid (MMG) concept started to be exploited in the late 2000s [59, 81–83], consisting on an extension of the MG concept to a higher level structure formed at the MV level, aggregating several MG, Distributed Generation (DG) and MV loads on adjacent MV feeders, governed by a hierarchical control scheme enabling its proper control and management [81].

The MMG concept was initially applied to AC grids, and the research focused on AC MMG remains of upmost relevance specially with the recent inclusion of ST [84, 85]. But in recent years, the MMG concept was extended to DC grids [86–88]. The Hybrid AC/DC Multi-Microgrid (HMMG) concept was also introduced recently [89, 90]. However, HMMG based on ST remain largely unexplored in the literature, although some elementary concepts that can be classified as HMMG have started to emerge [91, 92]. Regarding real-world applications, besides laboratory-scale test infrastructures [93], no real-world demonstration or commercial implementation of MMG currently exist.

## 2.2 Smart-Transformer: Architectures and Operation Modes

The Smart-Transformer (ST) concept is based on the Solid-State Transformer (SST) concept, but not all possible SST hardware architectures are preferred for the implementation of the ST concept. The basic concept of a SST is represented in Figure 2.3, which may be implemented through several hardware architectures as illustrated in



Figure 2.4 [47]. The SST is essentially an isolated AC-AC power converter, where the comparatively bulky Low-Frequency Transformer (LFT) is replaced by a smaller and lighter High-Frequency Transformer (HFT), interfaced with the MV and LV networks through electronic AC/AC power conversion. This fundamental aspect enables the SST to dynamically adjust its voltage transformation ratio and to operate with different frequencies in both terminals, thus enabling the integration of advanced control functionalities in comparison to the traditional LFT. In this matter, the control potentialities have increased in close relationship with the advancements in power electronics, namely regarding semiconductor technologies and conversion topologies [41, 47, 94–96]. However, *three stage* topologies, constituted by a MV AC/DC converter, an isolated DC/DC converter and a LV AC/DC converter as represented in Figure 2.5, are preferred for the implementation of the ST concept. This hardware topology provides DC-link connectivity in both MV and LV conversion stages, which enables a wider range of control possibilities [41]. No such DC-link connectivity is available in *one stage* topologies, while in *two stage* topologies the DC-link connectivity is available in only one conversion stage, thus providing better gains in terms of weight and volume. But the ST concept is precisely focused in the possible control functionalities that an SST can offer, relegating hardware advantages (such as weight and size reduction) to a secondary position [41].

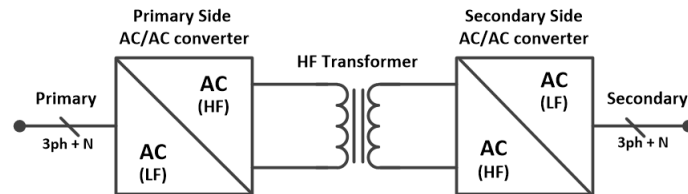
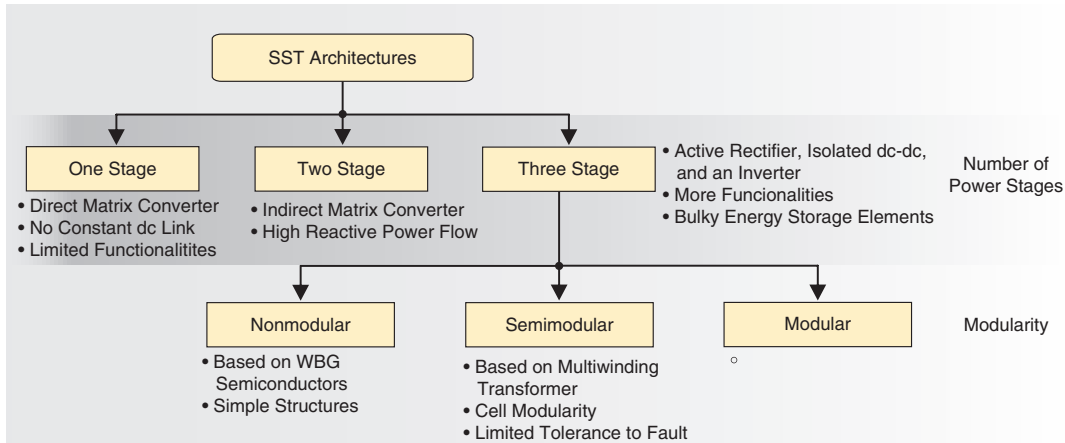


Figure 2.3: Conceptual representation of a SST.

The DC-link connectivity may be used to create MV and LV DC networks, which are better suited to integrate a range of distributed resources which are DC by nature, such as PV generation, bulk energy storage, EV charging stations, among others [41, 97]. An intermediate conversion stage (DC/AC conversion) is avoided in the user's side, thus improving the overall efficiency. The DC links also allows the separation of AC power flow between MV and LV networks, making possible to control MV and LV networks independently. For these reasons, the *three stage* group is the most attractive for the implementation of the ST concept, as it offers greater advantages from the perspective of provision of advanced functionalities to the distribution and transmission networks [41, 47, 98].





**Figure 2.4:** The classification of the SST architecture according to the number of power conversions and modularity (adapted from [47]).

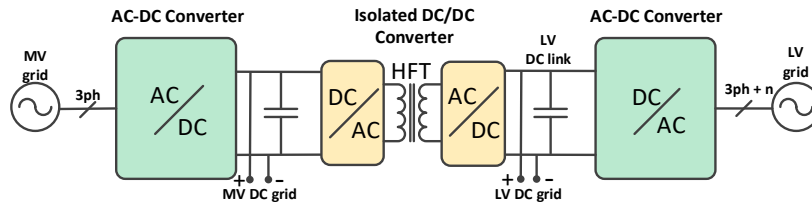


**Figure 2.5:** Conceptual representation of a ST based on a three-stage topology.

A review of the main converter topologies and control methodologies for ST based on *three stage* topologies is presented in the following sections.

### 2.2.1 Medium-Voltage Converter

The MV converter is responsible to interface the ST with the upstream power system. There are several topologies proposed for the MV inverters. Some of the most popular topologies are depicted in Figure 2.6: The Three-level Neutral Point Clamped, Cascaded H-bridge and Modular Multilevel.

Three-level Neutral Point Clamped and the Modular Multilevel topologies have been the most attractive since the MV DC-link required to obtain a three-stage ST is available. The Three-level Neutral Point Clamped has the advantage of being simpler as well as widely adopted in industry [47]. In contrast, the Modular Multilevel offers greater modularity and can operate with lower switching frequencies [47]. However, recent advances in the SiC semiconductor technology promises to further reduce the complexity of MV inverters, with improved efficiency and robustness [95, 99, 100].

Besides the aforementioned hardware topologies, there are also several control approaches that may be evaluated for ST's MV converters [101–104]. The vast majority

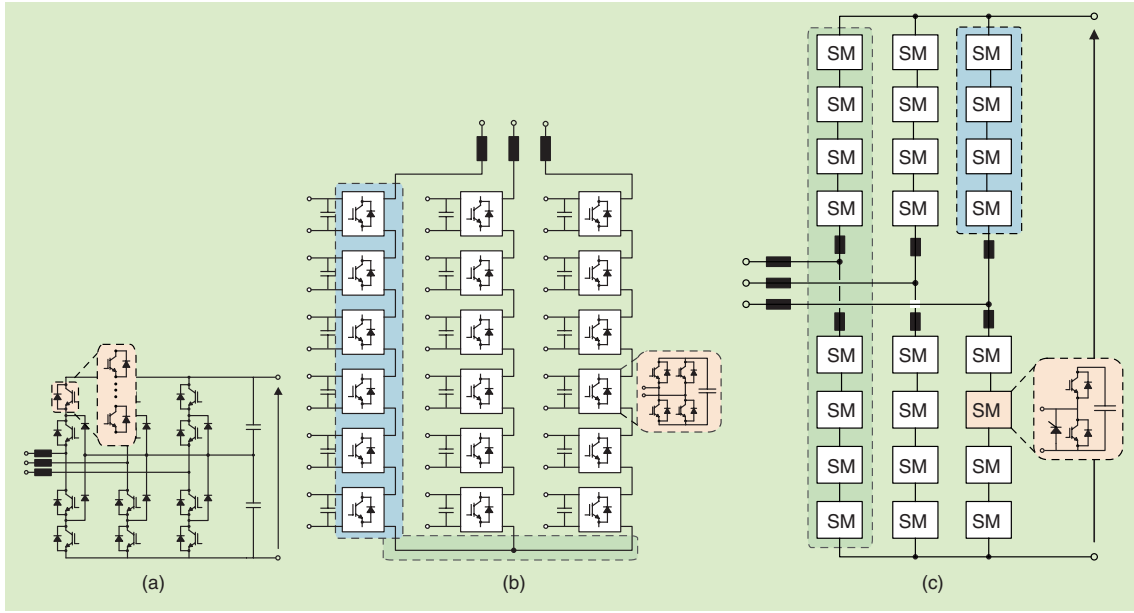


**Figure 2.6:** MV converter topologies: Three-level Neutral Point Clamped (a) Cascaded H-bridge (b) and Modular Multilevel (c) [47].

of the proposed control approaches may be classified according to two operation modes:

- **Grid-Forming:** In this operation mode, the MV inverter operates as a voltage source with a low series impedance [102], capable to regulate its voltage amplitude and frequency, which among other possibilities, can be exploited to support AC MMG autonomous operation [84] and black start [85, 105]. The grid-forming control approaches identified in [101] can be divided in two important groups: the grid-connected grid-forming controllers and the pure grid-forming controllers.
- **Grid-Following:** In this operation mode, the MV inverter operates as a current source with a high parallel impedance [102], synchronized with the voltage and frequency measured in the MV grid. The main functionality of the MV converter is to regulate the power flow between the ST and the upstream MV grid according to the needs of the ST's distribution networks [47].

The next subsections present a brief description of the most relevant control approaches.

#### 2.2.1.1 Pure Grid-Forming

Several control approaches for pure grid-forming operation are proposed in the literature [101, 102]. According to [101], the most relevant approaches can be classified as follows:

- **Droop-Based methods:** These methods are among the most popular due to their relative simplicity, with special consideration for the parallel synchronization of several grid-forming converters. The operation principle is based on the use of proportional control rules (*droops*) as depicted in Figure 2.7. According to equations shown in Figure 2.7, the regulation of voltage amplitude ( $U$ ) and frequency ( $f$ ) generated by the power inverter is function of its output reactive ( $Q$ ) and active ( $P$ ) power respectively.  $k_p$  is the proportional gain (droop) applied to the inverter's output power in order to obtain the pretended voltage magnitude and frequency modulation. Offset values also be incorporated in the droop controller in order to adjust its base operation point.  $U_0$  and  $f_0$  are the base values for the voltage magnitude and frequency respectively. Set-points can also be incorporated in the droop controller in order to adjust its base output power.  $P_0$  and  $Q_0$  are respectively the active and reactive power set-points for the power converter if the voltage frequency and magnitude at its terminals equal  $f_0$  and  $U_0$  respectively.

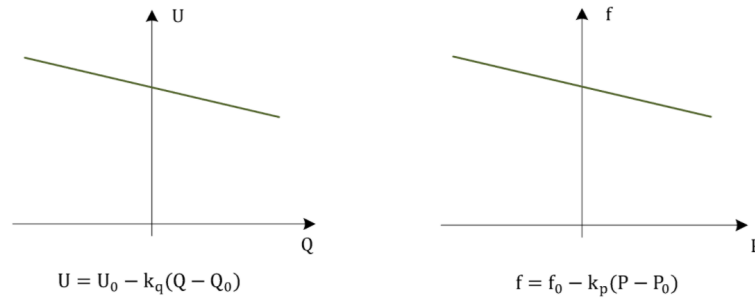


Figure 2.7: Basic droop characteristics for GF MV inverters [101].

- **Power Synchronization Loop:** The operation principle of this method is illustrated in Figure 2.8. It consists in generating a phase angle variation ( $\Delta\theta$ ) as a function of the active power error defined as the difference between an active power reference ( $P_{ref}$ ) and the measured active power ( $P$ ) in the power inverter. The generated  $\Delta\theta$  is added to a base angular position value ( $\omega_{ref}t$ ) defining the base frequency for the voltage generated by the power converter.  $\omega t$  is the final reference for the generated voltage's angular position.

This method seeks to replicate the synchronization mechanism of a synchronous machine [106]. However, this grid-forming method does not establish a well delimited approach for Voltage/reactive power control (for example, a droop-based approach may be used), and may require a backup Phase-Locked Loop (PLL) mechanism in several situations such as during initial synchronization and

fault-ride-through provision during severe faults in the AC system [106].

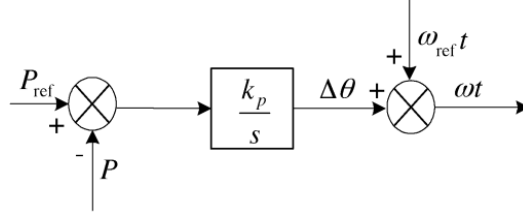


Figure 2.8: Basic representation of the Power Synchronization Loop control [106].

- **Voltage Controlled Inverter and Virtual Synchronous Machine:** The Voltage Controlled Inverter method, proposed in [107], intends to emulate the behavior of a synchronous machine, including inertia emulation and oscillation damping, but neglects the non-linearity of a real synchronous generator. Instead of relying in any representation of the swing equation, other control approaches such as PI controllers can be used [107].

Regarding the Virtual Synchronous Machine concept, it intends to directly emulate a synchronous machine based on the swing equation in its various possible differential orders [101, 108]. Figure 2.9 illustrates a possible implementation of the Virtual Synchronous Machine concept.  $p_{ref}$  and  $q_{ref}$  are the reference active and reactive power respectively,  $p$  and  $q$  are respectively the active and reactive power at the power converter's output,  $f_0$  and  $U_0$  are respectively the base voltage frequency and magnitude, and  $\theta$  and  $U$  are respectively the angular position and magnitude of the voltage generated by the power converter. The statism and damping coefficients are represented by  $k_{pf}$  and  $k_{df}$  respectively.

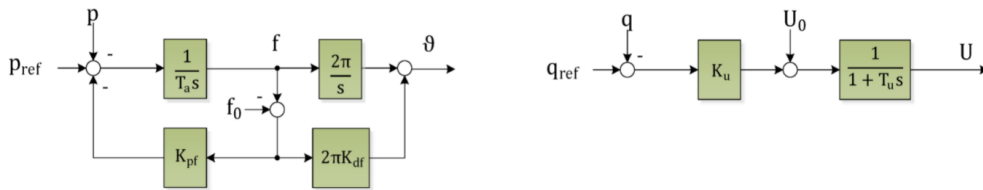


Figure 2.9: Example of a Virtual Synchronous Machine control [101].

- **Matching Control:** This approach exploits a duality between DC voltage and AC voltage angular speed in a power inverter [101, 109]. It exploits the converter's DC-link capacitance as a storage in the same way as the moment of inertia of synchronous generators stores kinetic energy. Any power unbalance in the DC-link translates into a DC voltage variation which, in turn, may be transformed in a frequency/phase angle compensation. This control approach can operate only

with the DC voltage measurement to perform self-synchronization [109]. Figure 2.10 illustrates a possible implementation of a matching control. The angular frequency  $\omega^*$  for the voltage generated by the power converter is function of the error between the measured DC voltage ( $V_{DC}$ ) and reference DC voltage ( $V_{DC}^{ref}$ ). The remaining elements of the equation seek to emulate the behavior of a synchronous machine, where  $K_T$  is the DC-link voltage tracking coefficient,  $K_J$  is the inertia emulation coefficient and  $K_D$  is the damping coefficient.

Regarding voltage/reactive power control, this grid-forming method is not limited to a specific approach. In the example depicted in Figure 2.10, a droop-based controller is used to regulate the voltage magnitude  $E$  as a function of a base voltage values  $V_0$  and the error between the reference and measured reactive power ( $Q_0$  and  $Q_E$  respectively).  $K_Q$  is the slope of the droop controller.

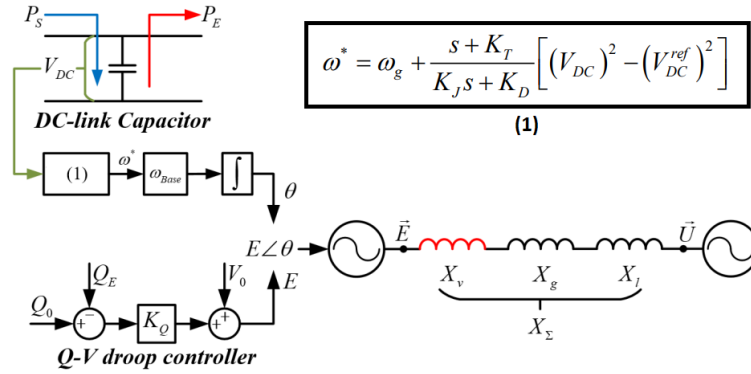
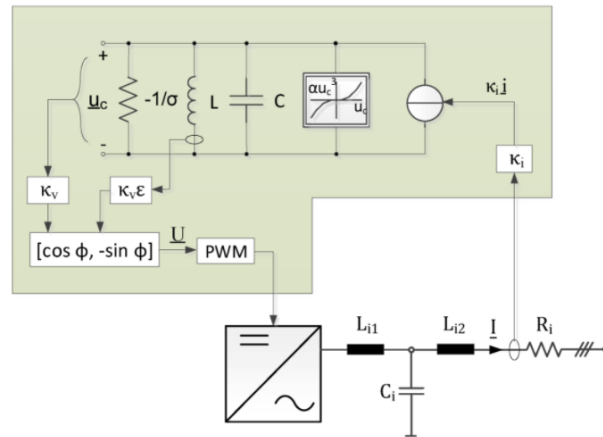


Figure 2.10: Block diagram of an example of a matching controller (adapted from [109]).

- **Virtual Oscillator Control:** This control method is very distinct from the previous methods because it is not based on phasor representation of voltages and currents, relying instead on a sinusoidal time domain representation [110]. It exploits the synchronization principle of coupled oscillators in complex networks, employing methods such as the *Van der Pol* oscillator (which uses a nonlinear differential equation to generate the virtual oscillator) [110], the virtual Dead-Zone oscillator [111] and the Space Vector oscillator [112].

Figure 2.11 illustrates an example of a Virtual Oscillator control based on a *Van der Pol* oscillator, presented in [101]. The circuit model of the Van der Pol oscillator is constituted by the parallel connection of an inductance ( $L$ ) and a capacitance ( $C$ ) tuned for resonate at the nominal frequency  $\omega_0$ , a negative conductance element ( $-1/\sigma$ ), and a cubic voltage-dependent current source ( $\alpha u_c^3$ ). The virtual oscillator interfaces with the physical electrical signals through the voltage and current scaling gains  $k_v$  and  $k_i$  respectively.



**Figure 2.11:** Block diagram of a virtual oscillator controller based on a Van der Pol oscillator (adapted from [101]).

Although a relatively recent research topic, Virtual Oscillator control methods are gaining increasing interest due to its very fast response capabilities, implementation simplicity (requires less sensors) and robust stability, added to power dispatch capabilities (Dispatchable Virtual Oscillator control [113]) and fault-ride-through capabilities (Unified Virtual Oscillator control [112]). However, it provides no inherent inertia emulation capabilities, thus requiring additional control mechanisms for that purpose.

### 2.2.1.2 Non-pure Grid-Forming

Besides pure grid-forming controllers, there are several grid-forming control approaches relying on grid's voltage/current measurements in order to perform self-synchronization during its normal operation. Given this dependence, power converters using these control approaches are not generally preferable to sustain islanded power grids, although there are research activities showing that power grids can be sustained solely by power converters using such control approaches [101]. The most relevant approaches described in the literature can be classified as follows:

- **Direct Power Control:** The working principle of this approach consists in using the converter's measured output power flow to directly estimate the converter's output AC voltage. A Phase-Locked Loop (PLL) may be used [101, 114] but it is not a requirement to estimate the converter's output AC voltage [101, 115]. An example of a PLL-free Direct Power Control (Grid Voltage Modulated - Direct Power Control) is presented in [115] and is illustrated in Figure 2.12. This approach offers the advantages of lower computational burden (no PLL nor Park transformation required) and better tracking performance comparatively to

control structures based on PLL [115].

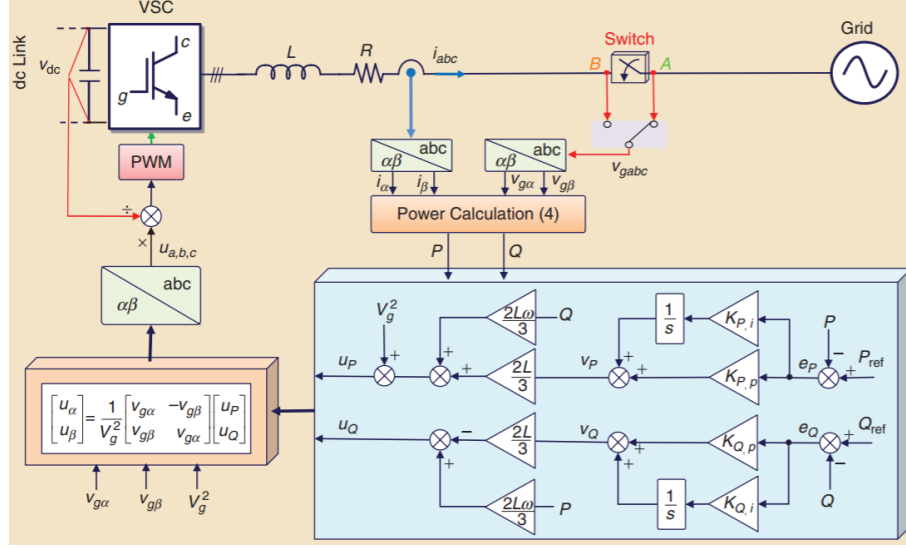


Figure 2.12: Block diagram of a PLL-free Direct Power Control [115].

- PLL-based Droop-Control:** This control approach is based on the previously addressed droop-based grid-forming approaches, but the value for the nominal frequency is replaced by the grid's frequency measured by a PLL [116]. An example of such approach is described in [116] and is depicted in Figure 2.13. The main advantage reported in [116] is the improvement of power sharing capabilities in power inverters, being possible to define and keep a steady-state power set-point regardless the existing grid's frequency. However, this particularity comes at the expense of greatly limiting frequency regulation capabilities by using this control approach.

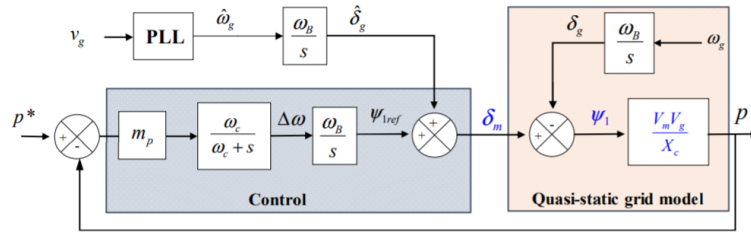


Figure 2.13: Droop-based Grid-forming control with PLL [116].

### 2.2.1.3 Grid-Following

Several control approaches for grid-following operation of power inverters have been studied and implemented as well [103, 104]. The most relevant grid-following control approaches can be classified as follows:

- **Voltage Oriented Control:** This control approach is based on the Field Oriented Control (FOC) approach widely applied in the control of AC synchronous and induction machines [117]. The basic principle consists in representing the three-phase voltages and currents as two orthogonal components —the direct and quadrature components —in a two coordinate time invariant referential (also denominated rotating dq reference frame) orientated to the grid voltage [118]. Both orthogonal component are decoupled and can be controlled as DC signals using, for instance, PI controllers. An example of such approach is described in [118] and is depicted in Figure 2.14.

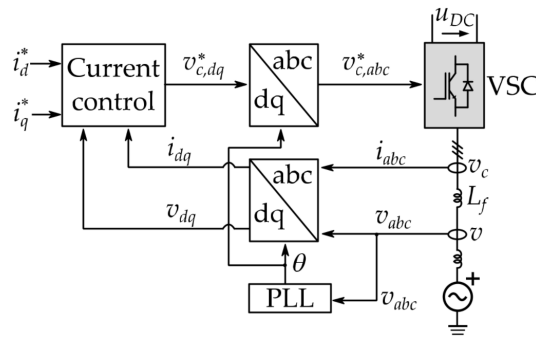
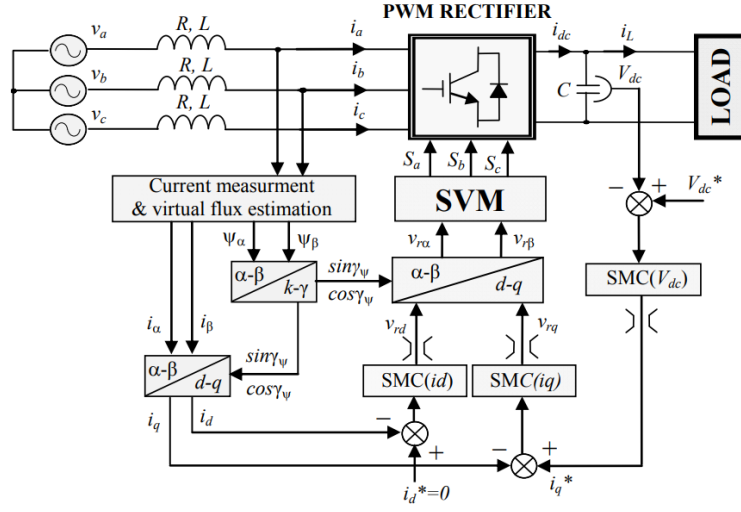


Figure 2.14: Example of a Voltage Oriented Control structure [118].

- **Virtual Flux Oriented Control:** Similarly to the Voltage Oriented Control (VOC), the Virtual Flux Oriented Control (VFOC) is also based on the FOC. However, while the VOC synchronizes with the grid voltage, the VFOC synchronizes with a hypothetical flux vector which a grid voltage would originate in an induction machine [119, 120]. This hypothetical flux vector is given by the integration of the grid voltage, which results in a flux vector displaced from the grid's voltage vector in  $90^\circ$  [119, 120]. As a result, contrarily to the VOC, the active power is controlled by the quadrature orthogonal component. An example of a VFOC control is described in [120] and is schematized in Figure 2.15.
- **Direct Power Control and Virtual Flux Direct Power Control:** The Direct Power Control (DPC) approach follows the basic principles of the DPC for grid-forming inverters addressed in section 2.2.1.2 [103]. The Virtual Flux Direct Power Control (VFDPC) is based on the DPC, but while the DPC synchronizes with the grid voltage, the VFDPC synchronizes with a hypothetical flux vector which a grid voltage would originate in an induction machine. An example of a VFDPC control is described in [103] and illustrated in Figure 2.16.





**Figure 2.15:** Example of a Voltage Field Oriented Control structure [120].

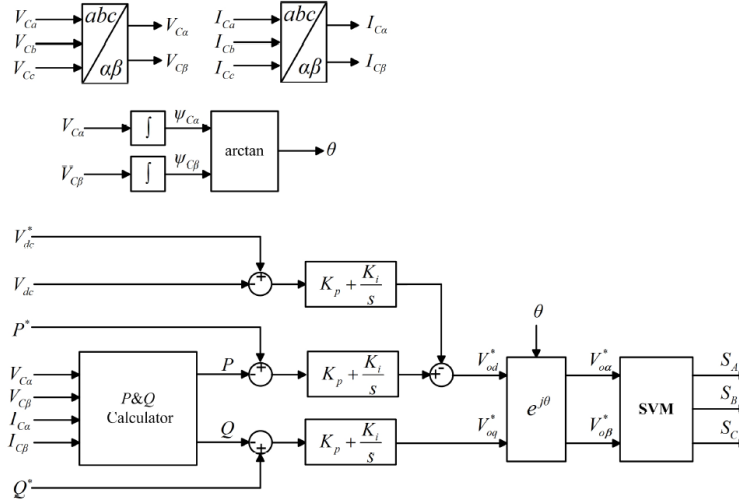


**Figure 2.16:** Example of a Virtual Flux Direct Power Control structure [103].

#### 2.2.1.4 PLL-based Modified Current Control Methods

The PLL-based Modified Current Control methods present a blurred line between grid-forming and grid-following control modes [101]. Although based on PLL-based current control methods (which typically fall in the grid-following group), these methods have shown to be able to sustain islanded power systems [121, 122], which is an important feature generally attributed to grid-forming control approaches. Power converters grid-following by nature (using a current control scheme) can become grid-forming with the addition of suitable outer control loop extensions, as demonstrated in [121, 122]. An example of such approach is described in [121] and is depicted in Figure 2.17.

Despite its potential (given that most power converters employed in DER rely on current control methods), these control methods require further investigation as

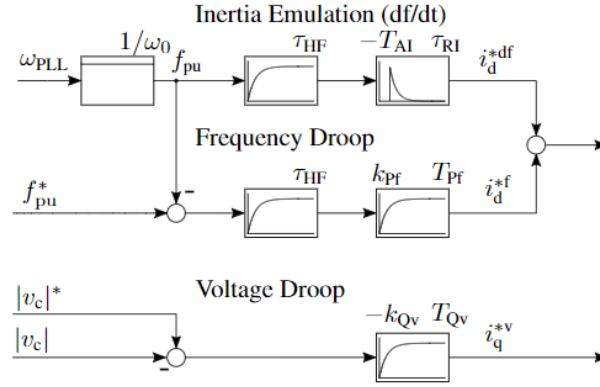


**Figure 2.17:** Example of a PLL-based Modified Current Control: Outer control loops for grid support [121].

they still have significant disadvantages regarding complexity and dynamic stability comparatively to the most typical grid-forming control methods [121].

### 2.2.2 Low-Voltage Converter

The LV converter is conceived to interface the ST with the LV AC network. A broader range of conversion topologies are available for the LV range [47]. The main requirement is the availability of the neutral wire, since one of the main ST targets is to replace the LFT. The half-bridge topology represents the simplest approach and a consolidated solution but three-level topologies have been accepted as feasible solutions as well, even by industry [41, 47]. The most popular topologies for LV inverters are represented in Figure 2.18. For higher currents in the ST's LV stage, several LV converters connected in parallel can be used.

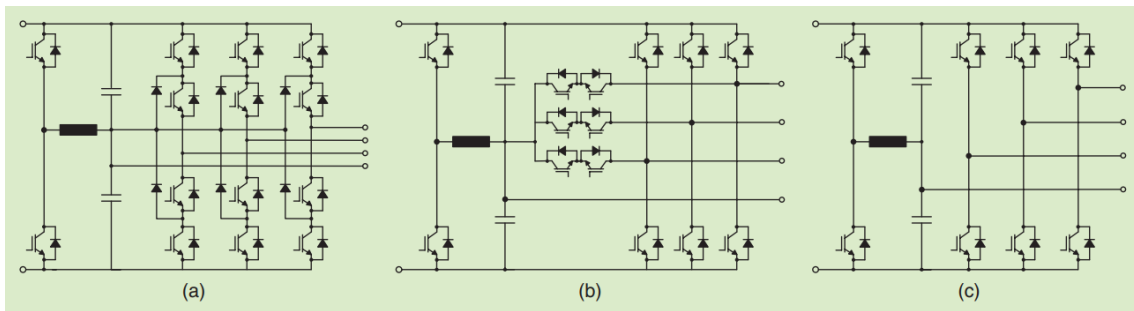


**Figure 2.18:** Four-wire topologies for the LV converter stage: Three-level Neutral Point Clamped - classic (a), Three-level Neutral Point Clamped - T-type (b) and Full-bridge (c) [47].

Usually the ST's LV converter is envisioned as the responsible for the formation of the LV AC network to which it connects, reason why the LV converter is usually conceived to operate in grid-forming mode in order to generate the magnitude and

frequency references for the voltage applied to the LV network. However, meshed LV AC networks involving other ST or conventional LFT may be considered as well. The several approaches addressed from section 2.2.1.1 to section 2.2.1.4 could be suitable candidates, according the AC LV grid topology and DER connected to it. For example, in [123] a Direct Power Control approach is used for both grid-forming and grid-following operation of the ST's LV inverter connected to a meshed LV network connected to a LFT.

### 2.2.3 Bidirectional Isolated DC-DC Converter

The Bidirectional Isolated DC/DC converter is responsible to provide galvanic isolation, to manage the active power transfer between MV and LV levels, and to adapt the DC voltage levels between both MV DC and LV DC links. The most investigated topologies for ST are the Dual-Active-Bridge (DAB) converter, the Series-Resonant converter and Multiple-Active-Bridge converter [47], represented in Figure 2.19. The DAB and the Series-Resonant converters have received more attention because of their advantages of soft-switching, high efficiency, and power density [41, 47, 124]. Nevertheless if output voltage control or power flow control is required, the DAB converter is preferable because it operates with active control of the transferred power [41, 47]. The Multiple-Active-Bridge converter has the same features as the DAB converter with the additional characteristic of reducing the number of high-frequency transformers because it integrates more active bridges to a single transformer [47].

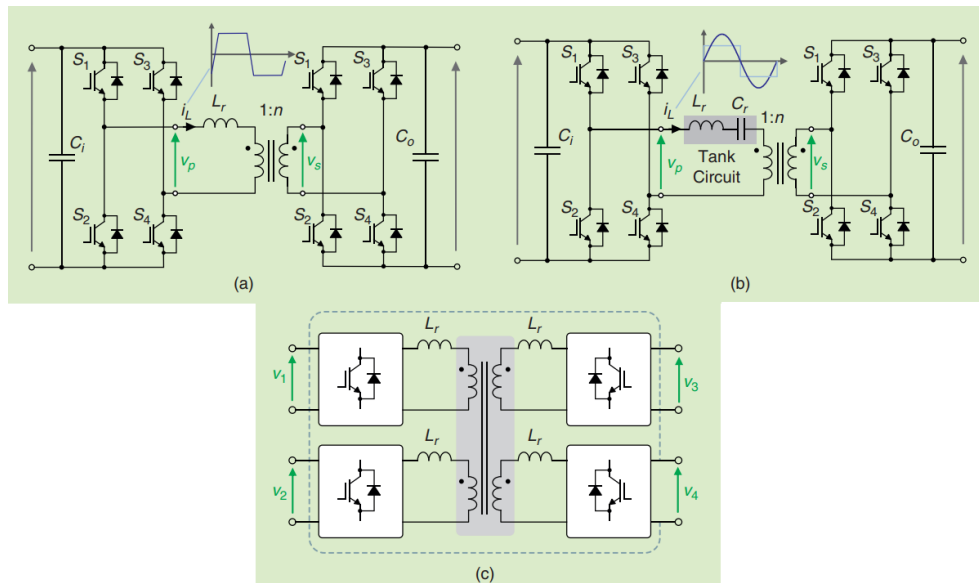


**Figure 2.19:** Topologies for the bidirectional isolated DC-DC converter stage: Dual-Active-Bridge (a), Series-Resonant (b) and Multiple-Active-Bridge (c) (adapted from [47]).

## 2.3 Microgrids and Multi-Microgrids: Concepts and Architectures

The microgrid (MG) concept is widely regarded as a key element within the smart-grids concept [125]. MG appears as a suitable solution to control and manage the integration of DG and other distributed resources such as EV and ESS in LV distribution networks [64, 125–127]. Moreover, MG promote several other advantages, such as improvements in grid resilience and quality of supply [125], as well as the possibility of operating as a grid cell while offering regulation services to the upstream power grid.

The Multi-Microgrid (MMG) concept consists of an extension of the MG concept to a higher level structure formed at the MV level, aggregating several MG, DG and MV loads on adjacent MV feeders, governed by a hierarchical control scheme enabling its proper control and management [81].

A review of the main concepts and architectures is presented in the next sections.

### 2.3.1 AC Microgrids

Due to historical and technical reasons, AC distribution grids have been the earliest and most straightforward platform to implement the MG concept [64, 125, 128]. Typical distribution networks are hereditarily AC which have a simpler design and are easier to synchronize with upstream AC systems, and most loads are prepared to work in AC networks. An example of an AC MG is illustrated in Figure 2.20 [129], where several key constituents are identified: the MG central controller (MGCC), load controllers (LC), microsource controllers (MC) and EV controllers (VC).

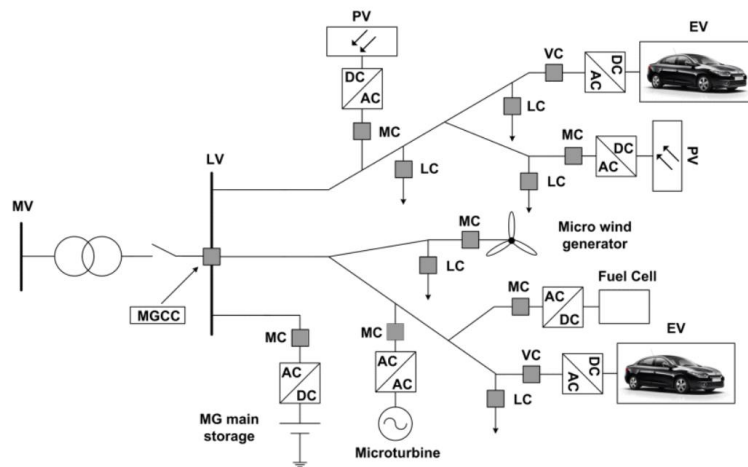


Figure 2.20: Basic architecture of an AC microgrid [129].

As pre-existing AC distribution grids can be used, besides switching equipment (to island and reconnect the MG), energy storage capacity (to sustain islanded operation) and eventually DG (to provide local generation), the required additional hardware investments to setup an AC MG are minimal compared to DC MG. Both radial and meshed AC distribution networks are suited for the AC MG concept [60, 130, 131].

Several control methodologies have been proposed for AC MG, with the most relevant comprising a hierarchical structure constituted by primary, secondary and tertiary control levels [132–135]. An example of such control structure is represented in Figure 2.21.

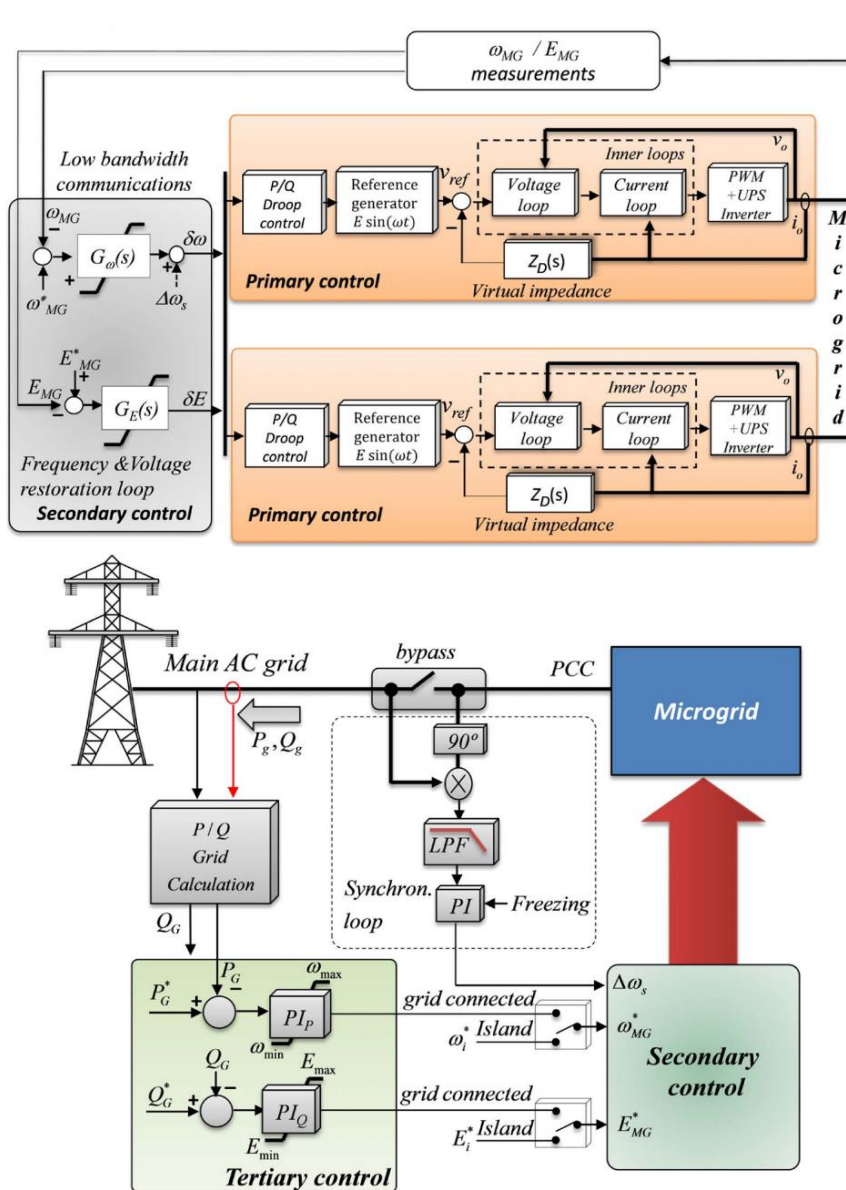
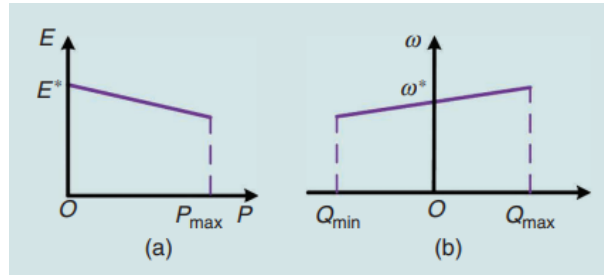


Figure 2.21: Example of a hierarchical control of an AC MG: Primary, Secondary and Tertiary control [135].

The primary control layer is responsible to adjust the voltage and frequency in the controllable DER resources integrating the MG in order to preserve the power balance in the MG and the synchronous operation of the involved DER units. According to [132, 133], the most popular primary control approaches for AC MG can be categorized as follows:

- **Droop-based control:** This control approach represents the most popular control approach to support the autonomous operation of AC MG. Several subcategories of droop-based controls are described in the literature [133], but the basic principle is the incorporation of proportional control rules through the MG's DER in order to obtain a distributed and communication-free primary control of MG's voltage and frequency as a function of the DER's active and reactive power outputs. A possible set of droop control rules for predominantly resistive MG is illustrated in Figure 2.22, where the voltage ( $E$ ) and frequency ( $\omega$ ) are function of the output reactive ( $Q$ ) and active ( $P$ ) powers respectively [133].



**Figure 2.22:** Example of droop characteristics for MG: Active power - voltage droop (a) and Reactive power - frequency droop (b) [133].

- **Master-Slave control:** This control approach, mainly devoted to support the autonomous operation of MG, offers a centralized but communication-reliant approach to control the MG's voltage and frequency. In this approach, the dominant DER can be assigned as the master unit, controlling MG's voltage and frequency within a permissible range (V-f unit), being the remaining units assigned as slave units operating in constant power control mode (P-Q units) [132, 133]. However, this approach is more difficult to expand and its reliance on communications and on a single master unit poses important reliability challenges [133].

The secondary control is responsible to restore the MG's voltage frequency and magnitude to the respective references after every change of load or generation inside the MG. As exemplified in Figure 2.21, the measured voltage frequency ( $\omega_{MG}$ ) and magnitude ( $E_{MG}$ ) are compared with the respective references ( $\omega_{MG}^*$  and  $E_{MG}^*$ ), being

the error used by the respective controllers ( $G_\omega(s)$  and  $G_E(s)$ ) to correct the MG's voltage frequency ( $\delta\omega$ ) and magnitude ( $\delta E$ ).

The tertiary control aims to control the power flow in the MG when the MG is operating in grid-connected mode [135]. The active and reactive power exchanged by the MG with the upstream power system is controlled by regulating the steady-state phase angle (by acting on the frequency) and voltage magnitude inside the MG. Its operations is exemplified in Figure 2.21.

### 2.3.2 DC Microgrids

Although AC MG were pioneer, subsequent developments in power electronics and protection technologies for high DC currents have dragged an increasing attention to DC MG. Comparatively to their AC counterpart, DC MG offer a set of potential advantages. DC MG provide a more efficient and reliable integration of DER being DC by nature (such as EV fast charging stations, ESS and PV generation), since the unnecessary AC/DC conversion stages can be dismissed [136, 137]. Other advantages have been highlighted, such as the absence of issues related to reactive power flow, voltage and load unbalances, synchronization, harmonics and frequency regulation [136, 137]. Both radial and meshed DC distribution networks are suited for the DC MG concept [137–139].

Several control methodologies have been suggested for DC MG as well. Similarly to AC MG, hierarchical structures constituted by primary, secondary and tertiary control levels have been also proposed for DC MG [134, 139].

Regarding primary control, the main approaches discussed in the literature resemble significantly those already mentioned for AC MG. However, in the DC MG, the DC is the single variable to be controlled. The most popular control approaches can be categorized as follows [134, 136]:

- **Droop-based control:** This control approach also represents the most popular approach to support the autonomous operation of DC MG, with several subcategories of droop-based controls discussed in the literature [139]. Similarly to AC MG, the basic principle is the incorporation of proportional control rules throughout the MG's DER in order to obtain a distributed and communication-free primary control of the MG. However, for DC MG, the droop-based controllers aim to regulate the DC voltage in the DC MG as a function of the DER's active power or current outputs. As exemplified in Figure 2.23, the DC voltage reference ( $V_{dc}^*$ ) is function of the output power ( $P_o$ ) or output current ( $I_o$ ) [136].



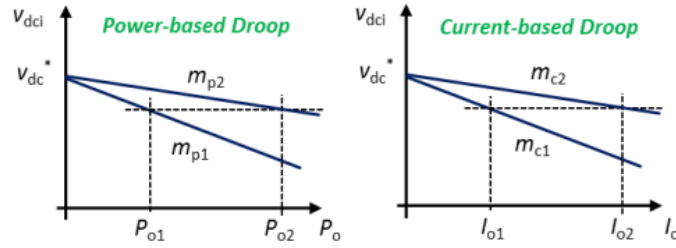


**Figure 2.23:** Example of droop characteristics for DC MG: Active power - DC voltage droop (left) and DC current - DC voltage droop (right) [136].

- **Master-Slave control:** The operation principles of this control approach are similar to those discussed for AC MG, but aiming to control the DC voltage in the DC MG. In this approach, the dominant DER can be assigned to control MG's DC voltage within a permissible range, being the remaining units controlled as power and current sources [136, 139]. This approach is more difficult to expand and its reliance on communications and on a single master unit poses important reliability challenges. However, regarding its reliability drawbacks, an hierarchical control approach can be adopted in order to hierarchically assign the master role to other DER in case of outage of the current master DER unit [136].

The secondary control for DC MG follows the rationale already described for AC MG. In DC MG, the secondary control aims to restore the reference DC voltage for the MG after every change of load or generation inside the MG [139].

Regarding the tertiary control, it aims to optimize the operation of the DC MG in islanded mode, or to regulate the active power exchanged with the upstream power system when the DC MG operates in grid-connected mode [134]. However, in grid-connected mode, the interface of the DC MG with the upstream power system involves a power converter at least if the upstream power system is an AC system. In this case, the power exchanged between the DC MG and the upstream power system is regulated by adjusting the phase angle and voltage magnitude in the power inverter (in the upstream grid side), which in turn can obtain the desired net power from the DC MG by regulating its DC voltage or using other control capabilities.

### 2.3.3 Hybrid AC/DC Microgrids

The total replacement of distribution AC networks by DC networks is unlikely. The existence of AC loads and AC DG units is expected to persist in the future, which are more efficiently integrated in AC systems. For that reason, structures such as Hybrid AC/DC MG (HMG) combining the merits of both AC and DC systems and



suitable control methodologies have been considered in the recent years in the literature [32–34, 128, 140].

### 2.3.3.1 Independent AC and DC Sub-Grids

Different topologies can be adopted for HMG, but the most usual approach has been the consideration of two independent AC and DC sub-grids, each one with its own loads, ESS and DG units, built to minimize power transfer between the two in order to minimize power losses during the conversion process [32–34, 71, 128]. In this regard, the most important identified configurations can be divided according the illustration presented in Figure 2.24.

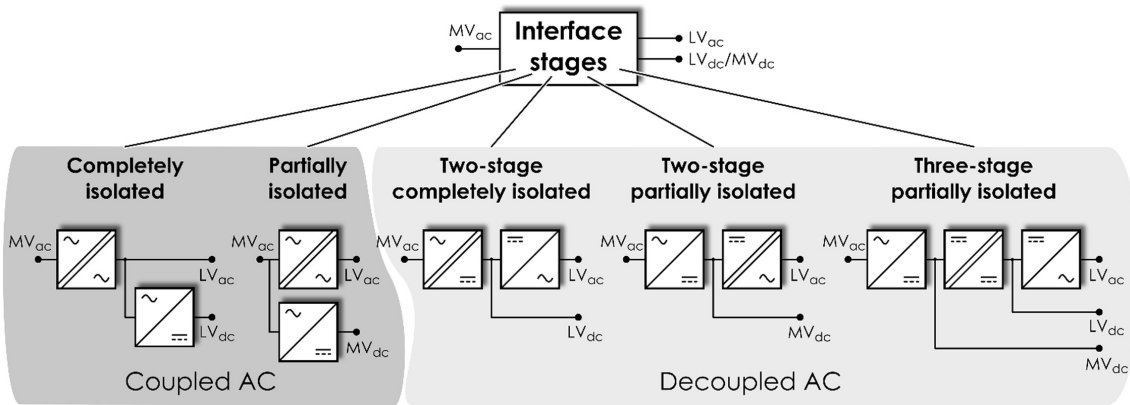


Figure 2.24: HMG architecture classification for independent AC and DC sub-grids [71].

- **Coupled AC Configurations:** In this configuration, the AC sub-network is directly connected to the upstream power system through a power transformer, usually a conventional LFT. In this case, the upstream system determines the operation of the AC sub-network. Additionally, the development of a coupled AC network is less expensive than the decoupled one, since a smaller AC/DC converter can be adopted just to handle the power flow between the utility grid and the DC network.

Within this configuration, two categories can be named: the completely isolated and the partially isolated configurations [71]. The completely isolated configuration offers the advantage of providing galvanic isolation to all HMG. Moreover, a LV AC/DC converter can be utilized since it connects directly to the LV AC network. In the partially isolated configuration, the AC/DC converter is directly connected to the upstream system. It offers the advantage of allowing a lower rated power for the LFT in comparison to the completely isolated configuration. However, no galvanic isolation is provided to the DC network.

- **Decoupled AC Configurations:** In this configuration, both AC and DC sub-networks are decoupled from the upstream power system through electronic power converters. This type of configuration has been gaining interest in the recent years because it offers important advantages in comparison to the coupled AC configurations [71]. Since the HMG is decoupled from the upstream system, this configuration provides fault isolation and independent control strategies for both AC and DC sub-networks. Moreover, the power interface device is responsible for the power flow monitoring and control of the entire HMG, an important feature that may be utilized for the coordination with upper level control platforms such as the supervisory control and data acquisition (SCADA) systems managed by electric companies.

This configuration is particularly suitable for the integration of SST [71]. Although, two-stage SST configurations are the most simple approaches for the formation of HMG in terms of conversion stages, three-stage SST configurations have gathered increasing attention due to its potential advantages regarding advanced control functionalities it may provide. The three-stage SST configurations have been regarded as the most promising for a maximum exploitation of the control capabilities offered by the ST concept [41].

Being the HMG a combination of AC and DC MG, the most popular primary control approaches for HMG draw much of the ideas developed for AC and DC MG. For that reason, the most popular primary control approaches for HMG are based on the principles of master-slave (including hierarchical approaches) and droop-based control approaches [32, 34, 141]. Secondary and tertiary control strategies designed for HMG have been gathering research interest as well [141, 142]. An example of a droop-based control approach for HMG is illustrated in Figure 2.25 [141], which shows the implementation of a droop-based controller for power sharing between AC and DC sub-grids through an interlinking converter, correlating the DC voltage ( $V_{pu}$ ) in the DC side with the frequency in the AC side ( $f_{pu}$ ).

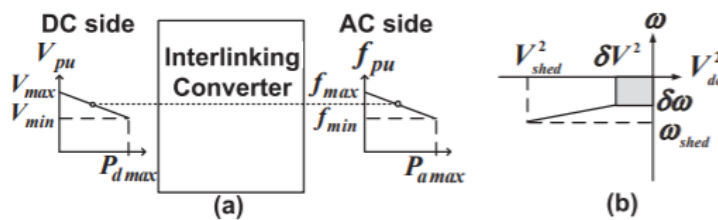


**Figure 2.25:** Proportional power sharing in HMG (a); Hybrid AC-DC droop with dead-zone (b) [141].

### 2.3.3.2 Meshed Hybrid AC/DC Microgrids

Alternatively to the HMG topologies based on independent AC and DC sub-grids, meshed HMG topologies have been proposed in recent years [143–145]. In comparison to HMG topologies based on independent AC and DC sub-grids, meshed HMG offer more than one connection point between AC and DC sub-grids, effectively creating a meshed network involving AC and DC sub-grids, as in the example represented in Figure 2.26.

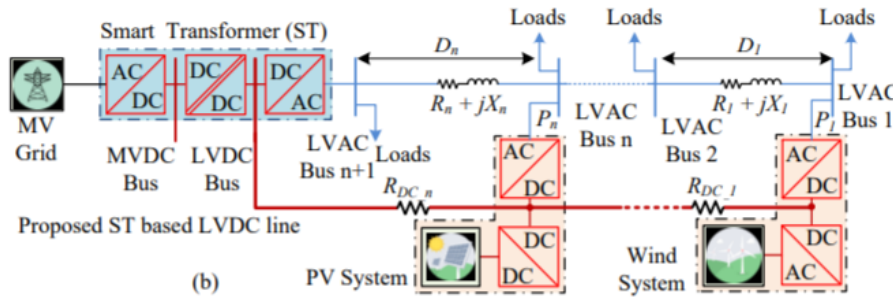


Figure 2.26: ST-based HMG [143].

The meshed HMG topologies are largely derived from the broader meshed hybrid AC/DC distribution grid concept [143, 146, 147], with the Smart-Transformer (ST) concept assuming a central role [143–145]. From the existing research related to meshed hybrid AC/DC distribution grid it is likely to infer that, comparatively to HMG based on independent AC and DC sub-grids, meshed HMG can offer improved flexibility, reliability, voltage profiles and losses reduction, and offer higher potential to postpone or avoid the reinforcement of distribution grids [146, 147].

However, to the best of the author's knowledge to date, the exploitation of control and operation architectures for meshed HMG, even if based on the ST concept, remains very limited in the literature with regard to all its potentialities. Broadly, the HMG concept based on ST continues to have important literature gaps regarding control and operation capabilities addressing its autonomous operation and the provision of grid support capabilities.

### 2.3.4 Multi-Microgrids

Under the Multi-Microgrid (MMG) concept, the many MG concepts previously addressed (AC MG, DC MG and HMG), jointly with MV loads and DG integrated at the MV level, are integrated in a higher level structure formed at the MV level capable to operate in islanded mode in the advent of loss of the upstream power system. There

are several MMG architectures proposed in the literature, which may be classified according the following categories:

#### 2.3.4.1 AC Multi-Microgrids

This category aggregates all MMG architectures involving solely AC grids, and is currently the most investigated category in the literature [81, 84, 148]. Topologies for AC MMG range from totally coupled AC grids [81, 148] to topologies using electronic power interfaces, most notably the SST and ST concepts, between individual MG and the rest of the AC MMG [84, 85]. An example of a totally coupled AC MMG is illustrated in Figure 2.27.

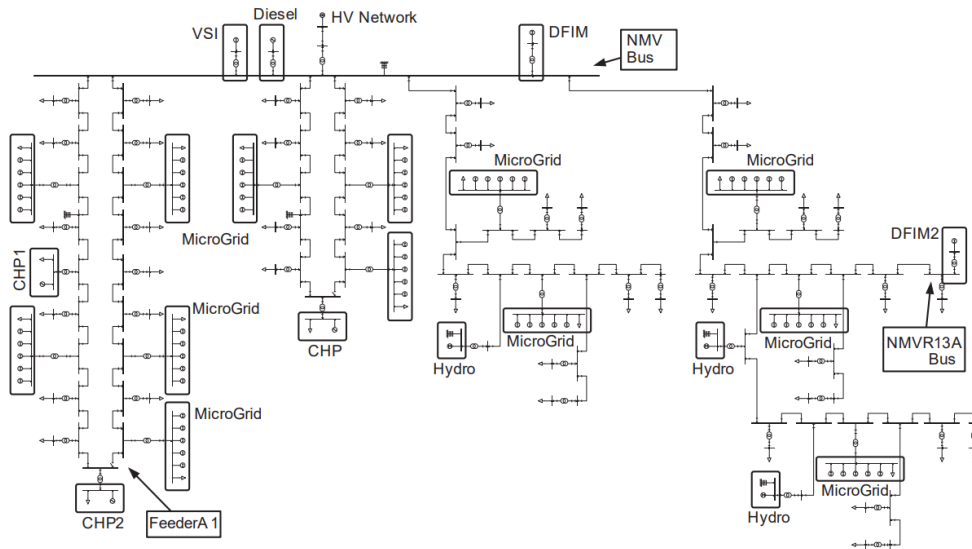


Figure 2.27: Example of an AC MMG [148].

Hierarchical control approaches for AC MMG have been discussed in the literature as well [81, 149, 150]. An example of an hierarchical control approaches for AC MMG is illustrated in Figure 2.28 [81]. At the top of the hierarchy, the Distribution Management System (DMS) is under the responsibility of the Distribution System Operator (DSO). The Central Autonomous Management Controller (CAMC) represents the intermediate managing control structure responsible for the MGG. The CAMC can react to power system frequency changes or to other disturbances such as load loss during islanded operation of the MMG, adjusting as necessary the power set-points for all MG (through the respective MGCC) and resources integrated at the MV level constituting the MMG [81]. The CAMC can be seen as one DMS application confined to the management of the part of the distribution network constituting the MMG. The

MGCC is available in each MG and is responsible for the direct management of the MG, but subordinated to the control actions issued by the CAMC.

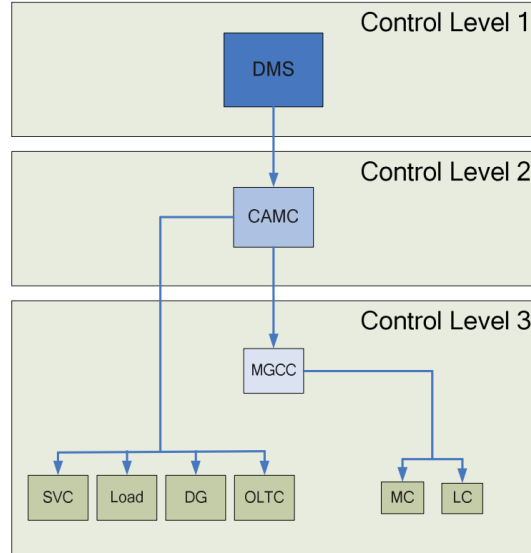


Figure 2.28: Example of a hierarchical control scheme for AC MMG [81].

### 2.3.4.2 DC Multi-Microgrids

This category aggregates all MMG architectures constituted solely by DC grids. The DC MMG topologies proposed in the literature include both radial configurations [86–88] and meshed configurations as the example illustrated in Figure 2.29 [151]. DC MMG aim to exploit the same fundamental advantages already identified for DC MG but expanded to the MV level. Theoretically, the hierarchical control approaches already identified for AC MG and AC MMG can be adapted for DC MMG as well.

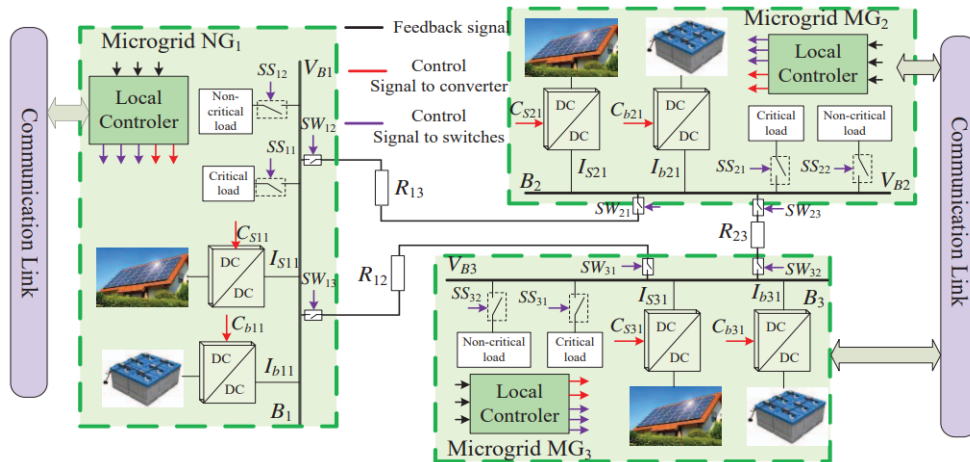


Figure 2.29: Example of a DC MMG [151].

### 2.3.4.3 Hybrid Multi-Microgrids

In spite of AC and DC MMG encompassing most of the MMG architectures proposed in the literature, hybrid AC/DC MMG (HMMG) constitute the most promising MMG architectures given its enhanced potentialities resulting from the combination of the inherent qualities of AC and DC grids. However, in spite of very recent developments, the research around this concept remains in its early stages, with a limited number of works found in the literature [89–92, 152, 153].

The most classical approaches suggest the use of AC/DC and DC/DC power converters to interface several AC and DC MG and other DER [90, 152]. However, the concept of energy router was also introduced to HMMG, offering a more promising approach to enhance communication and control capabilities of a HMMG [89, 153]. The energy router concept is not exclusive for HMMG, and three main approaches have been proposed: Based on Power Line Communications (PLC), based on SST and based on DC-links or Back-to-Back converters [89, 153]. In this regard, the ST concept (based on SST) starts to be considered as a possible building block for future HMMG given its unique characteristics and control potentialities, but the research in this possibility remains very limited [91, 92]. An example of what can be classified as a very simple HMMG architecture based of ST is illustrated in Figure 2.30, where a HMMG is formed by connecting two ST, each one forming its MG, through a MV DC line connecting the MV DC buses of both ST.

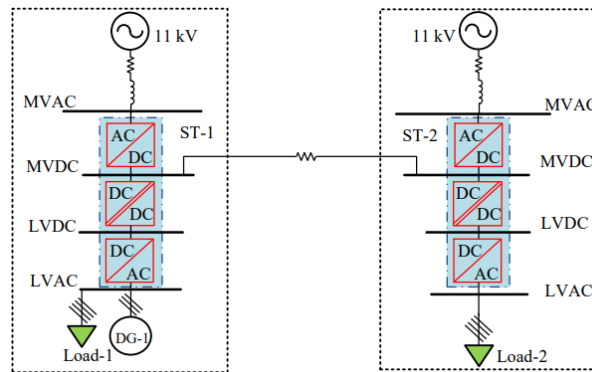


Figure 2.30: Example of a HMMG using ST [92].

The HMMG based on ST addressed in [91, 92] can theoretically be further expanded to develop the concept of HMMG with multi-terminal MV DC. In general terms, this concept consists in the interconnection of two or more ST based HMG through their MV AC and MV DC connections, creating thus a MV DC network with two or more interconnection points with the MV AC network. Such architecture can enable the

integration of large scale PV generation, ESS and EV charging sites directly to the MV DC level. Besides providing all the benefits offered by DC networks for the integration for this kind of DER, a HMMG with multi-terminal MV DC can enable the integration of large scale DER units with lower requisites in terms of rated power for the ST interfacing the MV DC sub-network with the main power system. Comparatively to what would be needed for a HMG interfaced through a single ST with the main power system, the burden posed by the active power demand/generation of a given large scale DER resource can be shared by several ST. The combination of this architecture with advanced control functionalities involving the ST and the DER available in the HMMG with multi-terminal MV DC would theoretically enable an optimal operation of all HMMG, minimizing losses and overload situations with the respectively necessary power curtailments.

Moreover, such architecture harbors the potential to increase overall reliability indexes. Some of the most relevant possibilities regarding this can be inferred from existing research voted for multi-terminal DC grids [154–156]:

- Instead of a single DC/AC interface, a given large-scale DER can make use of all ST available in the network to interface with the main power system.
- In case of fault disturbances in the MV AC network such as a voltage sags, the ST must be able to provide FRT but a ST may be unable to balance the active power in its MV DC link if the currents in the MV inverter saturate at its maximum limits. In such cases, the existence of a DC link connection between several ST can be used to balance the active power between different ST in order to reduce the probability of such occurrences. The distribution of the active power using a MV DC grid connecting several ST can be optimized throughout the HMMG, making a shared use of the existing energy storage capacity and controllability of the ST's HMG.
- MV DC networks can be built underground with reduced power losses comparatively to an equivalent MV AC network built using underground cables (no reactive currents). Consequently, wider underground DC grids become more appealing comparatively to current applications where MV AC grids based on overhead power lines are nowadays preferable. This potential shift to underground DC grids also offer better immunity against fault disturbances caused by natural phenomena in comparison with an equivalent MV AC grid based on overhead power lines.

Nevertheless, ST based HMMG with multi-terminal MV DC remain practically unexplored in the literature.



## 2.4 Advanced Functionalities for Hybrid Microgrids and Multi-Microgrids based on Smart-Transformers

Increasing penetration ratios of DG and EV in distribution networks are expected to cause adverse impacts in the power systems. Thus, besides new grid architectures, additional control capabilities will be required in order to mitigate those impacts. Due to its architecture and ability to fully control its terminal voltages and currents, the ST can enable such control capabilities and new network architectures in addition to isolation and voltage scaling [47].

With the ST at its core, HMG and HMMG configurations constitute the most promising approach to respond to the expected increasing penetration ratios of DG, EV and ESS in distribution grids. In this scope, this section presents a literature review of the main technical adverse impacts expected to become prominent in power systems as the penetration ratios of DG, EV and ESS in distribution grids increase, and which advanced control functionalities HMG and HMMG based on ST can provide to address those challenges. This includes a review of the potential and already developed solutions offered by the ST in this domain. Nevertheless, the main technical challenges facing the integration of HMG and HMMG based on ST are also addressed.

### 2.4.1 Voltage/Var Control in AC Grids

Increasing penetration ratios of DG are expected to affect the system's ability to perform voltage control. Such impact should affect not only at a specific grid section with high penetration of DG, but also system voltage stability [157–159]. Regarding distribution networks, the proliferation of DER is expected to affect the capability to perform voltage control in both MV and LV AC networks. In distribution AC networks, most of DG units based on power electronics are set as *grid-following* units, and thus, without intrinsic voltage control capabilities [160]. Depending on the possible intermittency of the resource exploited by DG, on the volume and distribution of DG in the distribution grid, and on the  $X/R$  characteristic of the distribution grid, the absence of voltage control capabilities on DG is expected to increase the frequency and severity of over-voltages in distribution networks in face of increasing penetration ratios of DG. By another hand, the proliferation of EV connected to distribution networks are expected to originate more frequent and severe voltage dips in distribution networks, as the overall load increases.

Currently, several solutions capable to provide voltage regulation to AC distribution



networks are already available as industrial products. Regarding regulation of voltage levels in AC LV networks, the traditional LFT can be extended with automatic on-load tap changers, without compromising the robustness nor the high efficiency of the LFT [161, 162]. Such an arrangement is known as Voltage Regulation Distribution Transformer, and commercial solutions are readily available. Other well established and mature technologies are also available as industrial products, such as the Dynamic Voltage Restorer (DVR) [163, 164], the Static Var Compensator (SVC) [165] and the STATCOM [166, 167], which can be installed in any location of the AC distribution networks.

However, the aforementioned solutions may be insufficient in face of increasing penetration ratios of DG. Thus, the incorporation of voltage/Var control capabilities in DG and even in EV connected to AC distribution grids has been a subject of great interest in the literature [168–170], with centralized and distributed approaches being proposed [171–176]. The DG and EV units itself can be used to regulate the voltage levels and voltage unbalances across the AC distribution network through the control of its active and reactive power output.

Meanwhile, several countries have already adapted their grid-codes in order to specify the connection requirements for DG for the provision of voltage regulation to AC distribution networks [177]. As exemplified in Figure 2.31, DG units can participate in voltage regulation on AC distribution networks by adjusting their power factor (PF), with both dynamic (e.g. power factor as a function of voltage ( $V(\%)$ )) and static (e.g. power factor as a function of output active power ( $P/P_n$ )) control approaches being suggested.

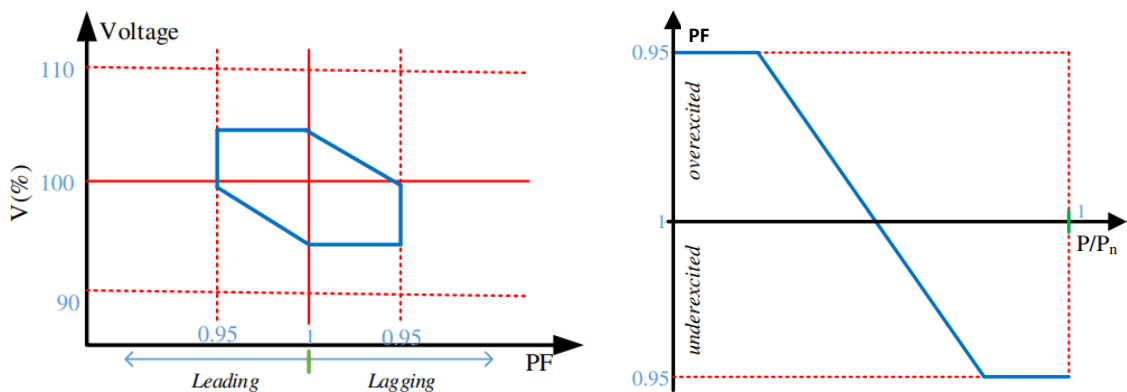


**Figure 2.31:** Typical requirements for power factor variation range in relation to the voltage (left) and static power factor–voltage regulation as a function of the active power in the German grid code (right) (adapted from [177]).

In this scope, the HMG and HMMG based on ST offer additional possibilities to

improve voltage regulation in AC grids. By one hand, by making use of the ST's capability to provide independent voltage regulation through its MV and LV inverters. In fact, the decoupled operation of the MV and LV inverters in terms of voltage/Var regulation represents a strong aspect of the ST. By another hand, by the fact that a share of the load and DER may be located in the DC sub-networks, being thus shielded from voltage variations and disturbances affecting AC grids.

It is already shown in the literature that the voltage levels in a MG connected to the upstream grid solely through a ST can be independently regulated [178, 179] while the ST's MV inverter provides voltage/Var regulation to the upstream system [180–182]. Since the provision of reactive power to the MV network does not need to involve the MG, additional energy losses are avoided in the MG. However, voltage levels in the MG can also be exploited to help the ST's MV inverter in the provision of voltage/Var control to the upstream grid, by exploiting MG's load voltage sensitivity in order to reduce the active power consumption in the MG [182, 183]. Moreover, the ST can also compensate voltage unbalancing in MG through the injection of a zero sequence voltage [184], and in MV networks by controlling of positive and negative voltage sequences generated by the MV inverter [178]. The ability of the ST to aggregate several capabilities regarding voltage/Var control is thus notorious, making it an attractive technical solution. From the system operators' point of view, the ST offers the possibility to consider a single unit instead of several distributed resources and other resources available in a given MG.

The research on voltage/Var regulation in HMG based on ST starts to be addressed in the literature [143]. In [143], the voltage levels in the LV AC sub-grid are kept on track by diverting the excessive load to the LV DC sub-grid through AC/DC converters interfacing AC and DC sub-grids and by having the DG units connected to the LV DC sub-grid.

However, the existing work regarding voltage/Var control in islanded MMG based on ST remains very limited in the literature, but this capability is deemed possible in existing research related to islanded MMG based on ST [84, 185]. Regarding voltage/Var regulation in HMMG based on ST, no reference in the literature was found.

### 2.4.2 Frequency Regulation and Support

A large penetration of DG units is also likely to affect the system's ability to regulate frequency, as the classical generation systems having the responsibility of this task

are progressively decommissioned. Most of DG units based on power electronics, connected to AC networks, are set as *grid-following* units [160], with no inherent capabilities to react with injected\absorbed active power in face of frequency disturbances as synchronous machines would do [186]. Without additional control mechanisms, DG units will freely ride on the efforts of the transmission grid operator to maintain system frequency [25, 187]. In order to address this subject, regulatory measures have been taken by many countries. For example, in EU, frequency sensitive operation modes (under and over frequency) are already mandatory from grid codes [188]. The active power reduction in case of over-frequency according to the German grid-code is exemplified in Figure 2.32 [177].

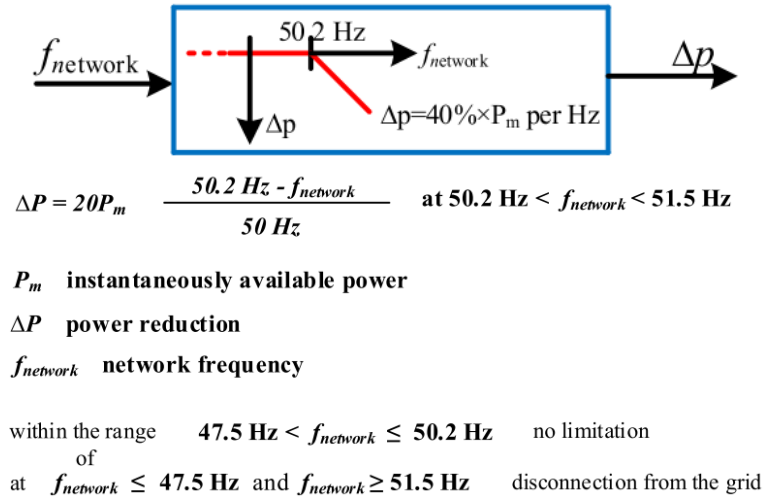


**Figure 2.32:** The active power reduction in case of over-frequency according to the German grid-code (adapted from [177]).

For that reason, the incorporation of frequency support capabilities in DG and even in EV has been a subject of great interest in the literature [187, 189–191]. Moreover, the use of ESS for this purpose has been widely considered as well, alone or combined with DG units [192–194]. Some DG technologies, such as PV or wind generation systems, are usually set to extract the maximum available power from the primary resource in order to maximize profitability. In these cases, these DG technologies cannot provide additional power in order to provide support to a decreasing frequency in the system. The association of ESS would provide proper power reserve capabilities for an adequate amount of time. Another possibility is the operation of these systems below its maximum extractable power (in de-load mode) in order to allow an acceptable power reserve [191].

In this scope, the ST offers a wider range of control possibilities. If the ST is part of an islanded MMG or is sustaining an islanded section of the MV grid, the direct

control of the frequency generated by its MV inverter can be a suitable approach. However, if connected to a wider power system, the most suitable approach for the ST to participate in frequency regulation and support to the upstream power system is by regulating the active power in its MV inverter interface. Such objective can be attained by using energy storage or by regulating the net power of its MG or distribution network using the voltage and frequency as control variables.

#### 2.4.2.1 Using Energy Storage

The use of energy storage is a relatively simple approach to obtain the required power modulation necessary to provide frequency support to the power system and to compensate the variability of RES. The ST can easily integrate ESS through its DC-link connectivity, which can potentially be dispatched by the system operator or incorporate advanced control functionalities capable to adjust its power output as a function of the frequency in the upstream system. The use of ST's energy storage capacity for frequency support and regulation in islanded MMG is addressed in [84, 185], but its application to provide frequency support to the wider upstream AC power system remains largely unexplored.

#### 2.4.2.2 Using Frequency Regulation

An important feature of the ST is the possibility to control the frequency in its MG independently of the frequency verified in the upstream AC system. This capability has been explored in the literature for several purposes. In [195, 196], the ST regulates the frequency in its MG in order to manage overload situations. The DG units available in the ST's MG are equipped with *active power - frequency* droop controllers, which are used by the ST to reduce their generated power by regulating the frequency in the MG. In [197], a frequency-adaptive ST is proposed, able to flexibly modify the LV side frequency with the purposes of achieving power sharing among different DG units and establishing power balance between production and consumption. According to [197], overload and reverse power flow issues can be largely avoided and therefore the power rating of controllable load or storage units can be reduced.

However, the application of such capability in ST-based MG to provide frequency support to the upstream power system remains largely unexplored in the literature. The ST can exploit actively controllable resources at its disposal in its MG, sensitive to LV network frequency, in order to obtain the power regulation necessary to provide

frequency support to the power system. Naturally, for ST-based HMG and HMMG, the frequency regulation capability is only applicable for the AC sub-networks.

#### 2.4.2.3 Using Voltage Regulation

The ST is also capable to take advantage of its voltage control capabilities over its MG in order to regulate the net active power of the ST's MG, by exploiting the voltage sensitivity of the resources connected to the LV grid fed by the ST. For the same purpose, it can also exploit the controllability of DER incorporating power control functionalities (such as voltage-active power droop controllers) sensitive to voltage levels in the distribution network. An interesting advantage of this approach, comparatively to the use of frequency regulation, is that it can be applied to both AC and DC sub-networks constituting a hybrid AC/DC network.

However, the application of this capability to ST-based MG is far from being extensively explored in the literature. This capability is partially explored in [181, 198], where the ST controls the active power demand in its LV AC network in order to provide frequency support to the upstream system. In this case, the ST only explores the passive load voltage sensitivity of its AC distribution network for that purpose. The inclusion of DER capable to actively adjust their power output as a function of the voltage levels is not considered. With regard to ST-based HMG and HMMG, the application of this capability, exploiting also the controllable DER connected to both AC and DC sub-networks and capable to actively adjust their power output as a function of the voltage levels, remains unexplored in the literature.

#### 2.4.2.4 Frequency and Voltage Regulation Strategies from non-ST-based HMG

HMG based on ST offer the possibility to provide frequency regulation and support to the upstream system not only by regulating voltage and frequency levels in its AC sub-grid, but also by regulating voltage levels in its DC sub-grid. Thus, HMG offer extended control possibilities in this regard comparatively to single AC or DC MG. However, the application of these control possibilities to ST-based HMG is still lacking proper investigation in the literature.

Nevertheless, there are several strategies for frequency regulation and support proposed for hybrid AC/DC networks not based on ST that can be potentially transposed to ST-based HMG [32, 34]. Among the investigated approaches, droop based controllers have been the most popular, such as *voltage-active power*, *frequency-active power* and *voltage-current* droop based controllers [32, 34].

Furthermore, communication based control strategies are also potential candidates for ST-based HMG, since the ST is expected to possess enough processing and communication capabilities to implement such approaches [47]. An overview of potential communication-based candidates is presented in [34]. From these, *centralized control* strategies are possibly the most straightforward approach given the central role of the ST in the management of its HMG.

### 2.4.3 Inertia Emulation

In a more global/systemic scope, large scale integration of DG is expected to reduce overall system inertia in a *business as usual* scenario. Nowadays large synchronous generators are fundamental to provide inherent inertia and power–frequency control capabilities to the system. Although it provides immediate power injection/absorption for a limited amount of time, it usually proves crucial to avoid the collapse of the entire system following a large load–generation unbalance which directly affects grid frequency and its rate–of–change over time. In comparison, DG units based on power electronics don’t inherently provide inertia to the system. Without inertia emulation capabilities, these systems do not provide meaningful contribution to system stability during large transient events [199, 200]. In order to address this limitation, the inclusion of inertia emulation capabilities in power electronic interfaced DG, and even in EV chargers, has been addressed in the literature [201–203].

The ST offers the possibility to provide inertia emulation to the upstream system acting as a front-end of its distribution network, from the perspective of the upstream grid. Such capability is partially explored in [204, 205], where the ST controls the active power demand in its LV AC network in order to emulate inertia to the upstream system, through the regulation of the voltage levels (exploring load voltage sensitivity) in the LV AC network.

Nevertheless, other resources and methodologies can be employed to obtain inertia emulation. The ST can easily integrate ESS through its DC-link connectivity, which can potentially incorporate inertia emulation functionalities. The ST can also exploit actively controllable resources, incorporating advanced control strategies sensitive to frequency and voltage variations, available in its distribution network. In this case, the ST can obtain a proper active power modulation suited to mimic inertial behavior, by modulating the frequency (AC LV network only) and voltage in its distribution network. However, these possibilities remain largely unexplored in the literature.



#### 2.4.4 Fault-Ride-Through Capabilities

In comparison to traditional LFT, the ST hardware has lower robustness with respect to short-circuit currents and no inherent FRT capabilities, a common limitation of electronic power converters in general [206]. The incorporation of FRT capabilities in electronic power inverters represents a major concern widely addressed in the literature [206], especially for Distributed Generation (DG) [207–210].

Nevertheless, the incorporation of FRT capabilities in ST remains largely unexplored. For a grid section fed by a ST, FRT capability is a major concern regarding continuity of supply. There are several FRT approaches already proposed in the literature for grid-following and grid-forming MV inverters [210–213]. However, none of the proposed approaches addresses its application to the ST and its particularities.

By one hand, it must be considered that the ST may be required to support the transition of a MMG or a section of a MV network to islanded mode, following a fault disturbance in the upstream system. The ST must remain connected while the MMG, or a section of a MV network where it connects to, is not isolated from the fault disturbance occurring in the upstream grid. If no proper FRT capabilities are available in the ST's MV inverter, the ST will not stand against the adverse conditions during the time interval between the appearance of the fault and its clearing, thus making it unavailable to support the islanded operation.

By another hand, it is also interesting to consider a ST without adequate energy storage capacity to operate its distribution grid in islanded mode alone. In such cases, in face of fault disturbances in the upstream system, the ST's MV inverter must remain connected and be able to mitigate the adverse effects of grid disturbances in its distribution grid. Without proper FRT capabilities available in the ST's MV inverter, the continuity and quality of service of the distribution grid will be compromised. Moreover, the existence of proper mitigation of the adverse effects of grid disturbances may avoid the disconnection of DER located in the ST's distribution grid without FRT capabilities by their own. Naturally, the investigation of FRT capabilities for HMG and HMMG based on ST remain unexplored as well.

#### 2.4.5 Islanding and Reconnection Capabilities on Meshed MG

Islanding and reconnection capabilities are fundamental features of MG. Such capabilities are widely investigated for AC MG [214–217]. The most important requisite to perform a successful islanding procedure in an MG is the existence of a slack unit or units capable to internally balance the power demand in the MG. Given this, the

islanding procedure can be planned or unplanned (i.e. following a fault disturbance, blackout or power outage affecting the upstream power system). But in order to execute a smooth reconnection procedure of an islanded AC MG to the upstream power system, a previous synchronization of voltages, frequency and phase angle in both sides of the point of common coupling is required [215, 216].

However, research regarding reconnection capabilities in AC MG integrated in meshed distribution grids and meshed MMG remains very limited in the literature. This mainly results from the fact that meshed operation of distribution grids has historically not been the preferred approach, in detriment to radial configurations which offer unidirectional power flows and simpler and more efficient protection schemes [218]. The implementation of meshed AC distribution grids needs to address important challenges such as coordination of protection schemes, voltage regulation, power flow control, and limitation of higher short-circuit currents [218–221]. In fact, the interest in meshed distribution grids seems to have grown as a result of the expected increase in DG integration in distribution AC grids. Comparatively to radial distribution AC grids, meshed distribution AC grids have the potential to accommodate higher shares of DG, while providing a more uniform power flow, improving voltage profiles, reducing power losses and balancing the exploitation of lines and transformers [218]. Nevertheless, islanding and reconnection capabilities for meshed AC MG started to receive attention very recently [222].

The introduction of power converters as interfaces between MG and the upstream power system opened a new range of control possibilities in this regard [223, 224]. Using back-to-back power converters to connect different AC feeders in order to form meshed grids greatly improves power flow and voltage control capabilities [223]. Further improvements could be envisioned by considering the ST concept as a key element in meshed distribution grids, specially with the emergence of ST-based meshed HMG and HMMG [143, 145, 146]. Besides the desired islanding and reconnection capabilities, ST-based meshed HMG and HMMG offer higher potential to improve grid flexibility and reliability, improve voltage and grid losses profiles, and postpone or avoid the reinforcement of distribution grids [146, 147]. This subject may be of major importance to improve reliability of meshed MG against fault disturbances within the MG itself, by enabling the isolation of a faulty feeder section and its posterior reconnection after the fault origin is resolved, without compromising the operation of the remaining MG. However, the application of such capabilities for ST-based MG remains mostly unexplored in the literature. Some interest starts to emerge for ST-based meshed AC MG [123, 225]. In [123, 225], communication-based strategies are



proposed to synchronize and reconnect two AC feeders (one fed by a conventional transformer and another fed by a ST), by exploiting the frequency and voltage control flexibility of a ST's LV inverter feeding one of the AC feeders.

However, no specific research in this matter was found for ST-based meshed HMG and HMMG. Worth to mention that the availability of DC sub-grids in meshed HMG and HMMG offer increased potentialities in this matter, as offline AC feeder sections can be energized from the DC sub-grid while their regular connection point to the AC grid is not reestablished. Additionally, communication-free strategies to perform synchronization between different AC and/or DC feeders within a ST-based meshed HMG or HMMG are lacking proper investigation as well.

## 2.4.6 Other Capabilities and Applications

Besides the already described capabilities and applications, further ST applications and control capabilities are worth mentioning.

### 2.4.6.1 Load Sensitive Identification

Among the advanced functionalities already addressed in the literature is the ST capability to provide load regulation and load sensitivity identification [226, 227]. The ST can explore the load dependency on voltage to calculate how the load in a LV grid varies with changes in voltage [226]. Using that information, it is possible to actively reduce the load in a LV grid by reducing the grid voltage, in order to avoid load shedding [227]. Although the performed load reduction is only possible in a relatively narrow band, it may be sufficient to solve, for example, overload problems in the ST without load shedding.

### 2.4.6.2 Self-Healing and Black-Start

The provision of self-healing capabilities for smart-grids based on ST is also demonstrated in the literature [228]. In order to improve reliability under disruptive events, coordination strategies for ST suited to provide healing capabilities and collective decision-making are proposed [228]. It is shown that a higher number of ST using this advanced functionality and coordinated among themselves can increase the reliability and the capability of a network to survive against disruptive events such as cascading failures or cyber-attacks [228].

The application of black-start strategies for MG and MMG by exploiting ST is also demonstrated in the literature [85, 229]. In [85], a set of procedures to integrate ST in

the MMG restoration process following a blackout event is proposed, where the need for power-frequency control and the coordination of the several resources connected to MV and LV grids are addressed. In [229], the emergency restoration of MG following a islanding procedure is addressed.

## 2.5 Technical Challenges

In spite of its potential, there are important technical challenges the ST must overcome in order to become a viable industrial solution, and consequently, enable the implementation of HMG and HMMG based on ST. It is expected that those challenges will be surpassed in the future, but the main consensus is that the ST will take some time until it become industrially attractive. The most relevant challenges are enumerated as follows:

- **Efficiency:** The main task of LFT in distribution grids is to provide galvanic separation and voltage scaling, ideally with very low losses. The efficiencies of typical oil-filled 1000 kVA LFTs are well above 99% for most of the load range [45]. However, the highest efficiencies values reached so far by SST do not match yet those provided by LFT [230]. The best industrial SST systems realized so far are generating about 3 to 6 times higher losses than a comparable LFT [45].
- **Costs:** Currently there are no ST products that would allow a direct comparison of prices. In general, the cost of a SST can be estimated based on the type, configuration, and control of the power electronic converters used in all stages, cost of auxiliary circuits (driver circuits, instrumentation circuits, etc.), filter circuits, cooling systems, communication devices, protection devices, and electromagnetic interference protection devices [230]. Estimations of the material costs of a 1000 kVA SST are found to be at least 5 times higher than those of an equally rated LFT [45].
- **Robustness and Reliability:** Regarding robustness and reliability, the traditional LFT has far less components and is more robust against lightnings and severe fault conditions like over-currents and over-voltages, which can easily damage power electronic components. Although very high levels of reliability can be achieved in an SST by implementing redundancy if multi-cell concepts are employed, non-redundant subsystems such as control electronics may limit the overall reliability of complex converter systems, in comparison to a passive LFT [45].
- **Compatibility with existing protection schemes:** The protection of LV grids

against short circuits is based on fuses and/or circuit breakers, arranged according a selectivity approach which tries to ensure that when a fault occurs, only the closest upstream protection device is triggered in order to contain the effects of a fault in a section of the grid as small as possible. In order to this protection scheme work properly, LFT are supposed to deliver up to 25 times their rated current for at least two seconds [45]. This is not an easy task for a SST, due to the relatively low current ratios of the most suitable semiconductor technologies industrially available nowadays, such as the IGBT and power MOSFET. High current ratios can be achieved associating several electronic switches in parallel, but with a considerable increase in costs and control complexity. However, a SST has the ability to limit short circuit currents, but the use of this nevertheless interesting feature remains largely unexplored. Possibly, advanced protection concepts involving communication between the SST and breakers and/or other switching devices in the grid would be required[45].

Given this, although the current alternatives to the ST (and SST in general) usually provide narrower control ranges, they are still often sufficient nowadays, thereby retaining the high efficiency and robustness of an LFT or limiting the power processed by power electronic stages to only a fraction of the total power. However, the validity of this consideration in face of higher penetration ratios of DG in future power systems must be evaluated. In face of the expected adverse effects of high penetration ratios of DG and EV on power system's operation and control and the consequent increased necessity for controllability, demands for new alternatives such as the ST, which is expected to have a key role in the future power systems.

Though, there are already some specific cases identified in the literature where the application of the Smart Transformer in the distribution grids is considered already feasible at least in a near future [45]:

- *AC-DC Applications:* ST can provide a DC interface that can be used to, for example [45]:
  - connect a PV generation unit or a large energy storage system to the MV grid
  - interface a DC Microgrid to the MV network,
  - connect a fast EV charging station that can also provide ancillary services to the grid if not in operation,
  - directly supply servers in a data-center from MV.

In such cases, the LV-side DC-AC conversion stage of the ST is not needed,

making the costs of a solution based on a ST close to those of a solution based on a LFT [45].

- *DC-DC Applications:* If galvanic isolation and/or a significant step-up or step-down of the voltage is required in DC distribution networks, a magnetic transformer must be used, and thus, there is no alternative to using a conversion system that can be seen as a ST [45].

## 2.6 Final Considerations - Literature Gaps

From the presented literature review, an important set of literature gaps regarding advanced control functionalities for ST-based HMG and HMMG were identified. Given the extent of the identified research gaps, it is not possible to address all of them with the deserved detail in this thesis. Thus, only a set of selected research topics, deemed as the most relevant according to the author's view, constitute the core background of the research plan for this thesis:

- **Power-Frequency support to the power system:** Power-Frequency support to the power system using the ST and ST-based HMG requires further investigation, namely using energy storage associated to the ST and the controllability of all the DER available in the ST-based HMG.
- **FRT capabilities for ST:** The incorporation of FRT capabilities in ST requires further investigation, namely in the following situations:
  - A ST has no adequate energy storage capacity to sustain islanded operation of its HMG following a fault disturbances in the upstream power grid.
  - The islanded operation of a section of a legacy MV AC network is to be supported by ST following a fault disturbances in the upstream power grid.
  - A ST-based HMMG should transit to islanded mode following a fault disturbances in the upstream power grid, and ride through fault disturbances occurring within the HMMG itself.
- **Reconfiguration of grid sections within HMMG:** The involvement of ST in the reconfiguration of grid sections within HMMG between radial and meshed configurations without interruption of supply requires further investigation, namely in the development of communication-free reconfiguration strategies.

## Chapter 3

# Modeling Principles for Hybrid Microgrids

The work developed in the scope of this PhD thesis resorted to computational simulation models to identify and develop advanced control strategies suited to address the previously identified research questions. In order to develop the computational simulation models, the following main steps were taken:

- Evaluation of the most appropriate computational modeling techniques and simulation approaches upon which the developed computational models will be based.
- Evaluation of existing low-level control solutions for voltage and current control in power electronic converters, suited for the power conversion stages constituting the developed models for Smart-Transformer (ST) and Distributed Energy Resources (DER).
- Development of advanced control functionalities for ST, aimed to enable advanced control strategies for Hybrid AC/DC Microgrids (HMG) and Multi-microgrids (HMMG). These developments represent the main contribution of this thesis, and are separately presented in chapter 4.
- Development of computational models for HMG and HMMG using the previously modeled ST as key elements. IEEE test grids are used as reference whenever appropriate for the modeled HMM and HMMG, with the necessary adaptations for the inclusion of ST, DC networks and DER.

### 3.1 Modeling and Simulation Approach

The computational simulation models were developed in MATLAB<sup>®</sup>/Simulink<sup>®</sup> environment. In this environment there are several numerical methods available, grouped in the following categories: discrete variable-step, discrete fixed-step and phasor modeling. In order to select the most adequate numerical approach, important considerations were made.

First, although the ST and many DER are based on power electronic converters, there is no need for a detailed modeling of the switching elements existing in power converters. Such detailed modeling is required if the high frequency phenomena occurring during the switching events were determinant for the dynamics of the phenomena under study in this PhD thesis. The phenomena under study are to take place at the fundamental frequency domain. However, the fastest response the controller of a power converter can achieve is limited by the switching frequency imposed to the power converter, thus making such high frequency phenomena mostly irrelevant for the dynamic performance of the power converter as a controllable element connected to a power system. Moreover, the impact of such high frequency events are greatly attenuated by the passive elements associated to power converters (e.g. output filters, DC link capacitors). The relevance of these considerations is that the simulation of detailed switching elements usually requires the use of discrete variable-step numerical approaches. In this context, discrete variable-step numerical approaches require considerably higher computational effort and simulation times in order to obtain a good numerical accuracy for the developed computational models. This burden is not justifiable given the lack of relevant contribution for the dynamics of the phenomena addressed in this PhD thesis.

Alternatively, the development of simulation models for electric power systems incorporating a large number of power-converter-based systems can use phasor modeling, as evidenced in [84, 231, 232]. The phasor modeling approach has been demonstrated to have adequate representativeness regarding the main dynamics of the system, while demanding a low computational burden. This is achieved by neglecting the switching nature of electronic switches in power converters, as well as harmonics. However, an important limitation of phasor modeling is that it provides a linearized numerical solutions for a given frequency (usually the grid frequency of the AC power system is selected). This particularity brings important numerical accuracy challenges when simulating computational models working with several harmonics. That is the case for

computational models for HMG and HMMG, where DC sub-grids have a frequency equal to zero. Possible solutions capable to conciliate several harmonics have been presented in the literature [233, 234], but the numerical accuracy still relies in the assumption that no significant deviations from the assumed harmonics will take place.

In the scope of the work developed in this thesis, a more attractive compromise between simulation speed and numerical accuracy was adopted: a discrete fixed-step numerical approach combined with a modeling technique designated as Dynamic Average Modeling (DAM) [235, 236]. Its application on the dynamic behavior analysis of Solid-State Transformers (SST) is demonstrated in [236], as well its advantages for the development of transient models for real-time simulation platforms. The DAM approach approximates the behavior of power electronic converters from a system-level perspective by applying the moving average operator at the switching frequency to the detailed switching model, thus removing the switching effects from the model but preserving the dynamic behavior of the power electronic converters [235, 236]. Using these properties, switching architectures of power converters can be represented by equivalent controllable voltage and current sources and larger simulation time steps can be adopted [235, 236]. Faster simulation of systems containing several power electronic converters is thus possible comparatively to a detailed model [236]. The equivalence between a detailed model and a model based on the DAM approach for a SST is illustrated in Figure 3.1.

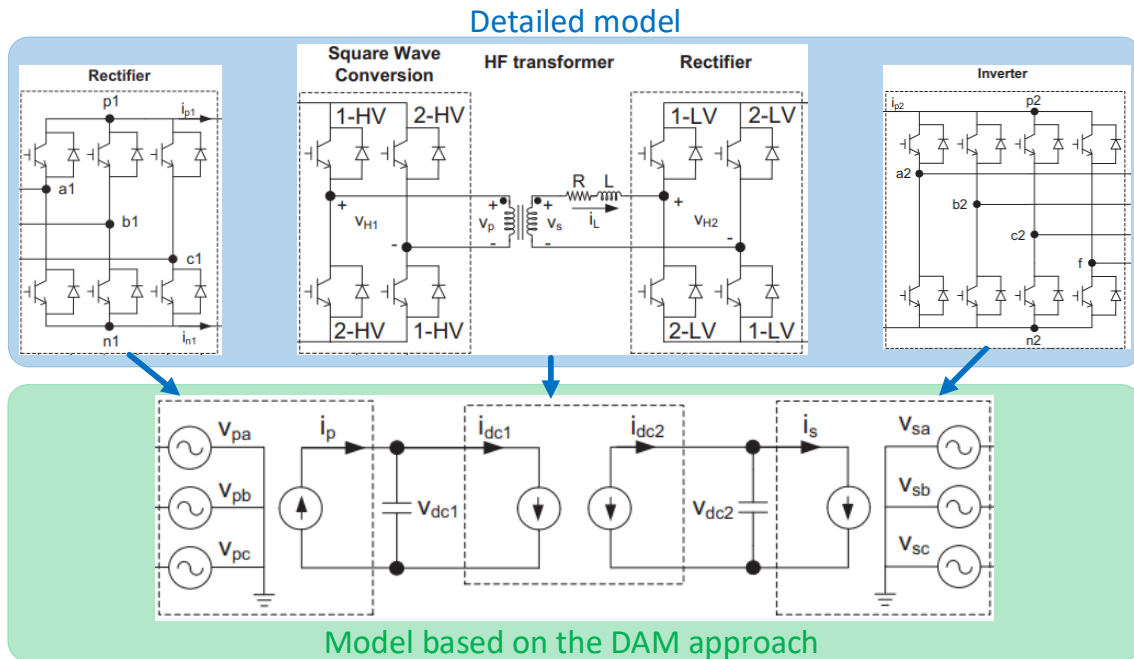


**Figure 3.1:** Equivalence between a detailed model of a SST and a model of a SST based on the DAM approach (adapted from [236]).



In order to effectively implement the DAM approach, a switching frequency of 20 kHz was adopted, which is assumed for all power converters modeled in the scope of the work developed in this thesis. A switching frequency of 20 kHz was chosen given it is a relatively realistic value when considering high power electronic converters [41, 237, 238].

It is worth to mention that the International System of Units (SI system) is adopted for all developed computational models. Nevertheless, the results exposed in chapters 5 and 6 are partially represented using the per-unit system (p.u.) in order to facilitate the interpretation of the presented results.

### 3.2 Smart-Transformers: Power Converter Architectures and Control

The computational modeling of the ST constitutes the core of the computational models developed in the scope of this thesis, including the advanced control functionalities proposed for ST which are described separately in chapter 4.

The base structure of the developed ST models is depicted in Fig. 3.2. A three-stage topology is adopted for the grid-following and grid-forming ST models. A local Energy Storage System (ESS) is also modeled. However, the operation of the grid-following ST without available local Energy Storage System (ESS) is also considered. A supercapacitor bank is also modeled for the grid-following ST, whose model is based on the model developed for the local ESS. Its purpose is described in section 3.2.3.

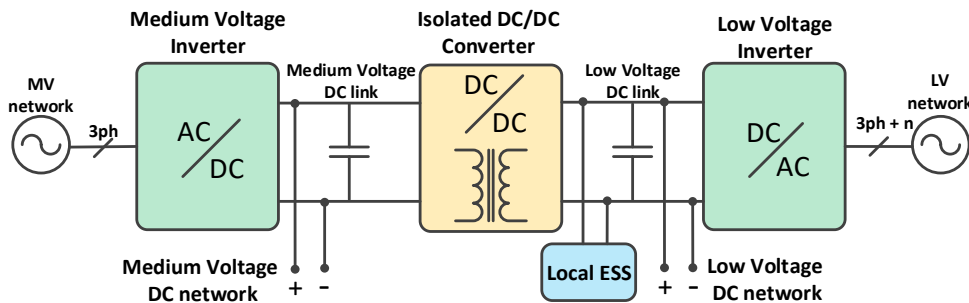


Figure 3.2: Overall structure of the modeled ST.

A modular approach was considered in order to improve flexibility, scalability and replicability of the performed studies. Two distinct models for ST were developed: a ST with its MV inverter operating in grid-following mode (hereinafter referred to as grid-following ST) and a ST with its MV inverter operating in grid-forming mode (hereinafter referred to as grid-forming ST). The developed models are intended to be



as generic as possible, being able to operate with all the proposed advanced control functionalities integrated.

Follows a detailed description of the developed computational models for ST, whose detailed parameterization is presented in Appendix A.

### 3.2.1 Medium-Voltage Power Converters

The major differences between the computational models developed for the grid-following and grid forming ST are located in the MV inverter. For that reason, the MV inverters for grid-following and grid-forming ST are described separately in the following subsections.

#### 3.2.1.1 Grid-Following Converter - Base Architecture and Control

The main hardware building blocks and control structure of the MV inverter are represented in Fig. 3.3. The advanced control functionalities proposed to be integrated in this converter, which are under the scope of this work, are not yet illustrated in Fig. 3.3, being its description reserved for chapter 4. This section is intended to present a detailed description of the modeling approach adopted for the main building blocks of the power converter stage.

In the modeled grid-following ST, the MV inverter operates in grid-following mode and is responsible to couple the ST with the MV AC network. It is also responsible to balance the DC voltage in the MV DC link of the ST. Controlled current sources are used to implement the average model of the power converter and the interface with the DC bus. The parameterization of the modeled grid-following converter is presented in Appendix A (Tables A.1 and A.2).

#### Power Architecture

The power converter is modeled by a three-phase controlled current source in star configuration with isolated neutral, but the neutral point is connected to the negative pole of the MV DC bus in order to ensure common voltage ground references for the MV DC bus and three-phase current source. The active power between the coupling *LC filter* and the MV DC bus is described by Equation (3.1).  $IDC_{MV}$  is the DC current in the MV inverter,  $VDC_{MV}$  is the DC voltage in the connection with the MV DC bus,  $v_{ab_{MV}}$ ,  $v_{bc_{MV}}$  and  $v_{ca_{MV}}$  are the phase-phase MV AC voltages (between phases *a*, *b* and *c*) in the MV inverter, and  $i_{a_{MV}}$ ,  $i_{b_{MV}}$  and  $i_{c_{MV}}$  are the AC currents in the MV

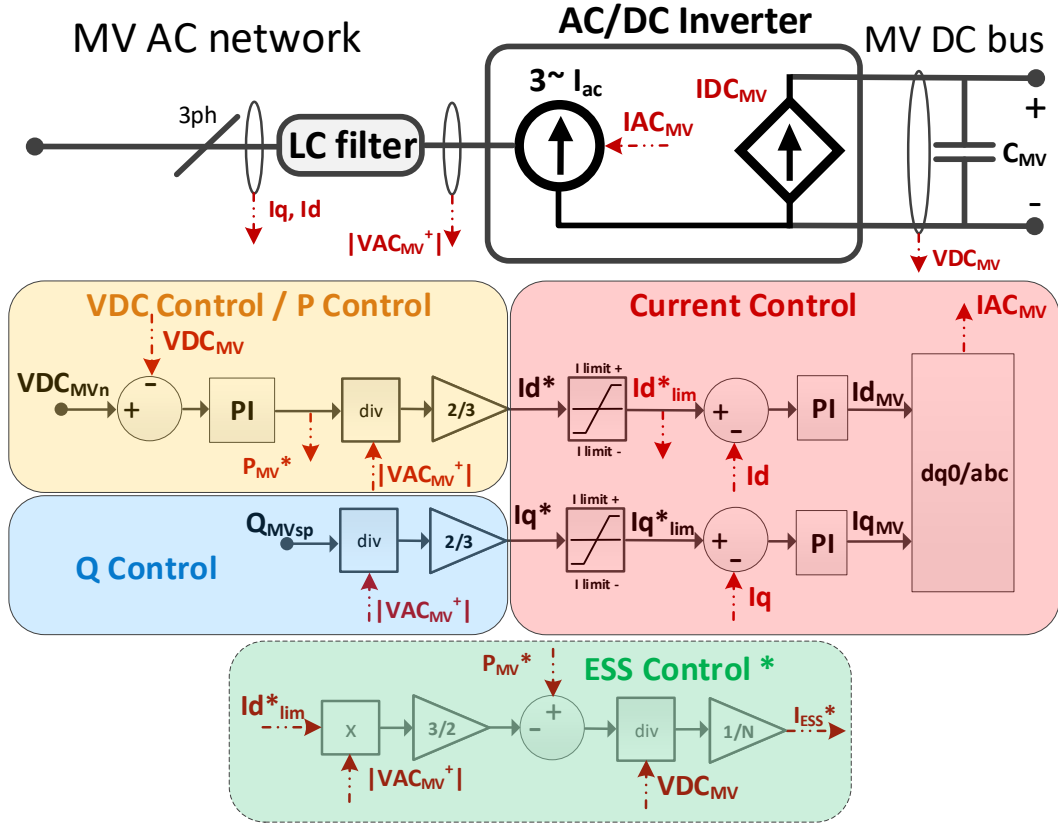


Figure 3.3: Block diagram of the MV Inverter of the grid-following ST - base architecture.

inverter's phases  $a$ ,  $b$  and  $c$  ( $I_{AC_{MV}}$ ). Equation (3.2) defines  $VDC_{MV}$ , where  $C_{MV}$  is the capacitance of the MV DC bus, and  $IDC_{MVbus}$  is the current exchanged by all devices and/or grids connected to the MV DC bus with  $C_{MV}$  excluding  $IDC_{MV}$ .

$$IDC_{MV} = \frac{1}{VDC_{MV}} [v_{ab_{MV}} - v_{ca_{MV}}, v_{bc_{MV}} - v_{ab_{MV}}, v_{ca_{MV}} - v_{bc_{MV}}] \cdot \begin{bmatrix} i_{a_{MV}} \\ i_{b_{MV}} \\ i_{c_{MV}} \end{bmatrix} \quad (3.1)$$

$$VDC_{MV} = \frac{1}{C_{MV}} \int (IDC_{MV} + IDC_{MVbus}) dt \quad (3.2)$$

By using controlled current sources to model the power converter, the coupling LC filter becomes redundant as there are no switching harmonics to mitigate. But since the coupling LC filter still impacts the dynamics of the power converter, it was modeled in order to be consistent with the defined hardware building blocks of the converter while integrating also the associate dynamics response on the developed models. The LC filter for the MV inverter was modeled according to the set of Equations in (3.3), where  $L_{MVf}$  is the filter inductance,  $C_{MVf}$  is the filter capacitance,  $f_c$  is the cut-off frequency,  $Z_0$  is the characteristic impedance of the filter,  $VDC_{MVn}$  is the nominal

voltage of the MV DC bus and  $IAC_{MVp}$  is the peak value of the nominal AC current of the MV inverter. A frequency of 2 kHz was considered to  $f_c$ , which provides an acceptable rejection of the harmonic content which would be generated in a detailed model of a power inverter switching at 20 kHz ( $-40$  dB/decade) while preserving an acceptable control bandwidth for the power inverter.

$$f_c = \frac{1}{2\pi\sqrt{L_{MVf}C_{MVf}}}; \quad Z_0 = \sqrt{\frac{L_{MVf}}{C_{MVf}}} = \frac{VDC_{MVn}}{IAC_{MVp}} \quad (3.3)$$

The size of the MV DC bus capacitance also impacts the dynamics of the ST. For that reason, the MV DC bus capacitance was modeled taking into consideration the voltage ripple in the DC bus which would be expected at the switching frequency on a detailed model of the MV inverter. The current flow in the MV DC bus capacitance ( $IDC_{MVcap}$ ) is defined by Equation (3.4). Assuming that the time needed to discharge the capacitance at the nominal value of the current  $IDC_{MV}$  is much larger than the switching interval of the MV inverter, Equation (3.4) can be fairly approximated by a linearized version of it. By linearizing Equation (3.4),  $dVDC_{MV}$  can be replaced by  $\Delta VDC_{MVsw}$  which is the amplitude of the voltage ripple in the MV DC bus which would result from the inverter's switching,  $dt$  by  $1/f_{sw}$  where  $f_{sw}$  is the switching frequency of the MV inverter, and  $IDC_{MVcap}$  by the nominal  $IDC_{MV}$ , equal to  $\sqrt{3}IAC_{MVn}$  for a worst case. As a result, the MV DC bus capacitance can be defined by Equation (3.5), by assuming a maximum admissible value for  $\Delta VDC_{MVsw}$ .

$$IDC_{MVcap} = C_{MV} \frac{dVDC_{MV}}{dt} \quad (3.4)$$

$$C_{MV} = \frac{\sqrt{3}IAC_{MVn}}{f_{sw}\Delta VDC_{MVsw}} \quad (3.5)$$

## Controller Architecture

The modeled control structure of the MV inverter is based on the Voltage Oriented Control (VOC) approach mentioned in section 2.2.1.3. Given that this thesis is not focused on the development of innovative low-level controllers for power electronic converters, this choice fits well the existing needs as VOC-based approaches are currently the most widely applied and consolidated control approaches for grid-following power electronic converters in DER. However, the lower-level voltage control signals, which on a VOC approach would be applied to controllable voltage sources,

are not represented in the developed models. As controllable current sources are used to model a current-controlled inverter, lower-level current control signals are modeled instead. This particularity simplifies the modeling of a grid-following control in MATLAB®/Simulink® environment without compromising the expected dynamics for the MV inverter [236, 239].

The following control structures are identified in Figure 3.3: *VDC Control / P Control*, *Q Control*, *Current Control* and *ESS Control*.

- **VDC Control / P Control:** This control structure is responsible to regulate the voltage in the MV DC link ( $VDC_{MV}$ ) by controlling the direct component of the reference current of the MV inverter ( $Id^*$ ) according to Equation (3.6), where  $|VAC_{MV}^+|$  is the module of the positive sequence component of the three-phase AC voltage in the MV inverter. For reasons related to the *ESS Control*, better explained further in this thesis, a reference for the active power ( $P_{MV}^*$ ) is generated instead of  $Id^*$  directly.  $P_{MV}^*$  is calculated (using a PI controller) from the error between the measured and reference values for the MV DC voltage ( $VDC_{MV}$  and  $VDC_{MVn}$ , respectively), according to Equation (3.7) expressed in the Laplace domain. The PI controller has an anti-windup mechanism to ensure its integrator does not accumulate beyond the output limits of the PI controller.  $K_p$  and  $K_i$  are respectively the proportional and integral gains of the PI controller.

$$Id^* = \frac{2}{3} \frac{P_{MV}^*}{|VAC_{MV}^+|} \quad (3.6)$$

$$P_{MV}^* = \left( K_p + \frac{K_i}{s} \right) (VDC_{MVn} - VDC_{MV}); \quad P_{MV}^* \in [-P_{MVn}, P_{MVn}] \quad (3.7)$$

- **Q Control:** Constitutes the base control structure for the reactive power exchanged with the MV AC network. The reference reactive power ( $Q_{MVsp}$ ) is used to control the quadrature component of the reference current of the MV inverter ( $Iq^*$ ) according to Equation (3.8).

$$Iq^* = \frac{2}{3} \frac{Q_{MVsp}}{|VAC_{MV}^+|} \quad (3.8)$$

- **Current Control:** This control structure is responsible to regulate the reference currents for the the MV inverter. The three-phase reference current  $IAC_{MV}$  is expressed by Equation (3.9) generated by applying the inverse Park Transformation given by Equation (3.14) to the references for direct and quadrature current  $Id_{MV}$  and  $Iq_{MV}$ .  $\omega t$  is the angular position measured from the MV AC

grid voltage.  $I_{dMV}$  and  $I_{qMV}$  are generated by PI controllers processing the error between the limited reference currents  $I_{dlim}^*$  and  $I_{qlim}^*$  (generated by *VDC Control / P Control* and *Q Control*) and the respective measured  $I_d$  and  $I_q$ , according to Equations (3.10) and (3.11) in the Laplace domain.  $K_{p1}$ ,  $K_{p2}$  are the proportional gains of the PI controllers,  $K_{i1}$ ,  $K_{i2}$  are the integral gains of the PI controllers, and  $I_d$  and  $I_q$  are measured applying the Park Transformation given by Equation (3.13) to the current measured after the LC filter  $IAC_{MVg}$ , as expressed in Equation (3.12).

$$IAC_{MV} = A_P^{-1} I_{dq0}; \quad I_{dq0} = \begin{bmatrix} I_{dMV} \\ I_{qMV} \\ 0 \end{bmatrix} \quad (3.9)$$

$$I_{dMV} = \left( K_{p1} + \frac{K_{i1}}{s} \right) (I_{dlim}^* - I_d) \quad (3.10)$$

$$I_{qMV} = \left( K_{p2} + \frac{K_{i2}}{s} \right) (I_{qlim}^* - I_q) \quad (3.11)$$

$$I_{dq0} = A_P IAC_{MVg}; \quad I_{dq0} = \begin{bmatrix} I_d \\ I_q \\ 0 \end{bmatrix} \quad (3.12)$$

$$A_P = \frac{2}{3} \begin{bmatrix} \sin(\omega t) & \sin(\omega t - \frac{2\pi}{3}) & \sin(\omega t + \frac{2\pi}{3}) \\ \cos(\omega t) & \cos(\omega t - \frac{2\pi}{3}) & \cos(\omega t + \frac{2\pi}{3}) \\ \frac{1}{2} & \frac{1}{2} & \frac{1}{2} \end{bmatrix} \quad (3.13)$$

$$A_P^{-1} = \begin{bmatrix} \sin(\omega t) & \cos(\omega t) & 1 \\ \sin(\omega t - \frac{2\pi}{3}) & \cos(\omega t - \frac{2\pi}{3}) & 1 \\ \sin(\omega t + \frac{2\pi}{3}) & \cos(\omega t + \frac{2\pi}{3}) & 1 \end{bmatrix} \quad (3.14)$$

- **ESS Control:** This control structure is suitable for grid-following ST with local ESS available. If a suitable local ESS is available, this control structure enables the ST continued operation when the current limits of the MV inverter are reached or when the upstream MV AC grid is lost (islanded mode), since the local EES will sink/source the necessary active power for the operation of the DC stages and low voltage inverter. In order to achieve this,  $P_{MV}^*$  is compared with the reference

power for the MV inverter determined by  $Id_{lim}^*$  and  $|VAC_{MV}^+|$ . The existing error is routed to the local ESS through the reference signal  $I_{ESS}^*$ , which is calculated according to Equation (3.15).  $N$  is the transformation ratio of the isolated DC-DC converter (see section 3.2.2). In case of outage of the upstream MV AC grid,  $P_{MV}^*$  is routed to the local ESS as the power reference determined by  $Id_{lim}^*$  and  $|VAC_{MV}^+|$  becomes zero.

$$I_{ESS}^* = \frac{1}{NVDC_{MV}}(P_{MV}^* - \frac{3}{2}Id_{lim}^*|VAC_{MV}^+|) \quad (3.15)$$

### 3.2.1.2 Grid-Forming Converter - Base Architecture and Control

In the modeled grid-forming ST, the MV inverter operates in grid-forming mode and is responsible to couple the ST with the MV AC network. The main hardware building blocks and control structure of the MV inverter are represented in Figure 3.4. As for the grid-following MV converter, the advanced control functionalities proposed for the grid-forming MV converter under the scope of this thesis are not illustrated in Figure 3.4 because its description is reserved for chapter 4. Controlled voltage sources are used to implement the average model of the power converter and a controlled current source is used to implement the interface with the MV DC bus. The ST resorts to a local ESS Energy Storage System (ESS) in order to properly balance the power and voltage in the ST's MV DC link and to ensure the operation of the MV converter in a grid forming mode. The parameterization of the modeled grid-forming converter is presented in Appendix A (Tables A.1 and A.3).

### Power Architecture

The power converter is modeled by a three-phase controlled voltage source in star configuration with isolated neutral, but the neutral point is connected to the negative pole of the MV DC bus in order to ensure common voltage ground references for the MV DC bus and three-phase voltage source. The active power between the coupling *LC filter* and the MV DC bus is also expressed by Equations (3.1) and (3.2) already described in section 3.2.1.1. Regarding the coupling LC filter and the MV DC bus capacitance, the same modeling approaches described in section 3.2.1.1 were adopted.

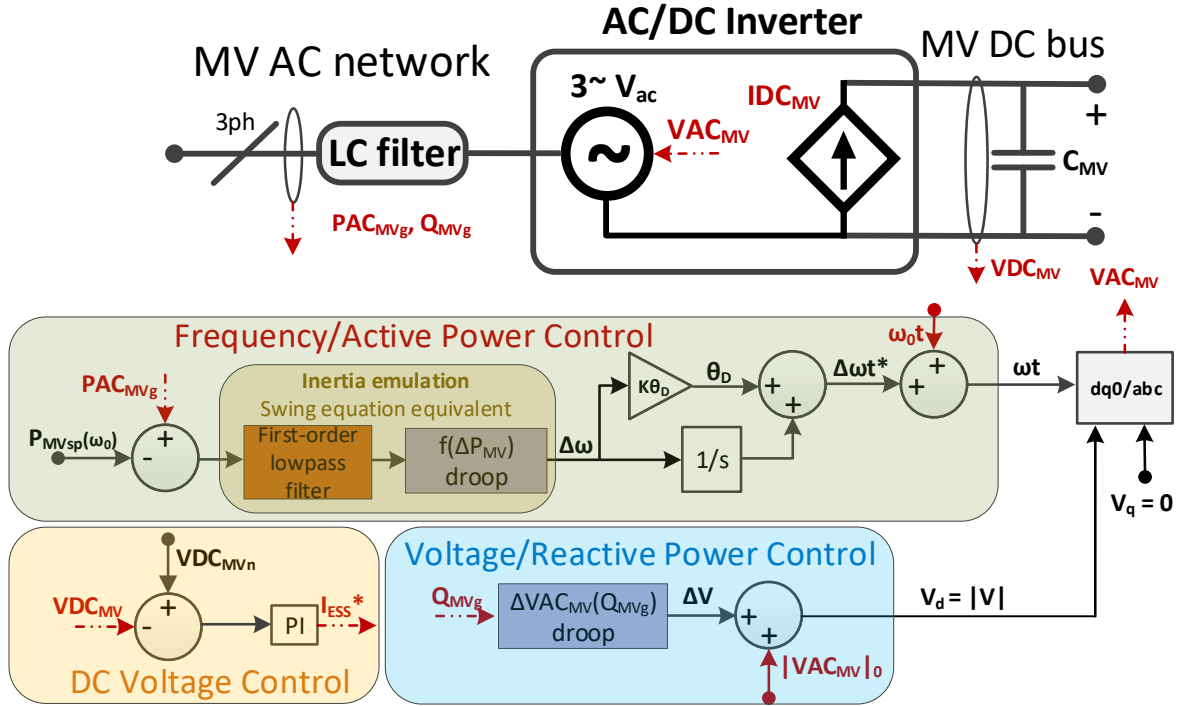
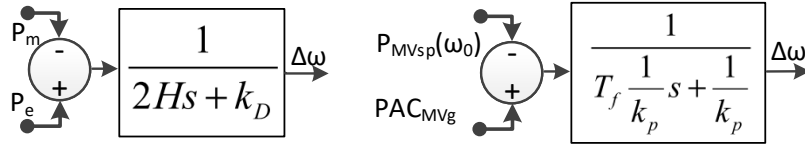


Figure 3.4: Block diagram of the MV Inverter of the grid-forming ST - base architecture.

### Controller Architecture

The base control structure modeled for the MV inverter is based on the Voltage Controlled Inverter approach mentioned in section 2.2.1.1, which is a consolidated approach for grid-forming inverters in DER capable to provide frequency control and inertia emulation. A first-order low-pass filter associated with a droop controller is used to implement the Voltage Controlled Inverter approach, which provides a relatively simple solution to approximate the swing equation of a conventional synchronous machine [201, 240]. Such equivalence is illustrated in Figure 3.5 and expressed by Equation (3.16) [240], where  $H$  is the constant of inertia,  $k_D$  is the damping coefficient,  $T_f$  is the time constant of the first-order low-pass-filter,  $k_p$  is the slope gain of the  $f(\Delta P_{MV})$  droop controller,  $\omega_0$  is the nominal angular frequency,  $S_{MVn}$  the nominal apparent power of the MV inverter,  $PAC_{MVg}$  is the active-power after the LC filter,  $P_{MVsp}(\omega_0)$  is the active-power set-point for the MV inverter at  $\omega_0$  in the MV AC grid, and  $P_e$  and  $P_m$  are the electrical active power and mechanical power of a synchronous machine respectively. Important to mention that positive values for active power correspond to consumed active power.

$$H = \frac{T_f}{2k_p} \frac{\omega_0}{S_{MVn}}; \quad k_D = \frac{1}{k_p} \frac{\omega_0}{S_{MVn}} \quad (3.16)$$



**Figure 3.5:** Equivalence between  $f(P)$  droop plus First-Order Low-pass Filter (right) and Swing Equation (left).

The  $f(\Delta P_{MV})$  and  $\Delta VAC_{MV}(Q_{MVg})$  droop controllers are defined according to Figure 3.6 and Equation (3.17), where  $m_d$  is the droop slope,  $Y$  is the droop output ( $\Delta\omega$  for the  $f(\Delta P_{MV})$  droop and  $\Delta V$  for  $\Delta VAC_{MV}(Q_{MVg})$  droop),  $X$  is the droop variable (active power signal from the low-pass filter for the  $f(\Delta P_{MV})$  droop and  $Q_{MVg}$  for  $\Delta VAC_{MV}(Q_{MVg})$  droop),  $Y_{min}$  and  $Y_{max}$  are the minimum and maximum droop output limits, and  $X_{min}$  and  $X_{max}$  are the input saturation limits of the droop control. Positive values for active and reactive power correspond to consumed active and reactive power.

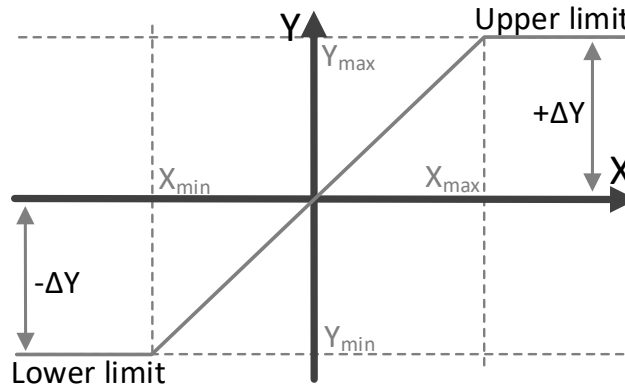


**Figure 3.6:** Control rule for  $f(\Delta P_{MV})$  and  $\Delta VAC_{MV}(Q_{MVg})$  droop controllers.

$$Y = \begin{cases} Y_{min} & \text{if } X \in ]-\infty, X_{min}] \\ m_d(X - X_{min}) + Y_{min} & \text{if } X \in ]X_{min}, X_{max}[ \\ Y_{max} & \text{if } X \in [X_{max}, \infty[ \end{cases} \quad (3.17)$$

Given that the development of low-level controllers for power electronic converters is not the focus of this thesis, the adopted control approach is suited for the work developed in this thesis. The following control structures are identified in Figure 3.4: *Frequency/Active Power Control*, *Voltage/Reactive Power Control* and *DC Voltage Control*

- **Frequency/Active Power Control:** This control structure is responsible to control the angular position (and consequently the frequency) of the voltage generated



by the MV inverter as a function of the error between the measured active power  $P_{AC_{MVg}}$  and active power set-point  $P_{MVsp}(\omega_0)$ . A swing Equation equivalent composed by a first-order low-pass filter and a  $f(\Delta P_{MV})$  droop control generates a frequency deviation ( $\Delta\omega$ ) relatively to  $\omega_0$  (given by the derivative of the reference angular position  $\omega_0 t$  represented in Figure 3.4). In order to further improve the stability of the controller, a damping component  $\theta_D$  is also included. The resulting reference for the angular position  $\omega t$  is expressed by Equation (3.18).

$$\omega t = \omega_0 t + K\theta_D \Delta\omega + \int \Delta\omega dt \quad (3.18)$$

- **Voltage/Reactive Power Control:** This control structure is responsible to control the reference for the voltage magnitude generated by the MV inverter. The generated voltage magnitude is aligned with the direct component ( $V_d$ ) as the angular position of the generated voltage is performed by the *Frequency/Active Power Control*. Consequently, quadrature component ( $V_q$ ) is set to zero.  $V_d$  is given by Equation (3.19), where  $|V_{AC_{MV}}|_0$  is the base voltage magnitude and  $\Delta V$  is the output of the  $Q_{MVg}$  droop controller.

$$V_d = |V| = |V_{AC_{MV}}|_0 + \Delta V \quad (3.19)$$

- **DC Voltage Control:** Corresponds to the base control structure responsible to regulate the voltage in the MV DC link ( $VDC_{MV}$ ).  $VDC_{MV}$  is regulated by using a local ESS integrated with the ST. Such regulation is performed by the reference current  $I_{ESS}^*$  for the ST's local ESS, generated by a PI controller processing the error between  $VDC_{MV}$  and the nominal DC voltage value  $VDC_{MVn}$ , as expressed by Equation (3.20) in the Laplace domain.  $K_p$  and  $K_i$  are respectively the proportional and integral gains of the PI controller.

The *DC Voltage Control* is shown as an independent control structure inside the controller of the MV inverter, but its actuation is influenced by the *Frequency/Active Power Control* which controls the active power balance in the MV DC bus, and consequently,  $VDC_{MV}$ . Such relationship is expressed by Equation (3.21) (derived from Equations (3.1) and (3.2)), where  $P_{MV}$  is the active power in the MV inverter.

$$I_{ESS}^* = \left( K_p + \frac{K_i}{s} \right) (VDC_{MVn}^* - VDC_{MV}) \quad (3.20)$$

$$VDC_{MV} = \frac{1}{C_{MV}} \int \left( \frac{P_{MV}}{VDC_{MV}} + IDC_{MVbus} \right) dt \quad (3.21)$$

At last, the three-phase voltage reference  $V_{AC_{MV}}$  is expressed by Equation (3.22), applying the inverse Park transformation expressed in Equation (3.14) to the references for  $V_d$  and  $V_q$ , using the generated  $\omega t$  reference for the angular position.

$$V_{AC_{MV}} = A_p^{-1} V_{dq0}; \quad V_{dq0} = \begin{bmatrix} V_d \\ V_q \\ 0 \end{bmatrix} \quad (3.22)$$

### 3.2.2 Isolated DC-DC Power Converters

A similar base structure for the isolated DC-DC power converter was modeled for both grid-forming and grid-following ST, which is illustrated in Figure 3.7. Only the base power and control architectures are addressed in this sub-section. The advanced control solutions proposed under the scope of this thesis are reserved for chapter 4.

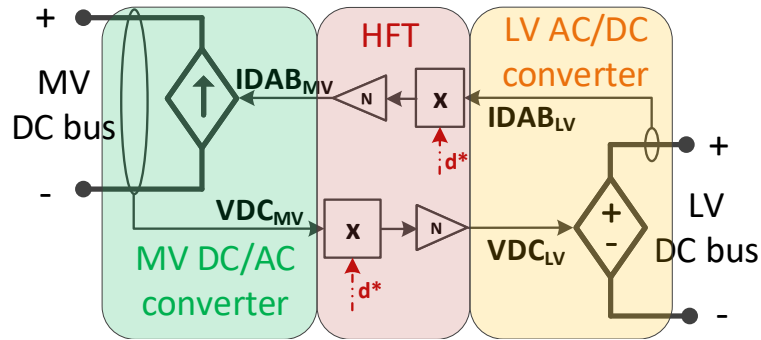


Figure 3.7: Block diagram of the DC/DC converter stage.

The isolated DC/DC converter was modeled according to the basic principles of an ideal Dual-Active (DAB) DC/DC converter, following the approach presented in [241]. The DAB topology was selected because it is a well investigated solution which allows the active control of the transferred power [41, 47], contrarily to the Series-Resonant converter as discussed in section 2.2.3. The DAB solution is adequate since the development of new hardware solutions for isolated DC/DC converters is not an objective of this thesis.

Three main components for the modeled DAB are identified in Figure 3.7: the *MV DC/AC converter* and *LV DC/AC converter* represent the DC/AC power conversion interfaces with the ST's MV and LV DC buses in both MV and LV sides of the DAB respectively, and the high-frequency transformer (HFT).

In an ideal DAB converter, the power output in the *LV DC/AC converter* ( $PDAB_{LV}$ ) is obtained using Equation (3.23), where  $VDC_{MV}$  is the voltage in the MV DC bus,  $VDC_{LV}$  the voltage in the LV DC bus,  $N$  is the transformation ratio of the HFT,  $X_L$  is the HFT's primary-referred leakage reactance,  $d$  is the duty-cycle applied to the square waveforms applied to the HFT,  $\phi$  is the phase-shift between the square waveforms applied to the HFT, and  $d^*$  is the external duty-cycle control.

$$PDAB_{LV} = \frac{VDC_{MV}^2}{X_L} d \phi \left( 1 - \frac{|\phi|}{\pi} \right); \quad d = \frac{VDC_{LV}}{2Nd^*VDC_{MV}}; \quad d^* \in [0, 1] \quad (3.23)$$

According to the results presented in [241], the dynamics of a DAB converter is much faster than the dynamics related to voltage variations in the MV DC bus. Therefore, two assumptions are made in the modeled DAB.

- The DAB is modeled using two controllable sources according to the DAM approach [236], which are electrically independent in order to consider galvanic isolation.
- The mathematical relations presented in Equations (3.24) and (3.25) are valid for an ideal DAB converter, where  $VDC_{MVn}$  and  $VDC_{LVn}$  are the nominal DC voltages in the MV and LV DC buses respectively,  $IDAB_{MV}$  is the DC current in the *MV DC/AC converter*,  $IDAB_{LV}$  is the DC current in the *LV DC/AC converter* and the remaining variables are as defined for Equation (3.23).

Given this, the control loops required to regulate  $d$  and  $\phi$  variables in Equation (3.23) are replaced by the simplified feedback control loops shown in Figure 3.7.

$$VDC_{MV}IDAB_{MV} = VDC_{LV}IDAB_{LV} \iff \frac{VDC_{LV}}{d^*N}IDAB_{MV} = VDC_{LV}\frac{IDAB_{MV}}{d^*N} \quad (3.24)$$

$$N = \frac{VDC_{LVn}}{VDC_{MVn}} \quad (3.25)$$

### 3.2.3 Local Energy Storage System and Supercapacitor Bank

An ESS is an important requirement for the operation of a grid-forming ST, being not essential for a grid-following ST. Nevertheless, even for grid-following ST, there is a need to mitigate voltage oscillations in the ST's DC buses in order to enable a feasible operation of DC grids derived from the ST's DC links. Such oscillations result from unbalanced operation conditions in AC grids interfaced by the ST, as well from harmonic components derived from non-linear loads in the LV AC grid interfaced by

the ST. For grid-forming ST, such task can be performed by the modeled local ESS. For grid-following ST where no local storage capacity is available, a simpler and less costly solution based on supercapacitors is assumed for supporting the proper DC voltage control and suppressing associated oscillations.

The models developed for the local ESS and the supercapacitor bank, very similar with minor changes, are described separately in the following subsections.

### 3.2.3.1 Local Energy Storage System

The modeled local ESS and respective control structure are shown in Figure 3.8. Given that the phenomena and simulation time frame under analysis in this thesis don't require a high energy volume, the sizing of the local ESS doesn't pose any relevant limitations, and thus, is not addressed. The local ESS and the associated DC/DC converter were modeled using a controlled current source based on the DAM approach. The low-level control structure of the DC/DC converter was also neglected, under the assumption that their dynamics is much faster in comparison to the dynamics related to the phenomena under study to which the local ESS must react.

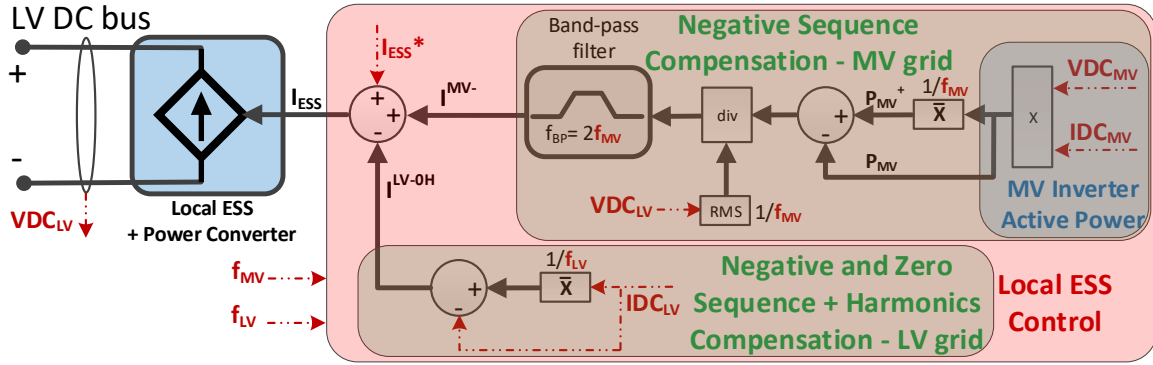


Figure 3.8: Block diagram of the modeled local ESS.

The current output of the local ESS is defined by Equation (3.26). The identified variables are described next.

$$I_{ESS} = I_{ESS}^* + I^{MV-} + I^{LV-OH} \quad (3.26)$$

For the grid-forming ST,  $I_{ESS}^*$  is responsible to keep the power balance in the DC links and is generated by the *DC Voltage Control* in the controller of the MV inverter as shown in Figure 3.4. For the grid-following ST, for the cases where a local ESS is considered,  $I_{ESS}^*$  is derived from  $P_{MV}^*$  (represented in Figure 3.3) according to Equation (3.15).

$I^{MV-}$  is the current compensation for power oscillations in the DC links resulting from the presence of a negative sequence component in the MV AC grid voltage at the connection point with the ST.  $I^{MV-}$  is obtained according to Equation (3.27) in the Laplace s-domain. A second-order band-pass filter captures the power oscillations resulting from the negative-sequence component present in the MV AC grid, using the error between the instantaneous ( $P_{MV}$ ) and positive-sequence ( $P_{MV}^+$ ) active power in the MV inverter.  $P_{MV}^+$  is captured by applying the mean operator to  $P_{MV}$  over a running window equal to the time period of the fundamental frequency in the MV AC grid ( $f_{MV}$ ).

$$I^{MV-} = \frac{P_{MV}^+ - P_{MV}}{VDC_{LV}} \frac{\sqrt{2}\omega_n s}{s^2 + \sqrt{2}\omega_n s + \omega_n^2}; \quad \omega_n = 2\pi f_{MV} \quad (3.27)$$

$I^{LV-0H}$  is the current compensation for power oscillations in the DC links resulting from unbalanced operation conditions as well from harmonic components derived from non-linear loads in the LV AC grid interfaced by the ST.  $I^{LV-0H}$  is given by Equation (3.28), where  $\overline{IDC_{LV}}$  is the mean value of  $IDC_{LV}$  over the time period of the fundamental frequency in the LV AC grid ( $f_{LV}$ ).

$$I^{LV-0H} = \overline{IDC_{LV}} - IDC_{LV} \quad (3.28)$$

The presence of a zero sequence component in the MV AC grid voltages is not considered because an isolated neutral point is considered for the MV inverter. Regarding the compensation of harmonic content in MV AC grid resulting from non-linear loads, it is assumed that its magnitude is relatively small in general [242], and consequently, poses no relevant impacts on the voltage stability in the DC links. The limited gains for the voltage stability in the DC links obtained by compensating the aforementioned harmonic content are not justifiable in face of the drawbacks regarding the deterioration of the dynamic response of the ST resulting from the introduction of additional time response delays. As such, the compensation of the aforementioned harmonic content is not considered.

### 3.2.3.2 Supercapacitor Bank (Grid-Following Smart-Transformer only)

The modeled supercapacitor bank and respective control structure are illustrated in Figure 3.9. The model for the supercapacitor bank is similar to the model for the local ESS described in section 3.2.3.1, except for the signal  $I_{ESS}^*$  which is absent given that no local ESS is considered.

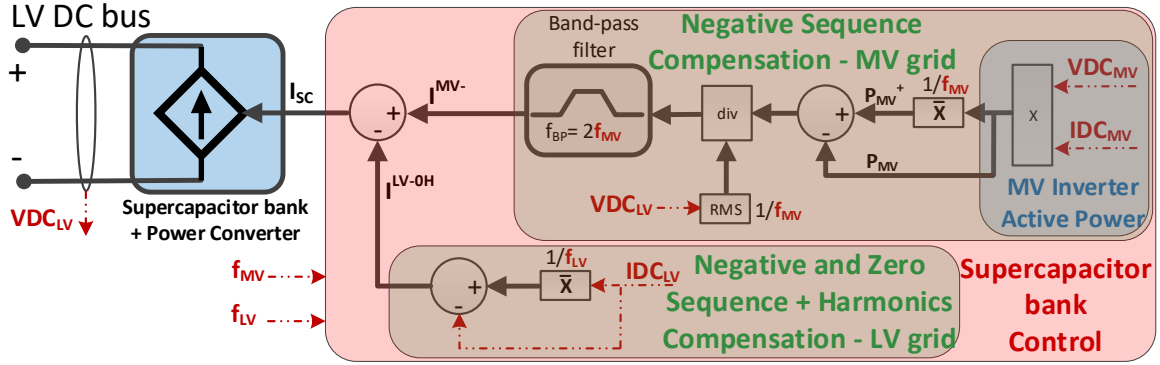


Figure 3.9: Block diagram of the modeled supercapacitor bank.

The supercapacitor bank and the associated DC/DC converter were modeled using a controlled current source based on the DAM approach, according to the considerations adopted in section 3.2.3.1 for the local ESS and respective DC/DC converter. Moreover, as shown in Appendix A (Table A.4), a relatively small supercapacitor bank is sufficient to meet the required energy storage and power output demanded to suppress the aforementioned power oscillations in the ST's DC links, with a sufficiently high margin to neglect the modeling of any energy and power constraints affecting the supercapacitor bank.

For grid-following ST with no local energy storage available, the use of a supercapacitor bank is justified as follows. The use of the MV inverter to compensate the power oscillations in the DC links could imply a considerable reduction in the transferable active power (positive-sequence component) through the MV inverter during severe unbalanced voltage sags in the MV AC grid. As evidenced in chapter 4, this would negatively impact the ST's ability to mitigate the adverse impacts on its hybrid AC/DC grid resulting from unbalanced fault disturbances in the upstream MV AC grid.

Alternatively, the power oscillations in the DC links could be mitigated by increasing the capacitance in the DC links, but such approach would require unrealistic bulky capacitors in order to achieve an acceptable maximum limit for the DC voltage ripple, which would significantly degrade the dynamics of the ST itself.

The use of a supercapacitor bank is able to avoid the aforementioned drawbacks. Besides preserving the transferable power in the MV inverter, it also preserves the dynamics of the ST against disturbances in the MV AC grid because it only actuates against power oscillations associated to the negative-sequence component, as explained in section 3.2.3.1. According to [243], the double fundamental frequency harmonic (related to the negative sequence component) is dominant in the DC link voltage ripple when an unbalanced operation condition occurs in the AC grids, being thus reasonable

to neglect the high frequency voltage ripple components.

Based on [243], and considering the possible maximum impacts from MV and LV AC grids interfaced by the ST, it is possible to derive Equation (3.29) to express the voltage ripple in the MV DC link ( $\Delta VDC_{MV_{pp}}$ ).

$$\Delta VDC_{MV_{pp}} = \frac{3M_{MV}f_{LV}|IAC_{MV}^-| + 3M_{LV}f_{MV}d^*N|IAC_{LV}^-|}{8\pi f_{MV}f_{LV}(C_{MV} + (d^*N)^2(C_{LV} + (\frac{V_{SC}}{VDC_{LV}})^2C_{SC}))} \quad (3.29)$$

$M_{MV}$  and  $M_{LV}$  are the modulation indexes for the MV and LV inverters respectively,  $IAC_{MV}^-$  and  $IAC_{LV}^-$  are the negative sequence components in the AC currents exchanged by the ST with the MV and LV AC grids respectively,  $f_{MV}$  and  $f_{LV}$  are the fundamental frequencies in MV and LV AC grids respectively,  $N$  and  $d^*$  are respectively the transformation ratio and external duty-cycle control for the isolated DC/DC converter,  $C_{MV}$  and  $C_{LV}$  are respectively the capacitance of the MV and LV DC buses,  $C_{SC}$  is the capacitance of the supercapacitor bank,  $V_{SC}$  is the DC voltage in the supercapacitor bank, and  $VDC_{LV}$  is the voltage in the LV DC bus.

From Equation (3.29), the maximum  $\Delta VDC_{MV_{pp}}$  can be confined according to Equation (3.30) by assuming the worst case scenario.  $M_{MV}$  and  $M_{LV}$  are maximum (equal to 1).  $IAC_{MV}^-$  and  $IAC_{LV}^-$  are in phase opposition, its module is equal to the respective nominal currents ( $IAC_{MVn}$  and  $IAC_{LVn}$ ), and they travel entirely through the MV and LV inverters ( $IAC_{LVn}d^*N = IAC_{MVn}$ ). It is also assumed that  $f_{MV}$  and  $f_{LV}$  are relatively close to the nominal frequency of AC grids ( $f_0$ ).

$$\Delta VDC_{MV_{pp}}^{max} = \frac{6|IAC_{MVn}|}{8\pi f_0(C_{MV} + (d^*N)^2(C_{LV} + (\frac{V_{SC}}{VDC_{LV}})^2C_{SC}))} \quad (3.30)$$

### 3.2.4 Low-Voltage Power Converters

The base structure for the modeled LV inverter existing in the ST, which is common for both grid-forming and grid-following ST, operates always in grid-forming mode and is responsible to interface with a LV AC network. The base architecture of the LV inverter is illustrated in Figure 3.10, where only the main hardware building blocks and control architecture are represented. The advanced control functionalities proposed for this converter, which are the focus of this thesis, are reserved for chapter 4. The parameterization of the modeled LV inverter is presented in Appendix A (Tables A.1 and A.5).



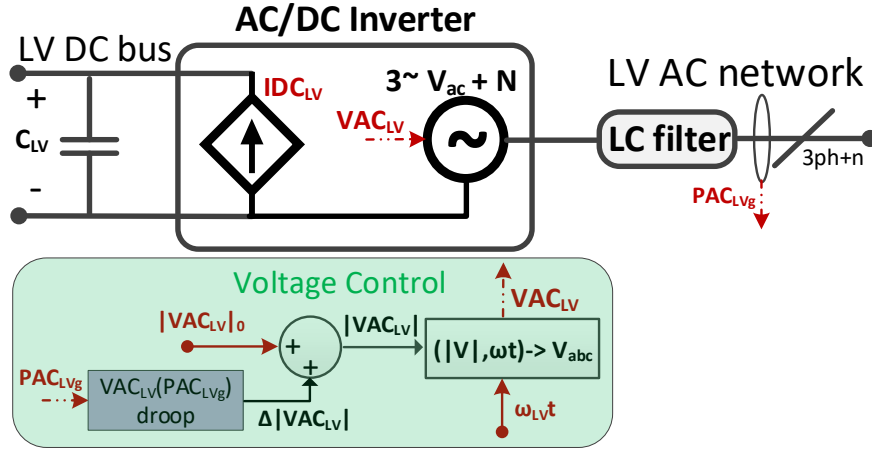


Figure 3.10: Block diagram of the LV inverter of the ST - base architecture.

### Power Architecture

The average model of the LV inverter is implemented with controlled voltage sources, whereas the interface of the LV inverter with the LV DC bus is modeled by a controlled current source. The power converter is modeled as a four-leg inverter, formed by a three-phase controlled voltage source in star configuration with grounded neutral connection available. A four-leg inverter was considered because a neutral wire path is necessary given the unbalanced nature of the LV AC sub-grid. The neutral point is also connected to the negative pole of the LV DC bus in order to ensure common voltage ground references for the LV DC bus and three-phase voltage source. The active power flow in the LV inverter is expressed by Equation (3.31), where  $IDC_{LV}$  is the DC current exchanged with the LV DC bus,  $VDC_{LV}$  is the LV DC bus voltage,  $v_{an_{LV}}$ ,  $v_{bn_{LV}}$  and  $v_{cn_{LV}}$  are the phase-neutral LV AC voltages (in phases  $a$ ,  $b$  and  $c$ ) in the LV inverter ( $VAC_{LV}$ ), and  $i_{a_{LV}}$ ,  $i_{b_{LV}}$  and  $i_{c_{LV}}$  are the three-phase AC currents (phases  $a$ ,  $b$  and  $c$ ) in the LV inverter ( $IAC_{LV}$ ).  $VDC_{LV}$  is defined by Equation (3.32), where  $C_{LV}$  is the capacitance of the LV DC bus, and  $IDC_{LVbus}$  is the current exchanged by all devices (including  $I_{ESS}$  or  $I_{SC}$ ) and/or grids connected to the LV DC bus with  $C_{LV}$ , excluding  $IDC_{LV}$ .

$$IDC_{LV} = \frac{1}{VDC_{LV}} [v_{an_{LV}}, v_{bn_{LV}}, v_{cn_{LV}}] \cdot \begin{bmatrix} I_{a_{LV}} \\ I_{b_{LV}} \\ I_{c_{LV}} \end{bmatrix} \quad (3.31)$$

$$VDC_{LV} = \frac{1}{C_{LV}} \int (IDC_{LV} + IDC_{LVbus}) dt \quad (3.32)$$

A coupling LC filter for the LV inverter was also modelled, based on the same con-



siderations presented in section 3.2.1.1. The LC filter for the LV inverter was modeled according to the set of Equations in (3.33), where  $L_{LVf}$  is the filter inductance,  $C_{LVf}$  is the filter capacitance,  $f_c$  is the cut-off frequency,  $Z_0$  is the characteristic impedance of the filter,  $VDC_{LVn}$  is the nominal voltage of the LV DC bus and  $IAC_{LVp}$  is the peak value of the nominal AC current of the LV inverter. A frequency of 2 kHz was considered to  $f_c$ , which provides an acceptable rejection of the harmonic content which would be generated in a detailed model of a power inverter switching at 20 kHz (−40 dB/decade) while preserving an acceptable control bandwidth for the power inverter.

$$f_c = \frac{1}{2\pi\sqrt{L_{LVf}C_{LVf}}}; \quad Z_0 = \sqrt{\frac{L_{LVf}}{C_{LVf}}} = \frac{VDC_{LVn}}{IAC_{LVp}} \quad (3.33)$$

The LV DC bus capacitance was also modeled based on the premises described in section 3.2.1.1. The current flow in the LV DC bus capacitance ( $IDC_{LVcap}$ ) is defined by Equation (3.34), which may be linearized under the same considerations admitted in section 3.2.1.1, as defined by Equation (3.35).  $dVDC_{LV}$  is replaced by  $\Delta VDC_{LVsw}$  which is the amplitude of the hypothetical voltage ripple in the LV DC bus which would result from the inverter's switching,  $dt$  by  $1/f_{sw}$  where  $f_{sw}$  is the switching frequency of the LV inverter, and  $IDC_{LVcap}$  by the nominal  $IDC_{LV}$ , equal to  $\sqrt{3}IAC_{LVn}$  for a worst case scenario. Given this, the LV DC bus capacitance can be defined by Equation (3.35) by assuming a maximum admissible value for  $\Delta VDC_{LVsw}$ .

$$IDC_{LVcap} = C_{LV} \frac{dVDC_{LV}}{dt} \quad (3.34)$$

$$C_{LV} = \frac{\sqrt{3}IAC_{LVn}}{f_{sw}\Delta VDC_{LVsw}} \quad (3.35)$$

The control of  $VDC_{LV}$  is related to the control of  $VDC_{MV}$  because the power balance in the DC links is performed by the controller of the MV inverter. In this task, the MV inverter in the grid-following ST resorts to the power availability in the upstream MV AC grid, while the MV inverter in the grid-forming ST resorts to the local ESS. Such relationship is expressed by Equation (3.36) which results from the combination of Equations (3.2), (3.24) and (3.32).

$$VDC_{LV} = \frac{d^*N}{C_{MV} - (d^*N)^2 C_{LV}} \int (IDC_{MV} + IDC_{MVbus} - d^*N(IDC_{LV} + IDC_{LVbus})) dt \quad (3.36)$$

### Controller Architecture

The base control structure of the LV inverter is based on Droop-Based control methods (already mentioned in section 2.2.1.1) to generate the reference three-phase AC voltage  $VAC_{LV}$  for the LV inverter.  $VAC_{LV}$  is generated according to Equation (3.37), where  $\omega_{LV}t$  and  $|VAC_{LV}|$  are respectively the reference angular position and magnitude for  $VAC_{LV}$ .

$$VAC_{LV} = \begin{bmatrix} V_a \\ V_b \\ V_c \end{bmatrix} = |VAC_{LV}| \cdot \begin{bmatrix} \sin(\omega_{LV}t) \\ \sin\left(\frac{-2\pi}{3} + \omega_{LV}t\right) \\ \sin\left(\frac{2\pi}{3} + \omega_{LV}t\right) \end{bmatrix} \quad (3.37)$$

$|VAC_{LV}|$  results from Equation (3.38), where  $|VAC_{LV}|_0$  is the base voltage magnitude and  $\Delta|VAC_{LV}|$  is output of the  $VAC_{LV}(PAC_{LVg})$  droop controller represented in Figure 3.10. The  $VAC_{LV}(PAC_{LVg})$  droop controller adjusts the amplitude of  $VAC_{LV}$  ( $|VAC_{LV}|$ ) as a function of the active power in the LV AC grid measured after the LV LC filter. The  $VAC_{LV}(PAC_{LVg})$  droop controller is defined according to Figure 3.6 and Equation (3.17), where  $m_d$  is the droop slope,  $Y$  is the droop output ( $\Delta|VAC_{LV}|$ ),  $X$  is the droop variable ( $PAC_{LVg}$ ),  $Y_{min}$  and  $Y_{max}$  are the minimum and maximum droop output limits, and  $X_{min}$  and  $X_{max}$  are the input saturation limits of the droop control.

$$|VAC_{LV}| = |VAC_{LV}|_0 + \Delta|VAC_{LV}| \quad (3.38)$$

The adopted control approach is appropriate since the development of innovative low-level controllers for power electronic converters is not the focus of this thesis.

## 3.3 Test Distribution Grids: Architectures and Control

In the scope of this thesis, a set of test grids were considered and modeled in order to evaluate the effectiveness of the advanced control functionalities developed for ST, described in detail in chapter 4. The base layouts of the modeled test grids are presented in Figure 3.11.

The first layout (top) consists of a Hybrid Microgrid (HMG) plus a MV DC grid connected to the relevant stages of a single ST, which is then connected to an upstream MV AC grid. This configuration is aimed to evaluate the advanced control strategies

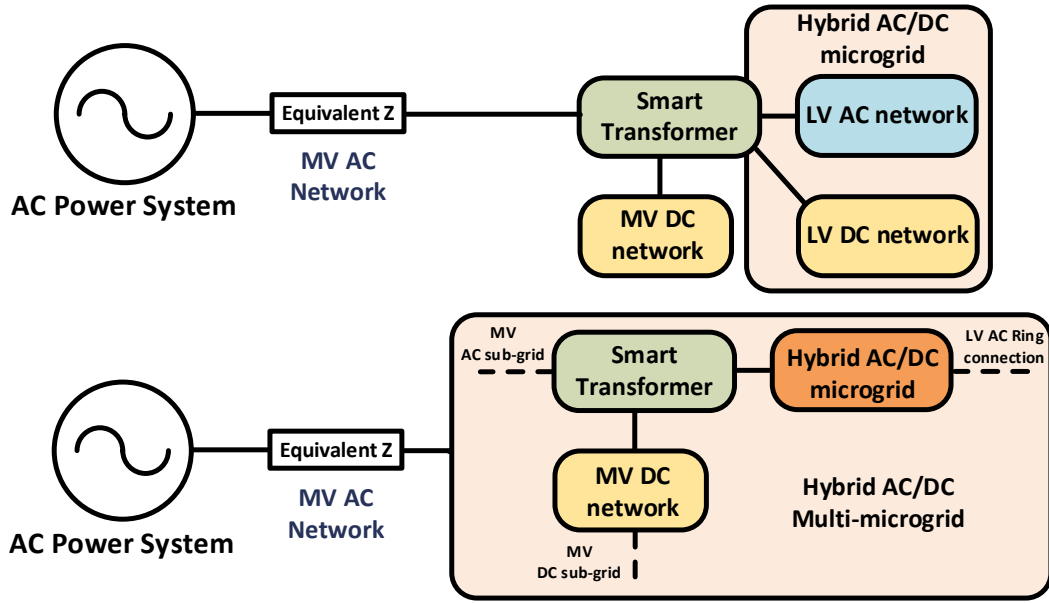


Figure 3.11: Base architecture for the modeled test grids.

proposed in chapter 4 for power-frequency regulation and Fault-Ride-Through (FRT) capabilities.

The second layout (bottom) consists of a Hybrid Multi-Microgrid (HMMG) incorporating several distribution grids based on ST or Low-Frequency Transformers (LFT), connected to an upstream MV AC grid. In this case, the MV DC grid can be connected to a wider MV DC grid connecting to other ST, whereas the ST-based LV AC grid can be exploited in ring configuration, connected both to a ST and to a conventional LFT. This configuration is aimed to evaluate the advanced control strategies proposed in chapter 4 for FRT and Islanding/Reconnection capabilities involving grid-sections of the HMMG.

The developed test grids were based on IEEE test grids whenever justifiable and possible, although no suitable IEEE test grids for HMG and HMMG incorporating ST were found in the literature at the time of writing of this thesis. The configuration of the modeled test grids and its various elements, including loads and Distributed Energy Resources (DER), are described in this section. The model parameters adopted for the different components constituting the test grids are presented in Appendix A.

### 3.3.1 Upstream AC Power System

The modeled HMG and HMMG have a connection available to a stronger upstream AC power system. But the modeling of a complex power system, or even the use of an IEEE test grid for this purpose, would not provide meaningful improvements in

the evaluation of the advanced control functionalities proposed for ST in this thesis. Thus, in order to discard the resulting unnecessary computational burden that such approach implies, a simplified Thevenin equivalent of the upstream AC power system seen from the MV level is adopted. The upstream AC power system is modeled by means of an equivalent synchronous machine and an equivalent load, as illustrated in Figure 3.12.

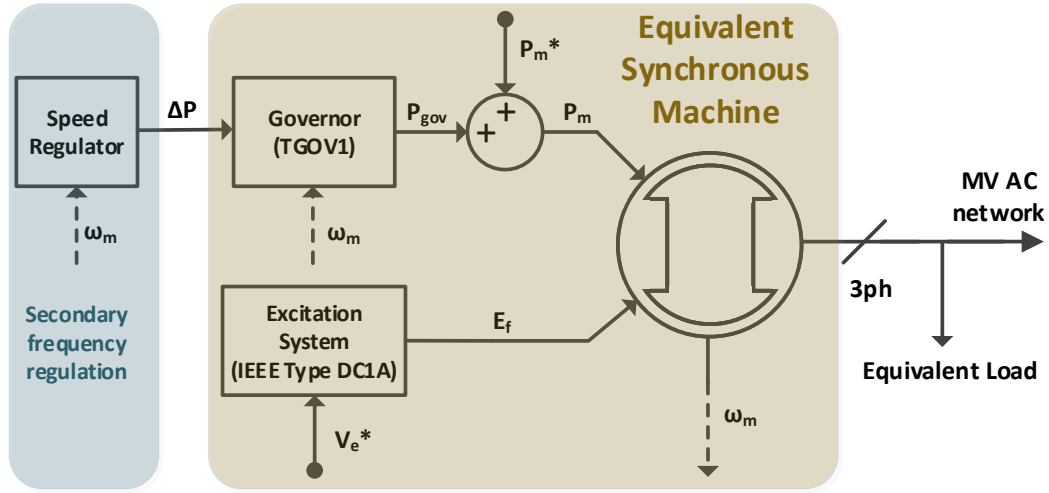


Figure 3.12: Equivalent computational model for the Upstream AC power system.

The adopted modeling approach is suitable to emulate representative frequency variations and fault disturbances, to which the ST is intended to provide active power-frequency support and FRT capabilities. The *Simplified Synchronous Machine* model available in the library of MATLAB®/Simulink® software was adopted to model the equivalent synchronous machine. In order to regulate the frequency and power output of the equivalent Synchronous Machine, a TGOV1 type governor and an IEEE Type DC1A excitation system were modeled with minor modifications. The TGOV1 type governor is described in [244] and is sufficient for the intended purposes in spite of being the simplest steam turbine model. The IEEE Type DC1A excitation system is based on [245] and is modeled in the library of MATLAB®/Simulink® software with minor changes. A speed regulator was also modeled in order to bring the Synchronous Machine to the nominal speed in the face of load changes. The speed regulator was modeled according to Equation (3.39) in the Laplace domain, where  $\Delta P_m$  is the mechanical power regulation,  $K$  is the regulator gain, and  $\omega_{0m}$  and  $\omega_m$  are respectively the nominal and measured mechanical angular speed of the synchronous generator.

$$\Delta P_m = \frac{K}{s}(\omega_{0m} - \omega_m) \quad (3.39)$$

The equivalent load is modeled as a constant impedance load using a three-phase series RL load model available in the library of MATLAB®/Simulink® software. This approach is sufficient for the intended purposes.

The parameterization of the various components of the modeled upstream AC power system is presented in Appendix A (Table A.6).

### 3.3.2 Hybrid AC/DC Microgrid based on ST

The base architecture of the considered ST-based HMG is illustrated in Figure 3.11. The LV AC and DC grids are connected to the corresponding stages of a ST. This HMG configuration provides the necessary flexibility in order to demonstrate the effectiveness of the ST because more complex HMG configurations are not required to demonstrate the advanced control functionalities described in chapter 4.

#### 3.3.2.1 Low Voltage AC grid in Radial Configuration

The modeled LV AC sub-grid integrating the ST-based HMG is based on the IEEE European Low Voltage Test Feeder described in [246] and illustrated in Figure 3.13. The original IEEE test grid consists of a radial distribution feeder operating at 50Hz, has a nominal phase-phase voltage of 416V, and is connected to an 11kV MV grid through a LFT [246].

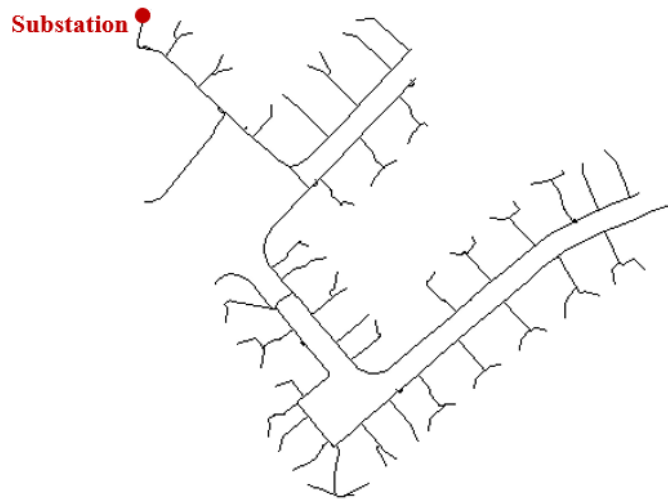


**Figure 3.13:** One-line diagram of the IEEE European low voltage test feeder (adopted from [246]).

However, the complete detailed model of the test network described in [246] would imply a considerable computational burden which is not required to evaluate the advanced control functionalities proposed for ST in this thesis. A simpler equivalent

model was adopted instead, but its parameterization is still based on the data provided in [246] and is presented in Appendix A (Tables A.7 and A.8). Thus, the modeled LV AC grid consists in a single main feeder with equivalent loads representing the derived feeders and other aggregated loads connected to the main feeder, and the different cable sections of the LV feeder are modeled as a three-phase RL branch without mutual inductance.

Moreover, in order to adapt the test network to the purposes discussed in this thesis, the following adaptations were made:

- The MV/LV substation is replaced by a ST.
- A phase-phase low-voltage of 400V was considered taking as reference a typical Portuguese distribution network.
- DER (PV generation, ESS and EV chargers) were added throughout the LV grid in order to fully evaluate the proposed advanced control functionalities involving the different type of resources expected to be available in a future LV distribution grid.

Given this, the resulting LV sub-grid considered for the modeled HMG was modeled according to the one-line diagram illustrated in Figure 3.14. The considered equivalent loads (L1 to L6) are aggregated according to the represented colors. The considered point of connection of the equivalent loads are signaled in the main feeder (red) with a dot with the respective color, being such locations considered to determine the equivalent cable sections between the equivalent loads and the ST's LV inverter.

As described in further detail in chapter 4, the evaluation of the advanced control functionalities proposed in this thesis also involves the exploitation of load-voltage and load-frequency sensitivities in AC networks. For this reason, models sensitive to the grid's voltage and frequency were adopted for the load and controllable DER located in the LV AC grid.

### Load modeling

The loads were modeled using exponential load models, which according to [247] have been the most frequently used static load models by TSOs worldwide. Based on the main considerations formulated in [247], Equations (3.40) and (3.41) are used to model the aggregated active ( $P$ ) and reactive ( $Q$ ) non-controllable load in the LV AC grid, where  $P_0$  and  $Q_0$  are respectively the active and reactive loads at the nominal voltage ( $V_{AC_{LVn}}$ ) and frequency ( $f_0$ ),  $f_{LV}$  is the LV AC network frequency,  $k_{pv}$  and  $k_{qv}$  are respectively the active and reactive power exponents determining the power-

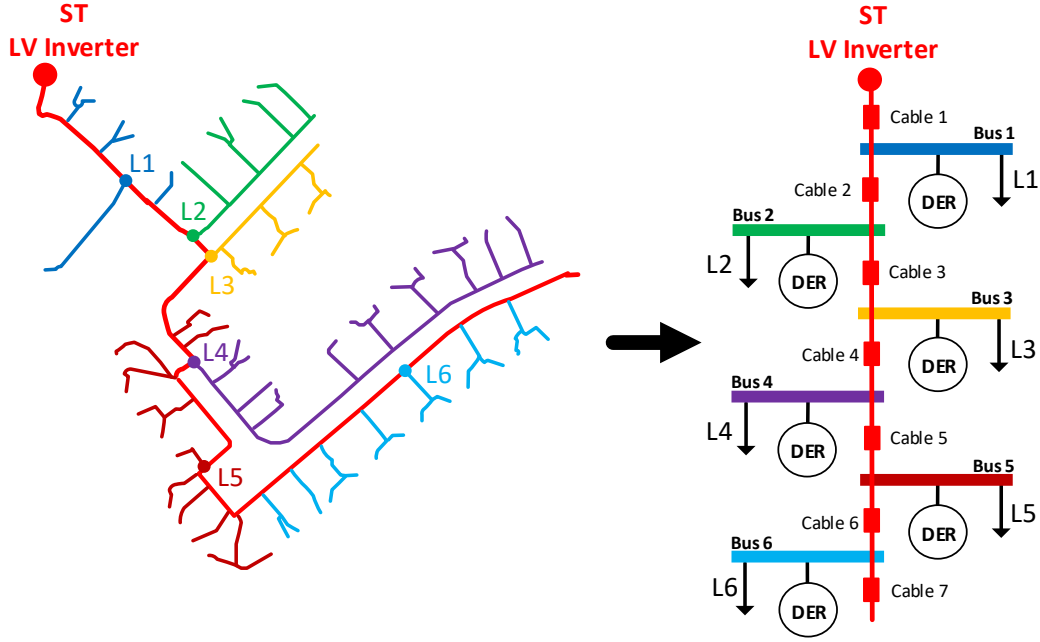


**Figure 3.14:** One-line diagram of the modeled LV AC sub-grid (right) based on the IEEE European low voltage test feeder (left).

voltage load sensitivity, and  $k_{qf}$  and  $k_{pf}$  are respectively the active and reactive power exponents determining the power-frequency load sensitivity.

$$P = P_0 \left( \frac{VAC_{LVg}}{VAC_{LVn}} \right)^{k_{pv}} \left( 1 + k_{pf} \frac{f_{LV} - f_0}{f_0} \right) \quad (3.40)$$

$$Q = Q_0 \left( \frac{VAC_{LVg}}{VAC_{LVn}} \right)^{k_{qv}} \left( 1 + k_{qf} \frac{f_{LV} - f_0}{f_0} \right) \quad (3.41)$$

The parameterization of  $k_{pv}$  and  $k_{qv}$  follows the average value estimations for the entire world presented in [247]. Regarding  $k_{qf}$  and  $k_{pf}$ , a range of values for residential load in North America is provided in [247], considered realistic to be used here. The parameterization values are summarized in Appendix A (Table A.9).

## DER modeling

The controllable DER were modeled according to the block diagram presented in Figure 3.15. The model presented in Figure 3.15 is used to model PV generators, distributed ESS and EV chargers connected to the LV AC grid. For distributed ESS and EV chargers, bidirectional power flow is allowed (V2G is considered for EV chargers), while only active power injection is considered for PV generation. Such distinction is achieved at the parameterization level, by setting the negative current limit ( $I_{limit-}$ )

to zero for PV generation.

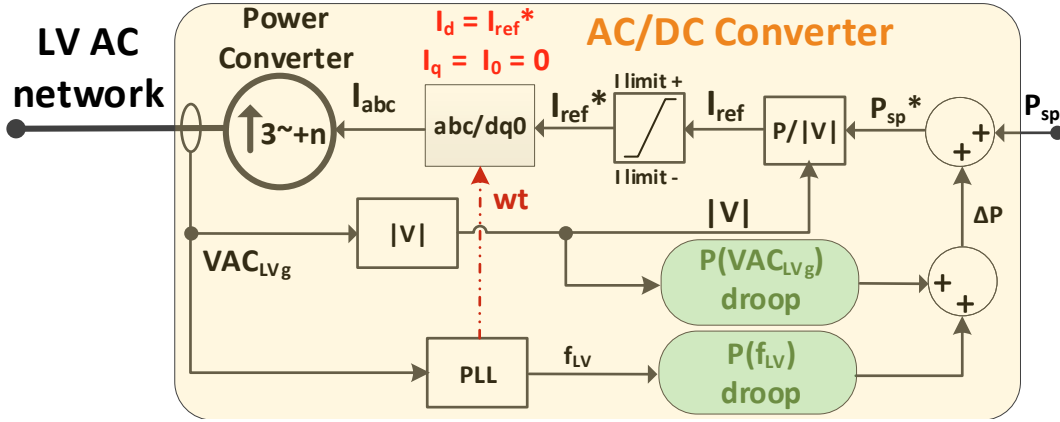


**Figure 3.15:** Block diagram of the developed computational models for the controllable DER units in the LV AC grid.

The average model of the DER's power converter is represented by a three-phase controlled current source with neutral point available in order to allow the modeling of single-phase DER units. At the base level, the DER units are modeled as constant power and constant current devices according to Equation (3.42), where  $|I|$  is the module of the output RMS current,  $I_n$  is the nominal RMS current and  $VAC_{LVg}$  is the three-phase voltage in the LV AC grid. For PV generation,  $I_n$  is defined in Figure 3.15 by  $I_{limit+}$  while in the controllable ESS and EV chargers is defined by  $I_{limit+}$  and  $I_{limit-}$ , with  $I_{limit+} = I_{limit-}$ .

$$\begin{cases} P = P_0; & |I| < I_n \\ P = P_0 \frac{VAC_{LVg}}{VAC_{LVn}}; & |I| = I_n \end{cases} \quad (3.42)$$

Reactive power is not considered in the modeled DER units because it is not object of evaluation in the work developed in this thesis. Thus, the generated reference current ( $I_{ref}^*$ ) represents only the direct current component. Additionally, the internal dynamics of the resources to be controlled (namely, the PV panels, EV batteries and ESS) are considered to be much faster than the dynamics of the power converters interfacing them with the LV AC grid. For this reason, the modeling of the resources to be controlled is neglected, being instead represented by an active power reference ( $P_{sp}$ ).

In order to endow the DER units with load-frequency and load-voltage sensitivity during their normal operation, active power–frequency ( $P(f_{LV})$ ) and active power–voltage ( $P(VAC_{LVg})$ ) droops were also included in the control structure of the modeled DER units [129, 175], as shown in Figure 3.15. The  $P(VAC_{LVg})$  and  $P(f_{LV})$  droop



controllers are defined according to Figure 3.16 and Equation (3.43). PV generation is assumed to operate with 10% of deloading reserve, which is activated in case of under-voltage or under-frequency.

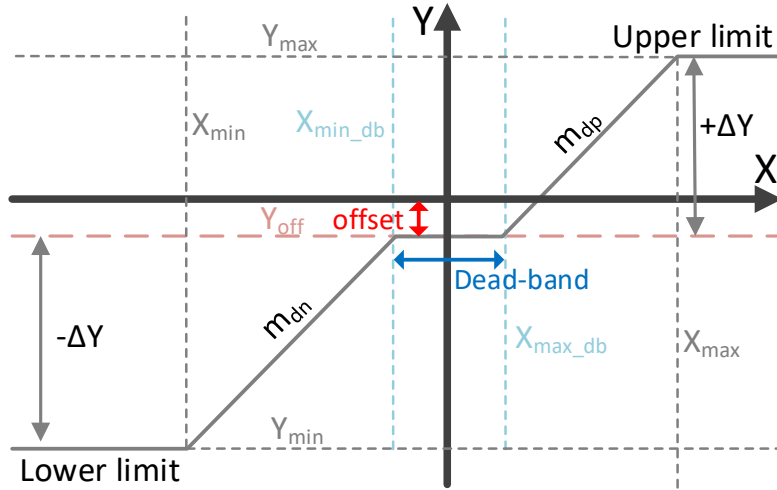


Figure 3.16: Control rule for  $P(VAC_{LV})$  and  $P(f_{LV})$  droop controllers.

$$Y = \begin{cases} Y_{min} & \text{if } X \in ]-\infty, X_{min}] \\ m_{dn}(X - X_{min}) + Y_{min} & \text{if } X \in ]X_{min}, X_{min\_db}] \\ Y_{off} & \text{if } X \in ]X_{min\_db}, X_{max\_db}[ \\ m_{dp}(X - X_{max\_db}) + Y_{off} & \text{if } X \in [X_{max\_db}, X_{max}[ \\ Y_{max} & \text{if } X \in [X_{max}, \infty[ \end{cases} \quad (3.43)$$

In Figure 3.16 and Equation (3.43),  $m_{dn}$  and  $m_{dp}$  are the droop slopes,  $Y$  is the droop output,  $X$  is the droop variable,  $Y_{min}$  and  $Y_{max}$  are the minimum and maximum droop output limits,  $X_{min}$  and  $X_{max}$  are the input saturation limits of the droop control,  $X_{min\_db}$  and  $X_{max\_db}$  define the dead-band interval of the droop control, and  $Y_{off}$  is the offset of the droop output. Positive values for active power correspond to consumed active power. The parameterization of the adopted DER models is summarized in Appendix A (Table A.10).

### 3.3.2.2 Low Voltage DC grid

No suitable IEEE test grid was found in the literature for a LV DC grid integrating the ST-based HMG. In this regard, the LV DC sub-grid illustrated in Figure 3.17 was adopted based on a set of assumptions considered to be realistic in a foreseeable future.

- The number of consumers connected to a DC network will not surpass the number of consumers connected to an equivalent AC network in short and medium term. Thus, based on an educated guess, it is assumed a LV DC grid with half of the size and non-controllable load comparatively to its counterpart LV AC grid.
- It is assumed that LV DC grids will accommodate more controllable DER comparatively to its counterpart LV AC grid. Resources such as PV generation, distributed ESS and DC EV charging have started to gain traction only in recent years. Being such resources DC by nature, its continued expansion may justify and follow the development of LV DC grids for its proper accommodation. Thus, based on an educated guess, it is assumed a LV DC grid with a double share of the controllable DER comparatively to its counterpart LV AC grid.

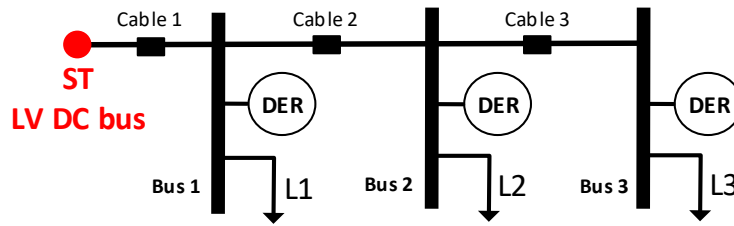


Figure 3.17: One-line diagram of the modeled LV DC sub-grid.

Regarding the line design, the monopolar line with returning conductor is adopted according to the recommendations in [248, 249]. This approach offers the same advantages in providing a return path verified for single-phase consumers in LV AC grids, while requiring only one fully insulated conductor. The cables impedance is modeled using a RL branch. The parameterization of the LV DC grid is provided in Appendix A (Tables A.11 and A.12).

As described in further detail in chapter 4, the evaluation of the advanced control functionalities proposed in this thesis also involves the exploitation of load-voltage sensitivities in DC networks. For this reason, models sensitive to the grid's voltage were adopted for the load and controllable DER located in the LV DC grid.

### Load modeling

The estimation of load voltage sensitivity in DC grids remains largely unexplored in the literature, but a large portion of the load in DC grids may consist of constant power loads since it is based on power electronic converters [250, 251]. Nevertheless, given the lack of extensive data, a scenario with a considerable share of constant power loads is

adopted from [227] to represent the non-controllable DC loads only modeled according to Equation (3.44) where  $P_0$  is the load power for the nominal voltage ( $VDC_{LVn}$ ) and  $VDC_{LVg}$  is the voltage in the LV DC grid.

$$P = P_0 \left( \frac{VDC_{LVg}}{VDC_{LVn}} \right)^{0.45} \quad (3.44)$$

### DER modeling

The controllable DER were modeled according to the block diagram presented in Figure 3.18, and is used to model PV generators, distributed ESS and EV chargers connected to the LV DC grid. For distributed ESS and EV chargers, bidirectional power flow is allowed (V2G is considered for EV chargers), while PV generation admits only power injection. Such distinction is achieved at the parameterization level, by setting the negative current limit ( $I_{limit-}$ ) to zero for PV generation.

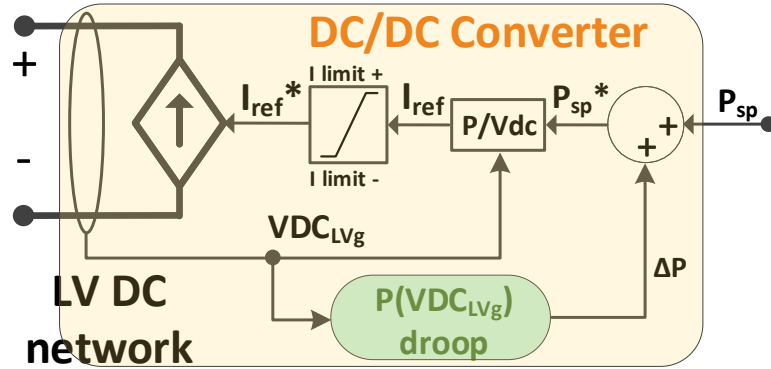


Figure 3.18: Block diagram of the developed computational models for the controllable DER units in the LV DC grid.

The average model of the DER's power converter is modeled by a controlled current source. At the base level, the DER units are modeled as constant power and constant current devices according to Equation (3.45), where  $|I|$  is the output current,  $I_n$  is the nominal current and  $VDC_{LVg}$  is the voltage in the LV DC grid. For PV generation,  $I_n$  is defined in Figure 3.18 by  $I_{limit+}$  while in the controllable ESS and EV chargers is defined by  $I_{limit+}$  and  $I_{limit-}$ , with  $I_{limit+} = I_{limit-}$ .

$$\begin{cases} P = P_0; & |I| < I_n \\ P = P_0 \frac{VDC_{LVg}}{VDC_{LVn}}; & |I| = I_n \end{cases} \quad (3.45)$$

Additionally, the internal dynamics of the resources to be controlled (namely, the PV panels, EV batteries and ESS) are considered to be much faster than the dynamics

of the power converters interfacing them with the LV AC grid. For this reason, the modeling of the resources to be controlled is neglected, being instead represented by an active power reference ( $P_{sp}$ ).

In order to endow the DER units with load-voltage sensitivity during their normal operation, an active power–voltage ( $P(VDC_{LVg})$ ) droop is part of the control structure of the modeled DER units, as shown in Figure 3.18. The  $P(VDC_{LVg})$  droop controller is defined according to Figure 3.16 and Equation (3.43). PV generation is assumed to operate with 10% of deloading reserve, which is activated in case of under-voltage or under-frequency.

The parameterization of the adopted DER models is summarized in Appendix A (Table A.13)

### 3.3.3 MV DC grid based on a single ST

According to the MG concept considered in section 2.3, a MV DC grid does not properly fit in the HMG concept. However, given the availability of a MV DC bus in the ST, a radial MV DC grid based on a single ST was modeled as well, which is suited to integrate high power loads and other controllable DER which are DC by nature. Given the unique features of the ST, the MV DC grid plus the ST-based HMG constitute an hybrid AC/DC grid with islanded operation capabilities.

No suitable IEEE test grid was found in the literature for an MV DC grid integrating such a ST-based hybrid AC/DC grid. Thus, the MV DC grid illustrated in Figure 3.19 was adopted based on a set of assumptions considered to be realistic in a foreseeable future.

- The load levels of a MV DC grid based on a single ST are limited by the power rating of the ST. Thus, a relatively small grid with few big loads and DER units is considered.
- It is assumed that MV DC grids will be an attractive option to connect big DER which are DC by nature. Based on this, a large PV generator and a fast EV Charger station are considered.

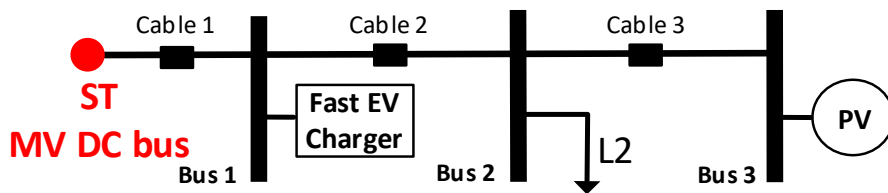


Figure 3.19: One-line diagram of the modeled MV DC sub-grid.

Regarding the line design, the same considerations made for the LV DC sub-grid described in subsection 3.3.2.2 are adopted. The cables impedance is modeled using a RL branch. The parameterization of the MV DC grid is provided in Appendix A (Table A.14).

### Load modeling and DER modeling

Differently to their counterparts in LV grids, it is reasonable to assume that almost all non-controllable load in MV DC grid would be based on power electronic converters. Due to this, the non-controllable loads in the MV DC grid are modeled as constant power and constant current according to Equation (3.46), where  $|I|$  is the output current,  $I_n$  is the nominal current and  $VDC_{MVg}$  is the voltage in the MV DC grid.

$$\begin{cases} P = P_0; & |I| < I_n \\ P = P_0 \frac{VDC_{MVg}}{VDC_{MVn}}; & |I| = I_n \end{cases} \quad (3.46)$$

The controllable DER were modeled according to the block diagram presented in Figure 3.20, following the same considerations made for DER connected to the LV DC grid in subsection 3.3.2.2. The DER units are modeled as constant power and constant current devices according to Equation (3.46). Following the same considerations described in subsection 3.3.2.2 for LV DC grids, an active power–voltage ( $P(VDC_{MV})$ ) droop is part of the control structure of the modeled DER units, as shown in Figure 3.20, in order to endow the DER units with load-voltage sensitivity during their normal operation. The parameterization of the adopted DER models is presented in Appendix A (Table A.15).

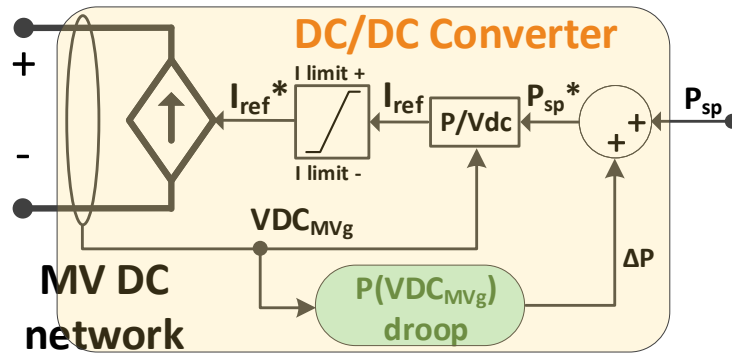


Figure 3.20: Block diagram of the developed computational models for the controllable DER units in the MV DC grid.

### 3.3.4 Hybrid AC/DC Multi-Microgrid based on Smart-Transformers

No suitable IEEE test grids for HMMG incorporating ST were found in the literature at the time of writing of this thesis. However, the IEEE 15 Bus Radial System addressed in [252, 253] and illustrated in Figure 3.21 was used as the basis for the HMMG's MV AC grid. The IEEE 15 Bus Radial System operates at 60Hz and has a 11kV phase-phase voltage [252].

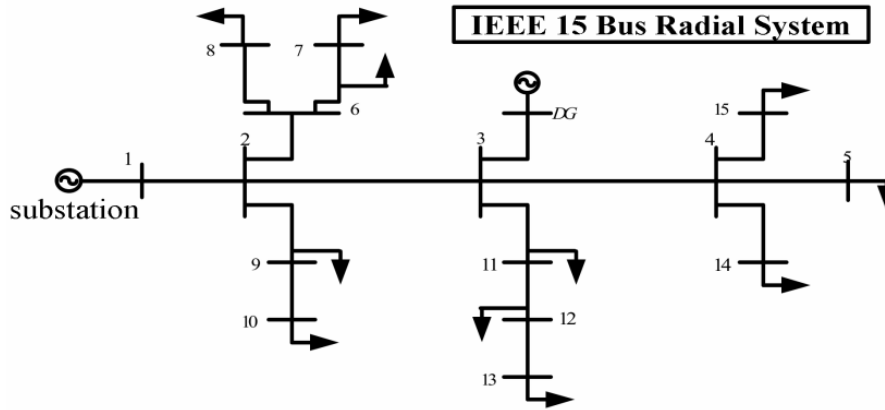


Figure 3.21: One-line diagram of the IEEE 15 Bus Radial System (adopted from [253]).

In order to model a HMMG suited to demonstrate the advanced control functionalities described in chapter 4 and using the IEEE 15 Bus Radial System as backbone for the MV AC grid, a set of adaptations and modifications were made:

1. The phase-phase voltage and frequency of the MV AC grid was modified to 15kV and 50Hz respectively, taking as reference the values of a typical Portuguese MV distribution network [254].
2. The branches departing from the main MV feeder (from bus 1 to bus 5) are aggregated in equivalent representations. This simplification reduces the computational burden of the overall model without compromising the validity of the evaluation of the advanced control functionalities proposed in this thesis.
3. Two branches (equivalent representation) are replaced by ST, a grid-following and a grid-forming unit. Two MV DC grid derived from both ST are also added. Also, the equivalent AC grid in the aforementioned branches are replaced by the LV AC grid described in subsection 3.3.2.1.
4. A LV AC grid is added in ring configuration, fed by a ST and a LFT.
5. The voltage source represented in *substation* is modeled by the equivalent upstream AC power system described in section 3.3.1.

Given this, the resulting HMMG is represented by the one-line diagram illustrated

in Figure 3.22. The parameterization of the MV AC sub-grid is still based on the data provided in [252, 253]. The cable sections of the MV and LV AC sub-grids are modeled as three-phase series RL branches. The represented MV and LV DC sub-grids are modeled according to subsections 3.3.3 and 3.3.2.2 respectively. The represented LV AC grids are modeled according to subsection 3.3.2.1 with minor changes regarding the parameterization of line sections in the LV AC grid in ring configuration. The LV AC grids represented in nodes 9 and 10 are replaced by the LV AC grid described in subsection 3.3.2.1, now supported by the grid following-ST. The LV AC grids represented in nodes 11, 12, 13 and 14 are replaced by LV AC grid described in subsection 3.3.2.1, now supported by a LFT and a ST in ring configuration. The complete parameterization of the HMMG is presented in Appendix A (Table A.16).

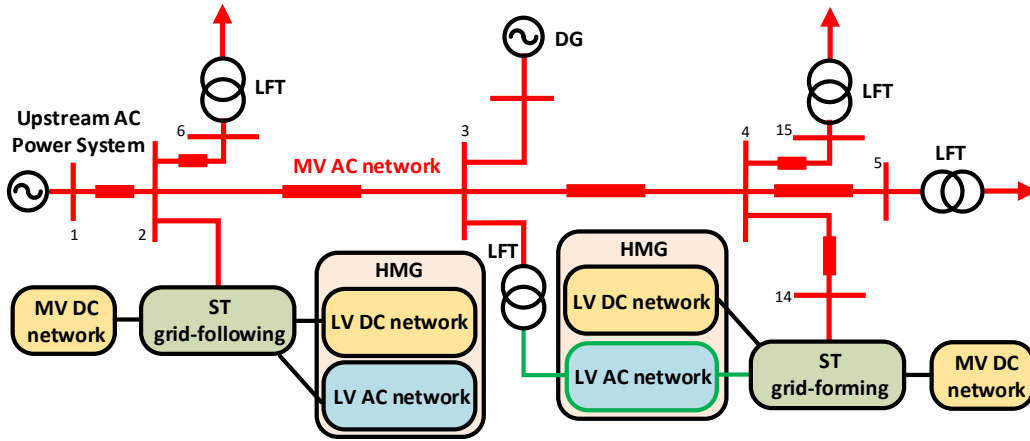


Figure 3.22: One-line diagram of the modeled HMMG.

### 3.4 Final Remarks - Summary

In this chapter, the base computational models developed in the scope of this thesis are presented and described. The description of the advanced control functionalities proposed in this thesis are reserved for chapter 4. The present chapter is summarized as follows:

- The developed computational models are based on discrete fixed-step numerical solvers combined with the Dynamic Average Modeling (DAM) technique, which enables an improved compromise regarding simulation speed and numerical accuracy.

- The base computational models for a grid-following ST and a grid-forming ST are described. For each one, the base computational models for the MV inverter, LV inverter, isolated DC-DC converter, local ESS and supercapacitor bank (grid-following ST only) are described.
- The computational models for the test distribution grids to be used as evaluation platforms for the advanced control functionalities proposed in this thesis are presented and described. The described test distribution grids encompass a LV AC grid, a LV DC grid, a MV DC grid and a Hybrid AC/DC Multi-Microgrid (HMMG). The modeling of all elements integrating the test distribution grids are described, such as cables, non-controllable loads and flexible resources.



## Chapter 4

# Advanced Control Strategies for Smart-Transformers

The advanced control functionalities for Smart-Transformers (ST) proposed in this thesis are aimed to improve the operation and control of Hybrid AC/DC Microgrids (HMG) and Hybrid Multi-microgrids (HMMG). Hence, the proposed control functionalities are first presented and discussed conceptually. Then, the necessary adaptations and/or evolutions of the computations models previously described in chapter 3 are also discussed in order to incorporate the envisioned functionalities. Therefore, as a final result, an advanced computational suite capable of simulating the operation and control of HMG and HMMG is achieved. Its computational modeling and simulation approach naturally follows the considerations already described in section 3.1. The advanced control functionalities proposed in this chapter are organized under three main domains of intervention, in line with the formulated objectives and research questions:

- **Power-Frequency support to the upstream power system:** Describes the proposed set of advanced control functionalities enabling the ST and ST-based HMG to provide power-frequency support to the upstream AC power grid to which it is interconnected.
- **Fault-Ride-Through (FRT) capabilities for ST:** Describes the proposed set of advanced control functionalities aimed to provide FRT capabilities to ST and ST-based HMG against fault disturbances in the upstream AC power system.
- **Grid reconfiguration capabilities on meshed HMMG:** Describes the proposed set of advanced control functionalities enabling the reconfiguration of grid sections within a HMMG, namely between radial and meshed configurations, without interruption of supply.

## 4.1 Power–Frequency Support

The advanced control functionalities for power–frequency support and the associated controlled variables in the ST-based HMG are summarized in Figure 4.1. As illustrated in Figure 4.1, the proposed power–frequency support strategy aims to exploit load–voltage and load–frequency sensitivities of non-controllable loads and power–voltage and power–frequency response capabilities in controllable DER units integrating ST-based HMG and MV DC grid. The goal is to aggregate in the ST the active power response capabilities offered by different resources available in the HMG and MV DC grid. The proposed power–frequency support mechanism integrated in the ST is based on droop controllers. The power–voltage and power–frequency response capabilities in controllable DER units are also based on droop controllers, and load–voltage and load–frequency sensitivities of non-controllable loads are determined according to the load models described in sections 3.3.2.1, 3.3.2.2 and 3.3.3 for LV AC, LV DC and MV DC grids respectively. The aforementioned functionalities are intended for complementary operation, contributing simultaneously for the single purpose of providing power–frequency support to the main power system by regulating the active power exchanged between the ST-based HMG and the MV DC grid with the upstream AC power grid.

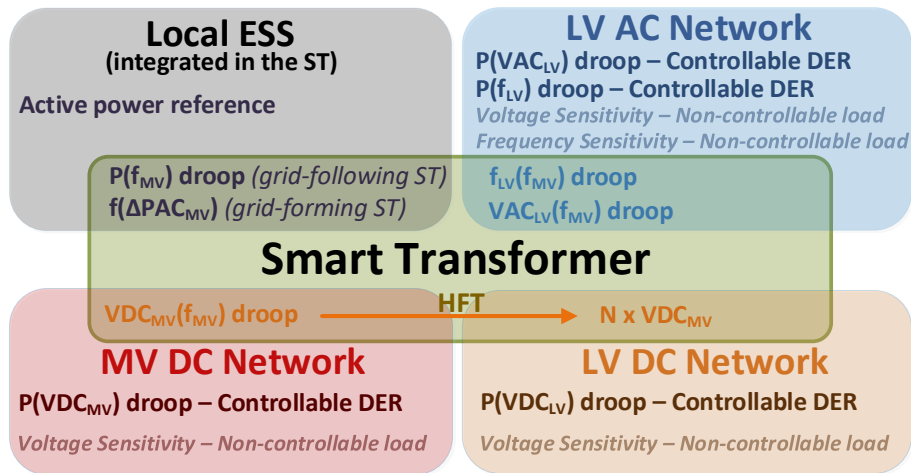


Figure 4.1: Schematic of the advanced functionalities to be exploited by the ST for power–frequency support.

### 4.1.1 Droop Controllers

As it was previously stated, droop-type controllers are proposed as the main control logic to drive the active power response from multiple type of resources. The response

of these controllers is activated by different variables. Hence, this section presents a detailed description of the various droop controllers aimed to provide power-frequency support. The control rules of the droop controllers follow the general representation depicted in Figure 4.2 and are expressed by Equation (4.1), except for the  $f(\Delta P_{MV})$  droop controller which is expressed by Equation (3.17) and represented in Figure 3.6, presented in section 3.2.1.2.

In Figure 4.2 and Equation (4.1), that corresponds to Equation (3.43) already presented in chapter 3,  $m_{dn}$  and  $m_{dp}$  are the droop slopes,  $Y$  is the droop output,  $X$  is the droop variable,  $Y_{min}$  and  $Y_{max}$  are the minimum and maximum droop output limits,  $X_{min}$  and  $X_{max}$  are the input saturation limits of the droop control,  $X_{min\_db}$  and  $X_{max\_db}$  define the dead-band interval of the droop control, and  $Y_{off}$  is the offset of the droop output. The parameterization of the modeled droop controllers is presented in Appendix A.

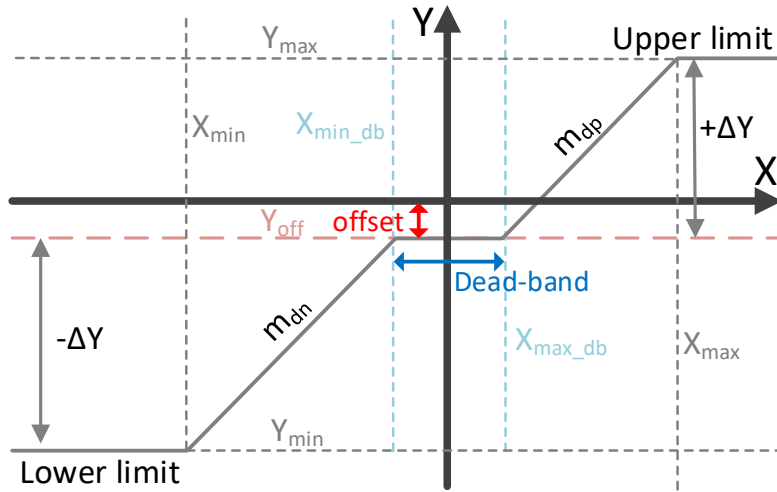


Figure 4.2: Control rule adopted by droop controllers for ST.

$$Y = \begin{cases} Y_{min} & \text{if } X \in ]-\infty, X_{min}] \\ m_{dn}(X - X_{min}) + Y_{min} & \text{if } X \in ]X_{min}, X_{min\_db}] \\ Y_{off} & \text{if } X \in ]X_{min\_db}, X_{max\_db}[ \\ m_{dp}(X - X_{max\_db}) + Y_{off} & \text{if } X \in [X_{max\_db}, X_{max}[ \\ Y_{max} & \text{if } X \in [X_{max}, \infty[ \end{cases} \quad (4.1)$$

#### 4.1.1.1 Active Power – Frequency

The grid-following and grid-forming ST have fundamental differences regarding the direct active power – frequency control due to their distinct working principles.

##### Active Power – MV Frequency : $P(f_{MV})$

This droop controller is adopted for the grid-following ST, aiming to directly regulate the active power set-point of the local ESS incorporating the ST, if it exists, as a function of the frequency deviations in the MV AC grid. The resulting reference  $I_{ESS}^*$  for the local ESS is given by Equation (4.2), where  $\Delta P_d$  is the contribution of the  $P(f_{MV})$  droop controller and the remaining variables are as described for Equation (3.15). The contribution for the active power flow in the local ESS determined by the  $P(f_{MV})$  droop is routed to the main power system by the ST's MV inverter, which is the responsible to keep the power balance between the grid-following ST and the MV AC grid. Positive values for active power correspond to active power consumed by the local ESS.

$$I_{ESS}^* = \frac{1}{NVDC_{MV}} (P_{MV}^* + \Delta P_d - \frac{3}{2} Id_{lim}^* |VAC_{MV}^+|) \quad (4.2)$$

##### Frequency – Active Power : $f(\Delta P_{MV})$

This droop controller already integrates the base control architecture of the MV inverter of the grid-forming ST, as described in section 3.2.1.2. The  $f(\Delta P_{MV})$  is fundamental to implement the base working principle of the grid-forming MV inverter.

However, contrarily to the  $P(f_{MV})$  droop controller, the  $f(\Delta P_{MV})$  droop controller aims to regulate the frequency of the MV inverter as a function of the active power exchanged with the upstream MV AC grid. The steady-state equilibrium point is defined by Equation (4.3), which is a particular implementation of Equation (3.17).

$$\Delta\omega = \begin{cases} \Delta\omega_{min} & \text{if } P_{MV} \in ]-\infty, -P_{MVn}] \\ m_d(PAC_{MVg} - P_{MVsp} - P_{MVn}) + \Delta\omega_{min} & \text{if } P_{MV} \in ]-P_{MVn}, P_{MVn}[ \\ \Delta\omega_{max} & \text{if } P_{MV} \in [P_{MVn}, \infty[ \end{cases} \quad (4.3)$$

As a result, the steady-state active power in the MV inverter is indirectly regulated. Given that the power losses in the LC filter of the MV inverter are relatively negligible, the active power in the MV inverter  $P_{MV}$  is approximately equal to the active power measured after the LV filter  $PAC_{MVg}$  ( $P_{MV} \approx PAC_{MVg}$ ). As such, the steady-state value

for  $P_{MV}$  can be expressed as a function of the grid frequency according to Equation (4.4). Instead of imposing a direct power set-point to its local ESS, the grid-forming ST uses the local ESS to compensate for the power balance in the MV DC bus as a result of the actions of  $f(\Delta P_{MV})$ . A positive frequency variation in the MV AC grid should increase the active power in the local ESS, with positive active power values corresponding to consumed power.

$$P_{MV} \approx \begin{cases} -P_{MVn} & \text{if } \Delta\omega \in ]-\infty, \Delta\omega_{min}] \\ \frac{1}{m_d}(\Delta\omega - \Delta\omega_{min}) + P_{MVsp} + P_{MVn} & \text{if } \Delta\omega \in ]\Delta\omega_{min}, \Delta\omega_{max}[ \\ P_{MVn} & \text{if } \Delta\omega \in [\Delta\omega_{max}, \infty[ \end{cases} \quad (4.4)$$

An important aspect resulting from the operation principle of the grid-forming MV inverter, expressed in Equation (4.4), is that the grid-forming ST does not depend on the net load in the ST-based hybrid AC/DC grid to provide active power–frequency support to the upstream system. It only depends on the ability of the local ESS in keeping the power balance in the MV DC bus in face of the actuation of the  $f(\Delta P_{MV})$  droop controller. Thus, contrarily to the grid-following ST where the active power contribution of the local ESS adds up to the global contribution of the ST-based hybrid AC/DC grid for the provision of active power–frequency support, in the grid-forming ST the local ESS assumes all the active power regulation effort, being the contribution of the ST-based hybrid AC/DC grid irrelevant for the provision of instant active power.

Nevertheless, the remaining droop-based controllers, represented in Figure 4.1 and being described next, can reduce the net active power required to the local ESS to preserve the power balance in the MV DC bus by adjusting the net active power exchanged between the local ESS and the ST-based hybrid AC/DC grid as a function of the frequency in the MV inverter. This extends the autonomy of the local ESS, thus extending the availability of the grid-forming ST to provide active power–frequency support to the upstream power system. In this scope, the remaining droop-based controllers are also an integral part of the active power–frequency support mechanism for grid-forming ST. The steady-state relationship is expressed in Equation (4.5), where  $P_{HG}$  is the net active power in the ST-based hybrid AC/DC grid,  $E_{ESS}$  is the energy stored in the local ESS and  $E_{ESS_0}$  is the initial energy stored in the local ESS.

$$P_{ESS} = P_{MV} - P_{HG} \Rightarrow E_{ESS} = \int (P_{MV} - P_{HG}) dt + E_{ESS_0} \quad (4.5)$$

#### 4.1.1.2 LV Frequency – MV Frequency : $f_{LV}(f_{MV})$

This droop controller adjusts the frequency of the voltage generated by the ST's LV inverter for the LV AC network as a function of frequency deviations in the MV AC network, which otherwise would not be possible due to the inherent frequency decoupling between MV and LV AC networks provided by the ST. It enables a proper power–frequency response of the LV AC network as a function of the frequency in the MV network taking into account the characteristics of resources available in the LV AC network. This control functionality enables the exploitation of active power–frequency sensitivity of controllable DER units incorporating  $P(f_{LV})$  droop controllers as described in section 3.3.2.1. It also enables the exploitation of load-frequency sensitivity of non-controllable loads, which are modeled as described in section 3.3.2.1.

This control functionality is implemented for both grid-following and grid-forming ST, but can only operate over a LV AC grid fed only by the ST. In both cases, a positive frequency variation in the MV AC grid should increase the active power in the LV AC grid, with positive active power values corresponding to consumed power.

#### 4.1.1.3 LV AC voltage – MV Frequency : $VAC_{LV}(f_{MV})$

This droop controller adjusts the magnitude of the voltage generated for the LV AC network as a function of frequency deviations in the MV AC grid, enabling a proper power-voltage response of the LV AC grid as a function of the frequency in the MV AC grid according to the characteristics of the resources available in the LV AC network. This control functionality enables the exploitation of active power–voltage sensitivity of controllable DER units incorporating  $P(VAC_{LV})$  droop controllers as described in section 3.3.2.1. It also enables the exploitation of load-voltage sensitivity of non-controllable loads modeled as described in section 3.3.2.1.

This control functionality is implemented for both grid-following and grid-forming ST, but only grants effectiveness on a LV AC grid fed only by the ST. In both cases, a positive frequency variation in the MV AC grid should increase the active power in the LV AC grid, with positive active power values corresponding to consumed power.

#### 4.1.1.4 MV DC voltage – MV Frequency : $VDC_{MV}(f_{MV})$

This droop controller aims to adjust the voltage levels in the DC grids as a function of the frequency deviations in the MV AC grid, in order to enable a power-voltage response of DC grids as a function of the frequency in the MV AC grid according to the characteristics of the resources available in the DC grids. The  $VDC_{MV}(f_{MV})$

droop controller modulates the voltage in both MV and LV DC grids since  $VDC_{LV}$  is determined from  $VDC_{MV}$  by the transformation ratio in the High-Frequency Transformer (HFT) constituting the ST's isolated DC-DC converter. Thus, this control functionality enables the exploitation of active power-voltage sensitivity of controllable DER units incorporating  $P(VDC_{MV})$  and  $P(VDC_{LV})$  droop controllers as described in sections 3.3.3 and 3.3.2.2. It also enables the exploitation of load-voltage sensitivity of non-controllable loads modeled as described in sections 3.3.3 and 3.3.2.2. This control functionality is implemented for both grid-following and grid-forming ST, but only grants effectiveness on DC grids fed only by the ST. A positive frequency variation in the MV AC grid should increase the active power in the DC grids. Positive active power values correspond to consumed power.

#### 4.1.2 Droop Controllers integration in the overall ST Control Architecture

The droop controllers which constitute the strategy for the provision of power-frequency support to the upstream power system are incorporated in the ST's base control structures described in chapter 3 (sections 3.2.1.1, 3.2.1.2 and 3.2.4).

Figure 4.3 highlights the inclusion of the  $VDC_{MV}(f_{MV})$  and  $P(f_{MV})$  droop controllers in the control structure of the grid-following MV inverter. It is possible to observe that the  $VDC_{MV}(f_{MV})$  droop controller directly influences the reference value for the MV DC bus voltage  $VDC_{MV}$  as a function of the frequency  $f_{MV}$  in the upstream MV AC grid. As a result, voltage levels in MV and LV DC grids ( $VDC_{MVg}$  and  $VDC_{LVg}$ ) are modulated as a function of  $f_{MV}$  for reasons already explained in section 4.1.1. By other hand, the  $P(f_{MV})$  droop controller impacts directly the reference value for the active-power in the local ESS as a function of  $f_{MV}$ , if a local ESS is available.

The incorporation of the  $VDC_{MV}(f_{MV})$  droop controller in the control structure of grid-forming MV inverter is highlighted in Figure 4.4. The impact of this droop controller over  $VDC_{MV}$  follows the same rationale aforementioned for the grid-following ST.

Regarding the control structure of the LV inverter, the incorporation of the  $VAC_{LV}(f_{MV})$  and  $f_{LV}(f_{MV})$  droop controllers is highlighted in Figure 4.5.  $VAC_{LV}(f_{MV})$  influences directly the magnitude of the LV AC grid  $VAC_{LV}$  while  $f_{LV}(f_{MV})$  impacts the reference angular frequency of  $VAC_{LV}$  waveform, both as a function of  $f_{MV}$ .

The reaction chains triggered by the aforementioned droop controllers for the provision of power-frequency support are illustrated in Figures 4.6 and 4.7 for grid-



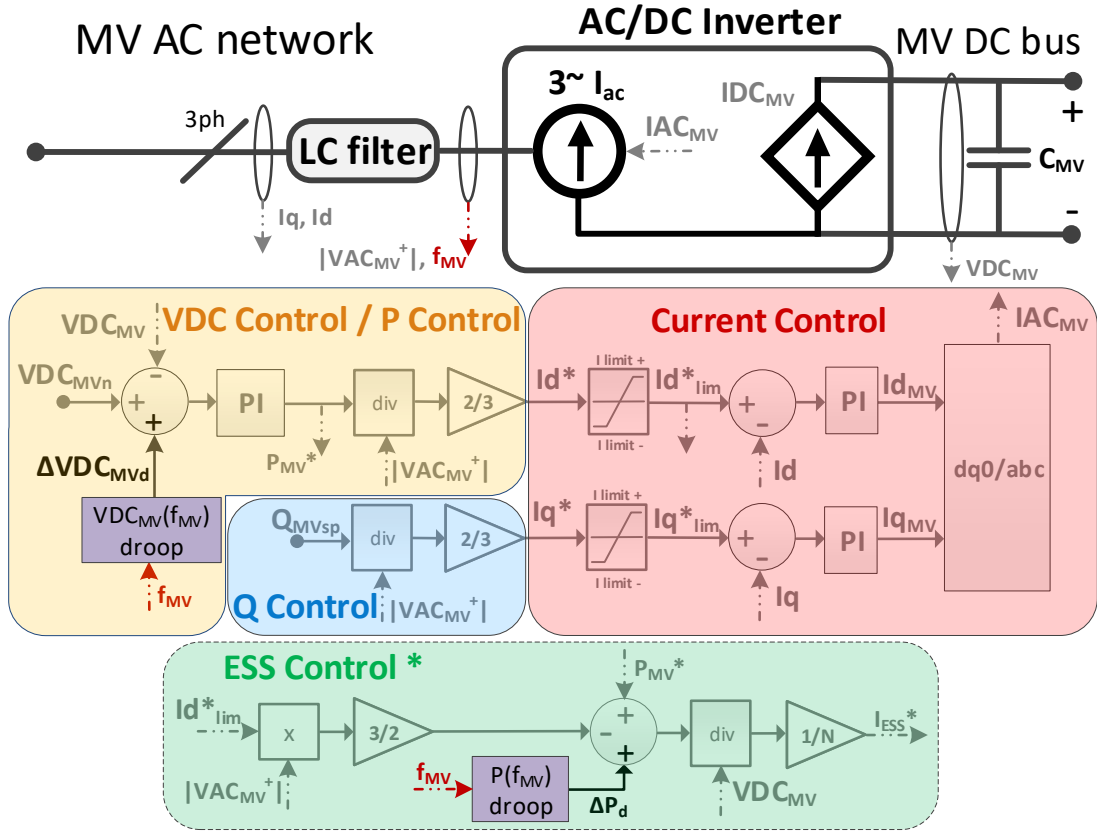


**Figure 4.3:** Block diagram of the MV Inverter of the grid-following ST including droop control functionalities for power-frequency support (highlighted).

following and grid-forming ST respectively.

The reaction chains are very similar for both grid-following and grid-forming ST with respect to the actuation of  $f_{LV}(f_{MV})$ ,  $V_{AC_{LV}}(f_{MV})$  and  $V_{DC_{MV}}(f_{MV})$  droop controllers (blue arrows). These droop controllers influence the targeted electrical quantities and controllable DER (light blue arrows) which in turn modulate the active power in the various sub-grids (red arrows). Consequently, the modulated active power influences the active power exchanged with the ST's DC buses (pink arrows).

However, important differences between the grid-following and grid-forming ST can be observed with regard to the control of the local ESS and the active power balancing in the ST. In the grid-following ST, the local ESS is not required to operate the ST, but if it exists, it is exploited as an additional resource suited to be controlled. In this case, aiming to integrate the local ESS in the active power–frequency support mechanism, the  $P(f_{MV})$  droop controller (blue arrow) regulates the active power in the local ESS (red arrow) which is then exchanged with the LV DC bus (pink arrow), as depicted in Figure 4.6. Regarding the active power balancing in the grid-following ST, it is ensured by the MV inverter which directly exchanges with the upstream power



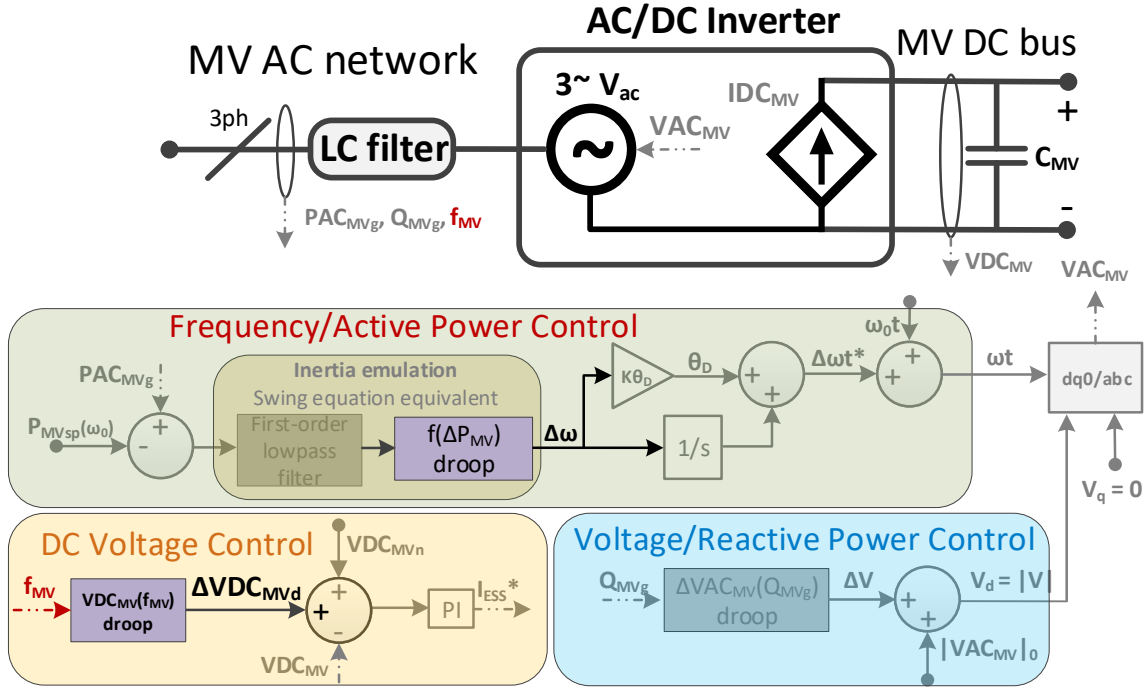


Figure 4.4: Block diagram of the MV Inverter of the grid-forming ST including droop control functionalities for power-frequency support (highlighted).

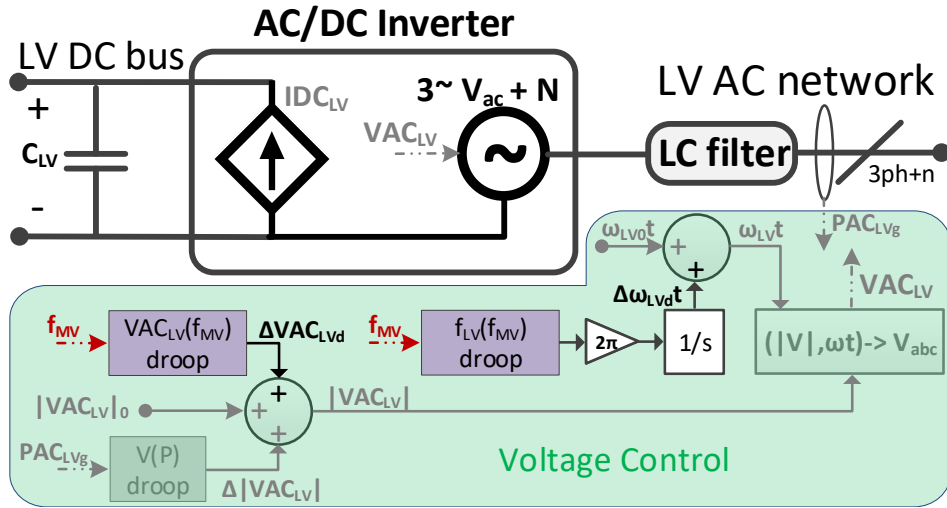
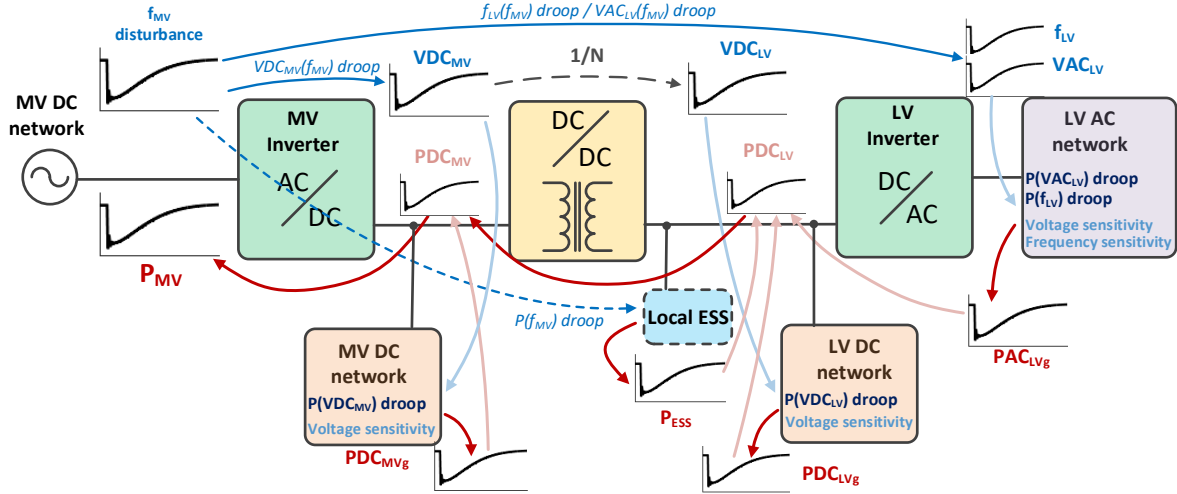


Figure 4.5: Block diagram of the ST's LV Inverter including the droop control functionalities for power-frequency support (highlighted).

system the necessary active power to do so (red arrow to  $P_{MV}$  in Figure 4.6).

The local ESS has a very distinct role in the grid-forming ST, as shown in the reaction chain illustrated in Figure 4.7. In this case, the active power in the local ESS is not directly regulated by any droop controller. Also, distinctively from the grid-following ST, the active power balance in the grid-forming ST is provided by the local ESS instead of the MV inverter. As a result, the local ESS acts as a power buffer

between the chain reaction associated to the  $f(\Delta P_{MV})$  droop controller and the chain reaction associated to the actuation of  $f_{LV}(f_{MV})$ ,  $VAC_{LV}(f_{MV})$  and  $VDC_{MV}(f_{MV})$  droop controllers (previously described), creating two distinct parallel reaction chains which converge in the MV DC bus.



**Figure 4.6:** Reaction chain triggered in the grid-following ST and its derived grids following a frequency disturbance in the MV AC grid. Positive values for the active power correspond to consumed active power.

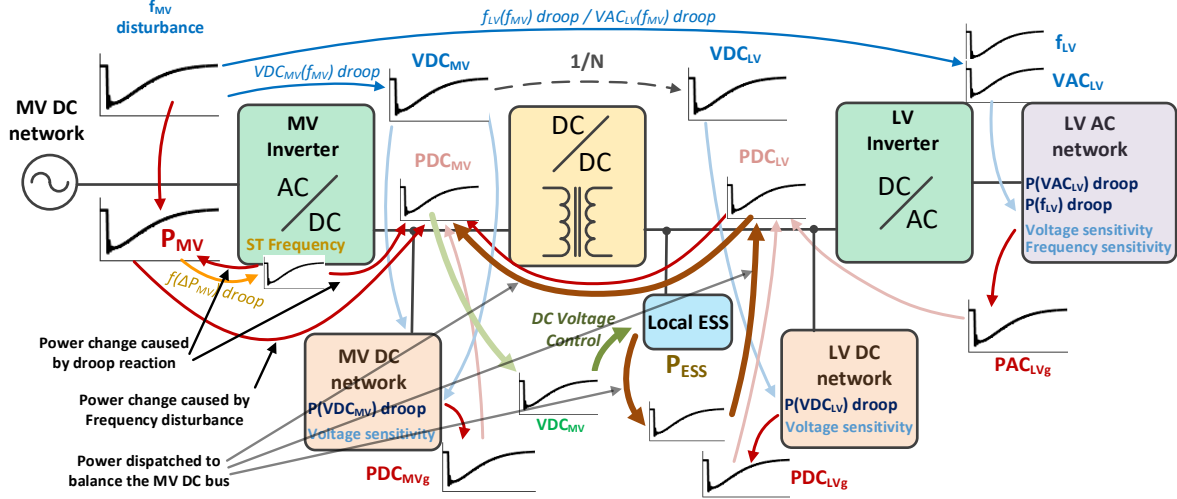


**Figure 4.7:** Reaction chain triggered in the grid-forming ST and its derived grids following a frequency disturbance in the MV AC grid. Positive values for the active power correspond to consumed active power.

As illustrated in Figure 4.7, any frequency disturbance in the upstream power system immediately impacts the active power in the MV inverter and MV DC bus (red arrows), but simultaneously, the  $f(\Delta P_{MV})$  also impacts the active power in the MV inverter and MV DC bus (red arrows). This actuation is not influenced in any

extent by  $f_{LV}(f_{MV})$ ,  $VAC_{LV}(f_{MV})$  or  $VDC_{MV}(f_{MV})$  droop controllers. Nevertheless, both reaction chains converge in the MV inverter, thus affecting  $VDC_{MV}$  (light green arrow). In order to preserve the power balance in the ST, the *DC Voltage Control* (illustrated in Figure 4.4) regulates  $VDC_{MV}$  using the local ESS (dark green arrow), which then exchanges with the DC buses the active power required to preserve the aimed power balance (bold brown arrows).

## 4.2 Fault-Ride-Through Capabilities

The advanced control functionalities aimed to provide FRT capability with respect to upstream AC grid faults for grid-following and grid-forming ST are described in this section. Two distinct approaches are proposed for grid-following and grid-forming ST. In the approach proposed for grid-following ST, the MV inverter limits its current output while aiming to remain connected to the upstream MV AC grid, being the flexibility offered by the local ESS (if it exists) and available in the ST-based hybrid AC/DC grid (HMG plus MV DC grid) is exploited to preserve the power balance in the MV DC bus. It can resort solely to the flexibility available in the ST-based hybrid AC/DC grid when the ST itself has no suitable local storage capacity for the task.

In the approach proposed for grid-forming ST, the MV inverter limits its current output and remains connected to the upstream MV AC grid while operating in voltage source mode, with the local ESS as the solo responsible to preserve the power balance in the MV DC bus. If applicable, it can also support the automatic transition of a section of the MV AC grid to islanded operation in the advent of its isolation from a fault disturbance occurrence in the upstream AC power system.

### 4.2.1 Fault-Ride-Through for Grid-following ST

The FRT strategy proposed in this section is oriented for grid-following ST, being specially designed to cope with the absence of local energy storage capacity fitted for the task. The limitation of MV inverter's current  $IAC_{MV}$  can be implemented by limiting the reference currents, as displayed in Figure 3.3 (represented by  $Id_{lim}^*$  and  $Iq_{lim}^*$ ), and therefore, FRT capabilities in grid-following ST can be provided with relative simplicity if a suitable local ESS is available. Without suitable ESS, the grid-following ST must resort to other resources, including those available in its hybrid AC/DC grid, in order to comply with the maximum current limits in its MV inverter.

The detailed description of the proposed FRT strategy is presented in section 4.2.1.3. The parameterization of the FRT mechanism is presented in Appendix A. The proposed FRT mechanism includes a dump-load connected to the MV DC bus and a non-isolated bidirectional DC-DC converter in the connection of the MV DC grid with the MV DC bus, whose purposes and description are presented in sections 4.2.1.1 and 4.2.1.2 respectively. The inclusion of these hardware elements in the grid-following ST is depicted in Figure 4.8.

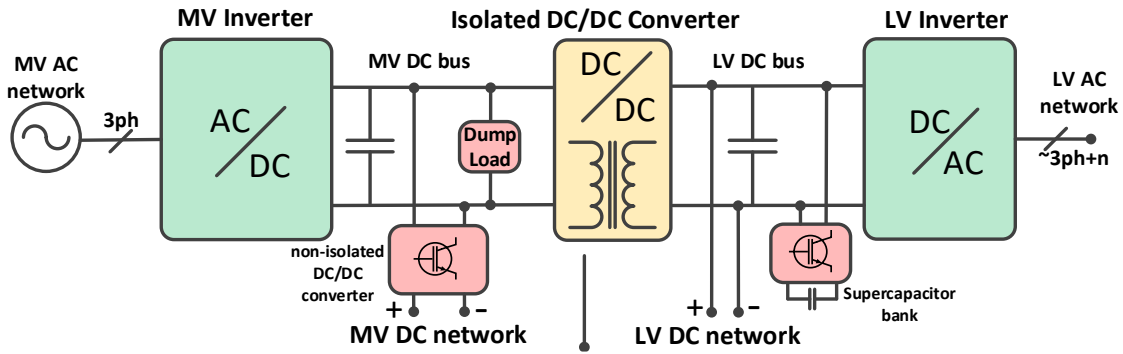


Figure 4.8: Grid-following ST with no ESS available incorporating the additional FRT hardware requirements.

Worth to mention that, although Figure 4.8 is relative to a grid-following ST with no local ESS, the proposed FRT mechanism can operate with a grid-following ST with local ESS as well, as explained in section 4.2.1.3.

#### 4.2.1.1 Dump Load

The dump-load is modeled according to Figure 4.9. In accordance with the adopted DAM technique, the electronic converter controlling the power flow in the dump-load's resistor was modeled using a controlled current source, whose reference current  $I_{DL}$  is generated by the FRT control described in section 4.2.1.3. The parameterization of the modeled dump-load is presented in Appendix A.

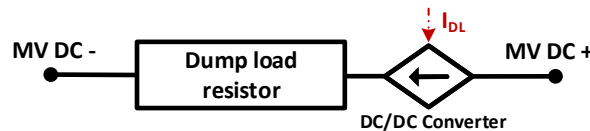


Figure 4.9: Computational model for the Dump-Load.

The dump-load is aimed to actuate during net generation scenarios in the ST-based hybrid AC/DC grid if no local energy storage capacity is available to absorb the power surplus when the MV inverter reaches its technical current limits. In this scenario, the

dump-load dissipates the net generation in the hybrid AC/DC grid that cannot be delivered to the main power system through the MV inverter. The proper mitigation of net generation existing downstream the ST is crucial for the FRT strategy. If not properly contained, it risks DC over-voltages since the existing active power cannot be injected to the upstream AC grid as a result of the AC current limits of the MV inverter. The use of a dump-load for this purpose greatly reduces the need to exploit power-voltage and power-frequency sensitivities in the ST-based hybrid AC/DC grid in order to eliminate its excessive net generation, thus greatly mitigating the need to modulate the voltages and frequency in the ST-based hybrid AC/DC grid for this purpose.

#### 4.2.1.2 Non-Isolated DC-DC Converter

The inclusion of the MV DC grid in the FRT mechanism is relevant since it may concentrate a large share of the total load and DER of the ST-based hybrid distribution network. As such, its inclusion can reduce the required burden (and the resulting adverse impacts) over the ST-based LV AC and DC grids. However, contrarily to the voltage levels in the LV DC bus which can be widely modulated by the isolated DC/DC converter, the voltage levels in the MV DC bus ( $VDC_{MV}$ ) have stricter limits. The MV AC voltage in the MV inverter ( $VAC_{MV}$ ) is imposed by the upstream MV AC grid, hence large variations in  $VDC_{MV}$  can in practice originate passive rectification in the MV inverter. Passive rectification is an uncontrolled operation mode which can occur when  $VDC_{MV}$  is not enough to block the intrinsic diodes existing in the electronic switches constituting the MV inverter. Such uncontrolled currents can damage the MV inverter in real applications.

In order to circumvent this limitation, a non-isolated bidirectional DC-DC converter is proposed to be inserted between the MV DC grid and the MV DC bus. The non-isolated bidirectional DC-DC converter provides the required additional degree of freedom to control the voltage levels in the MV DC grid ( $VDC_{MVg}$ ) in order to enable its reduction as much as necessary to support the provision of FRT during voltage sags in the MV AC grid while preserving  $VDC_{MV}$  within its required operational limits. The computational model for the non-isolated bidirectional DC-DC converter is represented in Figure 4.10.

There are several non-isolated bidirectional DC-DC converter topologies addressed in the literature including mature and relatively simple solutions suitable for the task [255, 256]. However, by assuming that the DC-DC converter is ideal (no losses) and

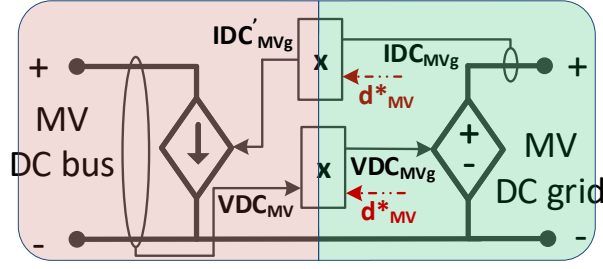


Figure 4.10: Computational model for the non-isolated bidirectional DC-DC converter.

its dynamics is much faster than the dynamics related to voltage variations in the MV DC bus, the fast phenomena characteristic of a given topology such as switching patterns, low-level control loops and power interactions among passive elements can be neglected by applying the DAM approach with no meaningful prejudice of the model accuracy. As such, the power conversion stages can be modeled using two controllable sources according to the DAM approach, governed by simplified feedback control loops defined by Equations (4.6) and (4.7), as illustrated in Figure 4.10.  $IDC'_{MVg}$  is the DC current in the MV DC bus related to the MV DC grid,  $IDC_{MVg}$  is the DC current in the MV DC grid, and  $d_{MV}^*$  is the duty-cycle signal generated by the FRT control described in Section 4.2.1.3.

$$VDC_{MVg} = d_{MV}^* VDC_{MV} \quad (4.6)$$

$$IDC'_{MVg} = d_{MV}^* IDC_{MV} \quad (4.7)$$

No galvanic isolation is considered for the DC-DC converter, but such feature would not be available by default anyway in a MV DC grid directly connected to the MV DC bus. During normal operation conditions,  $d_{MV}^*$  is equal to 1 and  $VDC_{MVg}$  equals  $VDC_{MV}$ .

#### 4.2.1.3 FRT Control Strategy

The underlying rationale of the FRT strategy proposed for grid-following ST consists in diverting and/or eliminating any excessive net active power (load or generation) from the ST-based hybrid AC/DC grid that cannot be balanced by the MV inverter without violating its current limits. This can be achieved if a suitable ESS is integrated locally with the ST. However, if the ST has no local ESS or the existing ESS has no sufficient power/energy capacity, the proposed FRT mechanism resorts to the existing dump-load (described in section 4.2.1.1) and/or to the exploitation of power-voltage and power-frequency sensitivity in the ST-based hybrid AC/DC grid. The control structure

enabling the aforementioned possibilities is depicted in Figure 4.11, incorporated in the MV inverter as illustrated in Figure 4.12, upon the incremented control structure for the MV inverter depicted in Figure 4.3.

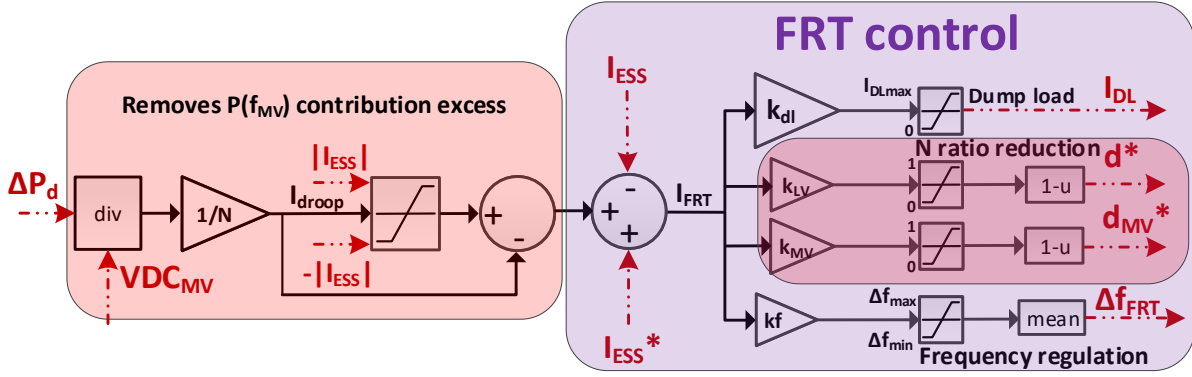


**Figure 4.11:** Block diagram of the proposed Fault-Ride-Through control mechanism for grid-following ST.

Similarly to the power–frequency support mechanism described in section 4.1, the proposed FRT mechanism also relies on droop-based controllers to exploit power–voltage and power–frequency sensitivities of non-controllable loads and controllable DER integrating the ST-based hybrid distribution grid. However, in contrast to the power–frequency support mechanism, the proposed FRT mechanism cannot rely solely on such droop-based controllers because it must guarantee that all excess net active power in the ST-based hybrid AC/DC grid that the MV inverter cannot handle is diverted and/or eliminated. A dynamic parameterization of such droop-based controllers would be required according to factors such as the current capacity available in the MV inverter, severity of the voltage sag in the upstream MV AC grid and the non-linear nature of power–voltage and power–frequency sensitivity of non-controllable loads.

A much simpler alternative is the use of the reference current for the local ESS ( $I_{ESS}^*$ ), generated by the *ESS Control* illustrated in Figure 4.12. Equation (4.2) shows that  $I_{ESS}^*$  is non-zero when the reference power for the MV inverter ( $P_{MV}^*$ ) cannot be followed by the MV inverter. This is the case when the maximum current limits of the MV inverter are reached due to net excess active power in the ST-based hybrid distribution grid. This originates a perturbation in  $VDC_{MV}$  that  $P_{MV}^*$  seeks to correct, with the PI controller in *VDC Control / P Control* (Figure 4.12) responsible to eliminate the steady-state error and thus preserve the power balance in the MV DC bus. If a capable local ESS exists,  $I_{ESS}^*$  drives it to compensate for the error. However, given the aforementioned capability of eliminating the steady-state error,  $I_{ESS}^*$  can be used



by the *FRT Control* as well. As such,  $I_{ESS}^*$  is the base for calculation of the reference current  $I_{FRT}$  for the *FRT Control*, which makes possible to eliminate and/or divert no more than the net excess active power from the ST-based hybrid distribution grid. This guarantees the required power balance in the MV DC bus while minimizing the required actuation of the FRT mechanism over the ST-based hybrid distribution grid.

As shown in Figure 4.11, the FRT mechanism is centered on  $I_{FRT}$ , generated according to Equations (4.8) to (4.10).  $I_{ESS}$  is the current measured in the local ESS,  $\Delta P_d$  is the contribution from  $P(f_{MV})$  (*ESS Control* depicted in Figure 4.12),  $I_{droop}$  is derived from  $\Delta P_d$  (Equation (4.10)) and  $I_{ESSn}$  is the nominal current of the local ESS.

$$I_{FRT} = \begin{cases} I_{ESS}^* - I_{ESS} + |I_{ESS}| - I_{droop} & \text{if } I_{droop} > |I_{ESS}| \\ I_{ESS}^* - I_{ESS} & \text{if } |I_{ESS}| \geq I_{droop} \geq -|I_{ESS}| \\ I_{ESS}^* - I_{ESS} - |I_{ESS}| - I_{droop} & \text{if } I_{droop} < -|I_{ESS}| \\ 0 & \text{if } |I_{droop}| \leq |I_{ESS}| \leq I_{ESSn} \end{cases} \quad (4.8)$$

$$I_{ESS}^* = I_{ESS} \quad \text{if} \quad |I_{ESS}| \leq I_{ESSn} \quad (4.9)$$

$$I_{droop} = \frac{\Delta P_d}{NVDC_{MV}} \quad (4.10)$$

*FRT Control* does not actuate if  $I_{FRT}$  is zero, which occurs when:

- The ST is in normal operation conditions – the limited current reference  $I_{lim}^*$  for the MV inverter is equal to the non-limited reference  $I_d^*$  generated by the *VDC Control* / *P Control*, as depicted in Figure 4.12.
- The MV inverter has reached the maximum current limits ( $|I_{lim}^*| < |I_d^*|$ ) but a local ESS is available and is capable to handle the excess current (fulfilling Equation (4.9) and the last condition of Equation (4.8)).

For the remaining cases  $I_{FRT}$  is non zero and *FRT Control* actuates:

- The MV inverter has reached the maximum current limits ( $|I_{lim}^*| < |I_d^*|$ ) but no local ESS is available. In this case,  $I_{ESS}$  is zero but not  $I_{ESS}^*$ .  $I_{droop}$  is non-zero as well. Thus,  $I_{FRT}$  fulfills the first or third conditions in Equation (4.8).
- The MV inverter has reached the maximum current limits ( $|I_{lim}^*| < |I_d^*|$ ). A local ESS is available but it cannot handle the excess active power alone. In this case, any of the first three conditions in Equation (4.8) can occur. The second condition occurs if  $I_{droop}$  does not exceeds  $I_{ESS}$ .



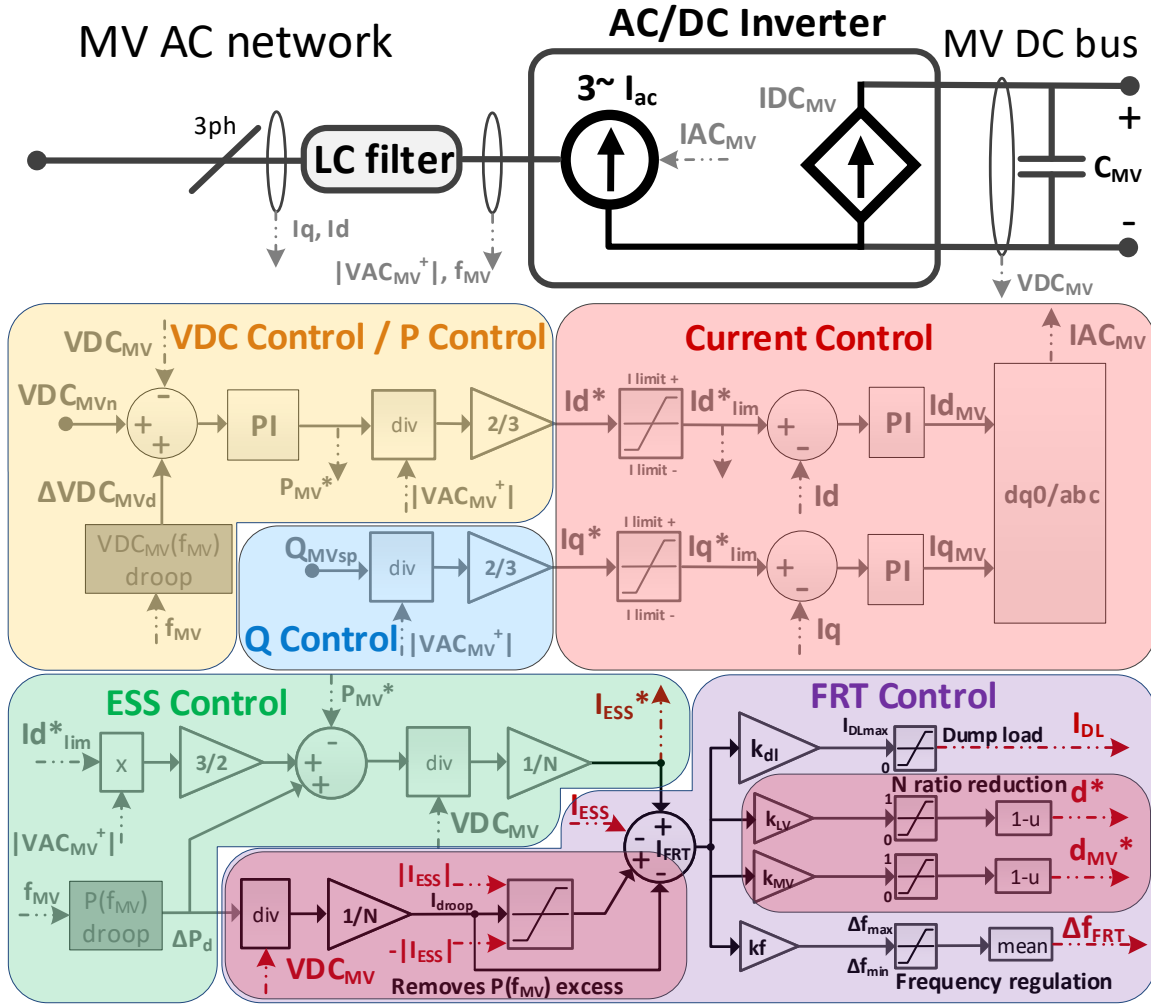


**Figure 4.12:** Block diagram of the grid-following ST's MV inverter incorporating the proposed Fault-Ride-Through control mechanism.

From Equation (4.8) is observed that priority is given to the actuation of the  $P(f_{MV})$  droop controller and to the available capacity in the local ESS, leaving the FRT control as the last resort. This is desirable because the actuation of the  $P(f_{MV})$  droop controller and of the local ESS do not perturb the normal operation of the ST-based hybrid AC/DC grid.

Regarding the actuation of the *FRT Control*, there are two distinct operation modes for net load scenarios and net generation scenarios in the hybrid AC/DC grid respectively. For net load scenarios in the hybrid AC/DC grid, the FRT mechanism modulates the voltage and frequency levels in the hybrid AC/DC grid if the MV inverter is not capable to balance the power in the hybrid AC/DC grid without violating its current limits. In this scenario,  $I_{FRT}$  is negative, and only the control signals  $d^*$ ,  $d_{MV}^*$  and  $\Delta f_{FRT}$  in *FRT control* became non-zero. Given that any steady-state error is handled by the PI controller in the *VDC Control / P Control* depicted in Figure 4.12,  $d^*$ ,  $d_{MV}^*$  and  $\Delta f_{FRT}$

control signals are generated from  $I_{FRT}$  resorting solely to proportional control rules, as shown in Figure 4.11. The generated control signals are described as follows:

- $d^*$ : Modifies the transformation ratio of the ST's isolated DC/DC converter in order to modulate the voltage levels in both LV AC and DC grids integrating the ST-based LV AC and DC grids, and thus exploit their active power – voltage sensitivity. This signal is already represented in the base model of the isolated DC/DC converter represented in Figure 3.7. The resulting modulated voltage for the LV AC inverter ( $VAC_{LV}$ ) and LV DC bus ( $VDC_{LV}$ ) are expressed by Equations (4.11) and (4.12) respectively.  $N$  is the transformation ratio of the HFT in the isolated DC-DC converter and  $k_{LV}$  is the coefficient for the  $N$  reduction.

$$VAC_{LV} = \frac{VDC_{LV}}{VDC_{LVn}} VAC_{LV0} \quad (4.11)$$

$$VDC_{LV} = \begin{cases} VDC_{MV} N; & \text{if } k_{LV} I_{FRT} \leq 0 \\ VDC_{MV} N(1 - k_{LV} I_{FRT}); & \text{if } 0 < k_{LV} I_{FRT} < 1 \\ 0; & \text{if } k_{LV} I_{FRT} \geq 1 \end{cases} \quad (4.12)$$

- $d_{MV}^*$ : Constitutes the duty-cycle of the non-isolated DC-DC converter, aiming to modulate the voltage levels in the MV DC grid. This signal is already represented in the model of the non-isolated DC-DC converter depicted in Figure 4.10. The resulting modulated voltage for the MV DC grid ( $VDC_{MVg}$ ) is expressed by Equation (4.13), where  $k_{MV}$  is the coefficient for the  $VDC_{MVg}$  reduction.

$$VDC_{MVg} = \begin{cases} VDC_{MV}; & \text{if } k_{MV} I_{FRT} \leq 0 \\ VDC_{MV}(1 - k_{MV} I_{FRT}); & \text{if } 0 < k_{MV} I_{FRT} < 1 \\ 0; & \text{if } k_{MV} I_{FRT} \geq 1 \end{cases} \quad (4.13)$$

- $\Delta f_{FRT}$ : Modifies the frequency in the LV AC grid in order to exploit the frequency-power sensitivity of the LV AC grid. The inclusion of  $\Delta f_{FRT}$  in the LV inverter is illustrated in Figure 4.13, based on the incremental model described in section 4.1. The resulting frequency adjustment for the LV AC grid ( $VDC_{MV}$ ) is expressed by Equation (4.14), where  $k_f$  is the coefficient for the  $f_{LV}$  adjustment.

$$\Delta f_{FRT} = \begin{cases} \Delta f_{min}; & \text{if } k_f I_{FRT} \leq \Delta f_{min} \\ k_f I_{FRT}; & \text{if } \Delta f_{min} < k_f I_{FRT} < \Delta f_{max} \\ \Delta f_{max}; & \text{if } k_f I_{FRT} \geq \Delta f_{max} \end{cases} \quad (4.14)$$

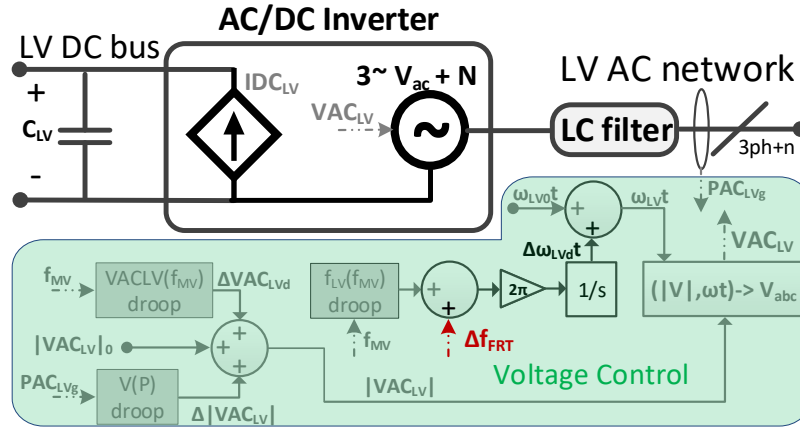


Figure 4.13: Block diagram of the ST's LV inverter incorporating the  $\Delta f_{FRT}$  signal.

For net generation scenarios in the hybrid AC/DC grid, the FRT control diverts any excess active power to the dump-load (described in section 4.2.1.1) and modulates the frequency in the LV AC grid. The modulation of the frequency in the LV AC grid aims to exploit the frequency-power sensitivity of the LV AC grid in order to decrease power generation and increase power consumption in the LV AC grid. In this scenario,  $I_{FRT}$  is positive, and only the control signals  $I_{DL}$  and  $\Delta f_{FRT}$  in *FRT control* are non-zero. For the same reasons described for the net load scenarios,  $I_{DL}$  and  $\Delta f_{FRT}$  control signals are generated from  $I_{FRT}$  resorting solely to proportional control rules. The  $\Delta f_{FRT}$  control signal is as described for the net load scenarios. The  $I_{DL}$  control signal constitutes the reference current for the dump-load, as represented in Figure 4.9.  $I_{DL}$  is non-zero only for positive values of  $I_{FRT}$  because it should only react to excess power occurrences during net generation scenarios in the hybrid AC/DC grid. The active power dissipated in the dump-load ( $P_{DL}$ ) is expressed by Equation (4.15), where  $k_{dl}$  is the modulation coefficient for the dump-load current  $I_{DL}$ .

$$P_{DL} = \begin{cases} VDC_{MV} I_{DLmax}; & \text{if } k_{dl} I_{FRT} \geq I_{DLmax} \\ VDC_{MV} k_{dl} I_{FRT}; & \text{if } 0 < k_{dl} I_{FRT} < I_{DLmax} \\ 0; & \text{if } k_{dl} I_{FRT} \leq 0 \end{cases} \quad (4.15)$$

It is worth to mention that the proposed FRT mechanism is suited to respond to

both symmetric and asymmetric voltage sags in the upstream MV AC grid. Any occurrence of oscillatory active power components in the MV inverter (result of a negative-sequence component in the MV AC grid voltage) is properly compensated by the supercapacitor bank illustrated in Figure 4.8, based on the control approach already described in section 3.2.3.2.

Another important remark is that the load and DER modeling adopted according to Equations (3.41), (3.40), (3.42), (3.44), (3.45) and (3.46) is usually considered valid for voltage and frequency changes relatively small. For more aggressive variations, such as those the FRT control can impose upon the ST-based hybrid AC/DC grid, many loads and DER with no FRT capabilities would switch off in the real world. This means that, in real world applications, the total load and/or generation in a ST-based hybrid AC/DC grid can be lower in the instants following the end of the actuation of the FRT control. However, since no satisfactory data on the subject was not found at the time of writing of this thesis, this occurrence is not considered nor modeled.

#### 4.2.1.4 Chain of Events induced by the FRT Control Strategy

The reaction chains triggered by the actuation of the aforementioned FRT mechanism are illustrated in Figures 4.14 and 4.15 respectively for net load and net generation scenarios in the ST-based hybrid AC/DC grid.

During net load scenarios in the ST-based hybrid AC/DC grid, if the MV inverter is not capable to balance active power in excess in its hybrid AC/DC grid in face of voltage sags in the upstream MV AC grid, the FRT mechanism is invoked as depicted in Figure 4.14. If no local ESS exists, the FRT mechanism modulates the voltage and frequency levels in the hybrid AC/DC grid (light blue arrows) through  $\Delta f_{FRT}$ ,  $d^*$  and  $d_{MV}^*$  control signals (blue arrows). As a result, the active power–voltage and active power–frequency sensitivities of non-controllable loads and controllable DER modulate the active power in the various sub-grids (red arrows), which in turn modulate the active power exchanged with the DC buses (pink arrows). But if a suitable local ESS is available, the FRT mechanism modulates the active power in the local ESS through  $I_{ESS}^*$  control signal (dashed arrows). All the contributions finally converge to the MV DC bus, whose power balancing is ensured by the MV inverter which directly exchanges with the upstream power system the resulting active power (red arrow to  $P_{MV}/IAC_{MV}$ ).

During net generation scenarios in the ST-based hybrid AC/DC grid, if the MV inverter is not capable to balance active power in excess in its hybrid AC/DC grid in face of voltage sags in the upstream MV AC grid, the FRT mechanism actuates

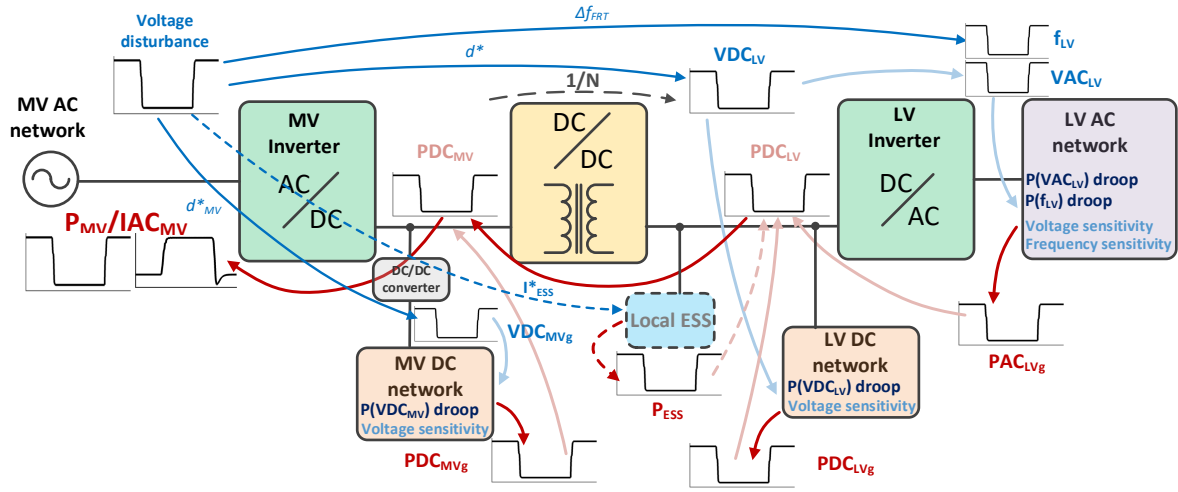


**Figure 4.14:** Reaction chain triggered for a net load scenario in the ST-based hybrid AC/DC grid following a voltage disturbance in the MV AC grid. Positive values for the active power correspond to consumed active power.

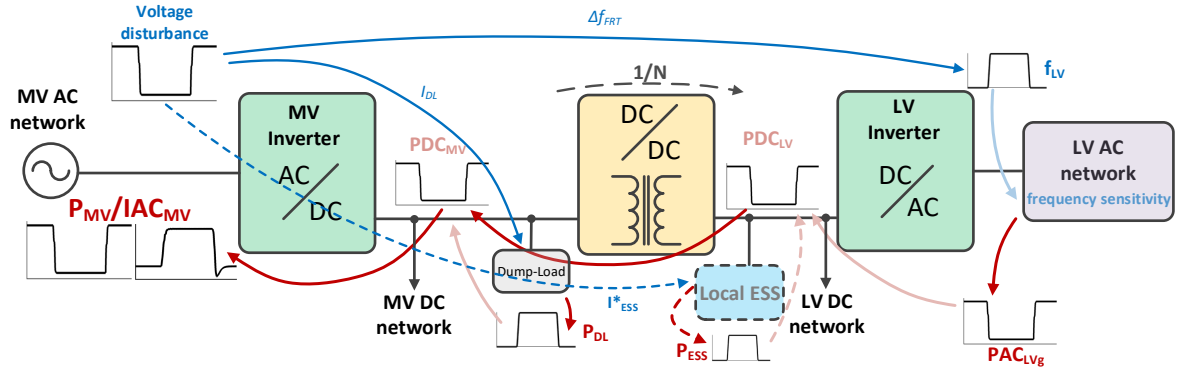


**Figure 4.15:** Reaction chain triggered for a net generation scenario in the ST-based hybrid AC/DC grid following a voltage disturbance in the MV AC grid. Positive values for the active power correspond to consumed active power.

as depicted in Figure 4.15. If no local ESS exists, the FRT mechanism modulates the frequency in the LV AC sub-grid (light blue arrow) and the current  $I_{DL}$  in the dump-load through the respective  $\Delta f_{FRT}$  and  $I_{DL}$  control signals (blue arrows). As a result, active power–frequency sensitivity of non-controllable loads and controllable DER modulates the active power in the LV AC sub-grid (red arrows), which in turn modulates the active power exchanged with the LV DC bus (pink arrows). By its turn, the dump-load dissipates the excess active power flowing to the MV DC bus that cannot be balanced by the MV inverter. But if a suitable local ESS is available, the FRT mechanism modulates the active power in the local ESS through  $I_{ESS}^*$  control signal (dashed arrows). The MV inverter then directly exchanges with the upstream power system the resulting active power (red arrow to  $P_{MV}/IAC_{MV}$ ).

### 4.2.2 Fault-Ride-Through for Grid-forming ST

The FRT strategy proposed in this section is designed for grid-forming ST. The main purpose is to provide current limiting capabilities to the MV inverter in the advent of a fault disturbance in the upstream AC MV grid, but more generic overload conditions are addressed as well. It also aims to enable the ST to support sections of the upstream MV AC grid in islanded operation mode following a fault disturbance in the upstream power system. It does not require detection mechanisms for fault or overload currents, nor redundant current-mode control structures to be activated specifically during overload conditions. Current limitation is provided with the MV inverter always in grid-forming mode without losing the synchronism with the main power system. The FRT control relies entirely on the ST's local ESS to provide the fast power balancing in the MV DC bus.

The FRT control mechanism is illustrated in Figure 4.16 and its integration in the overall control structure of the MV inverter is illustrated in Figure 4.17. The parameterization of the proposed FRT mechanism is presented in Appendix A.

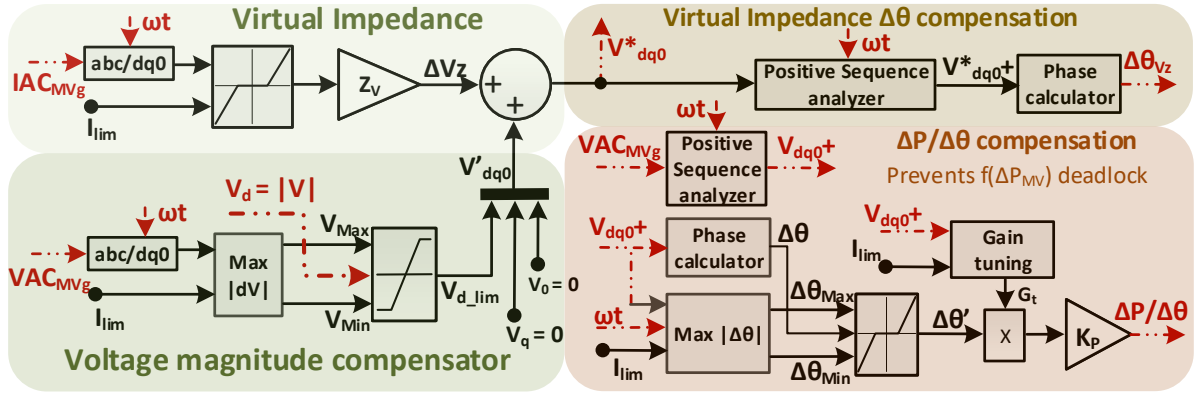
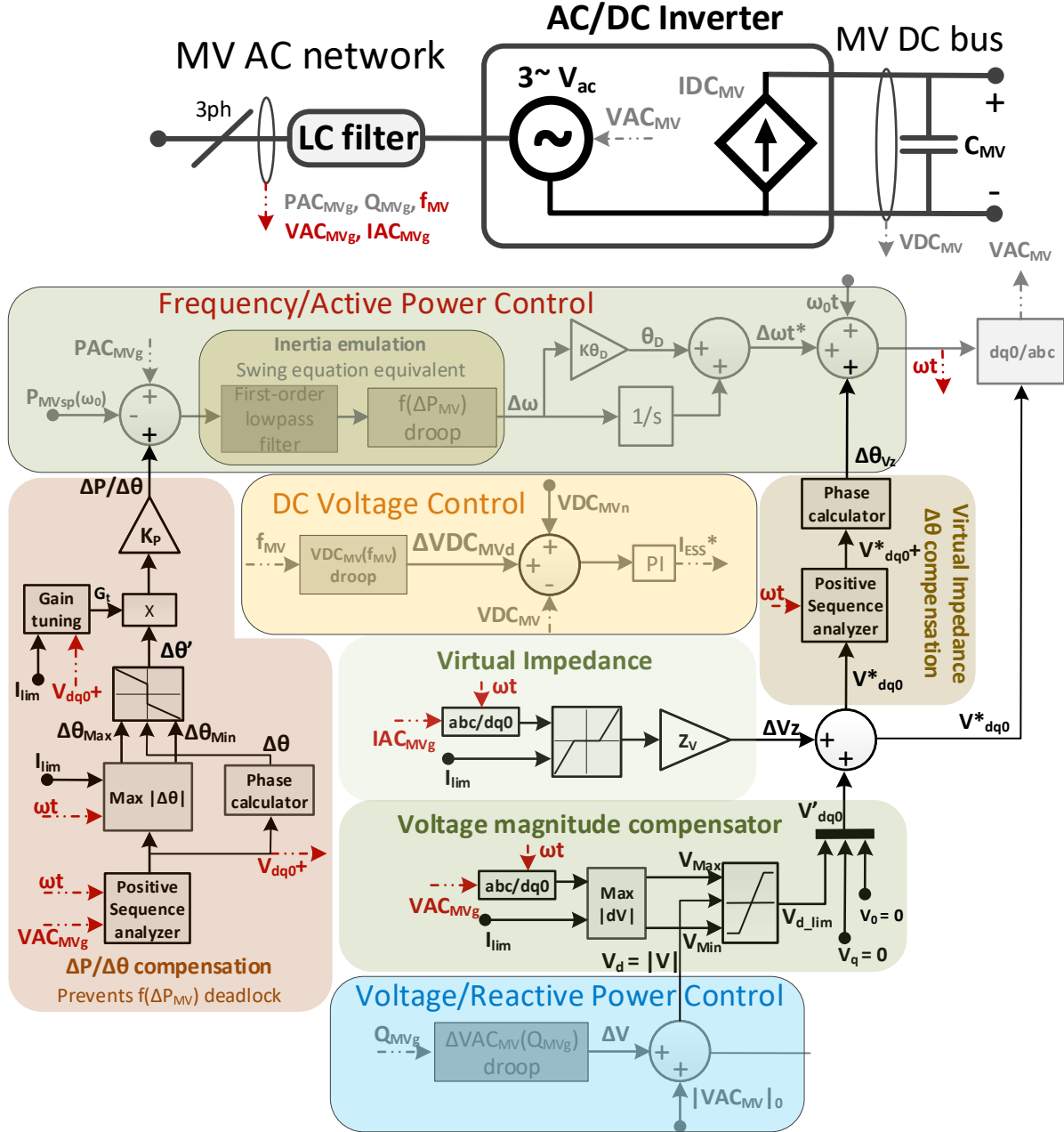


Figure 4.16: Block diagram of the proposed Fault-Ride-Through control mechanism for grid-forming ST.

The main rationale of the proposed FRT mechanism consists in limiting the voltage drop in the coupling MV DC filter of the MV inverter in order to control the current flowing through the MV inverter. Indeed, such relationship can be expressed by Equation (4.16), where  $IC_{MVf}$  is the current in the capacitor of the LC filter, and  $XL_{MVf}$  and  $XC_{MVf}$  are respectively the inductive and capacitive reactances of the LC filter at  $f_{MV}$ . The resistance in the reactive elements is considered much lower than their respective reactance ( $XL_{MVf}$  and  $XC_{MVf}$ ), being thus neglected. However,  $IC_{MVf}$  can be fairly neglected because  $XC_{MVf}$  is much larger than  $XL_{MVf}$ , as expressed by Equation (4.18), resulting in the approximation described by Equation (4.17). Equation (4.18) is derived

from the considerations for the MV LC filter made in section 3.2.1.1, where the cut-off frequency  $f_c$  and the characteristic impedance  $Z_0$  of the LC filter are as expressed in the set of Equations in (3.3), being  $f_c$  established at 2kHz.



**Figure 4.17:** Block diagram of the grid-forming ST's MV inverter incorporating the proposed Fault-Ride-Through control mechanism.

$$IAC_{MVg} = IAC_{MV} + IC_{MVf} = \frac{VAC_{MVg} - VAC_{MV}}{XL_{MVf}} + \frac{VAC_{MVg}}{XC_{MVf}} \quad (4.16)$$



$$IAC_{MVg} \approx IAC_{MV} \approx \frac{VAC_{MVg} - VAC_{MV}}{XL_{MVf}} \quad (4.17)$$

$$\frac{XL_{MVf}}{XC_{MVf}} = \left(\frac{f_{MV}}{f_c}\right)^2 \Rightarrow \frac{XL_{MVf}}{XC_{MVf}} \in [6.0025, 6.5025] \times 10^{-4} \quad \text{if } 49 \leq f_{MV} \leq 51 \quad (4.18)$$

The active power exchanged between the ST and the upstream MV AC system is determined by the reactance of the MV LC filter and the voltages applied to its terminals, as expressed in Equation (4.19).  $\delta_{MVf}$  is the phase angle between the AC voltages in the upstream MV AC grid ( $VAC_{MVg}$ ) and MV inverter ( $VAC_{MV}$ ) sides. Given that  $VAC_{MVg}$  is imposed by the upstream MV AC grid,  $VAC_{MV}$  is the only control variable available to the ST to control  $IAC_{MV}$ , and consequently  $PAC_{MVg}$ . As such, the proposed FRT mechanism regulates the magnitude and angular position of  $VAC_{MV}$  in order to control the voltage drop in the MV LC filter, aiming to preserve  $IAC_{MV}$  close to  $IAC_{MVn}$  in face of fault disturbances in the upstream MV AC grid.

$$PAC_{MVg} = \frac{VAC_{MVg} VAC_{MV}}{XL_{MVf}} \sin(\delta_{MVf}) \quad (4.19)$$

In order to implement this approach, the virtual impedance concept is adopted in combination with the estimation of the intervals for  $VAC_{MV}$  magnitude and for  $\delta_{MVf}$  where  $IAC_{MV} \leq IAC_{MVn}$ . The virtual impedance concept is adopted given its relative simplicity and increasing interest in applications aiming to limit overcurrents in grid-forming inverters [257, 258]. The virtual impedance is implemented as shown in Figure 4.17 and constitutes the most immediate response mechanism against overcurrents, generating a voltage correction in the  $dq0$  frame according to Equation (4.20), where  $Z_v$  represents the coefficients for the calculation of the direct, quadrature and zero sequence components of  $\Delta V_z$ , and  $I_{dq0g}$  corresponds to  $IAC_{MVg}$  in the  $dq0$  frame.  $I_{dq0g}$  is calculated according to Equation (4.21), where  $A_p$  is expressed by Equation (3.13) and corresponds to the amplitude-invariant Park transformation with the rotating frame aligned 90 degrees behind the phase A axis ( $|A| = 1; A/\theta = 0 \rightarrow A_d = 1; A_q = 0$ ) and  $\omega t$  is the reference angular position for  $VAC_{MV}$ .

$$\Delta V_z = \begin{cases} Z_v(I_{dq0g} - I_{lim}) & \text{if } I_{dq0g} \geq I_{lim} \\ 0 & \text{if } -I_{lim} < I_{dq0g} < I_{lim} \\ Z_v(I_{dq0g} + I_{lim}) & \text{if } I_{dq0g} \leq -I_{lim} \end{cases} \quad (4.20)$$

Being  $I_{lim}$  the current limits for the direct, quadrature and zero sequence compo-



nents in  $I_{dq0_g}$ , the limits for each sequence component are determined as shown in the set of Equations in (4.22). Priority is given to the active power during current limitation, and for that reason the direct component of  $I_{lim}$  ( $I_{lim_d}$ ) is set to  $IAC_{MVn}$ . The quadrature component of  $I_{lim}$  ( $I_{lim_q}$ ) is dynamically calculated as a function of  $I_{d_g}$ . Since the absolute current limit for the MV inverter is defined by  $IAC_{MVn}$ ,  $I_{lim_q}$  is dynamically defined to the current capacity not allocated to  $I_{d_g}$ . Given that the MV inverter is modeled by a three-phase controlled voltage source in star configuration with isolated neutral, the zero sequence current is not present. As such, the zero sequence in the virtual impedance is not required and is set to zero ( $Z_v = 0$ ) and  $I_{lim_0}$  is not deemed necessary.

$$I_{dq0_g} = A_P IAC_{MVg} \quad (4.21)$$

$$Z_v = \begin{bmatrix} Z_{v_d} \\ Z_{v_q} \\ 0 \end{bmatrix}; I_{dq0_g} = \begin{bmatrix} I_{d_g} \\ I_{q_g} \\ I_{0_g} \end{bmatrix}; I_{lim} = \begin{bmatrix} I_{lim_d} \\ I_{lim_q} \\ I_{lim_0} \end{bmatrix} = \begin{bmatrix} IAC_{MVn} \\ \sqrt{IAC_{MVn}^2 - I_{d_g}^2} \\ 0 \end{bmatrix} \quad (4.22)$$

As expressed in Equation (4.20), the virtual impedance only actuates when  $I_{dq0_g}$  violates  $I_{lim}$  in order to avoid its undesired interference with the normal operation of the ST. This way,  $Z_v$  coefficients can be sufficiently aggressive in order to properly control  $IAC_{MVg}$  in face of the most severe fault disturbances in the MV AC grid with no undesired impacts on  $VAC_{MV}$  during the normal operation of the ST.

Although the virtual impedance is capable to cushion most of the current transients affecting the MV inverter in the advent of a fault disturbance in the upstream AC MV grid, it is not capable to strictly impose  $I_{lim}$  alone due to the fact that the virtual impedance is essentially a proportional-based control mechanism with no capability to eliminate the steady-state error between  $I_{lim}$  and  $I_{dq0_g}$ . The steady state error between  $I_{lim}$  and  $I_{dq0_g}$  can greatly vary throughout the full range of disturbance scenarios the grid-forming ST must endure. Regarding this, the performance of the virtual impedance can be improved by observing the intervals for  $VAC_{MV}$  magnitude and for  $\delta_{MVf}$  related to the maximum voltage drop in the MV LC filter where  $IAC_{MV} \leq IAC_{MVn}$ . To achieve this, a set of supplementary control mechanisms complementing the control action provided by the virtual impedance are proposed to react to the violation of the aforementioned intervals and to impose fast corrections to the magnitude and phase shift of  $VAC_{MV}$  in relation to  $VAC_{MVg}$  accordingly. Consequently, these additional control mechanism greatly reduce the required actuation range of the

virtual impedance, permitting a better optimization in the parameterization of  $Z_v$  coefficients, and thus, to further minimize the aforementioned steady-state error.

The purpose and description of the aforementioned supplementary control mechanisms, which are illustrated in Figure 4.17, are described in subsection 4.2.2.1, as follows.

#### 4.2.2.1 Supplementary FRT Control Mechanisms

##### Voltage Magnitude Compensator

Being possible to determine the maximum voltage drop in the MV LC filter that would enable the limiting of  $IAC_{MVg}$  to  $IAC_{MVn}$ , limits for the initial reference voltage magnitude generated in *Voltage/Reactive Power Control* ( $|V|$ ) can be deterministically calculated. This mechanism aims precisely to dynamically determine the acceptable limits for  $|V|$ , which constitutes the base reference to generate  $VAC_{MV}$ . By imposing such limits, a major mitigation of the reactive component of the fault currents in the MV inverter can be obtained straight away, and the parameterization of  $Z_v$  in the virtual impedance can be optimized for a narrower actuation band with more focus in the limitation of the active component of the current in the MV inverter.

The initial reference voltage magnitude is generated according to Equation (4.23), where  $|VAC_{MV}|_0$  is the base voltage for the MV inverter and  $\Delta V$  is the contribution of the  $\Delta VAC_{MV}(Q_{MVg})$  droop controller.

$$|V| = V_d = |VAC_{MV}|_0 + \Delta V \quad (4.23)$$

The voltage limits to be imposed to  $|V|$  are defined according to Equations in (4.24), where  $V_{max}$  and  $V_{min}$  are respectively the maximum and minimum limits for the initial reference voltage magnitude  $|V|$ .  $V_{max}$  and  $V_{min}$  are centered around the direct component of the measured  $VAC_{MVg}$  ( $V_{d_g}$ ) because  $|V|$  is synchronized with the reference angular position  $\omega t$  generated by the controller of the MV inverter. Thus, the quadrature component of  $VAC_{MVg}$  is not considered for the calculation of  $V_{max}$  and  $V_{min}$  since only the direct component is generated ( $|V| = V_d$ ).  $R_{MVf}$  and  $L_{MVf}$  are the resistance and inductance in the MV LC filter.  $I_{d_g}$  is as described for the set of Equations in (4.22).  $V_{d_g}$  is calculated according to the set of Equations in (4.25), where  $A_p$  is as defined in Equation (3.13).

$$\begin{cases} V_{max} = |V_{d_g}| + R_{MVf}IAC_{MVn} + 2\pi f_{MV}L_{MVf}\sqrt{IAC_{MVn}^2 - I_{d_g}^2} \\ V_{min} = |V_{d_g}| - R_{MVf}IAC_{MVn} - 2\pi f_{MV}L_{MVf}\sqrt{IAC_{MVn}^2 - I_{d_g}^2} \end{cases} \quad (4.24)$$

$$V_{dq0_g} = A_P VAC_{MVg}; V_{dq0_g} = \begin{bmatrix} V_{d_g} \\ V_{q_g} \\ V_{0_g} \end{bmatrix}; \quad VAC_{MVg} = \begin{bmatrix} V_{a_g} \\ V_{b_g} \\ V_{c_g} \end{bmatrix} \quad (4.25)$$

The limitation of  $|V|$  ( $V_{d_{lim}}$ ) using  $V_{max}$  and  $V_{min}$  is expressed in Equation (4.26), which results in a dynamic limitation of  $|V|$  as a function of  $VAC_{MVg}$ . Finally,  $V_{d_{lim}}$  is adjusted to the  $dq0$  frame representation  $V'_{dq0}$  by adding the quadrature and zero sequence elements, which are set to zero given the alignment of  $|V|$  with  $\omega t$  and the isolated neutral connection in the MV inverter.

$$V_{d_{lim}} = \begin{cases} V_{max} & \text{if } V_d \geq V_{max} \\ V_d & \text{if } V_{min} < V_d < V_{max} \\ V_{min} & \text{if } V_d \leq V_{min} \end{cases}; \quad V'_{dq0} = \begin{bmatrix} V_{d_{lim}} \\ 0 \\ 0 \end{bmatrix} \quad (4.26)$$

The final reference  $VAC_{MV}$  is then determined according to Equation (4.27), which results from the contributions provided by *Voltage Magnitude Compensator* ( $V'_{dq0}$ ) and *Virtual Impedance* ( $\Delta V_z$ ) multiplied by the inverse Park transformation  $A_p^{-1}$  expressed by Equation (3.14).

$$VAC_{MV} = A_p^{-1}(\Delta V_z + V'_{dq0}) \quad (4.27)$$

### Virtual Impedance $\Delta\theta$ Compensation

During normal operation conditions, the *Virtual Impedance* is not actuating ( $\Delta V_z = [0; 0; 0]$ ) and the limited signal for the initial voltage reference  $V_{d_{lim}}$  is aligned with  $\omega t$  (and thus,  $VAC_{MV}$  is aligned with the direct axis). As such, no quadrature component for the voltage exists during normal operation.

However, when the *Virtual Impedance* response becomes non-zero following a violation of current limits in the MV inverter, a non-zero quadrature voltage compensation may be present in  $\Delta V_z$  in order to counteract the excess current in the quadrature components of  $IAC_{MVg}$ . A quadrature voltage compensation component in  $\Delta V_z$  will add a phase shift to the effective angular position of the final voltage reference  $VAC_{MV}$ . This phase shift is not inherently considered in the  $\omega t$  signal, resulting that  $VAC_{MV}$  is

not aligned with the direct axis while a non-zero quadrature component in  $\Delta V_z$  exists.

In order to correct the mismatch between  $\omega t$  and the effective angular position of  $VAC_{MV}$ , the phase shift generated by the virtual impedance ( $\Delta\theta_{Vz}$ ) is added to  $\omega t$ . The phase shift to be corrected is calculated according to Equation (4.28).  $\Delta\theta_{Vz}$  is determined using the positive sequence of the reference voltage  $VAC_{MV}$  in the  $dq0$  frame, represented by  $V_{dq0+}^*$ .  $V_{dq0+}^*$  is calculated applying the moving average operator to  $V_{dq0}^*$  over a running window defined by the reference angular frequency  $\omega$  in the MV inverter ( $\overline{V_{dq0}^*}$ ). The calculation of  $\overline{V_{dq0}^*}$  has an intrinsic delay equal to  $\frac{2\pi}{\omega}$  but it is sufficiently small to not have meaningful impact in the response of the FRT mechanism.

$$\Delta\theta_{Vz} = \tan^{-1} \left( \frac{V_{q+}^*}{V_{d+}^*} \right); \quad V_{dq0+}^* = \begin{bmatrix} V_{d+}^* \\ V_{q+}^* \\ V_{0+}^* \end{bmatrix} = \overline{V_{dq0}^*}; \quad V_{dq0}^* = \Delta V_z + V_{dq0}' \quad (4.28)$$

The positive sequence component related to  $VAC_{MV}$  is used because the calculation of direct and quadrature components of voltages and currents used by the controller of the MV inverter is dependent on the stability of  $\omega t$ . It prevents the introduction of oscillations in  $\omega t$  that would result from a negative sequence component in the fault currents to which the *Virtual Impedance* must respond.  $\omega t$  is given by Equation (4.29), where  $\omega_0 t$  is the nominal angular position over time at the nominal frequency  $\omega_0$  and  $\Delta\omega t^*$  is the angular position regulation performed by the *Frequency/Active Power Control* as depicted in Figure 4.17.

$$\omega t = \omega_0 t + \Delta\omega t^* + \Delta\theta_{Vz} \quad (4.29)$$

### $\Delta P/\Delta\theta$ Compensation

The purpose of this mechanism is to prevent the deadlock of the  $f(\Delta P_{MV})$  droop controller integrating the *Frequency/Active Power Control* represented in Figure 4.17 as a result of the actuation of the FRT mechanism. Through the signal  $\Delta\omega t^*$ , the  $f(\Delta P_{MV})$  droop controller adjusts the frequency of the MV inverter as a function of the active power  $PAC_{MVg}$  exchanged by the MV inverter with the upstream AC grid. However, as the FRT mechanism seeks to limit currents in the the MV inverter,  $PAC_{MVg}$  is affected as well. This may prevent the  $f(\Delta P_{MV})$  droop controller of adjusting  $\Delta\omega t^*$  to the necessary equilibrium point to stabilize the reference angular position  $\omega t$  (and thus, the reference frequency). The FRT mechanism continues to enforce the active current limitation, which tends to increase as the phase shift between the ST and the upstream

AC power system increases due to the lack of stabilization of the reference  $\omega t$  in a new equilibrium point. But the  $f(\Delta P_{MV})$  is waiting  $PAC_{MVg}$  to increase in magnitude (which implies no limitation of the active current by the FRT mechanism) in order to be able to stabilize the reference  $\omega t$ . The  $f(\Delta P_{MV})$  droop controller becomes deadlocked with the FRT mechanism. If such circumstance persists, the ST will eventually lose the synchronism with the upstream AC power system.

In order to prevent this occurrence, the signal  $\Delta P / \Delta \theta$  determined by equation (4.30) is added to  $PAC_{MVg}$  and  $P_{MVsp}$ .  $\Delta \theta$  is the phase angle obtained from the positive sequence of  $VAC_{MVg}$ , which effectively corresponds to the phase shift between  $VAC_{MVg}$  and  $VAC_{MV}$ , and is obtained through the set of Equations in (4.31).  $\Delta \theta_{Min}$  and  $\Delta \theta_{Max}$  are respectively the minimum and maximum dead-zone limits for the phase angle in the positive sequence of  $VAC_{MVg}$ , beyond which the deadlock of the  $f(\Delta P_{MV})$  droop controller may occur.  $G_t$  is a gain tuning which is function of the amplitude of the positive sequence of  $VAC_{MVg}$ , and  $K_p$  is the gain coefficient to produce the active power contribution  $\Delta P / \Delta \theta$ . In the set of Equations in (4.31),  $V_{dq0+}$  is the positive sequence of  $VAC_{MVg}$  in the  $dq0$  referential, and  $A_P$  is as defined in Equation (3.13).

$$\Delta P / \Delta \theta = \begin{cases} K_P G_t (\Delta \theta_{Min} + \Delta \theta) & \text{if } \Delta \theta \leq \Delta \theta_{Min} \\ 0 & \text{if } \Delta \theta_{Min} < \Delta \theta < \Delta \theta_{Max} \\ K_P G_t (\Delta \theta - \Delta \theta_{Max}) & \text{if } \Delta \theta \geq \Delta \theta_{Max} \end{cases} \quad (4.30)$$

$$\Delta \theta = \tan^{-1} \left( \frac{V_{q+}}{V_{d+}} \right); \quad V_{dq0+} = \overline{V_{dq0}} = \begin{bmatrix} V_{d+} \\ V_{q+} \\ V_{0+} \end{bmatrix}; \quad V_{dq0} = A_P VAC_{MVg} \quad (4.31)$$

$\Delta \theta_{Min}$  and  $\Delta \theta_{Max}$  are calculated according to Equation (4.32).  $R_{MVf}$  and  $L_{MVf}$  are respectively the resistance and inductance of the MV LC filter,  $|VAC_{MVg}^+|$  is the module of the positive sequence of  $VAC_{MVg}$  and  $I_{dg}^2$  is as defined in the set of Equations in (4.21) and (4.22).  $\Delta \theta_{Min}$  and  $\Delta \theta_{Max}$  relate to the maximum current  $IAC_{MVn}$ , and correspond to the minimum and maximum phase shift between the ST and the upstream AC power system to which no deadlock occurs in the  $f(\Delta P_{MV})$  droop controller. Outside that interval,  $\Delta P / \Delta \theta$  becomes non-zero in order to prevent the deadlock of the  $f(\Delta P_{MV})$  droop controller.  $VAC_{MVg}$  is used in this calculation because the phase shift to be calculated is always referenced to  $VAC_{MV}$ . The positive sequence of  $VAC_{MVg}$  is used in order to avoid the oscillations in  $\Delta \theta_{Min}$  and  $\Delta \theta_{Max}$  resulting from the presence of the negative sequence in  $VAC_{MVg}$ .

$$\Delta\theta_{Max} = -\Delta\theta_{Min} = \left| \tan^{-1} \left( \frac{|2\pi f_{MV} L_{MVf} I_{AC_{MVn}}| + |R_{MVf} \sqrt{I_{AC_{MVn}}^2 - I_{d_g}^2}|}{|VAC_{MVg}^+|} \right) \right| \quad (4.32)$$

The gain tuning  $G_t$  improves the response of  $\Delta P / \Delta \theta$  Compensation mechanism, by adjusting the  $K_p$  gain as a function of the magnitude of  $VAC_{MVg}$ , as described in Equation (4.33).  $|Z_{MVf}|$  is the scalar value of MV LC filter impedance and  $I_{AC_{MVn}}$  is the nominal current of the MV inverter. The phase shift between  $VAC_{MVg}$  and  $VAC_{MV}$  required to obtain  $I_{AC_{MVn}}$  in the MV inverter output is divided by its counterpart obtained using  $VAC_{MVn}$ , because the phase shift corresponding to  $I_{AC_{MVn}}$  is inversely proportional to the magnitude of  $VAC_{MVg}$ . As such,  $G_t$  adjusts  $\Delta\theta'$  for an enhanced  $\Delta P / \Delta \theta$  compensation, as a function of the magnitude of  $VAC_{MVg}$ .

$$G_t = \left| \frac{\sin^{-1} \left( \frac{I_{AC_{MVn}} |Z_{MVf}|}{|VAC_{MVg}|} \right)}{\sin^{-1} \left( \frac{I_{AC_{MVn}} |Z_{MVf}|}{VAC_{MVn}} \right)} \right| \quad (4.33)$$

Equations (4.30) to (4.33) show that the  $\Delta P / \Delta \theta$  compensation only actuates when the phase shift measured in  $VAC_{MVg}$  goes outside the interval defined by  $\Delta\theta_{Min}$  and  $\Delta\theta_{Max}$ , beyond which the deadlock of the  $f(\Delta P_{MV})$  droop controller can occur.

#### 4.2.2.2 Chain of Events induced by the FRT Control Strategy

The reaction chains triggered by the actuation of the FRT control strategy proposed for grid-forming ST is illustrated Figure 4.18.

The current limitation imposed by the FRT control (blue arrow) impacts directly the power balance in the MV DC bus. Simultaneously, the variation of  $VAC_{MVg}$  following a fault disturbance in the upstream AC system also impacts the power balance in the MV DC bus, even if the FRT control does not actuate, because the active power exchanged by the ST with the upstream AC system is impacted by variations in  $VAC_{MVg}$ . Also, the active power exchanged by the ST with the upstream AC system impacts the actuation of the  $f(\Delta P_{MV})$  droop controller, which impacts the power balance in the MV DC bus.

These active power reaction chains (thin red arrows) converge in the MV inverter, affecting  $VDC_{MV}$  (light green arrow). The deviation of  $VDC_{MV}$  from the set-point defined by the *DC Voltage Control* (illustrated in Figure 4.17) immediately prompts its regulation (dark green arrow) through the control of the current reference  $I_{ESS}^*$  of the local ESS which acts as a power buffer by injecting the necessary power (bold red arrows) in the DC buses in order to stabilize  $VDC_{MV}$  around the reference value.

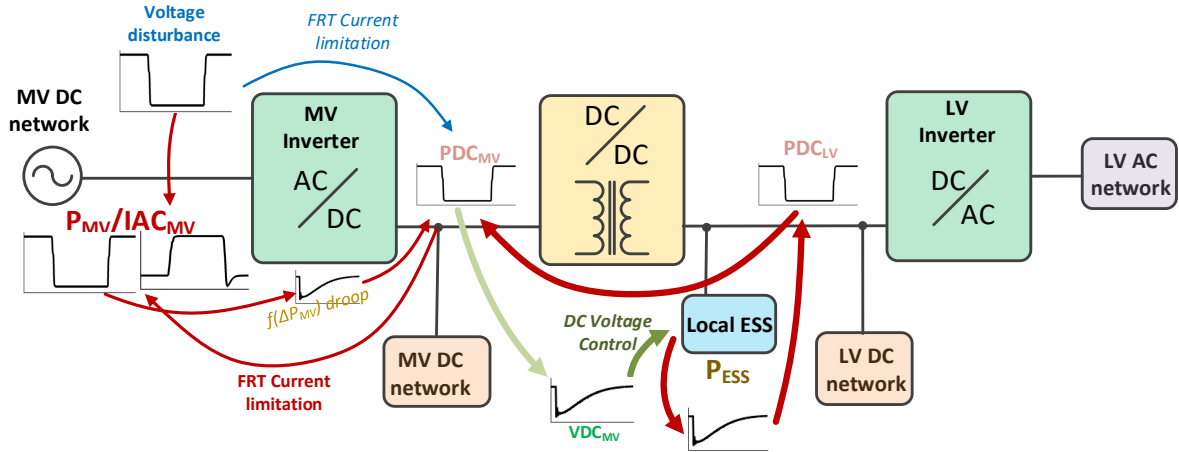


**Figure 4.18:** Reaction chain triggered in the grid-forming ST and its derived grids following a fault disturbance in the MV AC grid. Positive values for the active power correspond to consumed active power.

### 4.3 Reconfiguration Capabilities on Hybrid Multi-Microgrids

The control functionalities proposed in this section aim to enable the reconfiguration of grid sections within a HMMG in order to allow the permutation of grid sections between radial and meshed configurations without interruption of supply. The main purpose is to enable a ST-based LV AC subgrid to be reconfigured to operate in radial configuration or in meshed configuration jointly with other LV AC grids connected to other ST or fed from the MV AC grid through a conventional magnetic Low-Frequency Transformer (LFT). The novelty of the proposed approach is that it does not rely on communications to perform the synchronization of the LV grids to reconnect, in contrast with the solutions proposed in the literature so far which are reliant on communications and remote measurements [123, 225]. It solely relies on the electrical quantities measured locally at the ST level. The rationale of the proposed approach is conceptually illustrated in Figure 4.19, and its implementation in the control structure of the LV inverter is illustrated in Figure 4.20. The proposed synchronization mechanism is based on the assumption that all LV AC grids to be synchronized and reconnected are under the same MV AC grid. Existing LV grids are typically operated in a radial configuration with limited or no reconnection capabilities to neighboring LV grids. Nevertheless, in neighboring LV grids, the frequency at the connection point of the MV AC grid with the LFT or ST related to the LV AC grids to be synchronized and connected in a ring or meshed configuration is the same, with the phase angle differences among them



being usually small and depending on load profiles and line impedances in the MV AC side. As such, the synchronization phase and frequency to impose on LV AC grids amid its synchronization in a ring or meshed configuration can be solved by using the phase and frequency at the ST's connection point with the MV AC grid. This approach does not require communications between LV AC grids or distribution substations, nor detection mechanisms for phase crossing between LV AC grids. Follows a detailed description of the proposed synchronization mechanism. The parameterization of the synchronization mechanism is presented in Appendix A.

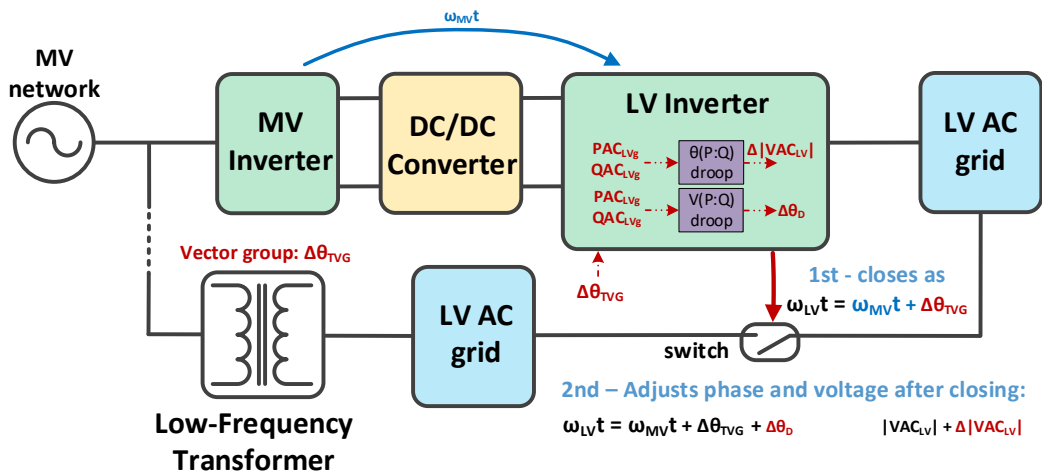


**Figure 4.19:** Conceptual representation of the proposed synchronization mechanism for the ST's LV inverter.

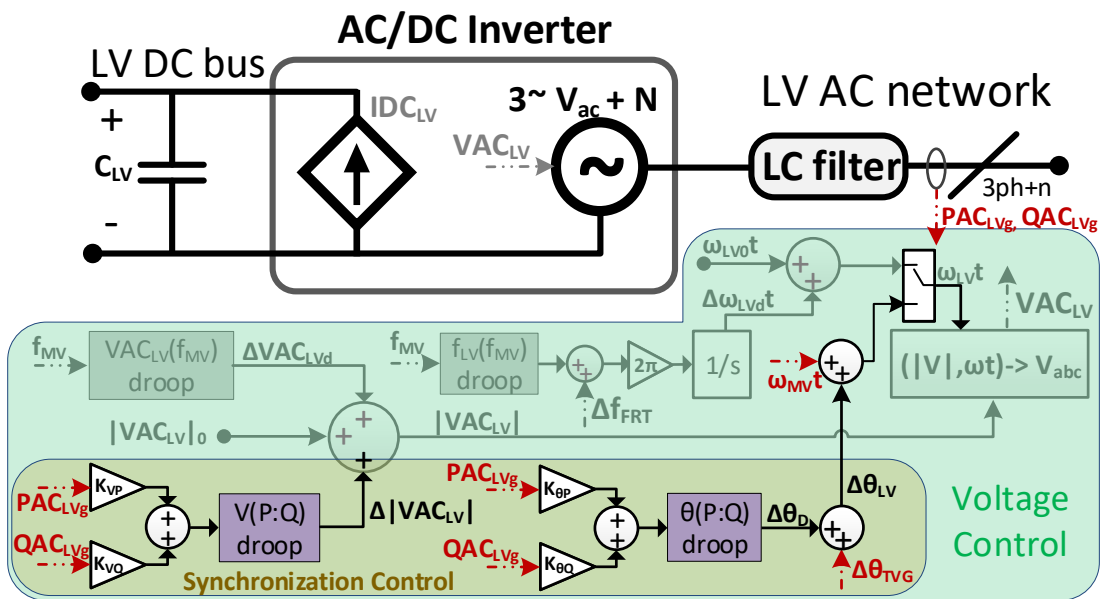


**Figure 4.20:** Block diagram of the ST's LV inverter incorporating the proposed synchronization mechanism.



As shown in Figure 4.20 it is possible to select between the reference angular position generated by the controller of the LV inverter ( $\omega_{LV}t + \Delta\omega_{LVd}t$ ) and the reference angular position determined according to Equation (4.34), where  $\omega_{MV}t$  is the reference angular position of the MV inverter,  $\Delta\theta_{TVG}$  is the phase adjustment related to the transformer vector group to be considered, and  $\Delta\theta_D$  is a phase adjustment function of  $PAC_{LVg}$  and  $QAC_{LVg}$ .  $\omega_{MV}t$  constitutes the base signal to equal the frequency in both MV and LV inverters.  $\Delta\theta_{TVG}$  is required since the ST-based LV AC grid can be connected to another LV AC grid based on a LFT with a characteristic transformer vector group whose phase shift in relation to the MV AC grid is not zero.

$$\omega_{LV_0}t = \omega_{MV}t + \Delta\theta_D + \Delta\theta_{TVG} \quad (4.34)$$

The calculation of  $\Delta\theta_D$  is based on the droop-based controller discussed in section 4.1.1, illustrated in Figure 4.2 and expressed by Equation (4.1). Based on Equation (4.1),  $\Delta\theta_D$  can be expressed according to Equations (4.35) and (4.36).  $m_{dp}$  and  $m_{dn}$  are respectively the positive and negative droop slopes, and  $K_{\theta P}$  and  $K_{\theta Q}$  are respectively the coefficients for the active and reactive power components contributing to  $\Delta\theta_D$ .  $K_{\theta P}$  and  $K_{\theta Q}$  should be determined according the typical X/R impedance ratio in the LV AC grid for an optimized performance.

$$\Delta\theta_D = \begin{cases} \Delta\theta_{Dmin} & \text{if } X \in ]-\infty, X_{min}] \\ m_{dn}(X - X_{min}) + \Delta\theta_{Dmin} & \text{if } X \in ]X_{min}, X_{min\_db}] \\ 0 & \text{if } X \in ]X_{min\_db}, X_{max\_db}[ \\ m_{dp}(X - X_{max\_db}) & \text{if } X \in [X_{max\_db}, X_{max}[ \\ \Delta\theta_{Dmax} & \text{if } X \in [X_{max}, \infty[ \end{cases} \quad (4.35)$$

$$X = K_{\theta P}PAC_{LVg} + K_{\theta Q}QAC_{LVg}; \quad K_{\theta P}, K_{\theta Q} \in [0, 1]; \quad K_{\theta P} + K_{\theta Q} = 1 \quad (4.36)$$

It is worth to mention that the LV inverter continues to operate in grid-forming mode under the proposed reconnection approach. Moreover, also using the aforementioned droop-based control approach, the magnitude of the reference voltage for the LV inverter ( $|VAC_{LV}|$ ) is also adjusted as a function of  $PAC_{LVg}$  and  $QAC_{LVg}$ , in order to minimize the mismatch of voltage magnitudes in the LV AC grids to be connected, in the connection point. The voltage adjustment is expressed by Equations (4.37) and (4.38).  $K_{VP}$  and  $K_{VQ}$  are respectively the coefficients for the active and reactive power components contributing to  $\Delta|VAC_{LV}|$ .  $K_{VP}$  and  $K_{VQ}$  should be determined according the

typical X/R impedance ratio in the LV AC grid for an optimized performance.

$$\Delta|VAC_{LV}| = \begin{cases} \Delta|VAC_{LVmin}| & \text{if } X \in ]-\infty, X_{min}] \\ m_{dn}(X - X_{min}) + \Delta|VAC_{LVmin}| & \text{if } X \in ]X_{min}, X_{min\_db}] \\ 0 & \text{if } X \in ]X_{min\_db}, X_{max\_db}[ \\ m_{dp}(X - X_{max\_db}) & \text{if } X \in [X_{max\_db}, X_{max}[ \\ \Delta|VAC_{LVmax}| & \text{if } X \in [X_{max}, \infty[ \end{cases} \quad (4.37)$$

$$X = K_{VP}PAC_{LVg} + K_{VQ}QAC_{LVg}; \quad K_{VP}, K_{VQ} \in [0, 1]; \quad K_{VP} + K_{VQ} = 1 \quad (4.38)$$

## 4.4 Final Remarks - Summary

In this chapter, the advanced control functionalities for ST proposed in this thesis are presented and described. The integration of the proposed control solution with the baseline computational models previously described in chapter 3 is also discussed. The present chapter is summarized as follows:

- Power-frequency support strategies for grid-following and grid-forming ST are described. The power-frequency support strategy for a grid-following ST exploits ST's local ESS and the power-voltage and power-frequency sensitivities of the ST-based hybrid AC/DC grid in order to modulate its active power, and thus, provide power-frequency support to the upstream AC system. The power-frequency support strategy for a grid-forming ST exploits the ST's local ESS for immediate power provision and the power-voltage and power-frequency sensitivities of the ST-based hybrid AC/DC grid to extend the longevity of the storage capacity of the local ESS. The power-frequency support strategies rely on droop-based controllers (in the ST and controllable DER) and on the exploitation of load-voltage and load-frequency sensitivities of non-controllable loads.
- FRT control strategies are proposed for grid-following and grid-forming ST. The FRT control strategy for grid-following ST relies on a dump-load and on the exploitation of the power-voltage and power-frequency sensitivities of the ST-based hybrid AC/DC grid in order to modulate its active power. Alternatively, relies on the ST's local ESS if available. The FRT control strategy for grid-forming ST relies on a virtual impedance complemented with supplementary mechanisms which limit the magnitude and phase angle in the voltages generated by the MV inverter, based on the maximum voltage drop in the ST's MV LC filter

corresponding to the maximum currents permissible in the MV inverter.

- A communication-free reconnection mechanism enabling the islanding and reconnection of ST-based LV AC grids with other LV AC grids in ring or meshed configurations is also described. The proposed strategy is suitable for LV AC grids under the same MV AC grid. The frequency and angular position of the MV AC grid measured locally by the ST are used to synchronize and reconnect the ST-based LV AC grid with other LV AC grids.

The effectiveness of the proposed solutions are to be tested on selected test grids described in chapter 3 and parameterized as specified in appendix A. The underlying results for different test cases and operating conditions are presented in the next chapters.



## Chapter 5

# Providing Power-frequency Regulation from Smart-Transformer connected Hybrid Microgrids - Numerical Results

Using the computational models presented and described in chapter 3 and in section 4.1, the effectiveness of the proposed control strategies for power–frequency support to the AC power system enabled by Smart-Transformers (ST) feeding hybrid AC/DC distribution grids is evaluated through computational simulation. As previously stated in chapter 3, the International System of Units (SI system) is adopted for all developed computational models. Nevertheless, for depicting some results alongside this chapter, the per-unit system (p.u.) is also used in order to facilitate the interpretation of the presented results.

### 5.1 Case Studies

In order to evaluate the effectiveness of the proposed control strategies for power–frequency support to the upstream AC power grid from ST-connected hybrid AC/DC grids, four case studies were considered for grid-following and grid forming ST:

- Over-frequency disturbances in the upstream AC power system and a net-load scenario in the ST-based Hybrid AC/DC grid.
- Over-frequency disturbances in the upstream AC power system and a net-generation scenario in the ST-based Hybrid AC/DC grid.
- Under-frequency disturbances in the upstream AC power system and a net-load scenario in the ST-based Hybrid AC/DC grid.

- Under-frequency disturbances in the upstream AC power system and a net-generation scenario in the ST-based Hybrid AC/DC grid.

The under-frequency and over-frequency disturbances in the aforementioned case studies result from load steps applied to the equivalent load considered for the upstream AC power system.

The computational models for the considered case studies follow the overall representation illustrated in Figure 5.1. The AC power system (including the equivalent load and generation) is modeled as described in subsection 3.3.1. The hybrid AC/DC grid is constituted by a Hybrid AC/DC Microgrid (HMG) and a MV DC grid. The HMG is modeled using the radial LV AC grid and the LV DC grid described in subsection 3.3.2. The MV DC grid is modeled using the MV DC grid described in subsection 3.3.3. Regarding the ST model, grid-following and grid-forming units were considered according to the respective models described in sections 3.2 and 4.1.

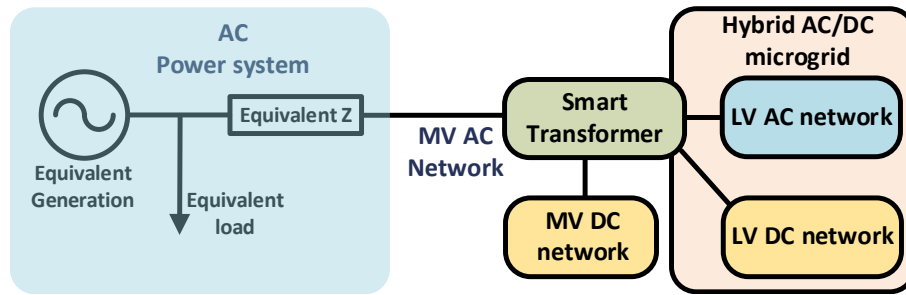


**Figure 5.1:** Overview of the computational models adopted for the evaluation of the advanced control functionalities for power-frequency support using ST.

Regarding the considered case studies, only the most relevant parameters for the ST and test grids are presented in this chapter. The complete parameterization of the ST and test grids can be found in Appendix A. The most relevant parameters for the ST are summarized in Table 5.1. The results in p.u. presented in section 5.2 use the nominal values presented in Table 5.1 as base values.

**Table 5.1:** Smart-Transformer: main parameters

Nominal Power	1 MVA
Nominal MV AC Voltage (ph-ph)	15000 V (RMS)
Nominal MV DC link Voltage	27000 V
Nominal LV DC link Voltage	720 V
Nominal LV AC Voltage (ph-n)	230 V (RMS)
Nominal frequency (MV and LV inverters)	50 Hz

Table 5.2 summarizes the relevant parameters for the upstream AC power system. The under-frequency and over-frequency disturbances were generated by applying

load steps (connection and disconnection) equivalent to 10% and 20% of the total generation capacity of the upstream AC power system (1GW) indicated in Table 5.2, which are always relative to the total load presented in Table 5.2.

**Table 5.2:** Upstream AC power system: main parameters

Generation capacity	1 GW
Total load	600MW/200Mvar
Equivalent system inertia (H)	2 s
Equivalent impedance (seen from MV connection)	$0.04 + j0.63 \Omega$

The most relevant parameters for the ST-based Hybrid AC/DC grid are presented in Table 5.3, where the steady-state conditions for net-load and net-generation scenarios and the installed capacity considered for the controllable resources are presented. Positive values correspond to consumed power, and negative values correspond to injected/generated power.

**Table 5.3:** Steady-state power and operation limits in the ST-based hybrid AC/DC grid

non-controllable load	PV generation	EV charging	Energy Storage
<b>Net-load scenario</b>			
LV AC network			
202 kW / 64 kvar	-75 kW (-210 - 0)	23 kW (0 - 86)	15 kW ( $\pm 42$ )
LV DC network			
105 kW	-150 kW (-420 - 0)	105 kW (0 - 140)	37 kW ( $\pm 84$ )
MV DC network			
175 kW	-500 kW (-1400 - 0)	525 kW (0 - 525)	–
grid-forming ST			
–	–	–	450 kW *
Total hybrid AC/DC grid			
482 kW	-725 kW	653 kW	52 kW
<b>Net-generation scenario</b>			
LV AC network			
202 kW / 64 kvar	-180 kW (-210 - 0)	23 kW (0 - 86)	15 kW ( $\pm 42$ )
LV DC network			
105 kW	-360 kW (-420 - 0)	105 kW (0 - 140)	37 kW ( $\pm 84$ )
MV DC network			
175 kW	-1200 kW (-1400 - 0)	525 kW (0 - 525)	–
grid-forming ST			
–	–	–	-450kW *
Total hybrid AC/DC grid			
482 kW	-1740 kW	653 kW	52 kW

\* Grid-forming ST only: imposed on the ST local ESS by the  $f(\Delta P_{MV})$  droop offset.

The steady-state values presented in Table 5.3 were obtained by applying multiplication factors to the load and generation profiles presented for the base test grids parameterized in Appendix A in order to obtain the desired net-load and net-generation scenarios. The base steady-state PV generation was multiplied by 2.5 and 6 for net-load and net-generation scenarios respectively. The installed PV generation capacity was multiplied by 7 in both net-load and net-generation scenarios. The base power profile for the remaining Distributed Energy Resources (DER) and non-controllable load was multiplied by 3.5 in both net load and generation scenarios. The impedance of the cable sections in the modeled test grids, whose base parameterization is presented in Appendix A, was divided by 3.5 to reflect the multiplication factor adopted for the non-controllable load and DER units excluding PV generation.

Table 5.3 also indicates that, for the scenarios involving the grid-forming ST, the active power in the ST MV inverter was adjusted by applying an offset to the  $f(\Delta P_{MV})$  droop controller in such a way that the steady-state active power exchanged by the MV inverter with the upstream MV AC grid approximates the net-power in the ST-based Hybrid AC/DC grid. Since the net-power in the ST-based Hybrid AC/DC grid is cushioned by the ST's local ESS, this power adjustment intends to consider a more realistic operation scenario for the ST, where most of the net-power in the ST-based Hybrid AC/DC grid is transferred to the upstream MV AC grid.

Regarding the droop-based controllers embedded in the ST and controllable DER, they are parameterized as described in Appendix A.

## 5.2 Simulation Results

The frequency disturbances resulting from the 10% and 20% load steps in the upstream AC power system are illustrated in Figure 5.2. The variable  $f_{MV}$  corresponds to the frequency measured at the ST connection point with the MV AC grid. As expected, larger load-steps result in larger frequency excursions. The reactions of the grid-following and grid-forming ST and its respective hybrid AC/DC grids are presented in the following subsections. The results presented in p.u. use the nominal voltages and frequency presented in Table 5.1 as base values. In the presented results, the start of the frequency disturbance occurs at  $time (s) = 0$ , and positive values for the active power correspond to consumed power whereas negative values correspond to injected/generated active power.



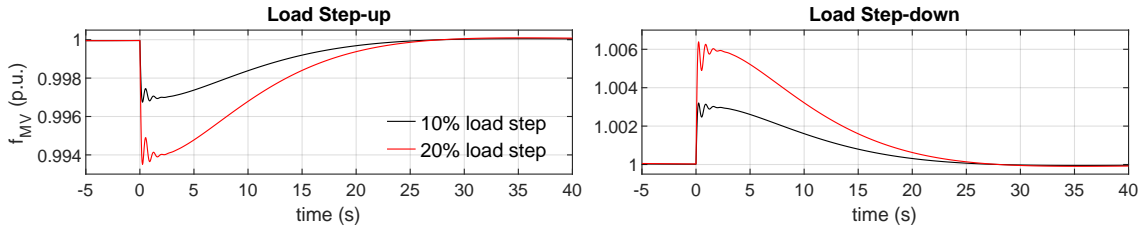


**Figure 5.2:** Over-frequency and under-frequency disturbances in the upstream AC power system for 10% and 20% load step-up and step-down variations in the upstream AC grid.

### 5.2.1 Grid-Following ST

In order to demonstrate the aggregated response of the active power – frequency support functionalities proposed for the ST and downstream hybrid AC/DC system, the presented results were obtained with the simultaneous operation of all droop controllers incorporated in the ST designed for that purpose. In response to the frequency disturbances illustrated in Figure 5.2 and considering net-load and net-generation scenarios, the operation of the droop-based controllers in the ST modulates the voltage and frequency levels in the ST-based hybrid AC/DC grid as depicted in Figure 5.3. The voltage and frequency levels in the LV AC sub-grid ( $V_{AC_{LV}}$  and  $f_{LV}$ ) are modulated by the  $V_{AC_{LV}}(f_{MV})$  and  $f_{LV}(f_{MV})$  droops respectively. The voltage levels in the MV and LV DC sub-grids ( $V_{DC_{MV}}$  and  $V_{DC_{LV}}$ ) are modulated by the  $V_{DC_{MV}}(f_{MV})$  droop. The voltage regulation performed over the MV DC network affects the voltage in the LV DC network since a fixed transformation ratio is defined for the isolated DC/DC converter in the ST. It is also possible to observe that the voltage and frequency curves expressed in Figure 5.3 stabilize before the frequency in the upstream AC grid (shown in Figure 5.2) returns completely to its nominal value. This results from the existence of dead-band limits in the aforementioned droop controllers responsible to modulate the voltage and frequency levels in the ST-based hybrid AC/DC grid.

From the modulation of voltage and frequency levels in the ST-based hybrid AC/DC distribution network, a response in terms of net active power is obtained from the hybrid distribution network. The global active power response to the frequency disturbances illustrated in Figure 5.2 is aggregated at the MV inverter of the ST and is shown in Figures 5.4 and 5.5. The results illustrated in Figures 5.4 and 5.5 include not only the contribution from the ST-based hybrid AC/DC grid but also the contribution of the local ESS integrating the ST, and are discriminated by sub-grid and type of resource constituting the hybrid AC/DC grid respectively. The contribution from the local ESS integrated in the ST for the overall power – frequency support is due to the actuation of the  $P(f_{MV})$  droop controller embedded in the ST.

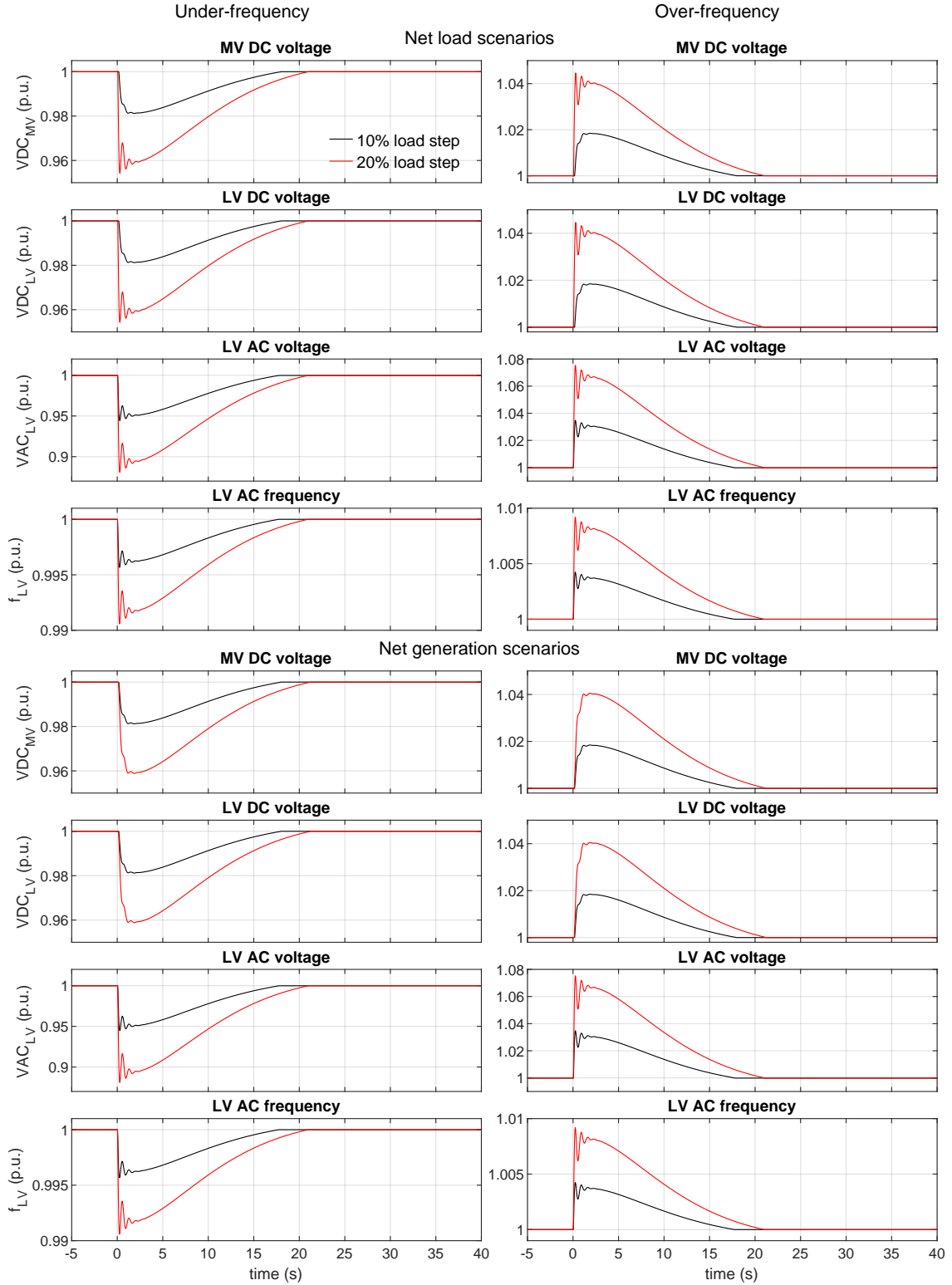


**Figure 5.3:** Frequency and voltage modulation in ST-based sub-grids following frequency disturbances in the upstream AC grid.

As expected, the active power consumed by the non-controllable loads scattered throughout the ST-based hybrid AC/DC grid is modulated according to its sensitivity

to voltage and frequency variations. Regarding the DER units, their embedded droop controllers react accordingly to the voltage and frequency modulations in the various sub-grids constituting the ST-based hybrid AC/DC grid. The PV generation is also able to respond to under-frequency disturbances by using its 10% deloading capacity and therefore increase its power output. It is also possible to observe in Figure 5.5 that the contribution of the PV generation is higher during over-frequency disturbances. The PV generation can be curtailed down to zero if necessary in order to help to counteract the temporary excess in generation in the upstream AC grid, while during under-frequency disturbances the PV generation can only be increased as far as the previously defined deloading operation margin of 10% permits.

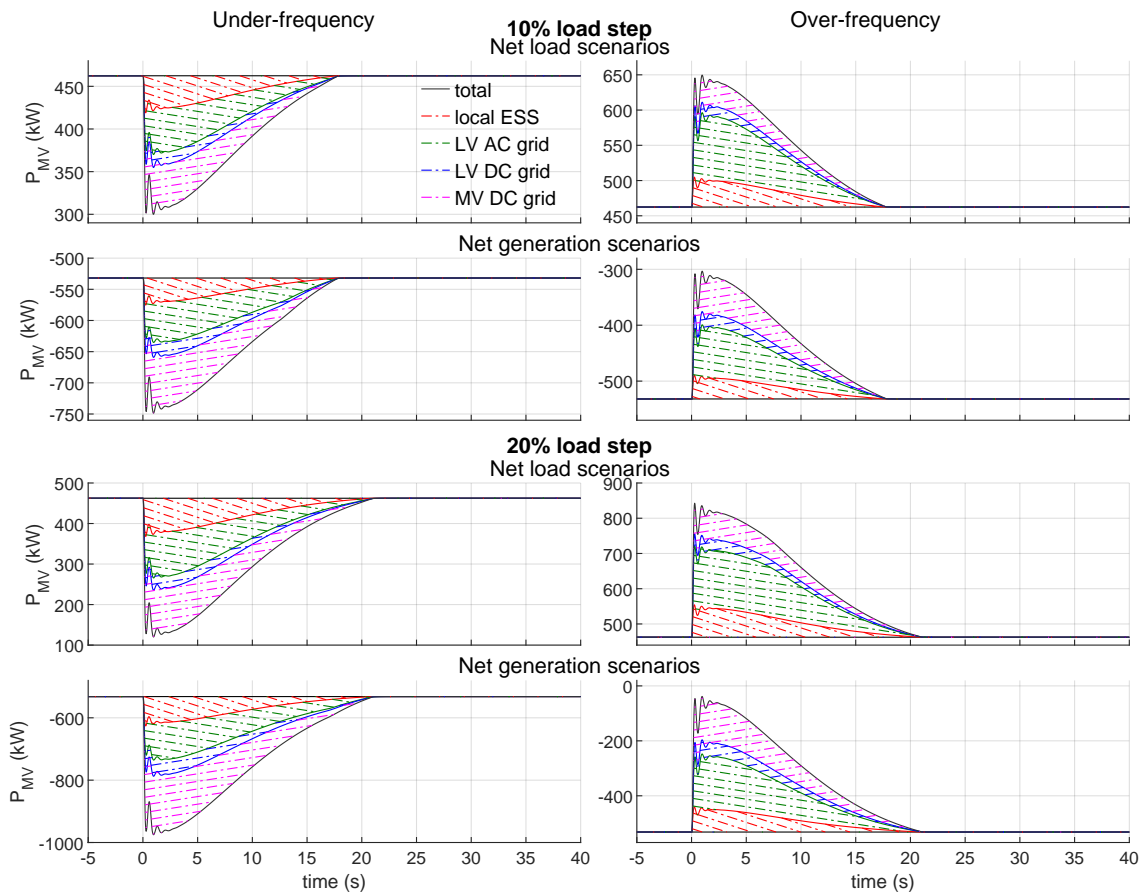


**Figure 5.4:** Active Power response in the ST's MV inverter following frequency disturbances in the upstream AC grid, discriminated by sub-grid contribution.

In general, the results illustrated in Figures 5.4 and 5.5 show that the provided power-frequency support increases with the magnitude of the frequency disturbance. In face of under-frequency disturbances in the upstream AC grid, the active power in the ST-based hybrid AC/DC grid decreases for net-load scenarios and increases for net-generation scenarios, thus contributing to the power – frequency regulation

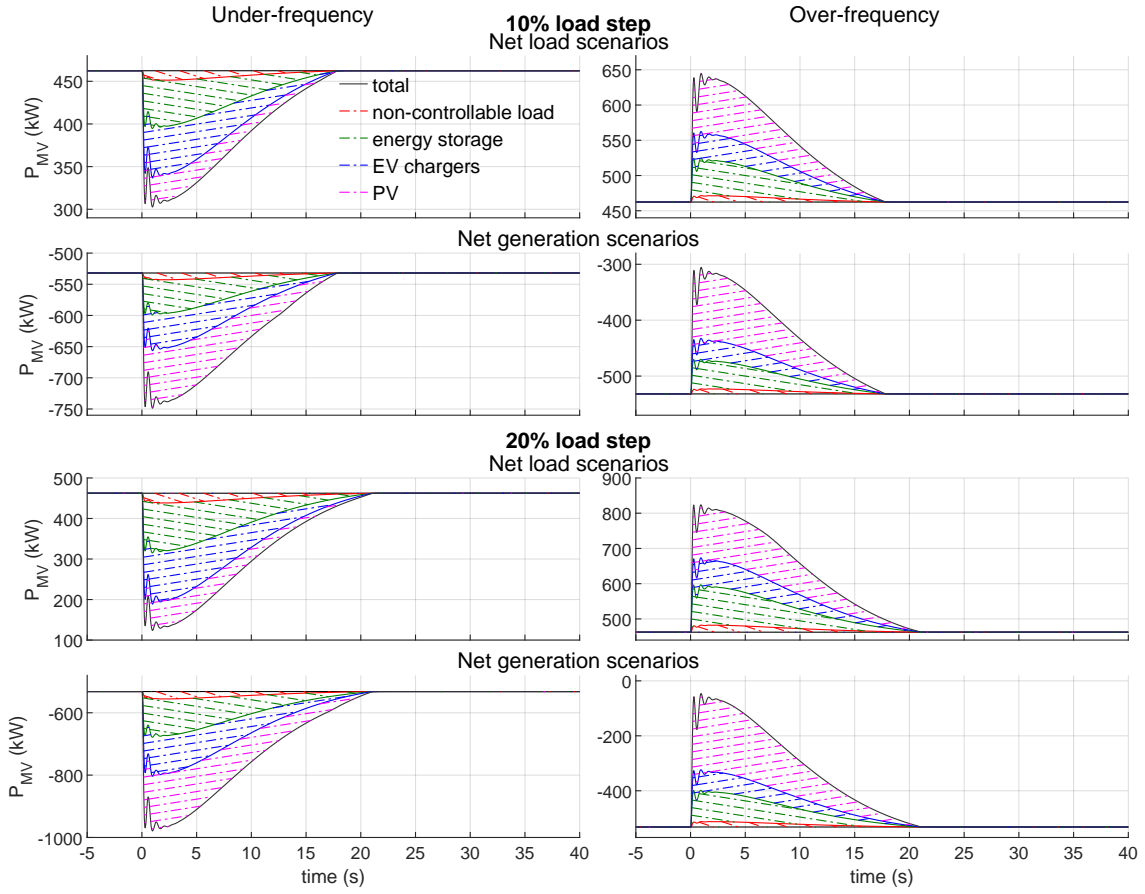


**Figure 5.5:** Active Power response in the ST's MV inverter following frequency disturbances in the upstream AC grid, discriminated by resource type contribution.

of the upstream AC power grid. By other hand, the active power in the ST-based hybrid AC/DC grid increases for net-load scenarios and decreases for net-generation scenarios when a over-frequency disturbance in the upstream AC grid occurs, thus contributing to reduce the temporary over-generation affecting the upstream AC grid.

The distribution observed per sub-grid and resource type for the contribution in the provision of power – frequency support shown in Figures 5.4 and 5.5 is naturally determined by the parameters selected for the droop controllers (embedded in the ST and in the DER connected to the ST-based hybrid AC/DC grid), constitution in terms of loads and resources of the various sub-grids and the voltage and frequency sensitivities of the various sub-grids. Different grids and parameterization of the droop controllers would produce different distributions per sub-grids and type of resources.

### 5.2.2 Grid-Forming ST

Distinctively from the grid-following ST, the reaction of the grid-forming ST in terms of active power to frequency disturbances in the upstream AC power system is solely

determined by the  $f(\Delta P_{MV})$  droop controller embedded in the controller of its MV inverter. This means that the power – frequency support provided to the upstream AC grid by the grid-forming ST is independent from the active power response occurring in the ST-based hybrid AC/DC grid. In fact, any discrepancy between the net-active power in the MV inverter and the ST-based hybrid AC/DC grid is cushioned by the local ESS, as illustrated by the chain of events in Figure 4.7 (subsection 4.1.2).

Nevertheless, the involvement of the ST-based hybrid AC/DC grid can considerably reduce the power and energy required to the local ESS to provide power – frequency support to the upstream AC power system. Such impact in the local ESS is illustrated in Figure 5.6, where it is possible to observe how a proper coordination between the  $f(\Delta P_{MV})$  droop controller in the ST's MV inverter and the active power modulation in the ST-based hybrid AC/DC grid can greatly reduce the intervention of the local ESS in the power – frequency support to the upstream AC grid.

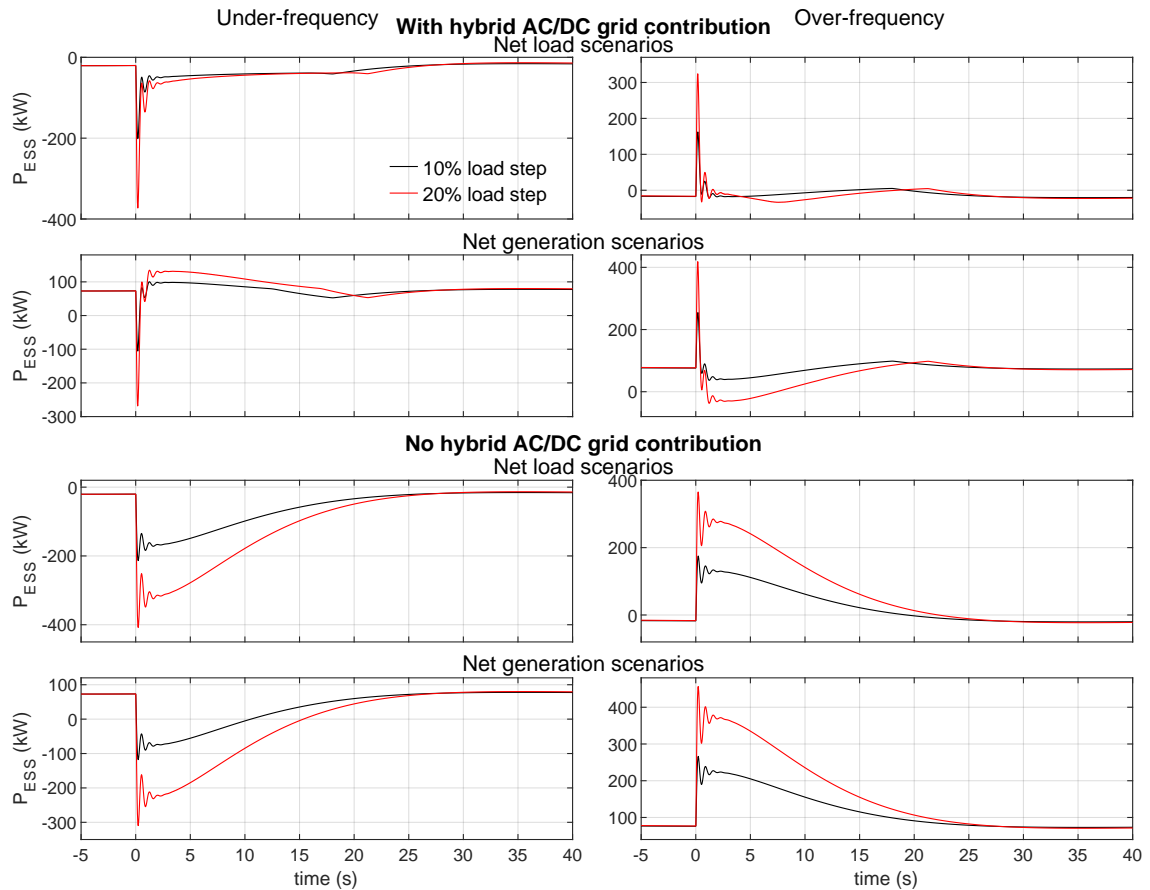


**Figure 5.6:** Active Power response in the local ESS in the absence of response in the ST-based sub-grids, following frequency disturbances in the upstream AC grid.

Thus, the global active power support provided through the ST's MV inverter remains unchanged whether the ST-based hybrid AC/DC grid participates or not

in the provision of power – frequency support to the upstream AC power system. When the ST-based hybrid AC/DC grid is not involved in the provision of power – frequency support, the transient power modulation in the ST’s MV inverter is practically supported by the local ESS of the ST. This is illustrated in the results presented in Figures 5.7 and 5.8, which relate to under-frequency and over-frequency scenarios respectively, and illustrate the provision of power – frequency support through the ST’s MV inverter discriminated by provenience (local ESS and ST-based sub-grids) and compares between the scenarios where the ST-based hybrid AC/DC grid participates or is absent from the provision of power – frequency support.

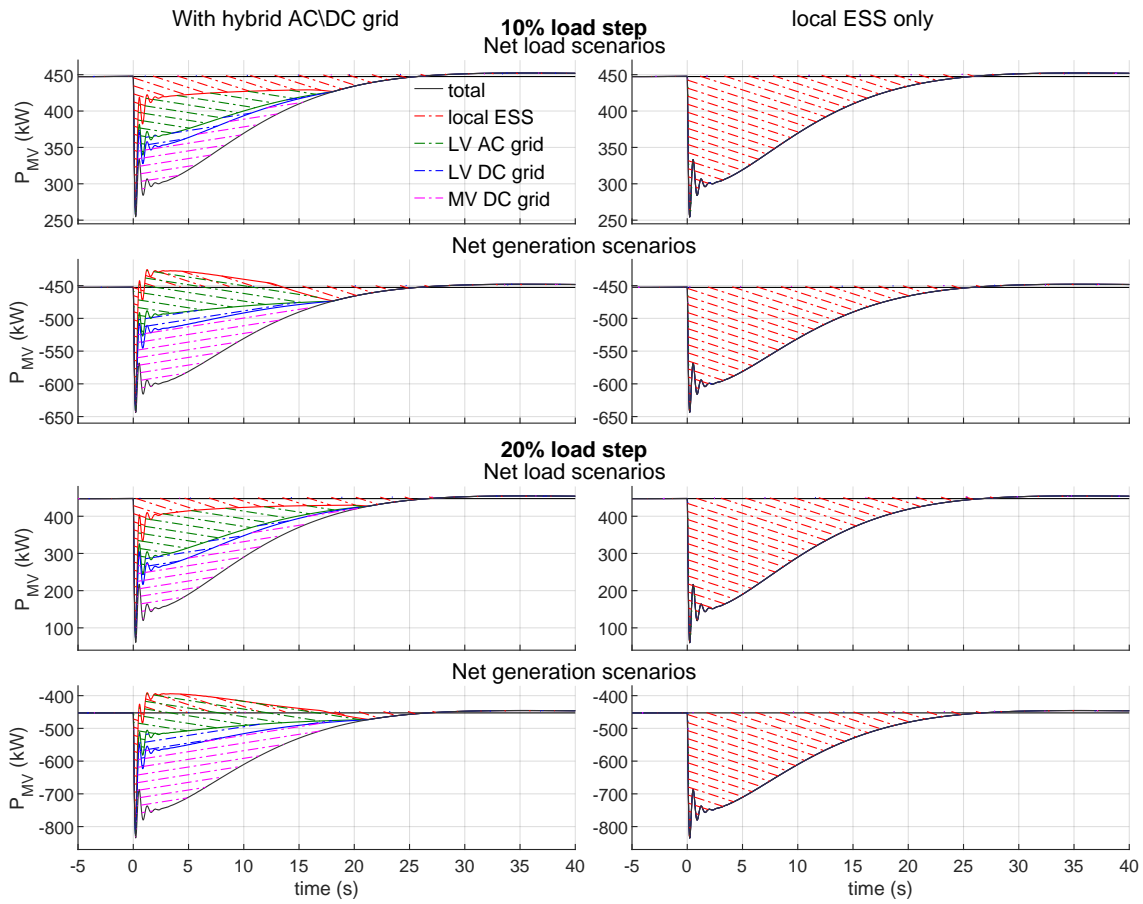


**Figure 5.7:** Active Power response in the ST’s MV inverter following under-frequency disturbances in the upstream AC grid, discriminated by resource type.

Moreover, it is also possible to observe that the power reaction of the local ESS is not always aligned with the overall response of the ST-based hybrid AC/DC grid. If the reaction of the ST-based hybrid AC/DC grid in terms of active power to frequency disturbances in the main power system surpasses the active power reaction dictated by the  $f(\Delta P_{MV})$  to the MV inverter of the ST, the local ESS will compensate the difference by reacting in the opposite direction. This can be observed in the results presented

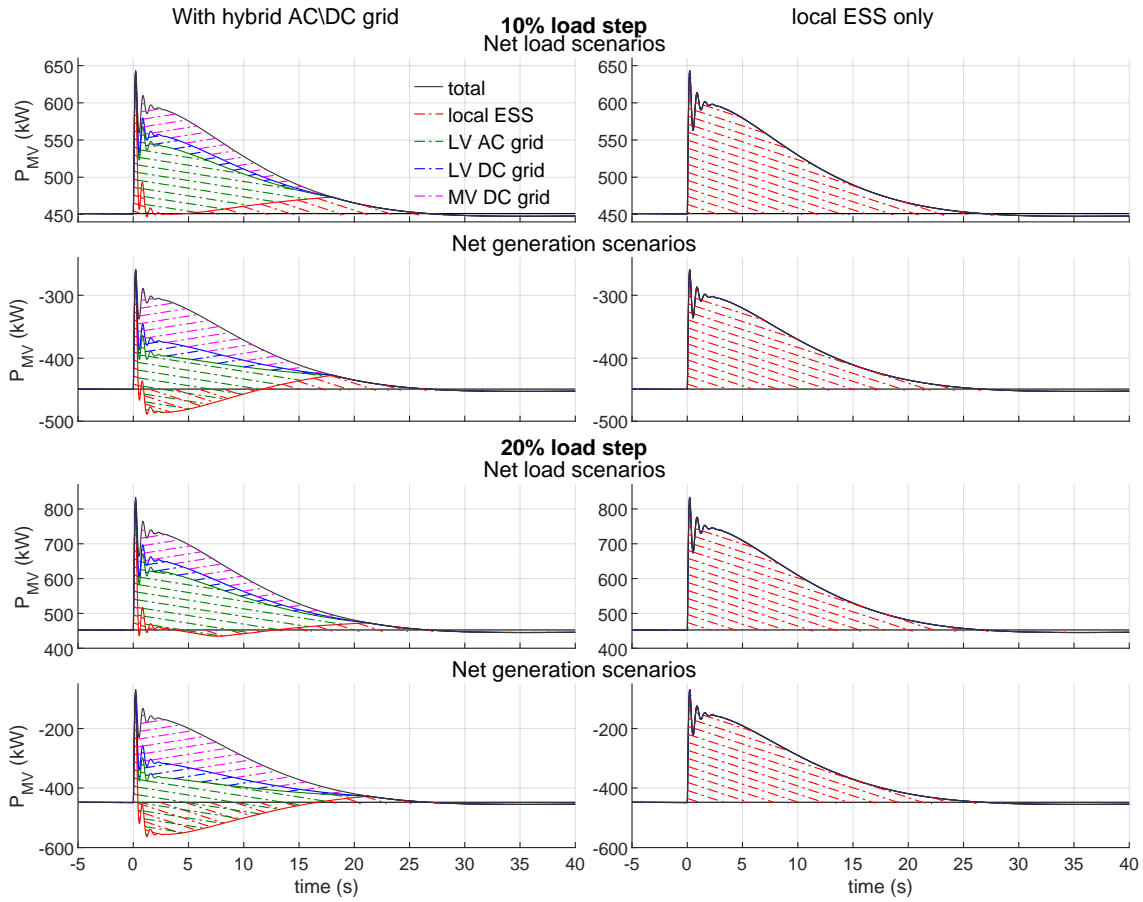


**Figure 5.8:** Active Power response in the ST's MV inverter following over-frequency disturbances in the upstream AC grid, discriminated by resource type.

in Figures 5.7 and 5.8 specially in the net-generation scenarios. The aggregate active power response is given by the curve labeled *total*, which is the sum of the contributions from the local ESS and ST-based sub-grids. It is possible to observe that there are instants where the active power in the local ESS is opposite to the total active power reaction, which means that the local ESS is absorbing part of the active power reaction originating from the hybrid AC/DC grid.

When the contribution of the ST-based hybrid AC/DC grid is considered for the provision of power – frequency support, the modulation of the voltage and frequency levels in the ST-based hybrid AC/DC grid is very similar to the results already exposed in Figure 5.3, as shown in Figure 5.9. The reason is that the parameterization of the common droop controllers embedded in the ST itself and the adopted hybrid AC/DC grid (including the parameterization of the droop controllers embedded in DER units) are similar to what was adopted for the grid-following ST. As described for the grid-following ST, is the also the modulation of voltage and frequency levels in the ST-based hybrid AC/DC distribution network by the droop controllers embedded in the ST that



originates the response of the hybrid distribution network in terms of net active power observed in Figures 5.7 and 5.8.

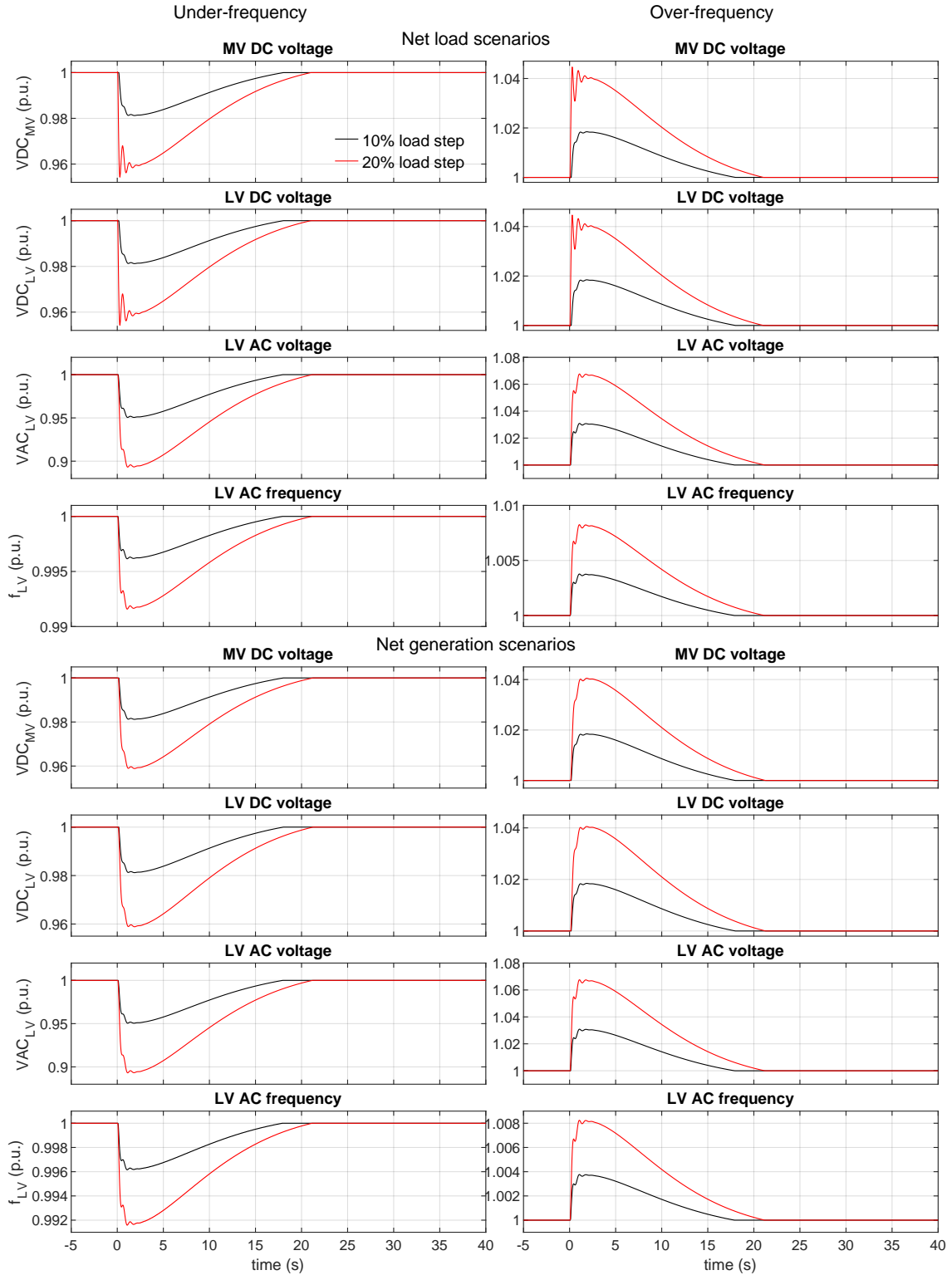


**Figure 5.9:** Frequency and Voltage modulation in ST-based sub-grids for 10% and 20% load step variation in the upstream AC grid.



Figure 5.10 presents the global active power response of the grid-forming ST and its hybrid AC/DC grid already shown in Figures 5.7 and 5.8, but now discriminating by contribution from each type of resource in the ST-based hybrid AC/DC grid. The active power consumed by the non-controllable loads is modulated according to its sensitivity to voltage and frequency variations, and the droop controllers embedded in the DER units react to the same voltage and frequency modulations. The PV generation is also able to respond to under-frequency disturbances by using its 10% deloading capacity, being possible to observe that the contribution of the PV generation is higher during over-frequency disturbances, for the same reasons already mentioned in the analysis of the results related to the grid-following ST.

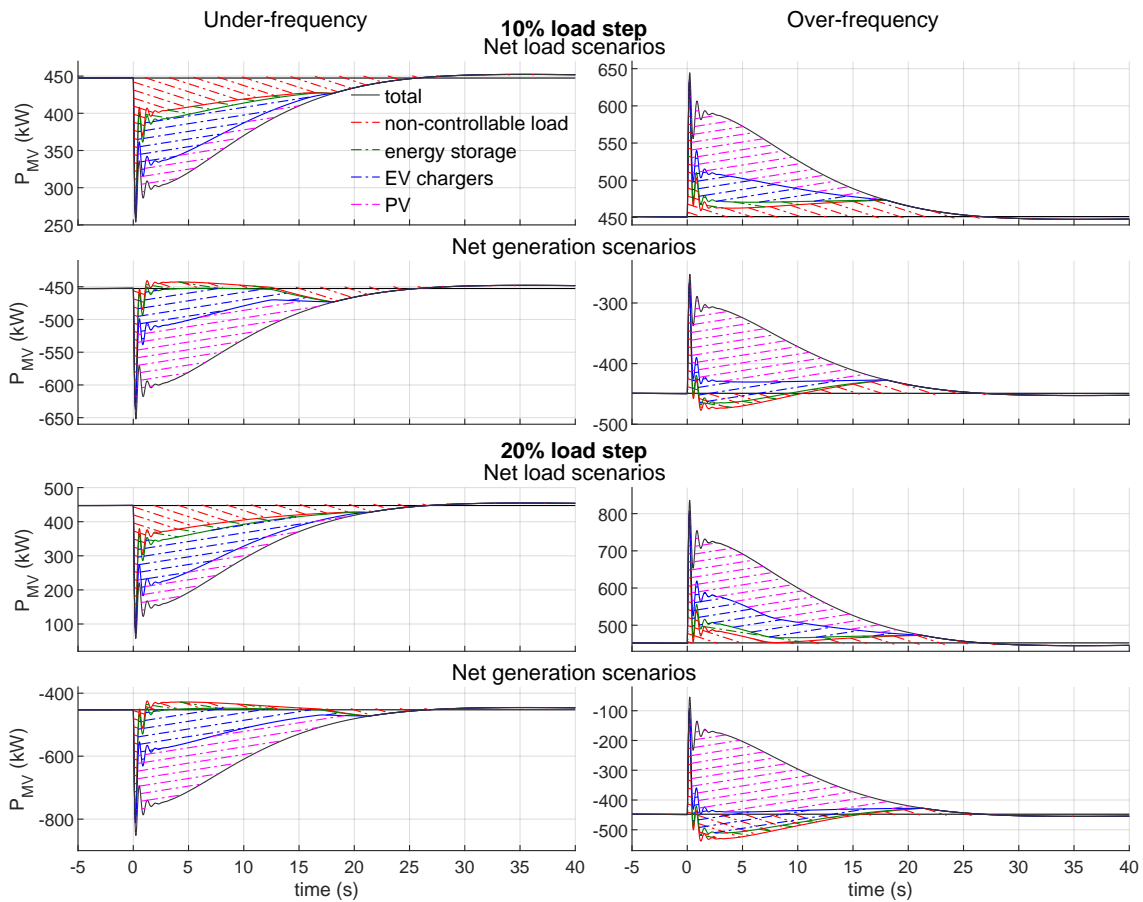


**Figure 5.10:** Active Power response in the ST's MV inverter following frequency disturbances in the upstream AC grid, discriminated by resource type contribution.

Contrasting with the results verified for the grid-following ST (see Figure 5.5), the contribution provided by the combined energy storage capacity (including the ST's local ESS) differs significantly for the grid-forming ST and its hybrid AC/DC grid, since the local ESS can assume a power flow contrary to the total active power reaction observed in the hybrid AC/DC grid, as already shown in Figures 5.7 and 5.8.

### 5.3 Final Remarks - Summary

This chapter describes the case studies adopted and the respective results demonstrating the capability of ST and ST-based hybrid AC/DC grids to provide active power – frequency support to the upstream AC power system:

- It is demonstrated that a grid-following ST is capable to modulate the active power in its local ESS and in the resources available in its hybrid AC/DC grid in order to obtain the active power contribution required for the provision of power – frequency support.
- It is demonstrated that a grid-forming ST can rely solely on its local ESS to provide immediate power – frequency support to the upstream AC grid, but can exploit the active power sensitivity of its hybrid AC/DC grid in order to reduce the power and energy required to the ST's local ESS to perform such task.

The proposed control strategies rely in a set of droop-based controllers incorporated in the ST power conversion stages that are responsible to modulate its electrical variables (DC grids voltage, LV AC grid voltage and frequency) as well as the local ESS active power. Moreover, droop based controllers are also associated to controllable DER available in the hybrid distribution network, making them responsive to electric variables generated by the ST. The load-voltage sensitivity of AC and DC connected loads is also exploited as a possible contribution within the scope of the active power-frequency regulation.

The presented numerical simulation results, illustrated in different operating scenarios of a hybrid AC/DC network connected to a ST and showing the effectiveness of the proposed approaches, provide support to the possibility of further exploiting the proposed solution in ST connected hybrid AC/DC distribution grids regarding the need of providing active power - frequency regulation services to the upstream power grid.

## Chapter 6

# Validation of Advanced Control Strategies for Fault-Ride-Through and Grid Reconfiguration on Hybrid Multi-Microgrids

This chapter presents the evaluation and performance assessment of the advanced control strategies for Fault-Ride-Through (FRT) and grid reconfiguration on Hybrid Multi-Microgrids (HMMG), proposed for Smart-Transformers (ST) and hybrid AC/DC grids supported by them. Numerical simulation results presented in this chapter were obtained using the computational models described in chapter 3 and in sections 4.2 and 4.3. The International System of Units (SI system) is adopted for all developed computational models, but the results presented in this chapter are partially represented using the per-unit system (p.u.) in order to facilitate the interpretation of the presented results.

### 6.1 Case Studies

In order to evaluate the proposed control strategies, the following case studies were considered involving the grid-following and grid-forming ST.

1. A fault disturbance occurs in the MV AC grid between a grid-following ST and the upstream AC power system, without suitable energy storage capacity locally available for the ST.
2. A fault disturbance occurs in the MV AC grid between a grid-forming ST and

the upstream AC power system, with suitable energy storage capacity locally available for the ST.

3. A fault disturbance occurs in the MV AC grid between a grid-forming ST and the upstream AC power system.
4. A fault disturbance occurs in the MV AC grid between a HMMG and the upstream AC power system, followed by the islanding of the HMMG.
5. A LV AC grid integrating a HMMG and operating in ring configuration suffers an interruption of supply in one of the two available feeding points. The disrupted feeding point corresponds to a MV/LV substation based on a low-frequency transformer (LFT) while the feeding point remaining connected is provided by a grid-forming ST. After this occurrence, the LV AC grid is automatically reconfigured to operate in radial configuration, with the ST being responsible to feed it. Afterwards, the MV/LV substation based on a LFT is made available to start operating, and the ST performs the required pre-synchronization of the LV AC grid in order to allow the reconfiguration of the LV AC grid to ring configuration again.

As it was previously discussed, in a grid-following type ST (may include or not an energy storage device), the MV-side power converter operates in a grid following mode. Conversely, a grid-forming type ST includes an energy storage system in the DC bus, allowing the MV side power converter to operate as a grid forming unit.

The case studies 1 and 2 are related to the control strategies presented in subsection 4.2.1, while case study 3 is related to the control strategies presented in Section 4.2.2, and case study 4 relates the control strategies presented in subsections 4.2.1 and 4.2.2, aiming to exploit them in the context of an islanded operation of a HMMG. Case study 5 is related to the control strategies presented in Section 4.3.

### 6.1.1 Case Studies 1, 2 and 3

The computational models for the first, second and third case studies follow the overall representation illustrated in Figure 6.1.

The upstream AC power system is modeled as described in subsection 3.3.1. The hybrid AC/DC grid is constituted by a Hybrid AC/DC Microgrid (HMG) and a MV DC grid, where the HMG is modeled using the radial LV AC and LV DC grids described in subsection 3.3.2, and the MV DC grid is modeled as described in subsection 3.3.3. Grid-following and grid-forming ST units were considered according to the respective models described in sections 3.2 and 4.1. An additional *MV cable* was also considered

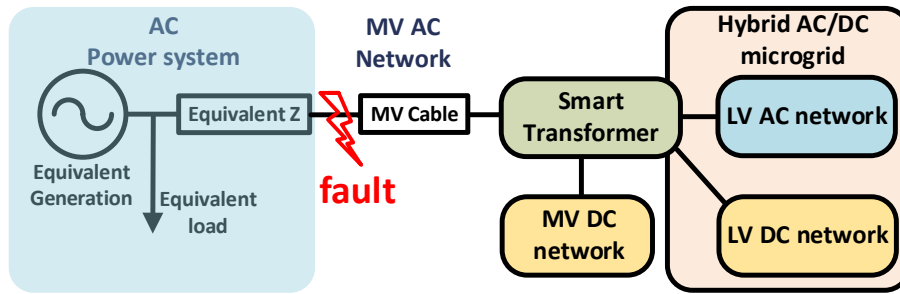


**Figure 6.1:** Overview of the computational models adopted in case studies, 1, 2 and 3 for the evaluation of the advanced control functionalities for FRT provision.

between the ST and the simulated faults, reflecting the electrical distance between the fault location and the point of connection of the ST. In order to simulate the fault disturbances, the *Three-Phase Fault* model available in the library of MATLAB<sup>®</sup>/Simulink<sup>®</sup> software was adopted. This block allows to simulate symmetric and asymmetric faults with a pre-defined time duration and to configure the phase-phase and phase-ground fault impedance.

Regarding the equivalent impedance (*Equivalent Z*) in the upstream AC power system, the considered parameters are presented in Table 6.2. A single equivalent impedance scenario was considered for case studies 1 and 2, but two scenarios are considered for case study 3. The purpose of this distinction is to evaluate the influence of frequency excursions occurring in the upstream AC power system (resulting from the simulated fault disturbances) in the performance of the FRT mechanism and operation of the grid-forming ST following a fault disturbance. Contrarily to the grid-following ST in case studies 1 e 2, the grid-forming ST does not resort to frequency tracking mechanisms (such as PPL) to synchronize with the upstream AC power system, relying instead on its  $f(\Delta P_{MV})$  droop controller, sensitive to the active power exchanged with the upstream AC power system. As a result, the grid-forming ST is more sensitive to frequency excursions in the upstream AC power system specially if facing severe voltage sags originated by faults disturbances in the upstream AC power system. Different values for the equivalent impedance result in different power unbalances in the upstream AC power systems (since the short-circuit power changes), and thus, in different frequency excursions in the upstream AC power system.

As a result, a total of 30 fault disturbance scenarios were evaluated for case studies 1 and 2, while for case study 3 a total of 60 fault disturbance scenarios were evaluated, resulting from all combinations possible from the parameters presented in Tables 6.1 and 6.2. The large number of considered operating scenarios, network and fault conditions, constitutes a large-scale sensitivity study with respect to the proposed

solutions, being the associated results presented and discussed in this chapter.

**Table 6.1:** Simulated fault disturbances: main parameters

<b>R phase-phase / phase-ground *</b>	<b>Fault type</b>	<b>Time duration</b>
0.02Ω / 0.001Ω	Phase-ground	0.2s
0.06Ω / 0.001Ω	Phase-phase	0.5s
0.2Ω / 0.001Ω	Three-phase	
0.5Ω / 0.001Ω		
1.5Ω / 0.001Ω		

*\* phase-ground impedance applies only to ground faults*

**Table 6.2:** Equivalent impedance: main parameters

<b>Case study</b>	<b>Equivalent Z</b>
1 an 2	0.02 + j0.23 Ω
3	0.4 + j0.94 Ω
	0.02 + j0.23 Ω

Regarding the parameterization of the ST and test grids, only the most relevant parameters are presented in this chapter. Its complete parameterization can be found in Appendix A. The most relevant parameters for the ST are summarized in Table 6.3. The results in p.u. presented in section 6.2 use the nominal values presented in Table 6.3 as base values. Table 6.4 summarizes the relevant parameters for the upstream AC power system.

**Table 6.3:** Smart-Transformer: main parameters

Nominal Power	1 MVA
Nominal MV AC Voltage (ph-ph)	15000 V (RMS)
Nominal MV DC link Voltage	27000 V
Nominal LV DC link Voltage	720 V
Nominal LV AC Voltage (ph-n)	230 V (RMS)
Nominal frequency (MV and LV inverters)	50 Hz

**Table 6.4:** Upstream AC power system: main parameters

Generation capacity	1 GW
Total load	600MW/200Mvar
Equivalent system inertia (H)	2 s
Equivalent impedance (seen from MV connection)	0.04 + j0.63 Ω

The most relevant parameters for the ST-based hybrid AC/DC grid are presented in Table 6.5 for the case studies 1 and 2 and in Table 6.6 for the case study 3. Positive values

correspond to consumed power, and negative values correspond to injected/generated power. The steady-state values presented in Tables 6.5 and 6.6 were obtained by applying multiplication factors to the load and generation profiles presented for the base test grids parameterized in Appendix A in order to obtain the desired net-load and net-generation scenarios.

**Table 6.5:** Steady-state power and operation limits in the hybrid AC/DC grid based on the grid-following ST for case studies 1 and 2

fault type *	non-controllable load	PV generation	EV charging	Energy Storage
Net-load scenario				
LV AC network				
p-g	202 kW / 64 kvar	-30 kW (-210 – 0)	23 kW (0 – 86)	15 kW (± 42)
p-p		-45 kW (-210 – 0)		
p-p-p		-75 kW (-210 – 0)		
LV DC network				
p-g	105 kW	-60 kW (-420 – 0)	105 kW (0 – 140)	37 kW (± 84)
p-p		-90 kW (-420 – 0)		
p-p-p		-150 kW (-420 – 0)		
MV DC network				
p-g	175 kW	-200 kW (-1400 – 0)	525 kW (0 – 525)	–
p-p		-300 kW (-1400 – 0)		
p-p-p		-500 kW (-1400 – 0)		
Total hybrid AC/DC grid				
p-g	482 kW	-290 kW	653 kW	52 kW
p-p		-435 kW		
p-p-p		-725 kW		
Net-generation scenario				
LV AC network				
p-g	144 kW / 64 kvar	-180 kW (-210 – 0)	17 kW (0 – 86)	11 kW (± 42)
p-p	173 kW / 64 kvar		20 kW (0 – 86)	13 kW (± 42)
p-p-p	202 kW / 64 kvar		23 kW (0 – 86)	15 kW (± 42)
LV DC network				
p-g	75 kW	-360 kW (-420 – 0)	75 kW (0 – 140)	27 kW (± 84)
p-p	90 kW		90 kW (0 – 140)	32 kW (± 84)
p-p-p	105 kW		105 kW (0 – 140)	37 kW (± 84)
MV DC network				
p-g	125 kW	-1200 kW (-1400 – 0)	375 kW (0 – 525)	–
p-p	150kW		450 kW (0 – 525)	
p-p-p	175 kW		525 kW (0 – 525)	
Total hybrid AC/DC grid				
p-g	344 kW	-1740 kW	467 kW	38 kW
p-p	413 kW		560 kW	45 kW
p-p-p	482 kW		653kW	52 kW

\* p-g: phase-ground; p-p: phase-phase; p-p-p: three-phase;

As shown in Table 6.5, different steady-state power profiles were adopted according to the fault type for case studies 1 and 2. The purpose was to identify different

**Table 6.6:** Steady-state power and operation limits in the ST-based hybrid AC/DC grid for case study 3

non-controllable load	PV generation	EV charging	Energy Storage
<b>Net-load scenario</b>			
LV AC network			
202 kW / 64 kvar	-75 kW (-210 – 0)	23 kW (0 – 86)	15 kW ( $\pm 42$ )
LV DC network			
105 kW	-150 kW (-420 – 0)	105 kW (0 – 140)	37 kW ( $\pm 84$ )
MV DC network			
175 kW	-500 kW (-1400 – 0)	525 kW (0 – 525)	–
local ESS in ST			
–	–	–	400 kW *
Total hybrid AC/DC grid			
<b>482 kW</b>	<b>-725 kW</b>	<b>653 kW</b>	<b>52 kW</b>
<b>Net-generation scenario</b>			
LV AC network			
202 kW / 64 kvar	-180 kW (-210 – 0)	23 kW (0 – 86)	15 kW ( $\pm 42$ )
LV DC network			
105 kW	-360 kW (-420 – 0)	105 kW (0 – 140)	37 kW ( $\pm 84$ )
MV DC network			
175 kW	-1200 kW (-1400 – 0)	525 kW (0 – 525)	–
local ESS in ST			
–	–	–	-400kW *
Total hybrid AC/DC grid			
<b>482 kW</b>	<b>-1740 kW</b>	<b>653 kW</b>	<b>52 kW</b>

\* Imposed on the ST local ESS by the  $f(\Delta P_{MV})$  droop offset.

operating condition that, for each fault type, lead the MV inverter of the ST to reach the maximum current limits, while in others the current in the MV inverter is kept below the maximum value. This diverse set of scenarios and faults is intended to demonstrate the effectiveness of the proposed approaches, namely in terms of its actuation only if the currents limits in the MV inverter are in cause. Given this, the base steady-state PV generation was multiplied by 6 for net-generation scenarios. For net-load scenarios, the base steady-state PV generation was multiplied by 1 for phase-ground fault scenarios, 1.5 for phase-phase fault scenarios, and 2.5 for three-phase fault scenarios. Nevertheless, the installed PV generation capacity was multiplied by 7 in all net-load and net-generation scenarios. Regarding the base power profile for the remaining DER and non-controllable load, is was multiplied by 3.5 for net-load scenarios, while for net-generation scenarios it was multiplied by 2.5 for phase-ground fault scenarios, 3 for phase-phase fault scenarios, and 3.5 for three-phase fault



scenarios. The impedance of the cable sections in the modeled test grids, whose base parameterization is presented in Appendix A, was divided by the multiplication factors adopted for the non-controllable load and DER units excluding PV generation. Worth to mention that the ST's local ESS is not represented in Table 6.5 because the local ESS is considered non existent in case study 1, whereas for case study 2 the local ESS is considered to have its steady-state active power at zero.

Regarding the case study 3, the steady-state values presented in Table 6.6 were also obtained by applying multiplication factors to the load and generation profiles presented for the base test grids parameterized in Appendix A, but no different steady-state power profiles were adopted according to the fault type considered. Such differentiation is not relevant in this case study because the MV inverter of the grid-forming ST resorts to the ST's local ESS to react to the fault disturbance in the upstream AC power system independently of the active power response occurring in the ST-based hybrid AC/DC grid, as illustrated by the chain of events presented in Figure 4.18 (subsection 4.2.2.2). Moreover, since grid-forming ST are more sensitive to the voltage levels in the upstream MV grid in comparison to what happens with a grid-following ST, any significant voltage sag at the ST connection point with the upstream AC grid will inherently lead to over-current phenomena in the ST's MV inverter, with the steady-state active power in the ST's MV inverter being less relevant in this regard. Given this, the base steady-state PV generation was multiplied by 2.5 and 6 for net-load and net-generation scenarios respectively, and the base power profile for the remaining DER and non-controllable load was multiplied by 3.5 in both net-load and net-generation scenarios. The installed PV generation capacity was multiplied by 7 in both net-load and net-generation scenarios. Nevertheless, the steady-state active power in the ST's MV inverter was adjusted by applying an offset to the  $f(\Delta P_{MV})$  droop controller in such a way that the steady-state active power exchanged by the MV inverter with the upstream MV AC grid approximates the net-power in the ST-based Hybrid AC/DC grid. This power adjustment intends to consider a more realistic operation scenario for the ST, where most of the net-power in the ST-based Hybrid AC/DC grid is transferred to the upstream MV AC grid.

Yet for case study 1, the actuation of the FRT mechanism jointly with the power-frequency support mechanism evaluated in chapter 5 is also analyzed, in order to observe the influence of the power-frequency support mechanism on the performance of the FRT provision. For this case, the droop-based controllers embedded in the ST and controllable Distributed Energy Resources (DER) are parameterized as described in Appendix A. For case study 3, this additional evaluation is irrelevant given the

shielding effect provided by the ST's local ESS.

### 6.1.2 Case Study 4

The computational models for this case study are based on the HMMG test grid described in subsection 3.3.4 (illustrated in Figure 3.22), properly adapted to simulate a set of fault disturbances intended to evaluate the effectiveness of the FRT mechanisms proposed for grid-following and grid-forming ST performing together. The overall representation of the resulting HMMG is illustrated in Figure 6.2. The grid-following and grid-forming ST were modeled according to the respective models described in sections 3.2 and 4.1. The LV AC grid connected to the grid-forming ST and to the LFT in bus 3 is exploited in radial configuration, with the LFT disconnected. The circuit breaker responsible to island and reconnect the HMMG to the upstream AC power system (*Breaker HMMG*) and the circuit breaker after the LFT connected to bus 3 (*Breaker*) are modeled using the *Three-Phase Breaker* model available in the library of MATLAB®/Simulink® software.

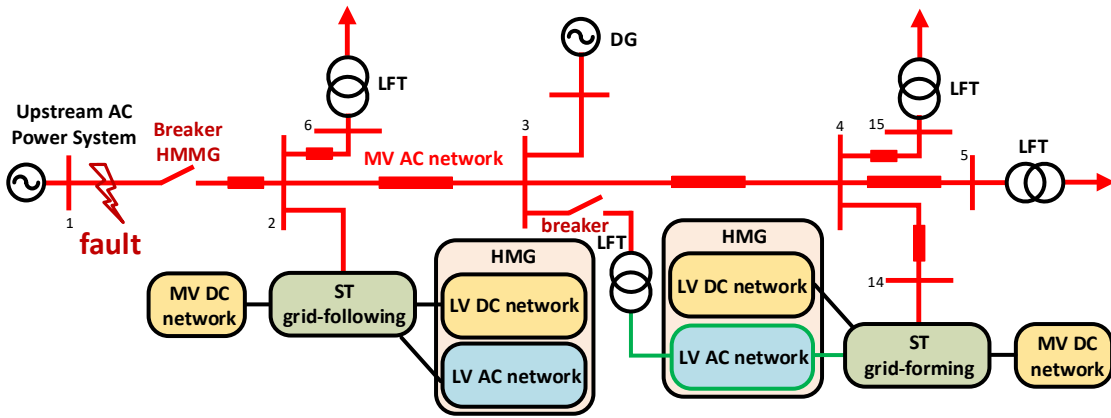


**Figure 6.2:** Overview of the computational models adopted in case study 4 for the evaluation of the advanced control functionalities for FRT provision.

In order to simulate the fault disturbances, the *Three-Phase Fault* model available in the library of MATLAB®/Simulink® software was adopted. This block allows to simulate symmetric and asymmetric faults with a pre-defined time duration and to configure the phase-phase and phase-ground fault impedance. In this case study, only the most severe fault disturbances considered in subsection 6.1.1 (presented in Table 6.1) are adopted (fault resistance of  $0.02\Omega$ ). This results on a total of 6 fault disturbance scenarios to be evaluated, resulting from all combinations possible from the parameters presented in Table 6.7. The parameterization of the ST and upstream AC power system follows the same assumptions adopted in subsection 6.1.1 (Tables 6.3 and 6.4). The

results in p.u. presented in section 6.2 use the nominal values presented in Table 6.3 as base values. Regarding the parameterization of the ST-based hybrid AC/DC grids, identical configurations were adopted for both grid-forming and grid-following ST-based grids. The most relevant parameters are presented in Table 6.8. Positive values correspond to consumed power, and negative values correspond to injected/generated power.

**Table 6.7:** Simulated fault disturbances: main parameters

Fault type	R phase-phase / phase-ground *	Time duration
Phase-ground	$0.02\Omega / 0.001\Omega$	0.2s
Phase-phase		0.5s
Three-phase		

\* phase-ground impedance applies only to ground faults

**Table 6.8:** Steady-state power and operation limits in a single ST-based hybrid AC/DC grid for case study 4

non-controllable load	PV generation	EV charging	Energy Storage
<b>Net-load scenario</b>			
LV AC network			
202 kW / 64 kvar	-75 kW (-210 – 0)	23 kW (0 – 86)	15 kW ( $\pm 42$ )
LV DC network			
105 kW	-150 kW (-420 – 0)	105 kW (0 – 140)	37 kW ( $\pm 84$ )
MV DC network			
175 kW	-500 kW (-1400 – 0)	525 kW (0 – 525)	–
local ESS in grid-forming ST			
–	–	–	400 kW *
Total hybrid AC/DC grid			
<b>482 kW</b>	<b>-725 kW</b>	<b>653 kW</b>	<b>52 kW</b>
<b>Net-generation scenario</b>			
LV AC network			
202 kW / 64 kvar	-180 kW (-210 – 0)	23 kW (0 – 86)	15 kW ( $\pm 42$ )
LV DC network			
105 kW	-360 kW (-420 – 0)	105 kW (0 – 140)	37 kW ( $\pm 84$ )
MV DC network			
175 kW	-1200 kW (-1400 – 0)	525 kW (0 – 525)	–
local ESS in grid-forming ST			
–	–	–	-400kW *
Total hybrid AC/DC grid			
<b>482 kW</b>	<b>-1740 kW</b>	<b>653 kW</b>	<b>52 kW</b>

\* Grid-forming ST only. Imposed on the ST local ESS by the  $f(\Delta P_{MV})$  droop offset.

The steady-state values presented in Table 6.8 were obtained by applying mul-

tiplication factors to the load and generation profiles presented for the base test grids parameterized in Appendix A in order to obtain the desired net-load and net-generation scenarios. The base steady-state PV generation was multiplied by 2.5 and 6 for net-load and net-generation scenarios respectively, and the base power profile for the remaining DER and non-controllable load was multiplied by 3.5 in both net-load and net-generation scenarios. The installed PV generation capacity was multiplied by 7 in both net-load and net-generation scenarios. Nevertheless, for the grid-forming ST, the steady-state active power in the ST's MV inverter was adjusted by applying an offset to the  $f(\Delta P_{MV})$  droop controller in such a way that the steady-state active power exchanged by the MV inverter with the upstream MV AC grid approximates the net-power in the ST-based Hybrid AC/DC grid. This power adjustment aims a more realistic operation scenario for the grid-forming ST where most of the net-power in the ST-based Hybrid AC/DC grid is transferred to the upstream MV AC grid.

Regarding the MV AC grid and remaining elements constituting the HMMG, the main characteristics are presented in Table 6.9. Net-load and net-generation scenarios are presented only for the bus bars involving the ST, where such scenarios were considered for their respective hybrid AC/DC grids.

**Table 6.9:** Main characteristics of the HMMG considered for case study 4

Buses		Lines		
Bus number	Load	Bus in	Bus out	Line Z
6	350 + j355 kVA	1	2	1.35 + j1.1 $\Omega$
DG	-300 + j10 kVA	2	6	2.55 + j1.43 $\Omega$
15	70 + j71 kVA	2	3	1.17 + j0.95 $\Omega$
5	44 + j45 kVA	3	4	0.84 + j0.69 $\Omega$
3 (LFT)	0 kVA	4	15	1.19 + j0.67 $\Omega$
<b>Net-load scenario</b>		4	14	2.23 + j1.25 $\Omega$
2 (ST)	462 kVA	4	5	1.53 + j0.85 $\Omega$
14 (ST)	400 - j25 kVA			
<b>Net-generation scenario</b>				
2 (ST)	-533 kVA			
14 (ST)	-400 + j60 kVA			

Regarding the configuration of the grid-following and grid-forming ST incorporated in the HMMG, this case study is also based on assumptions considered in case studies 1 and 3 described in subsection 6.1.1. The objective is to allow both ST to provide FRT during fault disturbances, but also power-frequency support specially during the islanded operation of the HMMG. The grid-forming ST operates with its FRT mechanism activated, with  $f(\Delta P_{MV})$  droop controller embedded in the controller of

the ST' MV inverter responsible for the provision of power-frequency support. The grid-following ST operates with its FRT mechanism activated but also with the power-frequency support mechanism activated (but with no local ESS available) in order to participate in the frequency regulation of the islanded HMMG.

### 6.1.3 Case Study 5

The computational models for this case study are based on the HMMG test grid described in subsection 3.3.4 (illustrated in Figure 3.22), which was properly adapted to evaluate the proposed grid reconfiguration mechanism based on ST described in section 4.3. The resulting test grid is illustrated in Figure 6.3.

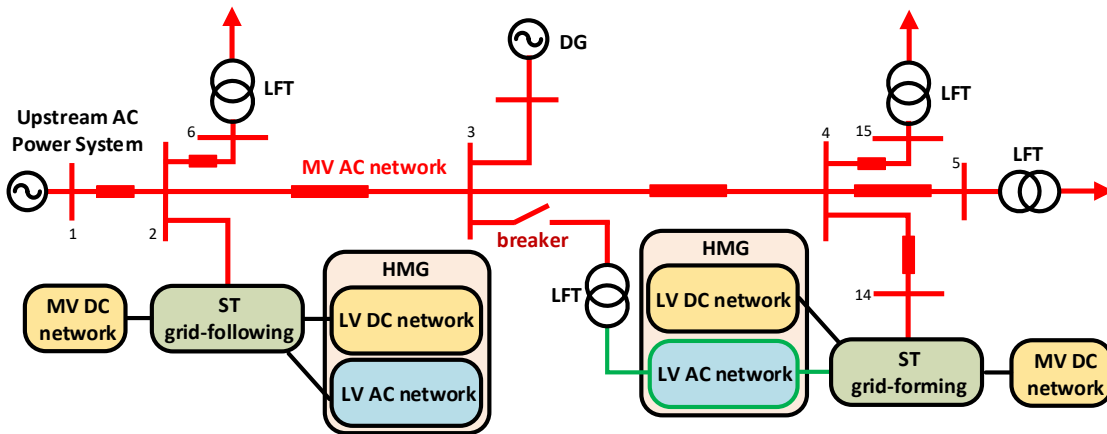


**Figure 6.3:** Overview of the computational models adopted in case study 5 for the evaluation of the grid reconfiguration mechanism.

A circuit breaker is added to the MV side of the LFT tied to bus bar 3 in order to enable the reconfiguration of the LV AC grid tied to the aforementioned LFT and the grid-forming ST between radial and ring configurations. By opening the circuit breaker, the LV AC grid tied to the LFT is automatically reconfigured to radial configuration, with a single feeding point maintained by the grid-forming ST. Afterwards, the MV/LV substation based on a LFT is considered available to start operating again. Then, the ST performs the required pre-synchronization of the LV AC grid in order to allow the reconfiguration of the LV AC grid to ring configuration again by closing the circuit breaker.

The grid-following and grid-forming ST were modeled according to the respective models described in sections 3.2 and 4.1. The parameterization of the HMMG (including the ST) follows the assumptions adopted in subsection 6.1.2 and expressed in Tables 6.3, 6.4, 6.8 and 6.9. The reconfiguration mechanism is evaluated for net-load

and net-generation scenarios according to the data presented in Tables 6.8 and 6.9. The LFT connected to the bus bar 3 is parameterized according to Table 6.10.

**Table 6.10:** MV/LV substation based on a low-frequency transformer: main parameters

Nominal Power	1 MVA
Primary nominal voltage (ph-ph)	15000 V (RMS)
Secondary nominal voltage (ph-n)	230 V (RMS)
Nominal frequency	50 Hz
Vector group	Dy11

## 6.2 Simulation Results

### 6.2.1 Case Studies 1 and 2

The results related to the evaluation of the case studies 1 and 2 are presented in this subsection. These case studies are presented together in order to allow a better understanding how the availability of a local ESS in the grid-following ST impacts the operation of the FRT provision mechanism over the ST-based hybrid AC/DC grid. A third set of results is also presented for case study 1 considering the simultaneous operation of the FRT mechanism with the power–frequency support mechanism already evaluated in chapter 5, but still with no local ESS available. In order to facilitate the reading of the presented results, the different sets of results are identified using the labels *No local ESS* for case study 1, *With local ESS* for case study 2, and *FRT plus frequency support* for the case study 1 including the power–frequency support mechanism. The results presented in p.u. use the nominal voltages and frequency presented in Table 6.3 as base values. In the presented results, the start of the fault disturbance occurs at  $time (s) = 0$ , and positive values for the active power correspond to consumed power whereas negative values correspond to injected/generated active power.

The profiles of the voltage disturbances following the fault disturbances described in Table 6.1 are illustrated in Figures 6.4 and 6.5, for fault disturbances with a duration of 0.2 and 0.5 seconds respectively. The profile of the frequency disturbances following the fault disturbances described in Table 6.1 are illustrated in Figure 6.6, for fault disturbances with a duration of 0.2 and 0.5 seconds. The time evolution of the frequencies depicted in Figure 6.6 are based on the equivalent generator rotational speed.

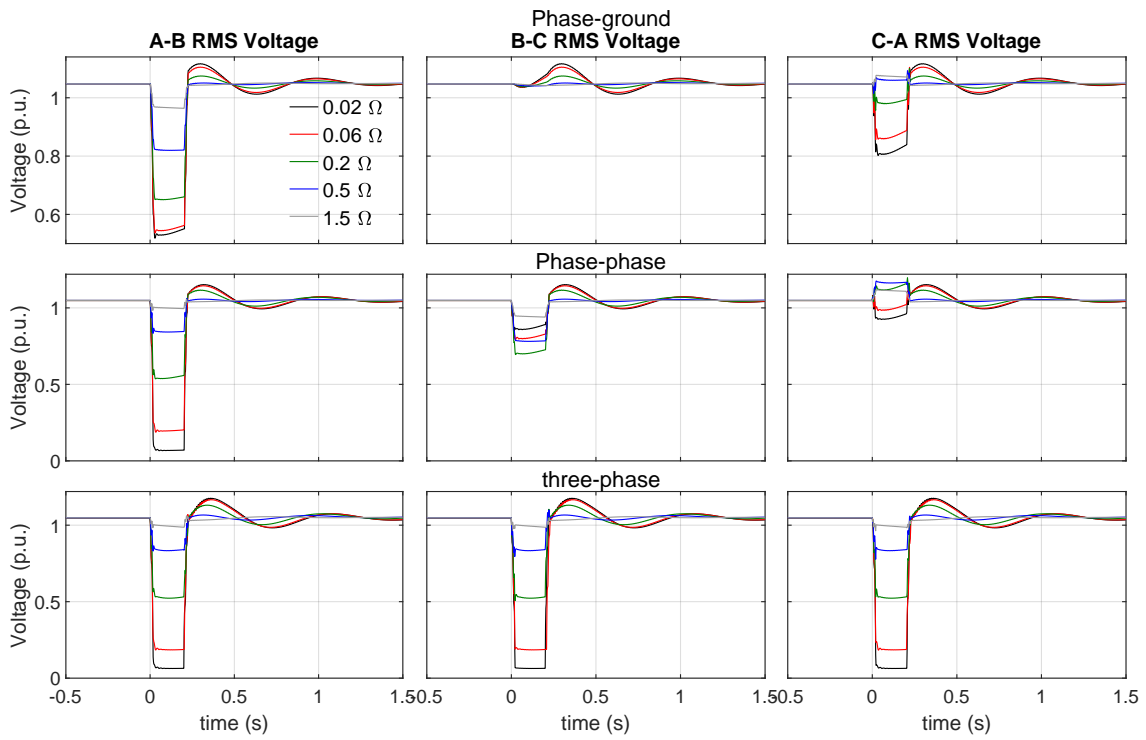


**Figure 6.4:** Voltage disturbances observed at ST's MV inverter resulting from fault disturbances in the upstream AC power system, for several fault impedances with a time duration of 0.2 s.

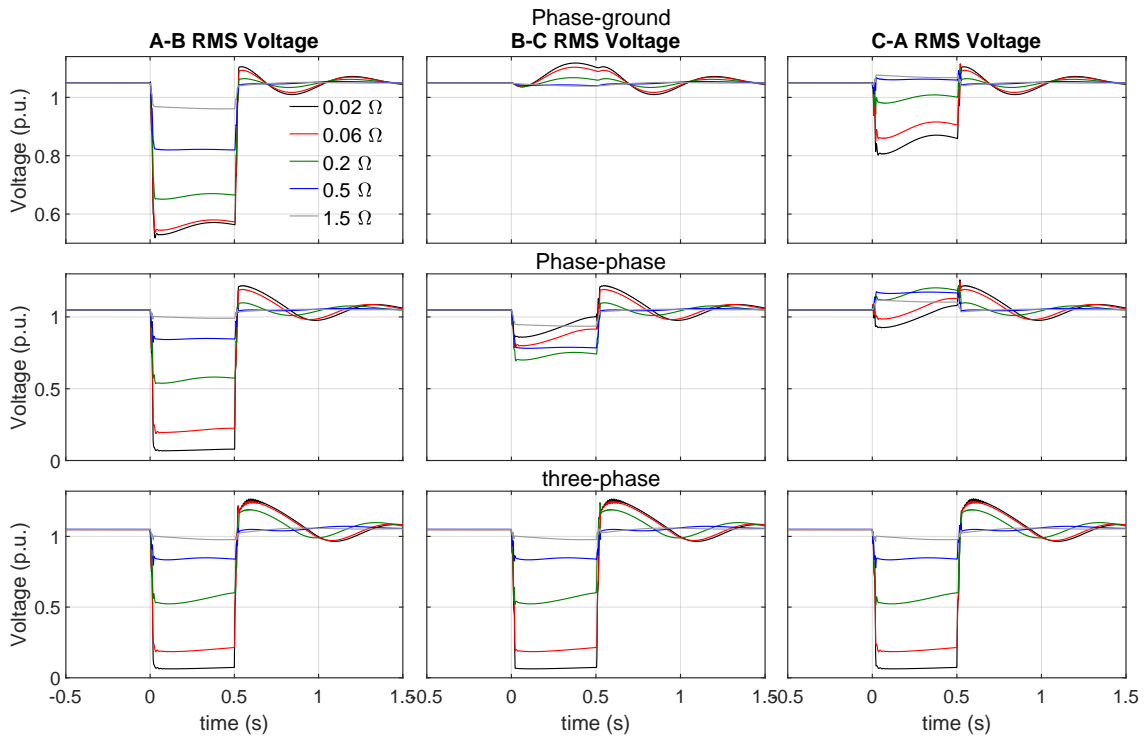


**Figure 6.5:** Voltage disturbances observed at ST's MV inverter resulting from fault disturbances in the upstream AC power system, for several fault impedances with a time duration of 0.5 s.



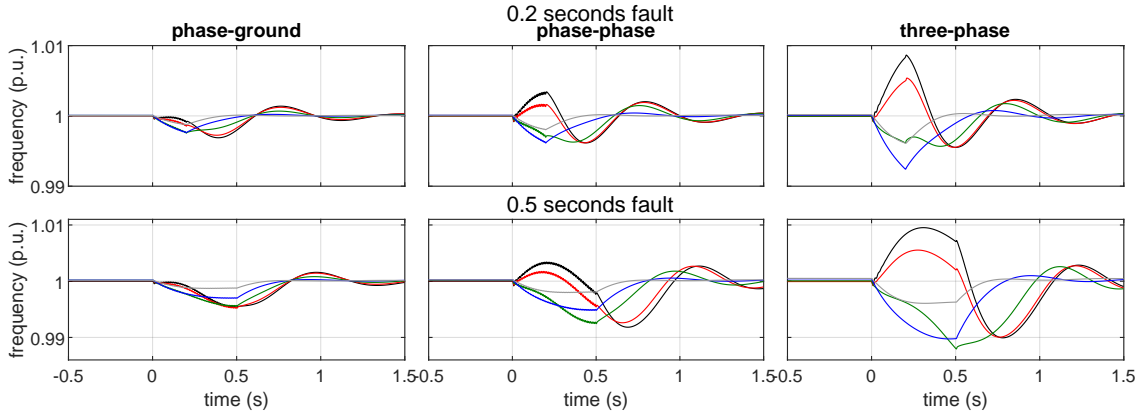


**Figure 6.6:** Frequency disturbances observed at ST's MV inverter resulting from fault disturbances in the upstream AC power system, for several fault impedances with a time duration of 0.2 s and 0.5 s.

The presented voltage and frequency profiles practically do not change as a result of the different operation regimes considered for the ST and its hybrid AC/DC grid, given that the ST-based hybrid is much smaller than the upstream AC system to which it connects to (1MVA maximum in a 1GW power system). It is also possible to observe that frequency disturbances are generally wider and more prolonged in time for the more prolonged fault disturbances, as expected. As a result of the simulated fault disturbances, the FRT mechanism incorporated in the grid-following ST is triggered whenever the ST is not capable to preserve the power balance in its MV DC bus without violating the maximum current limits of its MV inverter, except if the ST has a suitable local energy storage capacity at its disposal. The main resources exploited by the FRT mechanism to remove any excess net-load or net-generation from the ST-based hybrid AC/DC compromising the active power balance in the ST are the exploitation of the load-voltage and load-frequency sensitivities in the ST-based hybrid AC/DC grid (by modulating its voltages and frequency profiles) and a dump-load (used only for tackle excess net-generation).

The impact of the FRT mechanism over the voltages and frequency profiles in the ST-based hybrid AC/DC grid for case studies 1 and 2 and considering fault disturbances with time duration of 0.5 seconds are illustrated from Figures 6.7 to 6.10. In order to not overburden this chapter, the results related to the fault disturbances with time duration of 0.2 seconds are shown in Appendix B, from Figures B.2 to B.5. The results related to the fault disturbances with time duration of 0.5 seconds are presented in this chapter since they represent the most extreme scenarios, being thus the most relevant regarding the evaluation of the effectiveness of the proposed FRT mechanism.

The results related to the modulation of the voltage levels in the ST-based hy-



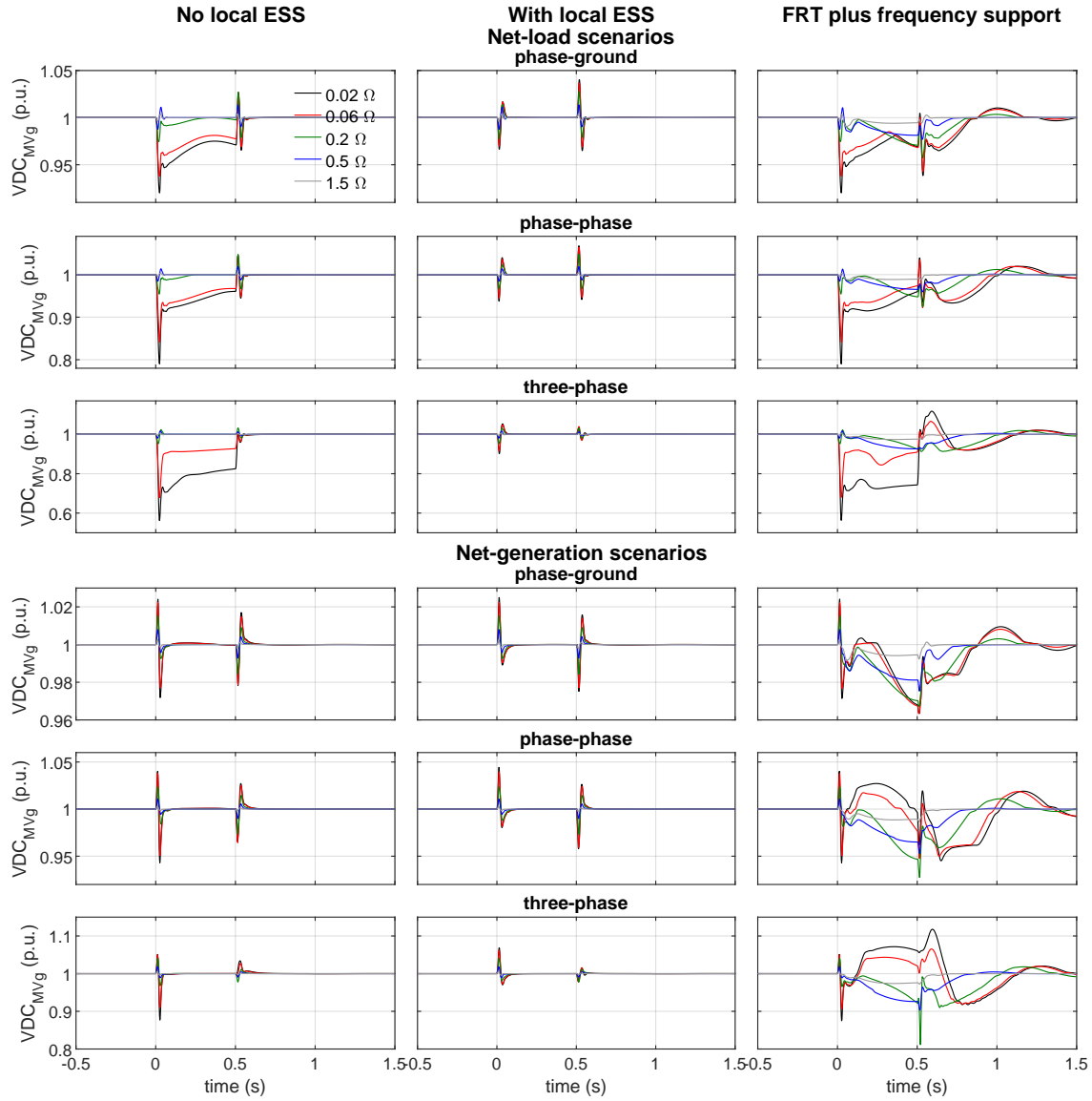


**Figure 6.7:** DC voltage in the ST-based MV DC grid for several fault impedances with a time duration of 0.5 s.

brid AC/DC grid following a fault disturbance in the upstream AC power system are presented in Figures 6.7 and B.2 for the voltage in the ST-based MV DC grid ( $VDC_{MVg}$ ), Figures 6.8 and B.3 for the voltage in the ST-based LV DC grid ( $VDC_{LVg}$ ), and Figures 6.9 and B.4 for the voltage in the ST-based LV AC grid ( $VAC_{LVg}$ ), for fault disturbances with time duration of 0.5 and 0.2 seconds. As expected,  $VDC_{MVg}$ ,  $VDC_{LVg}$  and  $VAC_{LVg}$  are modulated only in case study 1 for net-load scenarios where the current limits in the ST's MV inverter are reached (as shown in Figures 6.20 and 6.21 to be described later), remaining  $VDC_{MVg}$ ,  $VDC_{LVg}$  and  $VAC_{LVg}$  around their nominal values otherwise. During net-generation scenarios, yet in case study 1, the FRT mechanism activates the dump-load which is capable to dissipate excess net-generation which

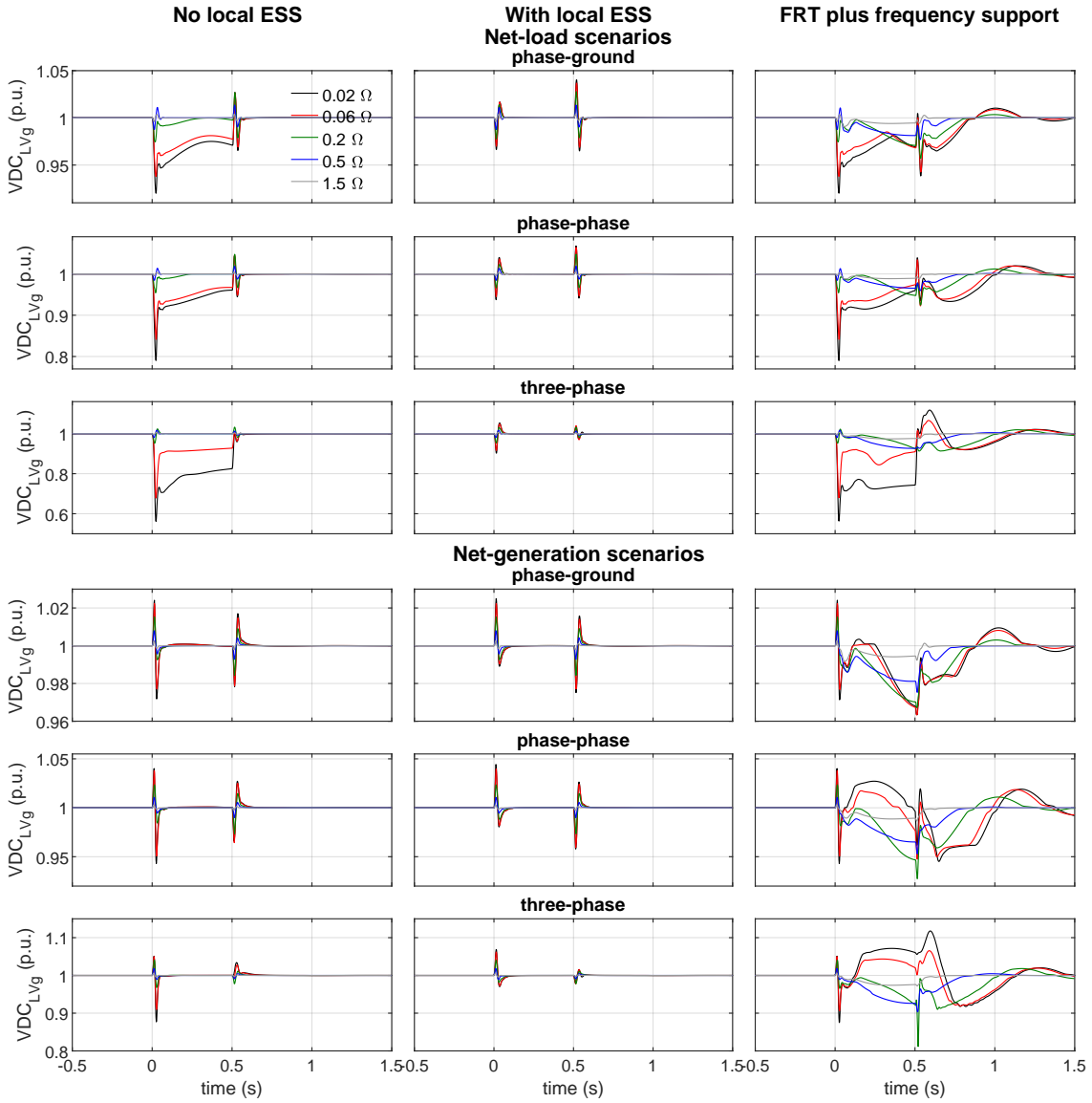


**Figure 6.8:** DC voltage in the ST-based LV DC grid for several fault impedances with a time duration of 0.5 s.

the ST cannot deliver to the upstream AC power system. The actuation of the dump-load removes the necessity to modulate the voltage levels in the ST-based sub-grids, thus minimizing the resulting impact in the normal operation of the ST-based hybrid AD/DC grid by the FRT mechanism. Regarding case study 2, the FRT mechanism does not actuate due to the presence of the local ESS, with  $VDC_{MVg}$ ,  $VDC_{LVg}$  and  $VAC_{LVg}$  remaining always around their nominal values. The brief transients observed for the case study 2 are not related to the FRT mechanism, resulting instead from the disturbance of the power balance in the ST originated by the surge and extinction of the fault disturbances occurring in the upstream AC grid. Such transients are rapidly eliminated by the DC voltage controller of the ST's MV inverter. Regarding the brief

transients observed for the net-generation scenarios in case study 1, the phenomena aforementioned for case study 2 adds to the response delay of the dump-load, whose control is performed by the FRT mechanism.

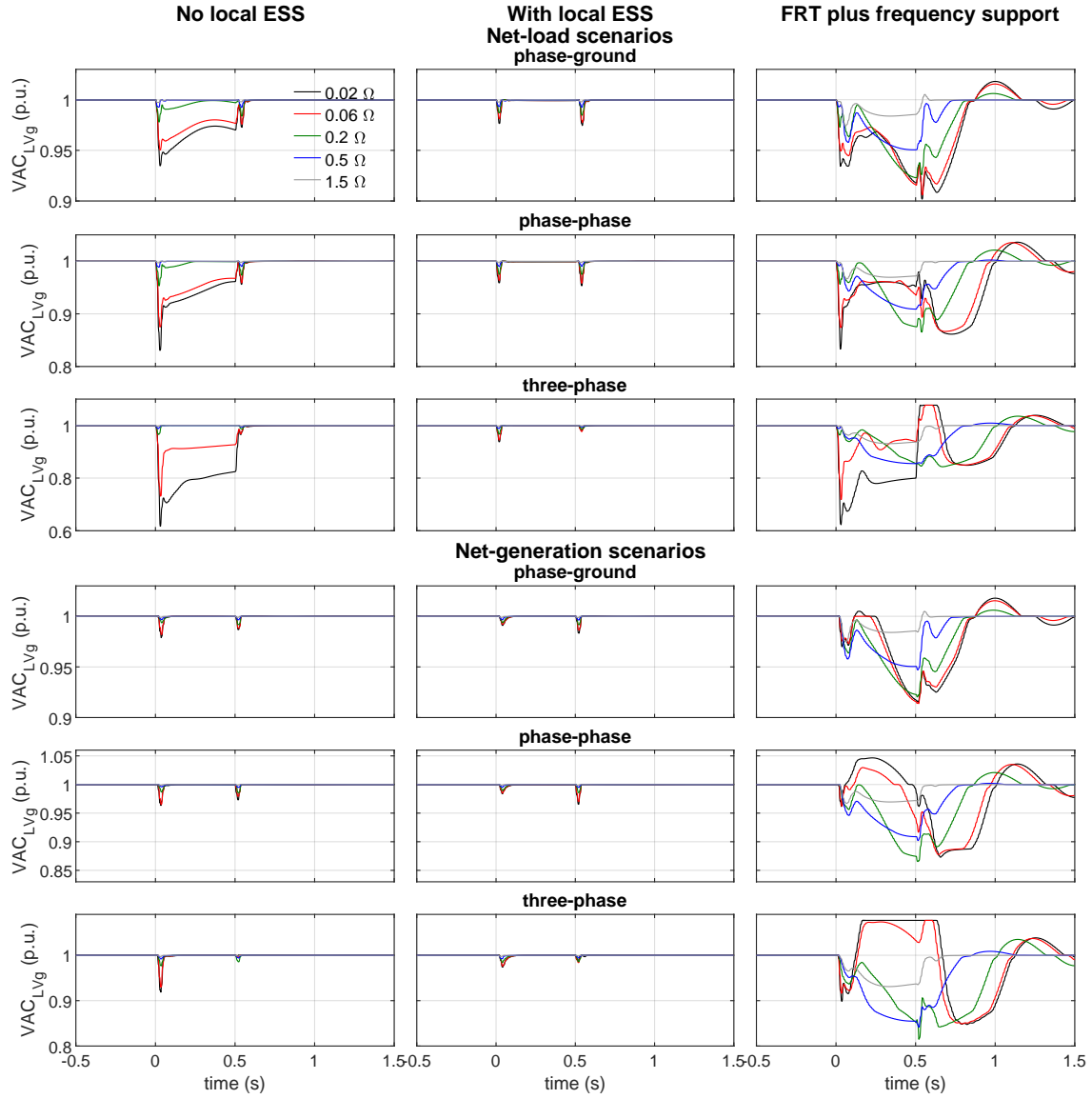


**Figure 6.9:** AC voltage in the ST-based LV AC grid for several fault impedances with a time duration of 0.5 s.

A detail worth to mention is the progressive increase of  $VDC_{MVg}$ ,  $VDC_{LVg}$  and  $VAC_{LVg}$  observed in several fault disturbance scenarios following the fault disturbance, as illustrated from Figures 6.7 to 6.9. It is possible to infer that the level of power curtailment in the ST-based hybrid AC/DC grid starts to reduce even before the fault become extinct. This results from an increase in the voltage levels in the power system as a result of the actuation of the voltage regulator of the upstream equivalent generator, in an effort to mitigate the voltage sag originated in the power system by the the fault

disturbance. As a consequence of the general increase in voltage levels, more active power can transit through the ST's MV inverter, resulting in a progressive reduction of the active power needing to be curtailed, and consequently, in a reduction of the intervention of the FRT mechanism over the voltage levels in the ST-based sub-grids.

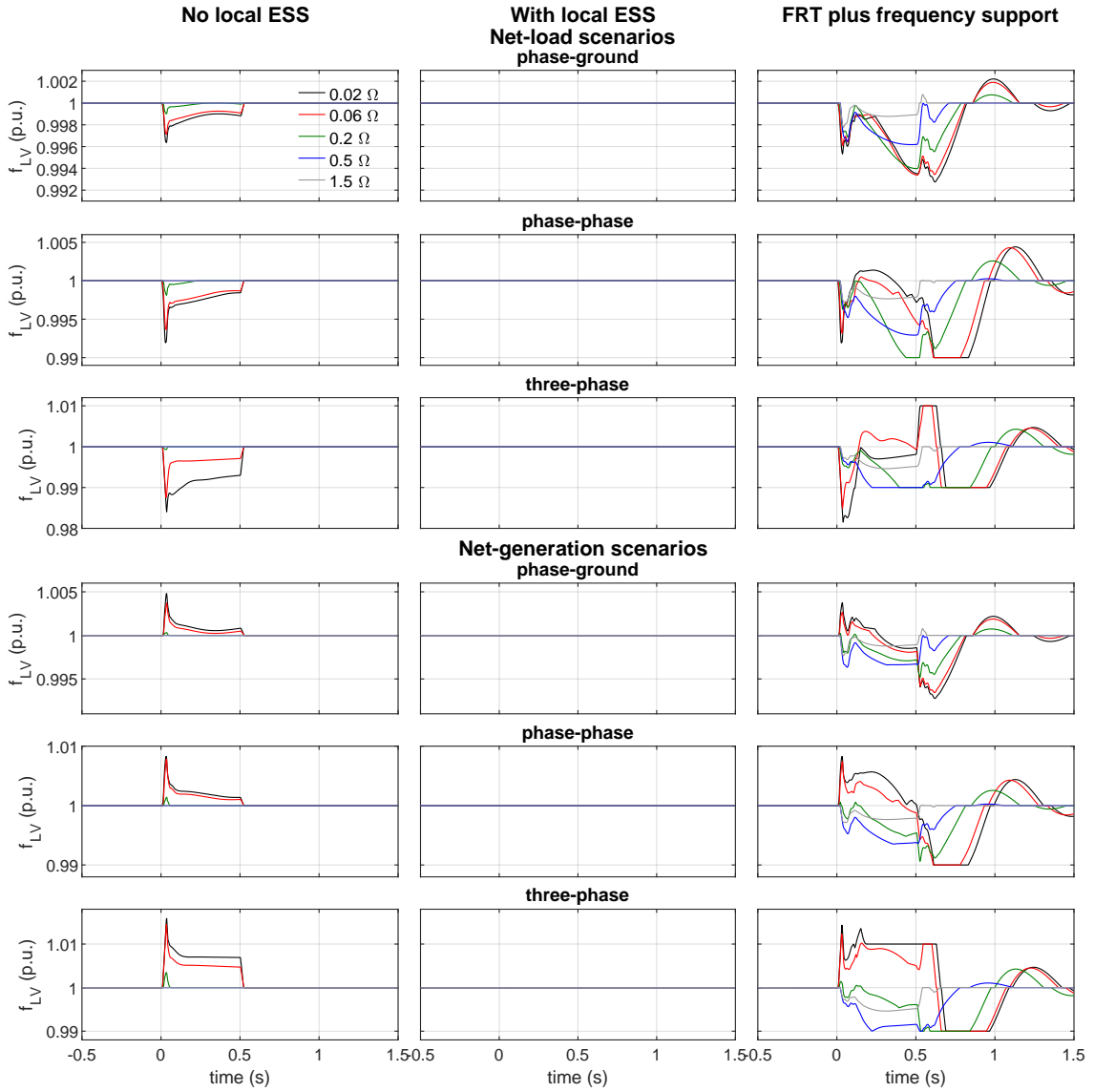


**Figure 6.10:** Frequency in the ST-based LV AC grid for several fault impedances with time duration of 0.5 s.

Regarding the frequency modulation in the LV AC sub-grid ( $f_{LV}$ ), it takes place in case study 1 for both net-load and net-generation scenarios, as shown in Figures 6.10 and B.5. The absence of frequency transients in case study 2 and for several fault disturbances in case study 1 (where the FRT mechanism does not need to intervene) is expected since  $f_{LV}$  is immune to the transient power unbalances affecting the ST (resulting from fault disturbances in the upstream AC power system). Indeed,  $f_{LV}$

is solely affected by the FRT mechanism (case study 1) and by the power–frequency support mechanism, as observed in Figures 6.10 and B.5.

It is also possible to observe that the power–frequency support mechanism is compatible for simultaneous operation with the FRT mechanism. As shown in Figures 6.19 and 6.20 (to be described later) for fault disturbances with a time duration of 0.5 seconds, the grid-following ST is capable to simultaneously provide FRT and power–frequency support while respecting the maximum current limits of its MV inverter. Nevertheless, a fundamental observation to be made is that the extent of the modulation of the voltage and frequency levels in the various ST-based sub-grids is inversely proportional to the impedance of the short-circuit characterizing the fault disturbance, and directly proportional to the number of phases involved in the fault-disturbance. This observation is in accordance with the expected results, given that a lower short-circuit impedance will result in lower voltage levels at the ST's terminals, which means that the transferable active power in the ST's MV inverter is lower. Also, an increasing number of phases involved in the short-circuit (phase-ground, phase-phase, and finally three-phase faults) also means a decreasing transferable active power in the ST's MV inverter given that the magnitude of the positive symmetric sequence of the AC voltage at the ST's terminals decreases.

The modulation of the voltage and frequency levels in the ST-based hybrid AC/DC grid results in the modulation of the active power in the various sub-grids constituting the ST-based hybrid AC/DC grid. Regarding this, the results obtained for case studies 1 and 2 considering fault disturbances with time duration of 0.5 seconds are illustrated from Figures 6.11 to 6.13. The results related to the fault disturbances with time duration of 0.2 seconds are shown in Appendix B (from Figures B.6 to B.8) in order to not overburden this chapter. The results related to the fault disturbances with time duration of 0.5 seconds are presented here since they present most extreme operation scenarios for the proposed FRT mechanism.

Once again, it is possible to observe the actuation of the FRT mechanism over the hybrid AC/DC grid for case study 1. For net-load scenarios in case study 1, the FRT mechanism modulates the active power in all ST-based sub-grids by exploiting its load–voltage and load–frequency sensitivities. Regarding net-generation scenarios in case study 1, the active power modulation by the FRT mechanism is only observed for the ST-based LV AC sub-grid (Figures 6.13 and B.8). This results from the fact that only the load-frequency sensitivity in the LV AC sub-grid is exploited during net-generation scenarios, with the remaining effort to balance the active power in the ST being assumed by the dump-load.

In case study 2, the local ESS accommodates the excess net load or generation in the ST-based hybrid AC/DC grid. The actuation of the ST's local ESS in case study 2 is illustrated in Figures 6.18 and B.1 for fault disturbances with duration of 0.5 and 0.2 seconds respectively.

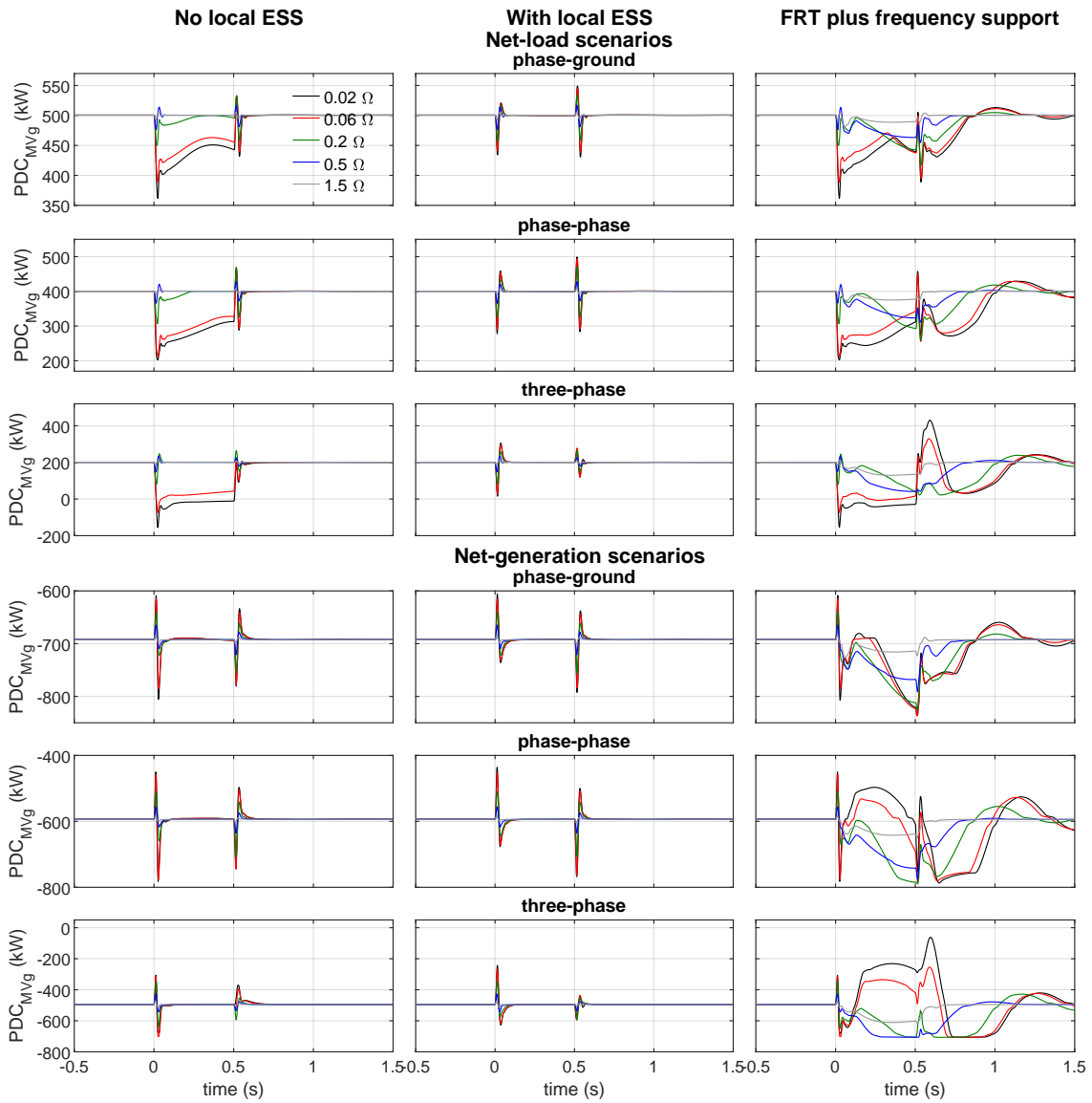


**Figure 6.11:** Active power in the ST-based MV DC grid for several fault impedances with a time duration of 0.5 s.

A discrimination of the active power per type of resources being activated through the proposed modulation strategies considering fault disturbances with time duration of 0.5 seconds is illustrated from Figures 6.14 to 6.17. In order to not overburden this chapter, only the results related to the fault disturbances with time duration of 0.5 seconds are presented here since they represent the most extreme scenarios. The results related to the fault disturbances with time duration of 0.2 seconds are shown

in Appendix B, from Figures B.9 to B.12. Given that only load-frequency sensitivity is exploited in the ST-based hybrid AC/DC grid during net-generation scenarios (in contrast to load-voltage and load-frequency sensitivities in net-load scenarios), a more modest active power modulation in the ST-based hybrid AC/DC grid is obtained for net-generation scenarios for all types of resources. Only the resources located in the LV AC sub-grid are involved, because it is the only sub-grid where load-frequency sensitivity can be exploited. The active power in PV generation can also be modulated (increased) during net-load scenarios since it operates with a 10% deloading capacity. Figures 6.15 and B.10 show that the active power modulation for PV generation during net-load scenarios does not surpass 10% of the previous steady-state power generation.

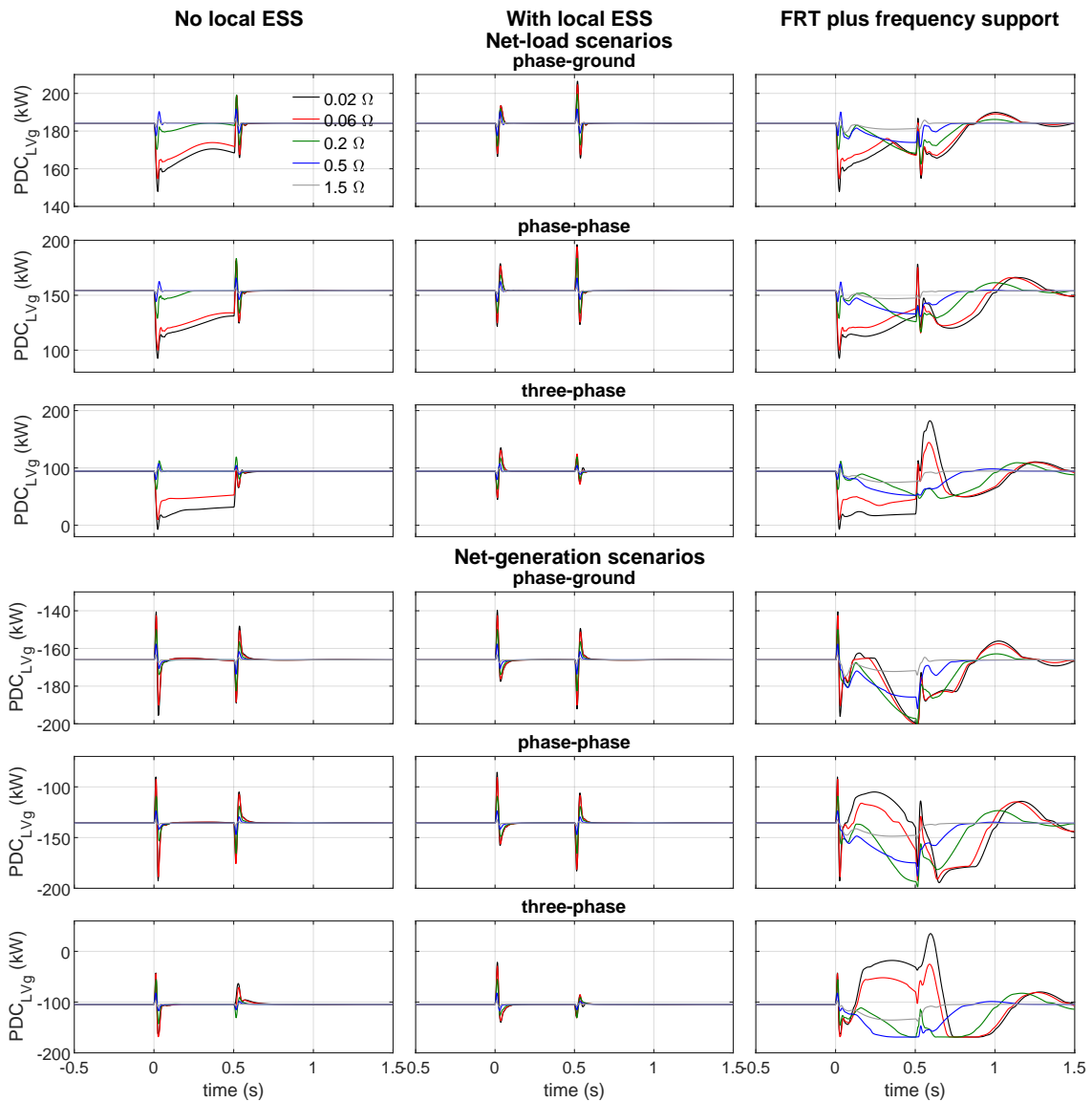


**Figure 6.12:** Active power in the ST-based LV DC grid for several fault impedances with a time duration of 0.5 s.

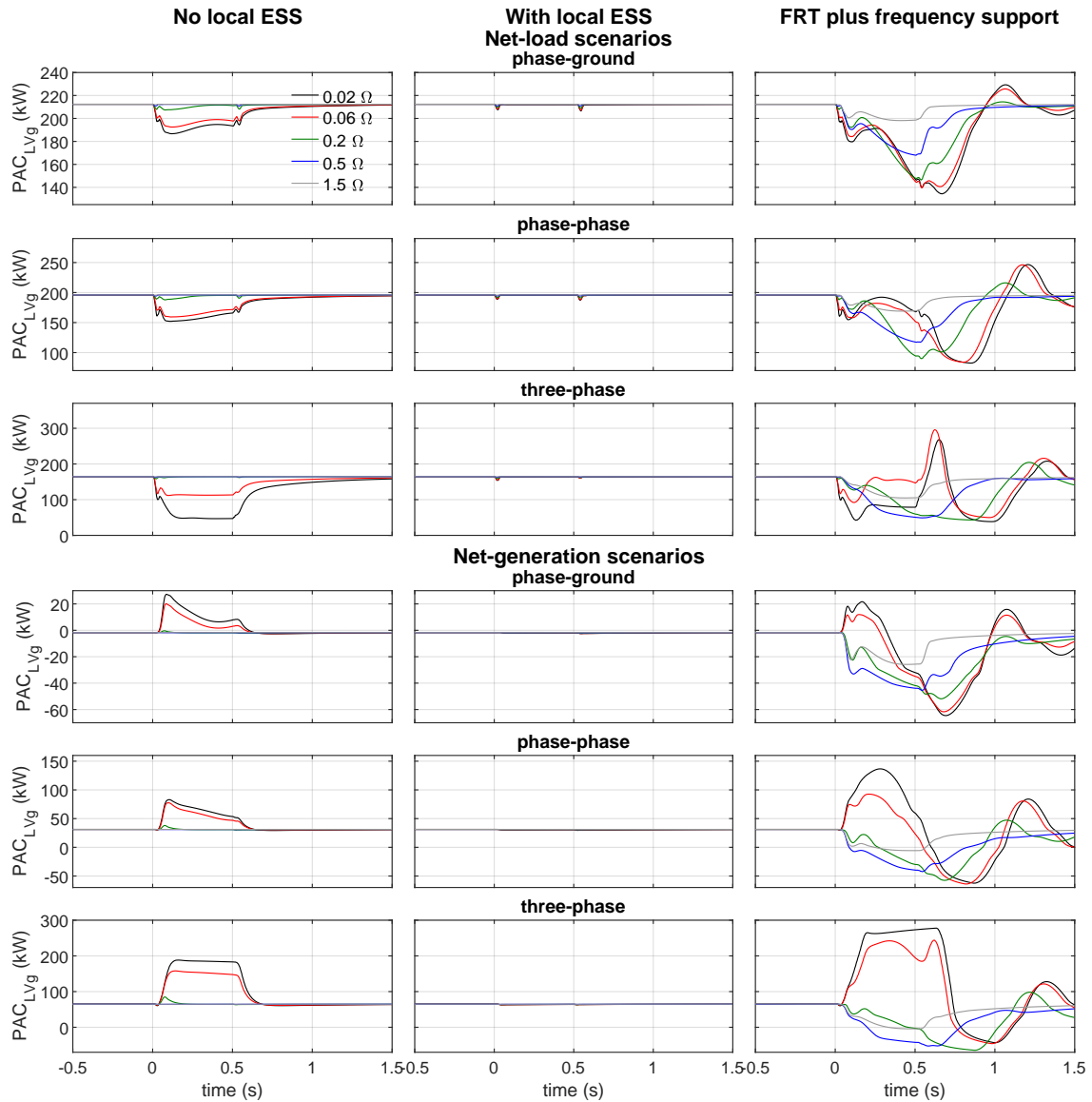


**Figure 6.13:** Active power in the ST-based LV AC grid for several fault impedances with a time duration of 0.5 s.

The small transient responses observed for the case study 2 and even for case-study 1, and the progressive decrease in the power curtailment in several disturbance scenarios after the start of the fault disturbances (more prominent for fault disturbances with a time duration of 0.5 seconds), have the same explanations already made for Figures 6.7 to 6.10. The same is valid regarding the simultaneous operation of FRT and the power-frequency support mechanisms.

Also important is the observation that the extent of the active power modulation in the various ST-based sub-grids (and in the ST's local ESS in case study 2) is inversely proportional to the impedance of the short-circuit characterizing the fault disturbance, and directly proportional to the number of phases involved in the fault-disturbance,



for the same reasons already described for the results from Figures 6.7 to 6.10.

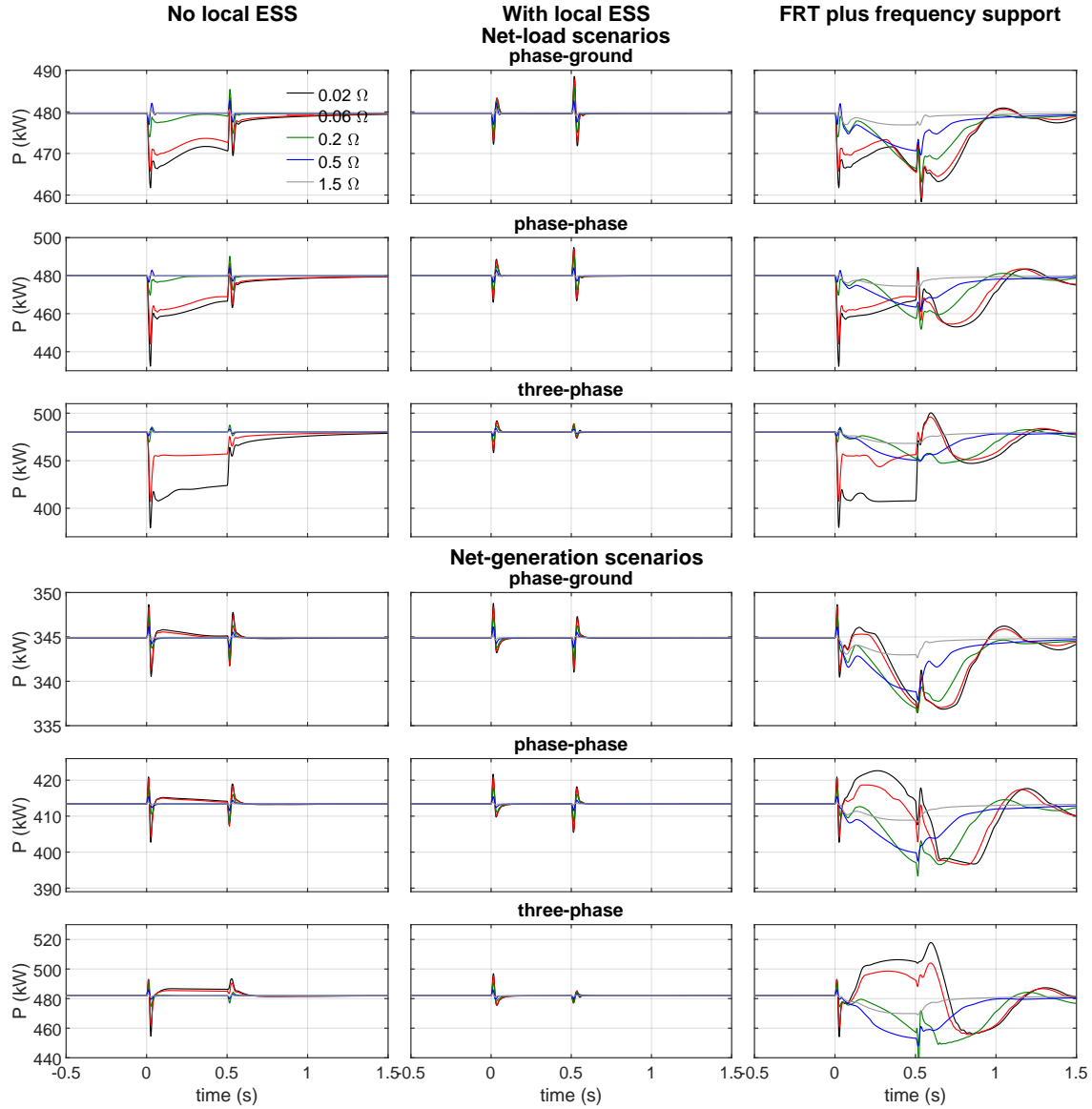


**Figure 6.14:** Active power in total non-controllable load in the ST-based hybrid grid for several fault impedances with a time duration of 0.5 s.

The aforementioned active power modulation in the various ST-based sub-grids and/or dump-load originates a reaction chain of events with the fundamental aim of modulating the active power in the ST's MV inverter in order to preserve the current levels in the ST's MV inverter within its admissible limits. Such chain of events is illustrated in detail in Figures 4.14 and 4.15 (subsection 4.2.1.4). The resulting active power modulation in the ST's MV inverter is illustrated in Figures 6.19 and B.13, relating to fault disturbances in the upstream AC power system with time duration of 0.5 and 0.2 seconds respectively. The RMS current profiles corresponding to the active power profiles represented in Figures 6.19 and B.13 are illustrated in Figures 6.20 and 6.21

respectively. It is possible to observe that the active power modulation in the MV inverter of the ST is the strictly necessary to respect the maximum current limits in the ST's MV inverter.

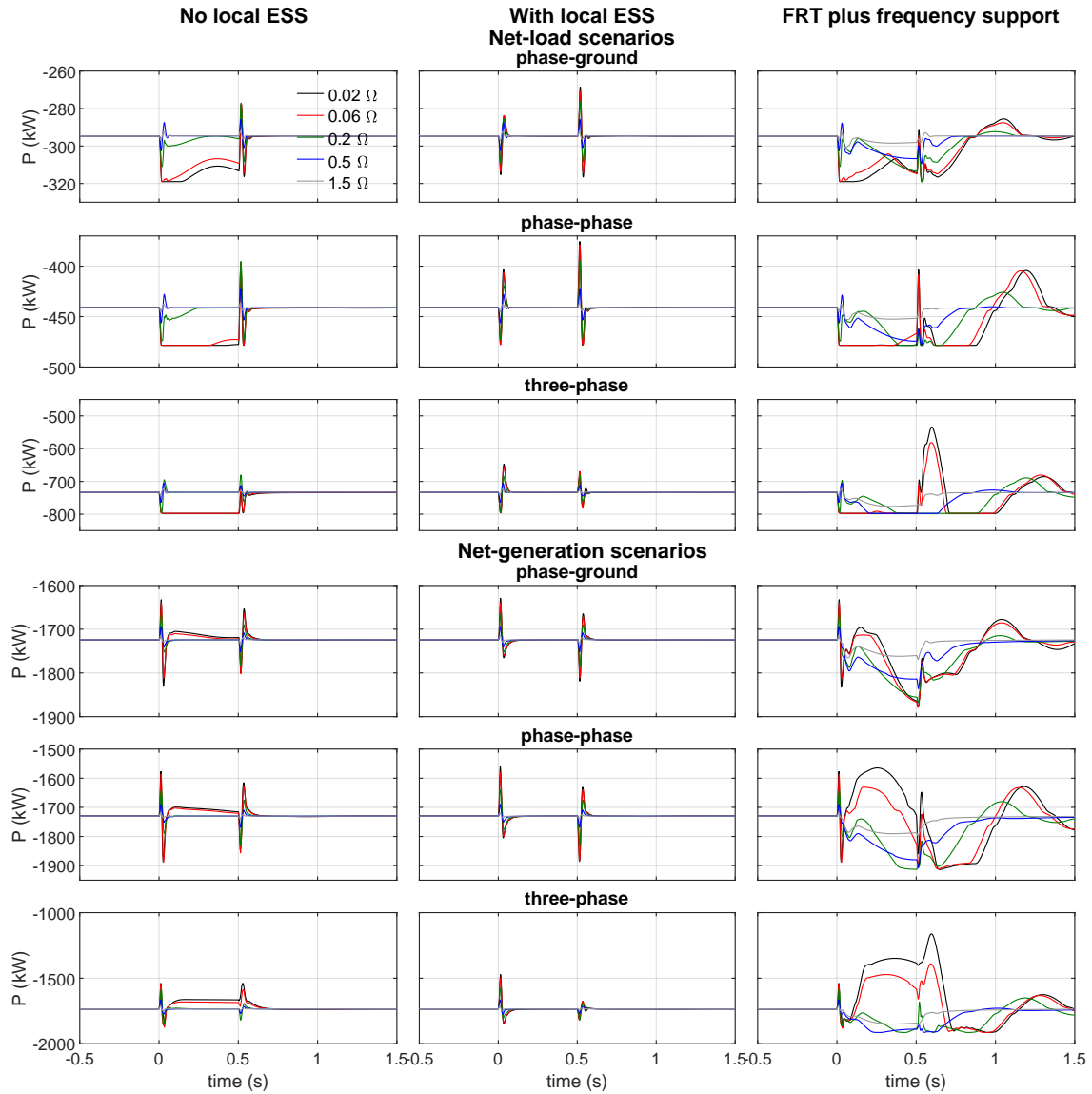


**Figure 6.15:** Active power in total PV generation in the ST-based hybrid grid for several fault impedances with a time duration of 0.5 s.

Figures 6.19 to 6.21 and Figure B.13 show that the FRT mechanism withstands all simulated fault disturbances, preserving the grid-following ST connected to the upstream AC grid by imposing the currents limits in the ST's MV inverter and by ensuring the power balance in the ST-based hybrid AC/DC grid. For case study 2, the observed active power modulation is endured by the ST's local ESS, hence justifying the active power modulation in the ST's MV inverter without power modulation occurring in the ST-based sub-grids. For net-generation scenarios in case study 1, the

observed active power modulation is enabled by the actuation of the dump-load and by the exploitation of the load–frequency sensitivity in the ST-based LV AC sub-grid. Regarding the net-load scenarios in case study 1, the observed active power modulation is enabled by the exploitation of the load–frequency and load-voltage sensitivities in all ST-based sub-grids. For case studies 1 and 2, the oscillatory behavior observed in the current profiles after the extinction of the fault disturbance is due to the voltage regulation in the equivalent generator of the upstream AC grid.

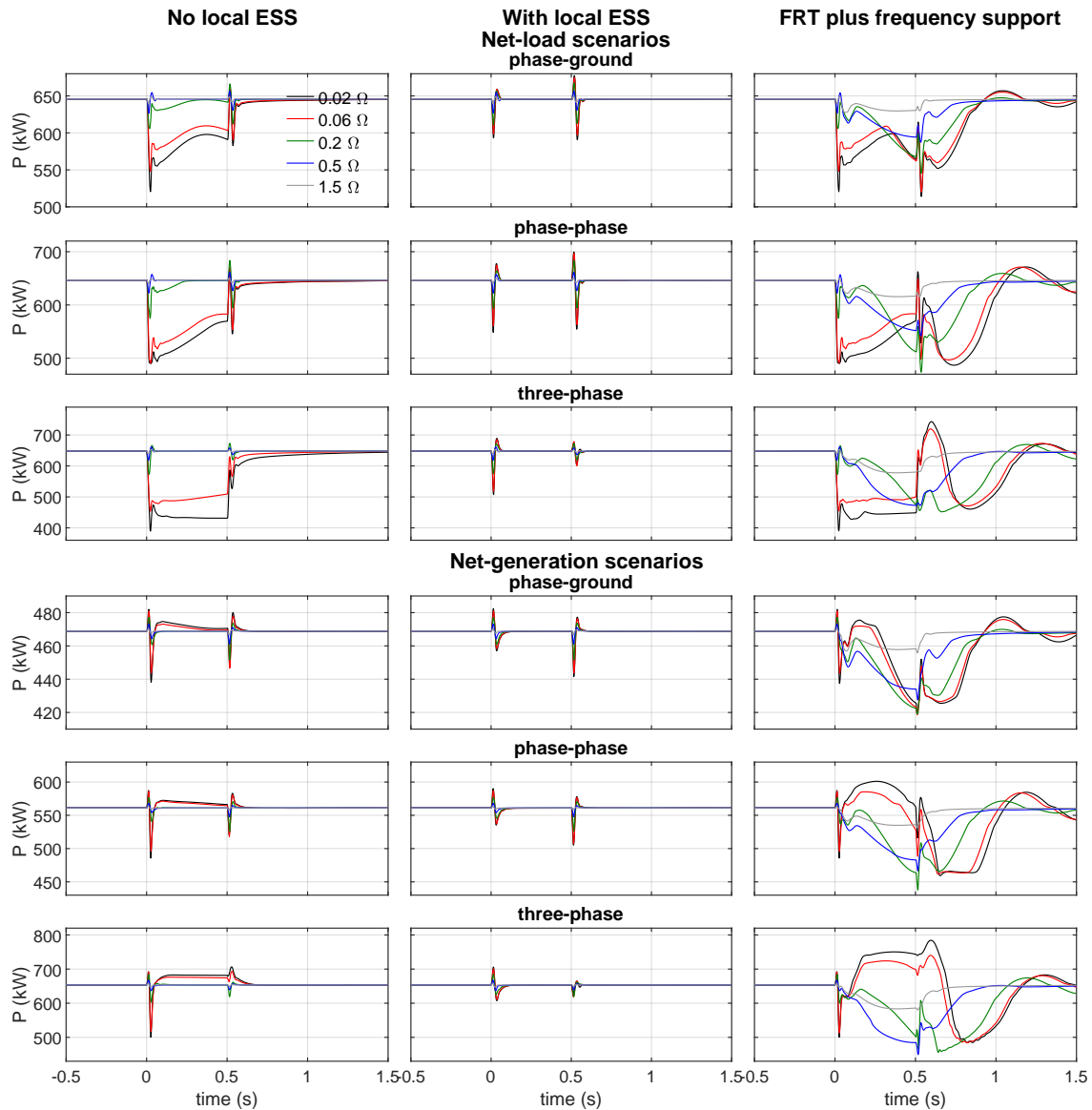


**Figure 6.16:** Active power in total EV chargers in the ST-based hybrid grid for several fault impedances with a time duration of 0.5 s.

The simultaneous operation of the FRT and power–frequency support mechanisms is also illustrated in Figures 6.19 and 6.20 for fault disturbances with a time duration of 0.5 seconds. The inclusion of the power–frequency support mechanism modifies

the power and current response observed in the MV inverter of the ST following the occurrence and clearance of the fault disturbance, but the simultaneous operation of the two mechanism is demonstrated to be possible and effective, always complying with the maximum current limits of the ST's MV inverter. The presented results reflect the efforts of the power–frequency support mechanism in counteracting the frequency excursions taking place during the fault disturbance and after its extinction (illustrated in Figure 6.6). Longer and more severe fault disturbances originate longer and more severe frequency disturbances, which in turn lead to stronger reactions of the power–frequency support mechanism, as expected.

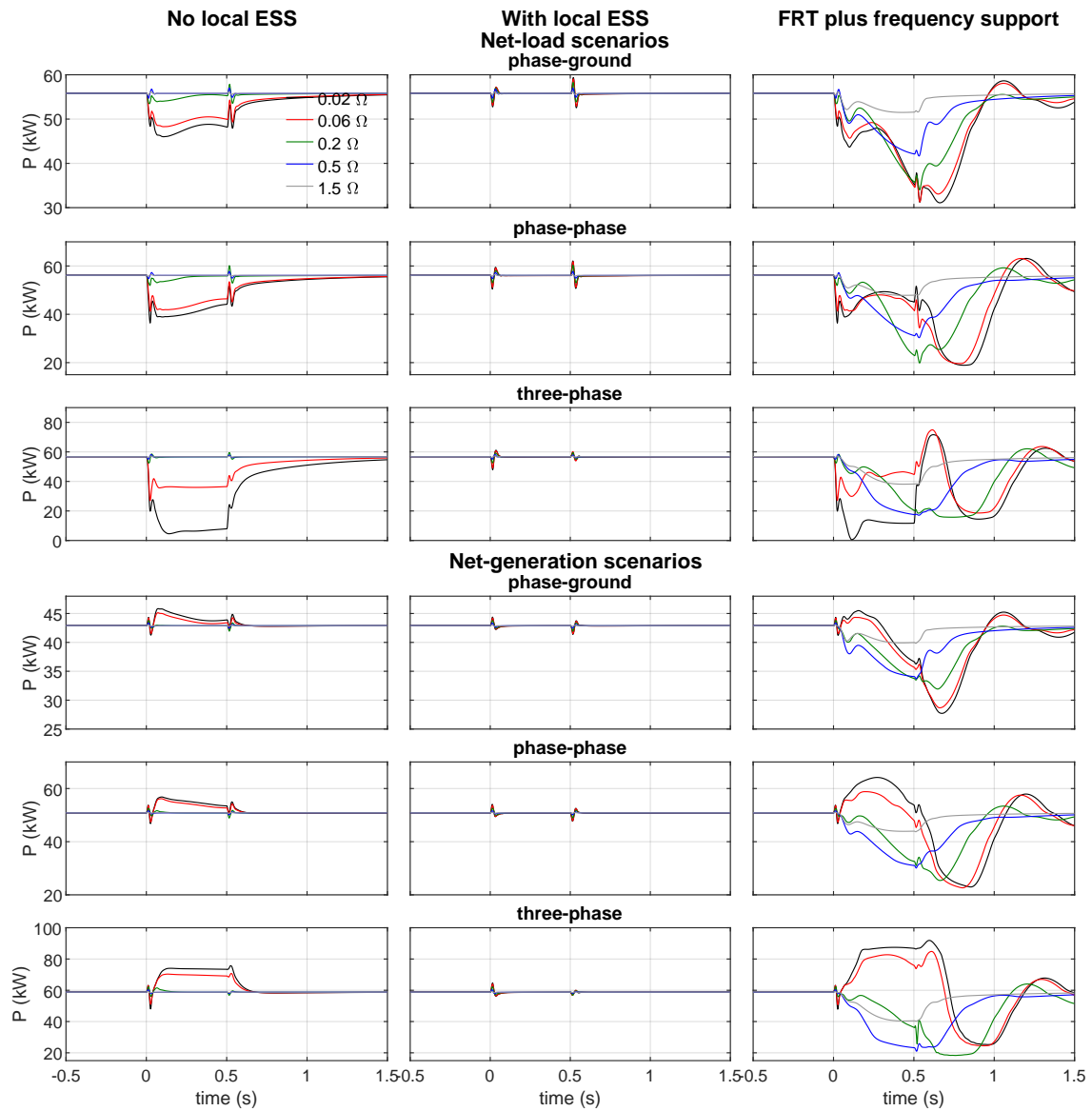


**Figure 6.17:** Active power in total energy storage available in the ST-based hybrid grid for several fault impedances with a time duration of 0.5 s.

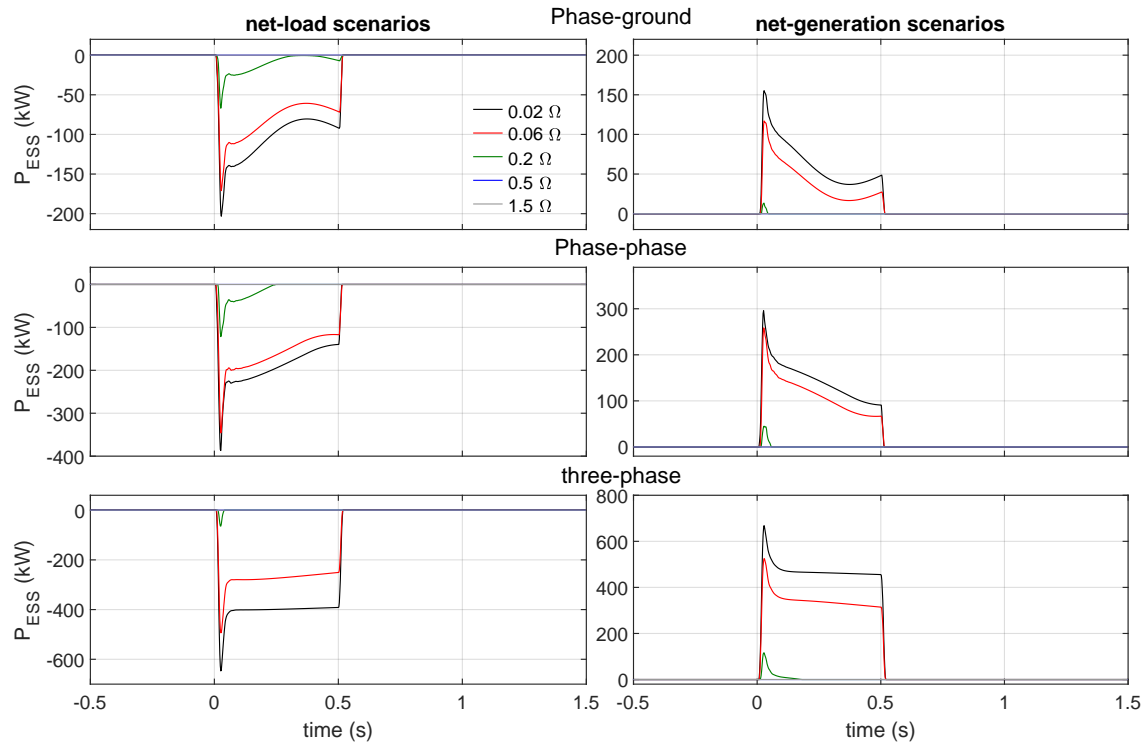


**Figure 6.18:** Case study 2 - Active power in the local ESS of the ST for several fault impedances with a time duration of 0.5 s.

At last, the detailed AC voltage and current waveforms in the ST's MV inverter, around the time instants where the surge and extinction of fault disturbances in the upstream AC power system take place, are also presented in Figures 6.22, 6.23 and B.14. The presented voltage and current waveforms are related to symmetric and asymmetric faults considering the lowest fault impedance presented in Table 6.1 ( $0.02\Omega$ ) and with time duration of 0.5 and 0.2 seconds. It is possible to observe that the currents in the ST's MV inverter do not present relevant distortion after and before the surge and extinction of the fault disturbances.

An increase in the voltage at the ST's terminals above 1 p.u. is visible after the extinction of the fault disturbances, which is more pronounced following fault disturbances with a time duration of 0.5 seconds. This increase is temporary and results from the voltage regulation performed by the equivalent generator in the upstream AC power system during the fault disturbance (see RMS voltage profiles in Figures 6.4 and 6.5). As long the fault disturbance is not cleared, the voltage regulator of the equivalent generator in the upstream AC power system will keep trying to increase the overall system's voltage, reason why after the extinction of the fault disturbance, the voltage increase is higher for fault disturbances with time duration of 0.5 seconds comparatively to fault disturbances with time duration of 0.2 seconds.

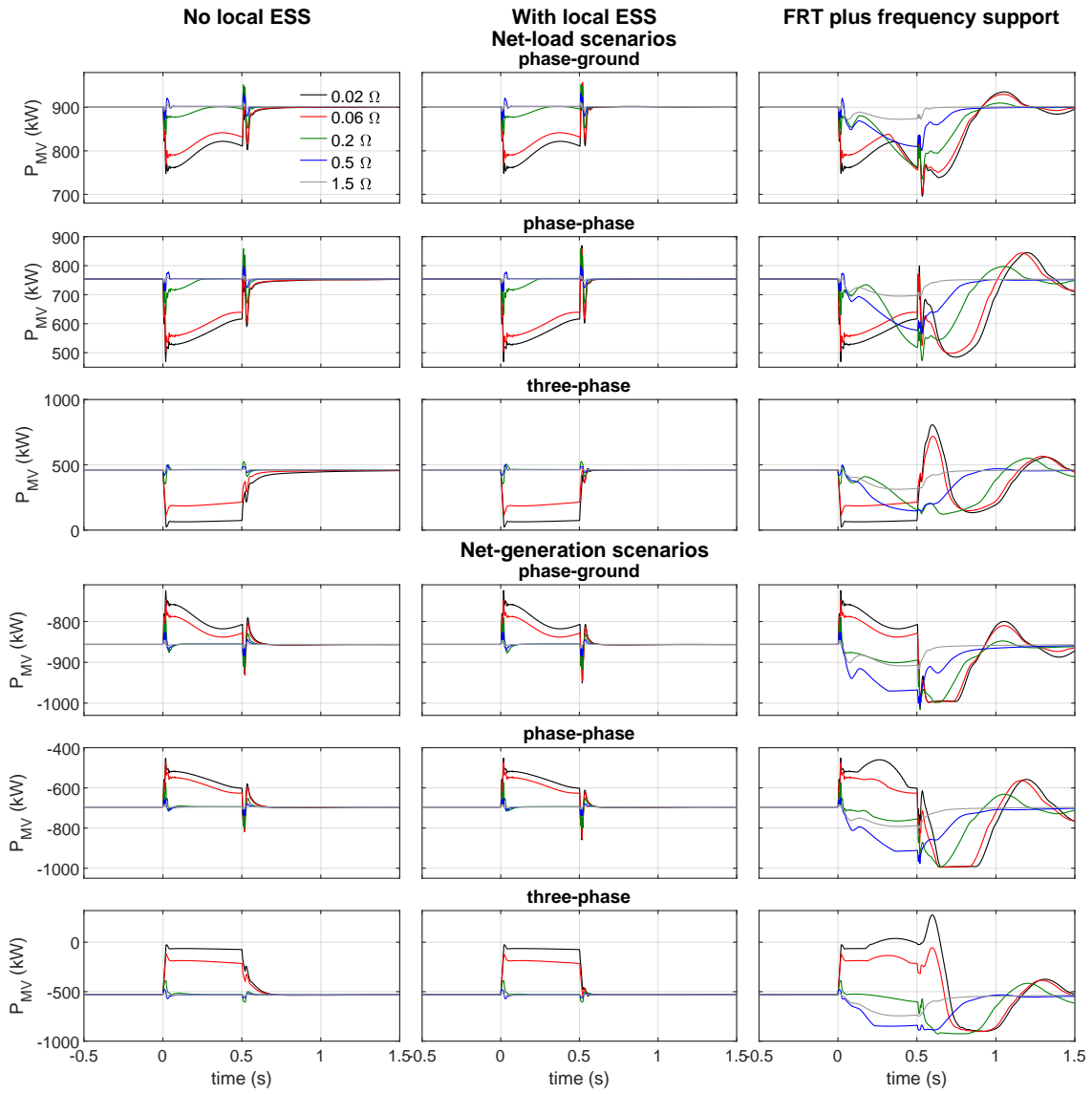
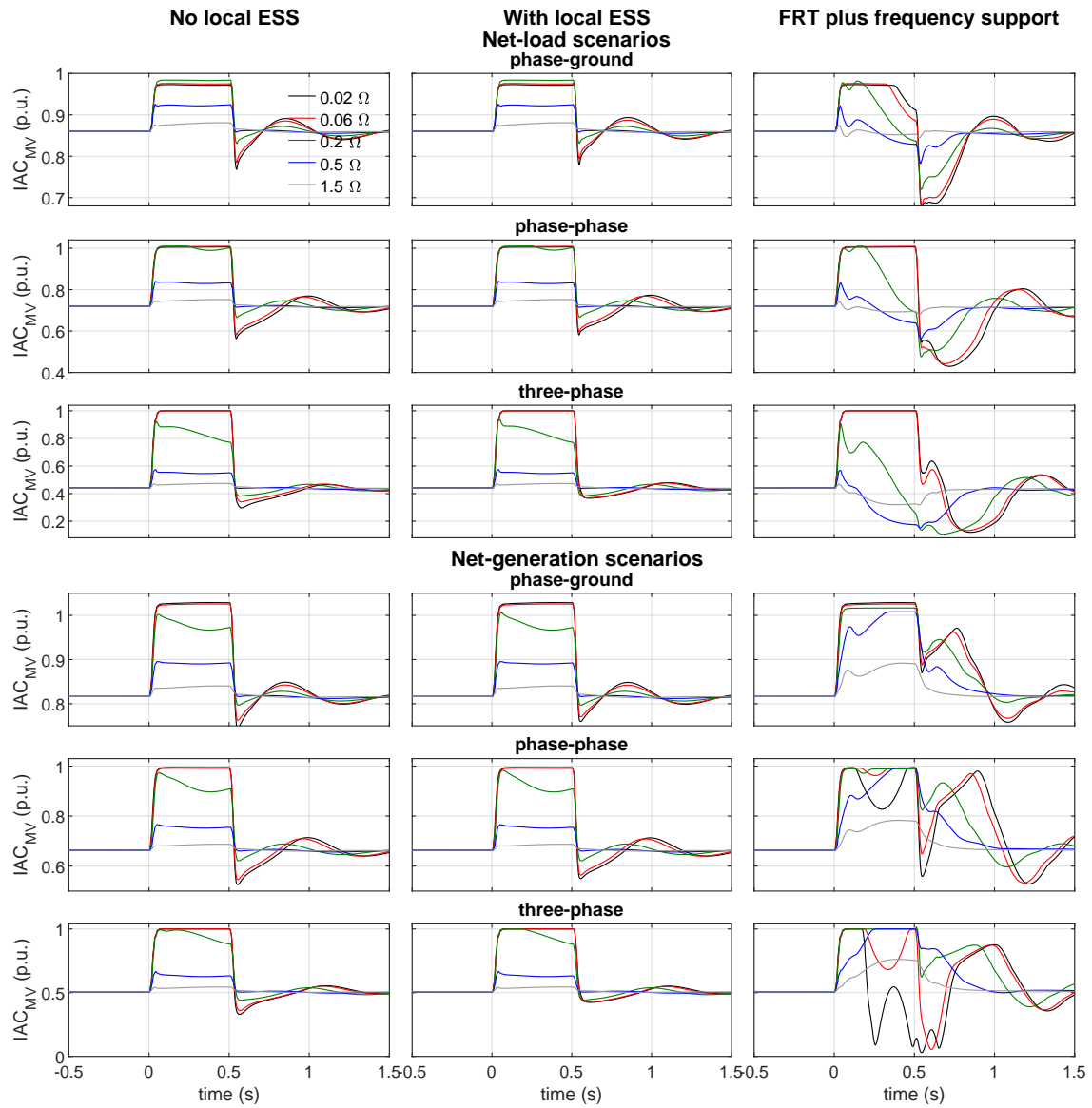
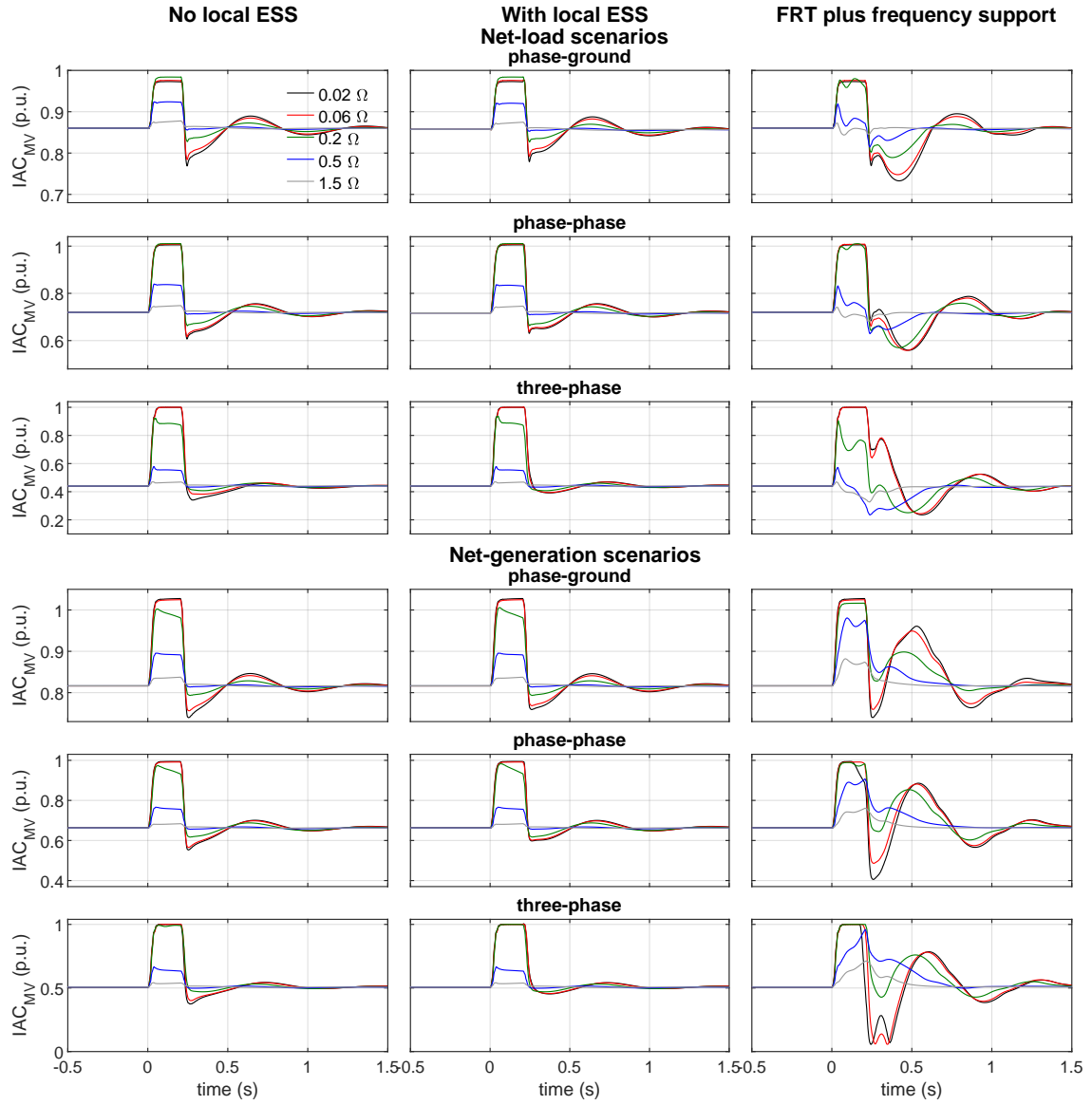


Figure 6.19: Active power in the ST's MV inverter for several fault impedances with a time duration of 0.5 s.



**Figure 6.20:** RMS current in the ST's MV inverter for several fault impedances with a time duration of 0.5 s.



**Figure 6.21:** RMS current in the ST's MV inverter for several fault impedances with a time duration of 0.2 s.



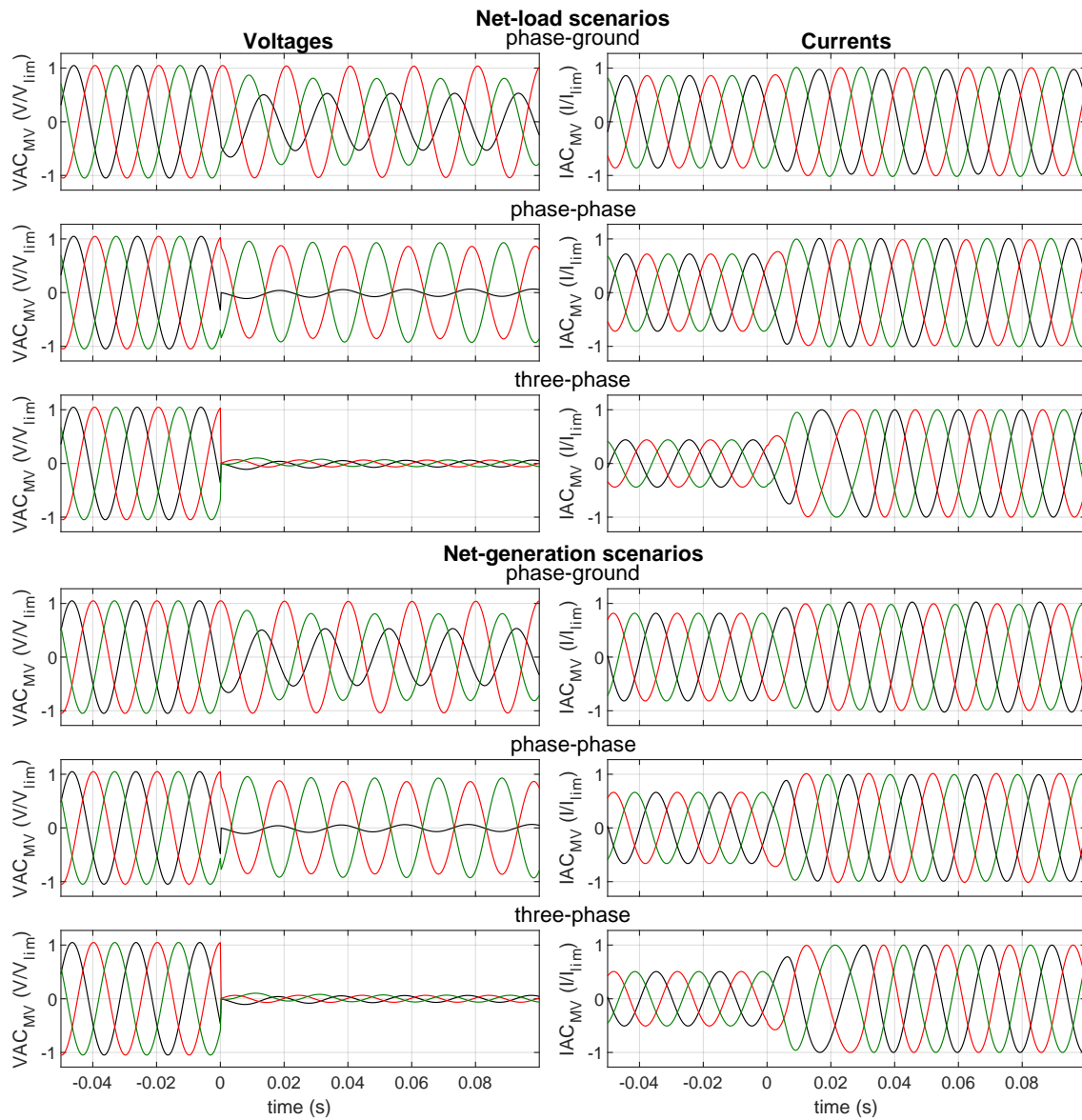


**Figure 6.22:** Three-phase voltage and current waveforms in the ST MV inverter during fault surge: fault impedance of  $0.02\Omega$  and time duration of 0.5 s. Black: phase-phase A-B voltage and phase A current; Red: phase-phase B-C voltage and phase B current; Green: phase-phase C-A voltage and phase C current.

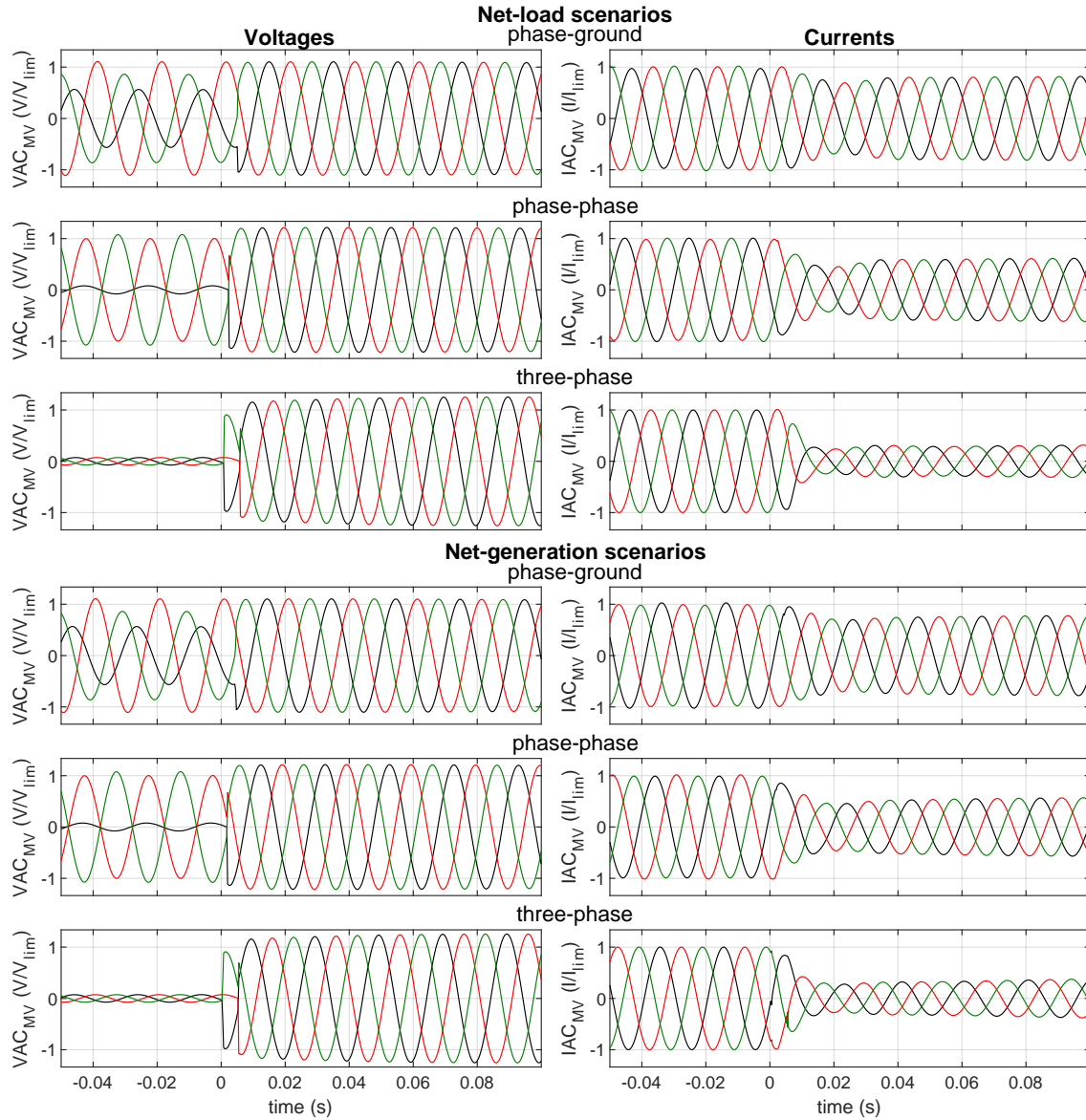


**Figure 6.23:** Three-phase voltage and current waveforms in the ST MV inverter during fault clearance: fault impedance of  $0.02\Omega$  and time duration of 0.5 s. Black: phase-phase A-B voltage and phase A current; Red: phase-phase B-C voltage and phase B current; Green: phase-phase C-A voltage and phase C current.

### 6.2.2 Case Study 3

The results related to the evaluation of the case study 3 are presented in this subsection. The results presented in p.u. use the nominal voltages and frequency presented in Table 6.3 as base values. In the presented results, the start of the fault disturbance occurs at  $time (s) = 0$ , and positive values for the active power correspond to consumed power whereas negative values correspond to injected/generated active power.

Different voltage and frequency disturbance profiles were obtained as a result

of fault disturbances described in Table 6.1 and the equivalent impedance values presented in Table 6.2. For the sake of simplicity, the equivalent impedance of  $0.4 + j0.94\Omega$  is designated henceforth in this subsection by  $Z_{eq1}$ , whereas the equivalent impedance of  $0.02 + j0.23\Omega$  is designated as  $Z_{eq2}$ .

The profiles of the frequency disturbances for fault disturbances with a duration of 0.2 and 0.5 seconds are illustrated in Figures 6.24 and 6.25 for the equivalent impedances  $Z_{eq1}$  and  $Z_{eq2}$  respectively. The profiles of the voltage disturbances for fault disturbances with a duration of 0.2 and 0.5 seconds are respectively illustrated in Figures 6.26 and 6.27 for the equivalent impedance  $Z_{eq1}$  and in Figures 6.28 and 6.29 for the equivalent impedance  $Z_{eq2}$ .

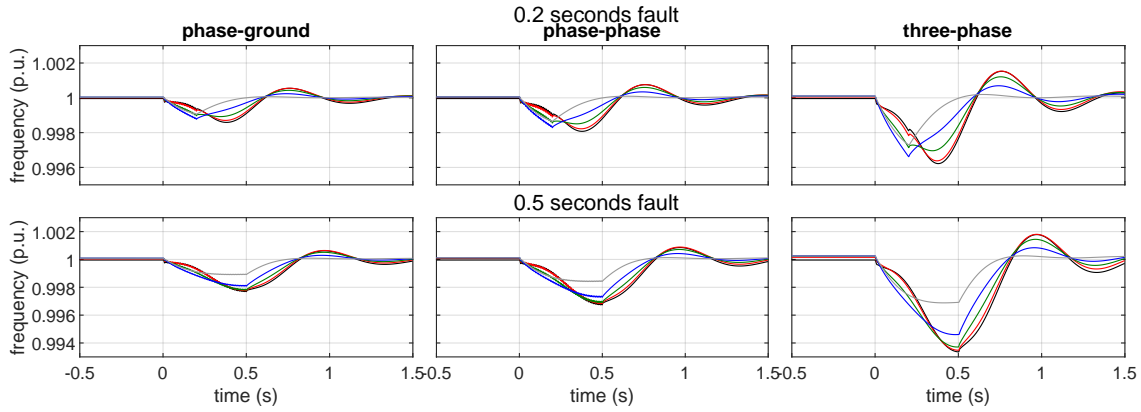


**Figure 6.24:** Frequency disturbances observed at ST's MV inverter resulting from fault disturbances in the upstream AC power system considering  $Z_{eq1}$ .

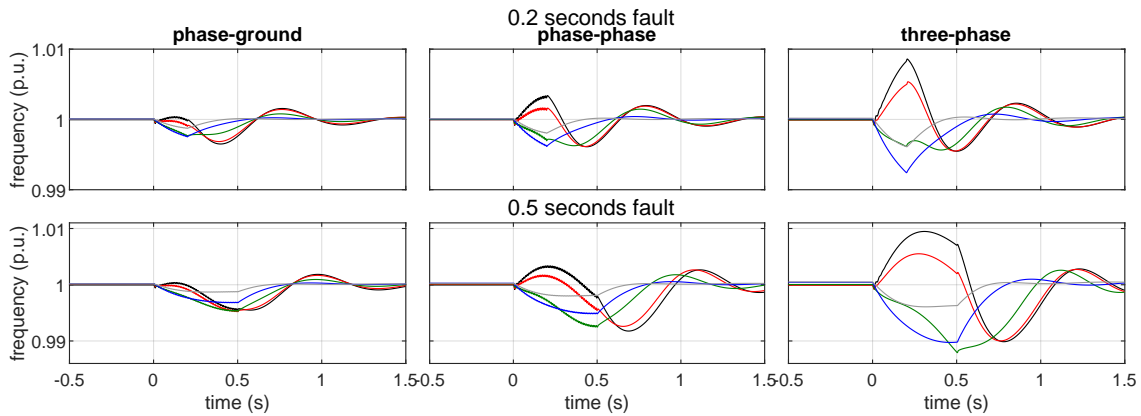


**Figure 6.25:** Frequency disturbances observed at ST's MV inverter resulting from fault disturbances in the upstream AC power system considering  $Z_{eq2}$ .

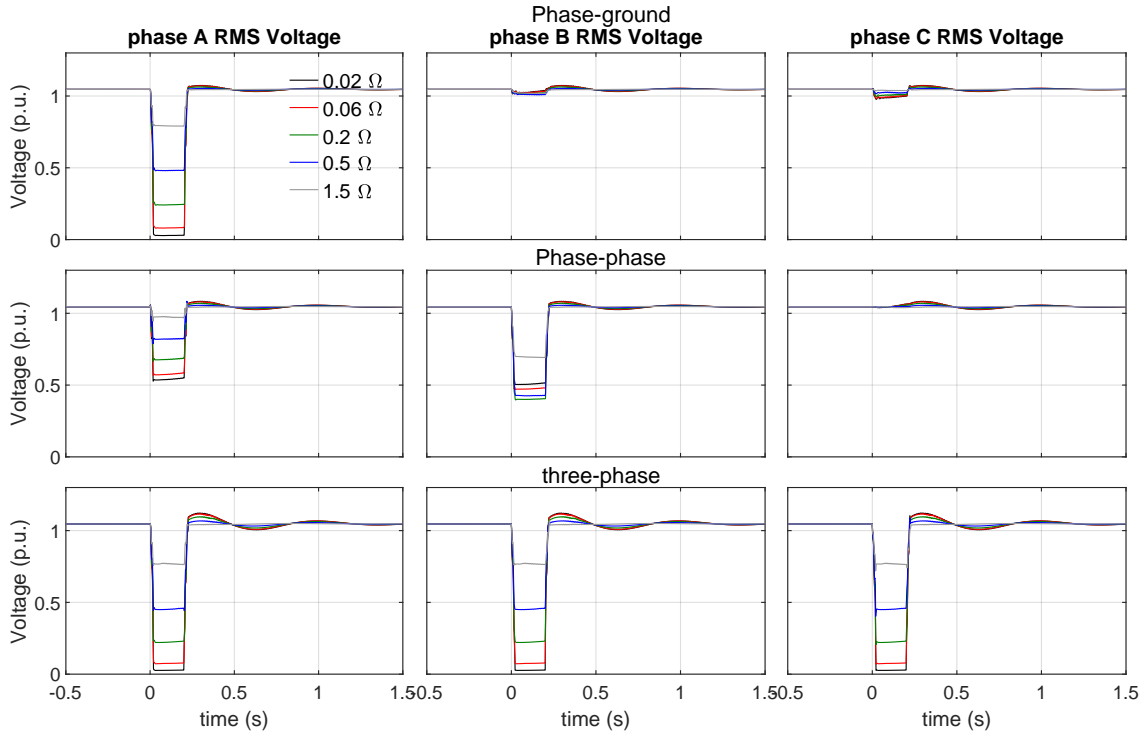


**Figure 6.26:** Voltage disturbances observed at ST's MV inverter resulting from fault disturbances in the upstream AC power system, considering  $Z_{eq1}$  and fault impedances with a time duration of 0.2 s.

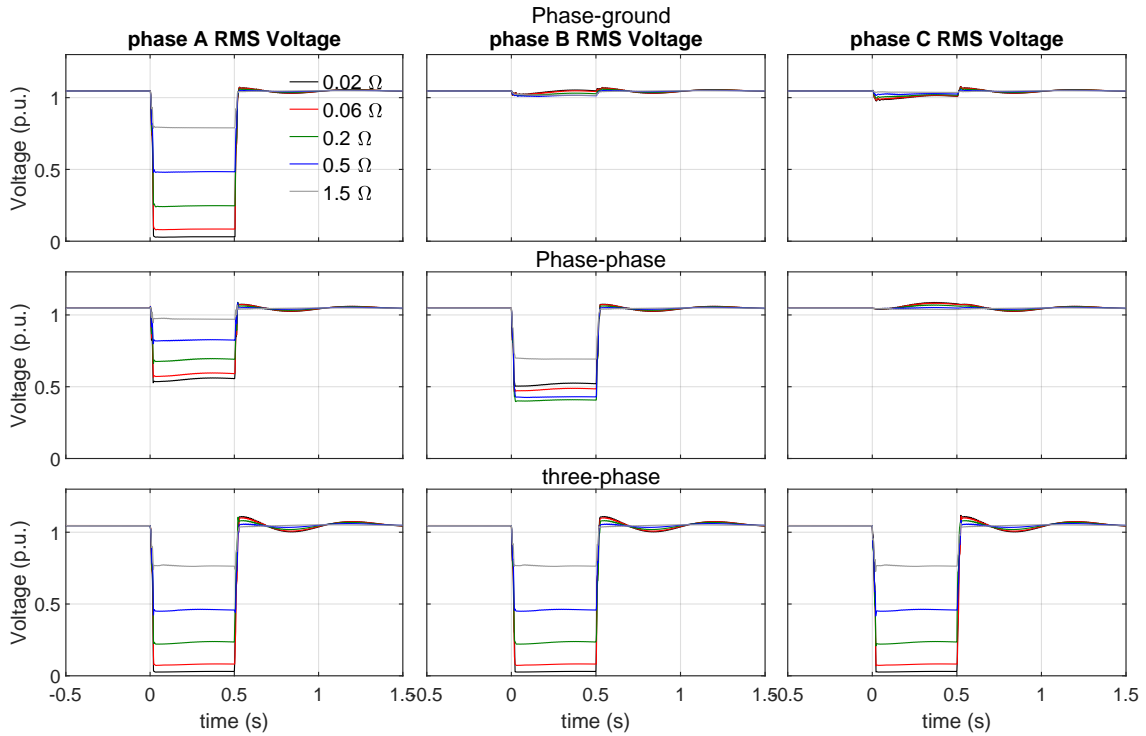


**Figure 6.27:** Voltage disturbances observed at ST's MV inverter resulting from fault disturbances in the upstream AC power system, considering  $Z_{eq1}$  and fault impedances with a time duration of 0.5 s.

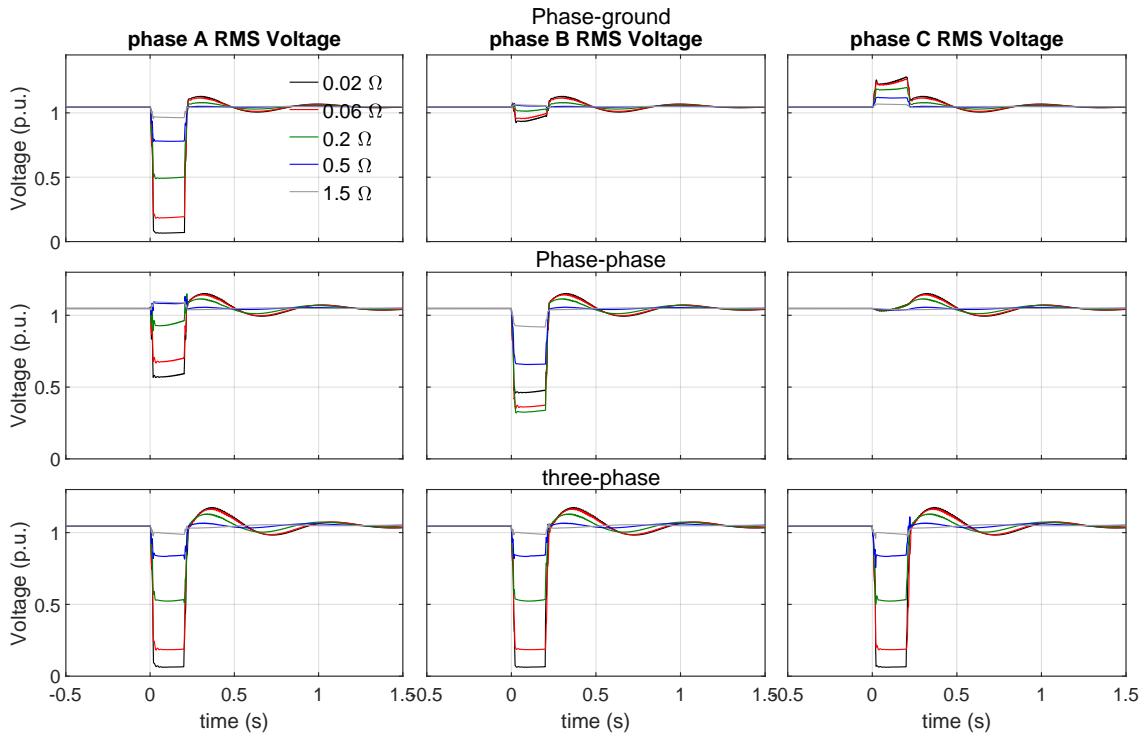


**Figure 6.28:** Voltage disturbances observed at ST's MV inverter resulting from fault disturbances in the upstream AC power system, considering  $Z_{eq2}$  and fault impedances with a time duration of 0.2 s.

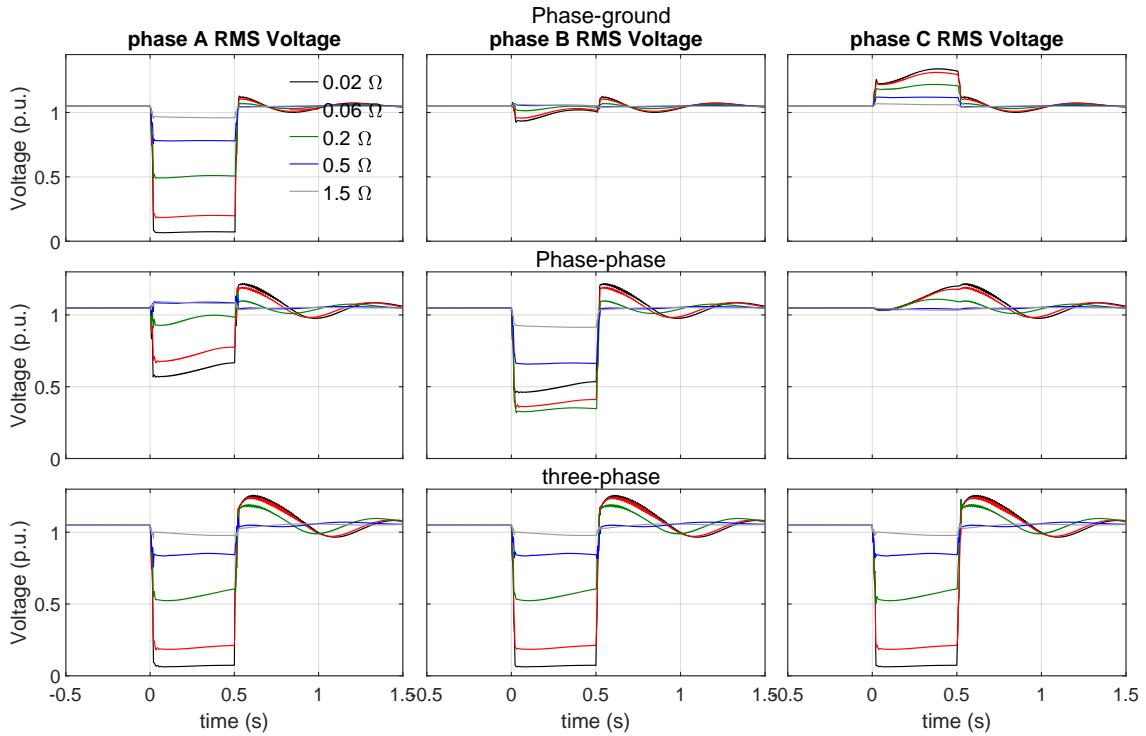


**Figure 6.29:** Voltage disturbances observed at ST's MV inverter resulting from fault disturbances in the upstream AC power system, considering  $Z_{eq2}$  and fault impedances with a time duration of 0.5 s.

The time evolution of the frequencies depicted in Figures 6.24 and 6.25 are based on the equivalent generator rotational speed. Comparatively to the results presented in case studies 1 and 2 where the equivalent impedance  $Z_{eq2}$  is considered, the voltage and frequency profiles presented in Figures 6.25, 6.28 and 6.29 are identical. This results from the fact that the ST-based hybrid AC/DC grid is much smaller than the overall upstream AC system (1MVA maximum in a 1GW power system), and thus, any active power variations in the ST-based hybrid AC/DC grid have a very small impact on the overall power system frequency and voltage levels.

Nevertheless, it is possible to notice that the voltage and frequency disturbances observed considering the equivalent impedance  $Z_{eq2}$  are more severe comparatively to the homologous disturbances considering the equivalent impedance  $Z_{eq1}$ .

It is also observable that the voltage levels at the ST's terminals are temporarily raised significantly above 1 p.u. after the extinction of the fault disturbances, a phenomena more pronounced following fault disturbances with time duration of 0.5 seconds and considering the equivalent impedance  $Z_{eq2}$ . This phenomena results from the voltage regulation performed by the equivalent generator in the upstream AC power system during the fault disturbance. As long the fault disturbance is not cleared, the voltage regulator of the equivalent generator will keep trying to increase the overall system's voltage, reason why after the extinction of the fault disturbance, the voltage increase is higher for fault disturbances with time duration of 0.5 seconds comparatively to fault disturbances with time duration of 0.2 seconds.

Following the aforementioned disturbances, the FRT mechanism incorporated in the grid-forming ST actuates if the maximum current limits of the ST's MV inverter are violated. Contrarily to the grid-following ST in case studies 1 and 2, the actuation of the FRT mechanism incorporated in the grid-forming ST is independent of the net active power in the ST-based hybrid AC/DC grid, given that the local ESS incorporated in the ST is the immediate responsible to preserve the power balance in the ST, as illustrated by the chain of events presented in Figure 4.18 (subsection 4.2.2.2). The same is valid regarding the exploitation of the ST-based hybrid AC/DC grid by the power-frequency support mechanism, as already evaluated in chapter 5, since the immediate power-frequency response provided by the grid-forming ST is solo determined by the  $f(\Delta P_{MV})$  droop controller incorporated in the controller of the ST's MV inverter. For this reason, the results related to the ST-based hybrid AC/DC grid following a fault disturbance in the upstream AC power system are not considered relevant at this point. The ST-based hybrid AC/DC grid continues to operate in its steady-state conditions (Table 6.6) as the ST's local ESS will shield it against any fault disturbance

in the upstream AC power system. Only the results related to the ST's MV inverter have relevance regarding the actuation of the FRT mechanism in this case study.

The results obtained for the three-phase current profiles in the ST's MV inverter ( $I_{AC_{MV}}$ ), considering fault disturbances with a time duration of 0.5 seconds and the equivalent impedance  $Z_{eq1}$  and  $Z_{eq2}$  are illustrated in Figures 6.30 and 6.31 respectively. In order to not overburden the chapter's reading, the results related to the fault disturbances with time duration of 0.2 seconds are shown in Appendix B, in Figures B.15 and B.16. The results related to the fault disturbances with time duration of 0.5 seconds are presented here since they represent the most extreme scenarios.

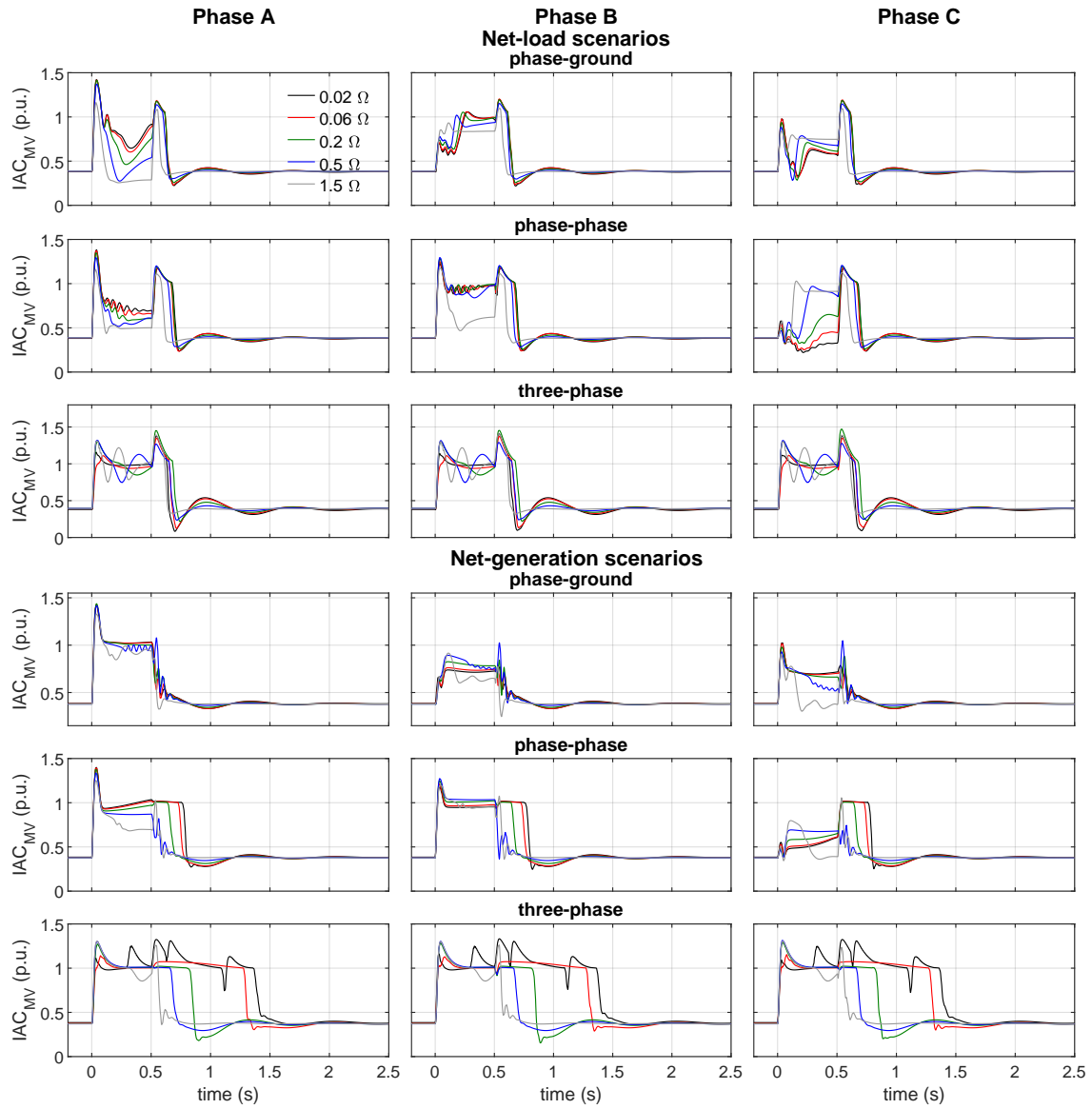


**Figure 6.30:** RMS current in the ST's MV inverter considering  $Z_{eq1}$  and fault impedances with a time duration of 0.5 s.



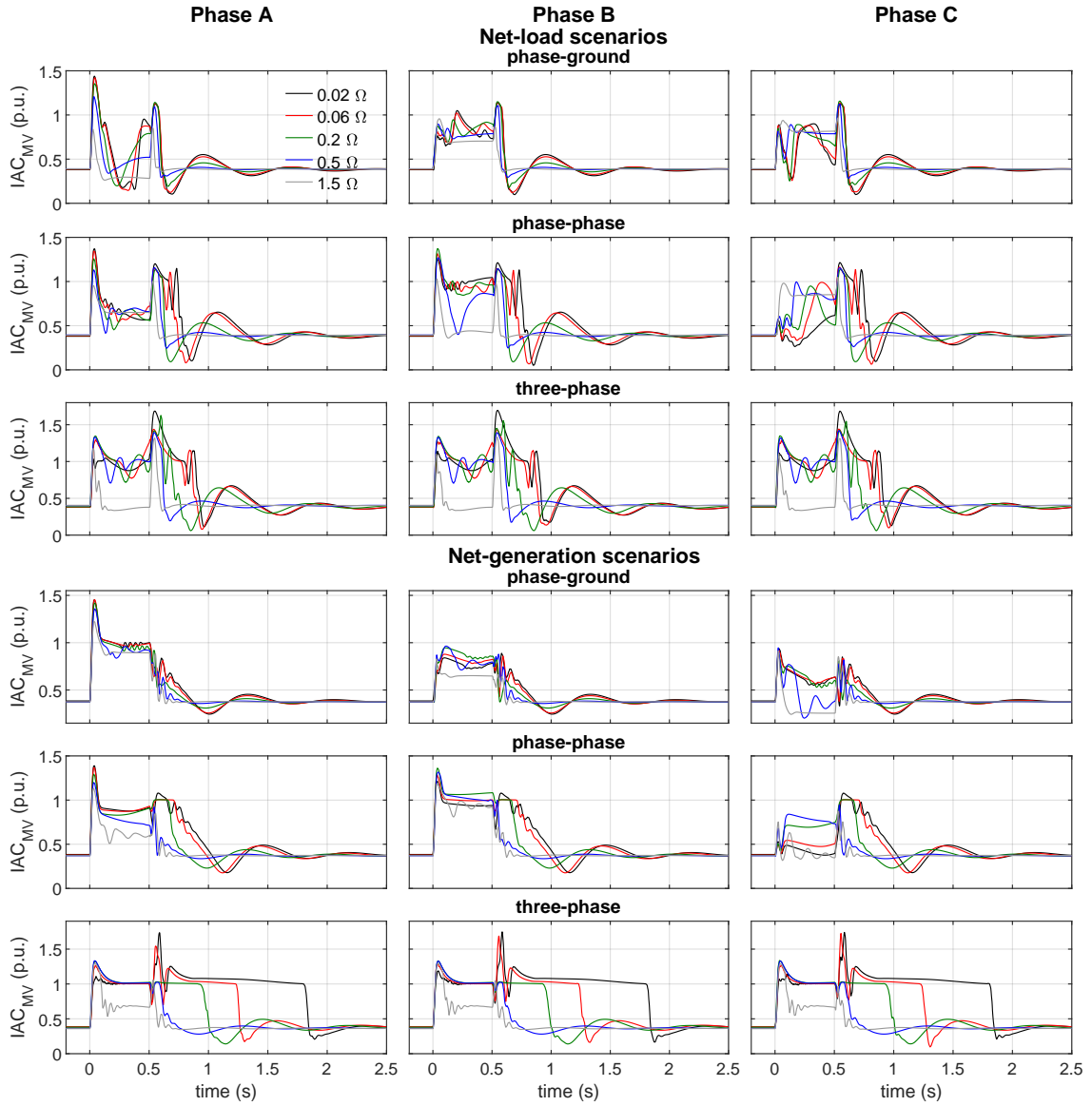


**Figure 6.31:** RMS current in the ST's MV inverter considering  $Z_{eq2}$  and fault impedances with a time duration of 0.5 s.

The nominal current of the MV inverter, which is defined as the maximum current limit, is set at 1 p.u. Observing the results, the actuation of the FRT mechanism presents in general two stages: a first stage between the surge and extinction of the fault disturbance, and a second stage after the extinction of the fault disturbance. The presented results show that for most of the simulated faults where the current limits of the MV inverter are tested, the first stage is generally characterized by a  $IAC_{MV}$  overshoot above 1 p.u. in the phases affected by the fault disturbance, followed by a stabilization of  $IAC_{MV}$  at 1 p.u. in the phases affected by the fault disturbance. This pattern is more evident for fault disturbances with a time duration of 0.5 seconds, given that  $IAC_{MV}$  has more time to settle at the nominal value. The second stage can



present a renewed  $IAC_{MV}$  overshoot or a saturation of  $IAC_{MV}$  around 1 p.u. in the initial instants, but eventually  $IAC_{MV}$  always settles at the pre-fault levels.

This behavior of  $IAC_{MV}$  is explained as follows. The grid-forming MV inverter is sensitive to the voltage drop in its output LC filter, and any sudden voltage or phase change in the upstream MV AC grid will originate inrush currents which will test the maximum current limits of the ST's MV inverter. Such sudden voltage and phase changes occur precisely at the surge and extinction instants of the fault disturbance, being the cause of the overshoots or saturation at 1 p.u of  $IAC_{MV}$  observed at the start of each stage identified for the actuation of the FRT mechanism.  $IAC_{MV}$  is naturally composed by active and reactive components, relating to the active ( $P_{MV}$ ) and reactive ( $Q_{MV}$ ) power in the ST's MV inverter. From Figures 6.32 to 6.35 and from Figures B.17 to B.20 it is possible to infer that the observed  $IAC_{MV}$  overshoots strongly correlate with the settling time delay observed for the phase shift ( $\theta$ ) and voltage drop magnitude ( $\Delta V$ ) in the output LC filter of the ST's MV inverter. The results related to the fault disturbances with time duration of 0.2 seconds are shown in Appendix B (from Figures B.17 to B.20) in order to not overburden the chapter's reading. The results related to the fault disturbances with time duration of 0.5 seconds are presented here since they represent the most extreme scenarios. Figures 6.32 to 6.35 and B.17 to B.20 show that the saturation of  $P_{MV}$  after a fault disturbance extinction is related to the settling time delay of the phase angle  $\theta$ , which mostly coincides with the saturation observed for  $IAC_{MV}$  in Figures 6.30, 6.31, B.15 and B.16. Meanwhile, by comparing  $IAC_{MV}$  with Figures 6.34, 6.35, B.19 and B.20, it is possible to infer that the  $IAC_{MV}$  overshoot observed in the first stage of the actuation of the FRT mechanism is generally more impacted by the evolution of  $\Delta V$  in the LC filter, but  $\Delta V$  shows to have a meaningful impact in the second stage of the actuation of the FRT mechanism as well. It is worth to mention that  $P_{MV}$  and  $Q_{MV}$  should not be erroneously considered not saturated or not overshooted when  $IAC_{MV}$  saturates or overshoots during the first stage of the actuation of the FRT mechanism, given that the voltage levels at the ST terminals are not at the nominal values following the occurrence of a fault disturbance, and the maximum limits for the active and reactive components of  $IAC_{MV}$  are defined according to Equation (4.22).

Given the explanation regarding the  $IAC_{MV}$  profiles observed for the simulated fault disturbances, important conclusions can be drawn regarding the operation of the FRT mechanism. It is evidenced that the limitation of  $IAC_{MV}$  is more challenging as the severity of the fault increases, whether by having a lower fault impedance or involving more phases, and for more aggressive voltage and frequency excursions

in the upstream AC power system. But overall, the FRT mechanism is able to limit  $IAC_{MV}$  for all considered fault disturbances within reasonable levels. The overshoot occurrences observed in  $IAC_{MV}$  after the surge and extinction of the simulated fault disturbances are relatively brief and are generally limited below 1.5 p.u., except for the symmetrical three-phase fault disturbances considering the equivalent impedance  $Z_{eq2}$  and fault disturbances with a time duration of 0.5 seconds, where brief over-currents close to 2 p.u. are observed. This events, although not intended in this case, usually represent manageable overload conditions in practical applications, being feasible to dimension a power electronic converter to withstand such over-currents without requiring the shutdown of a power converter [259].

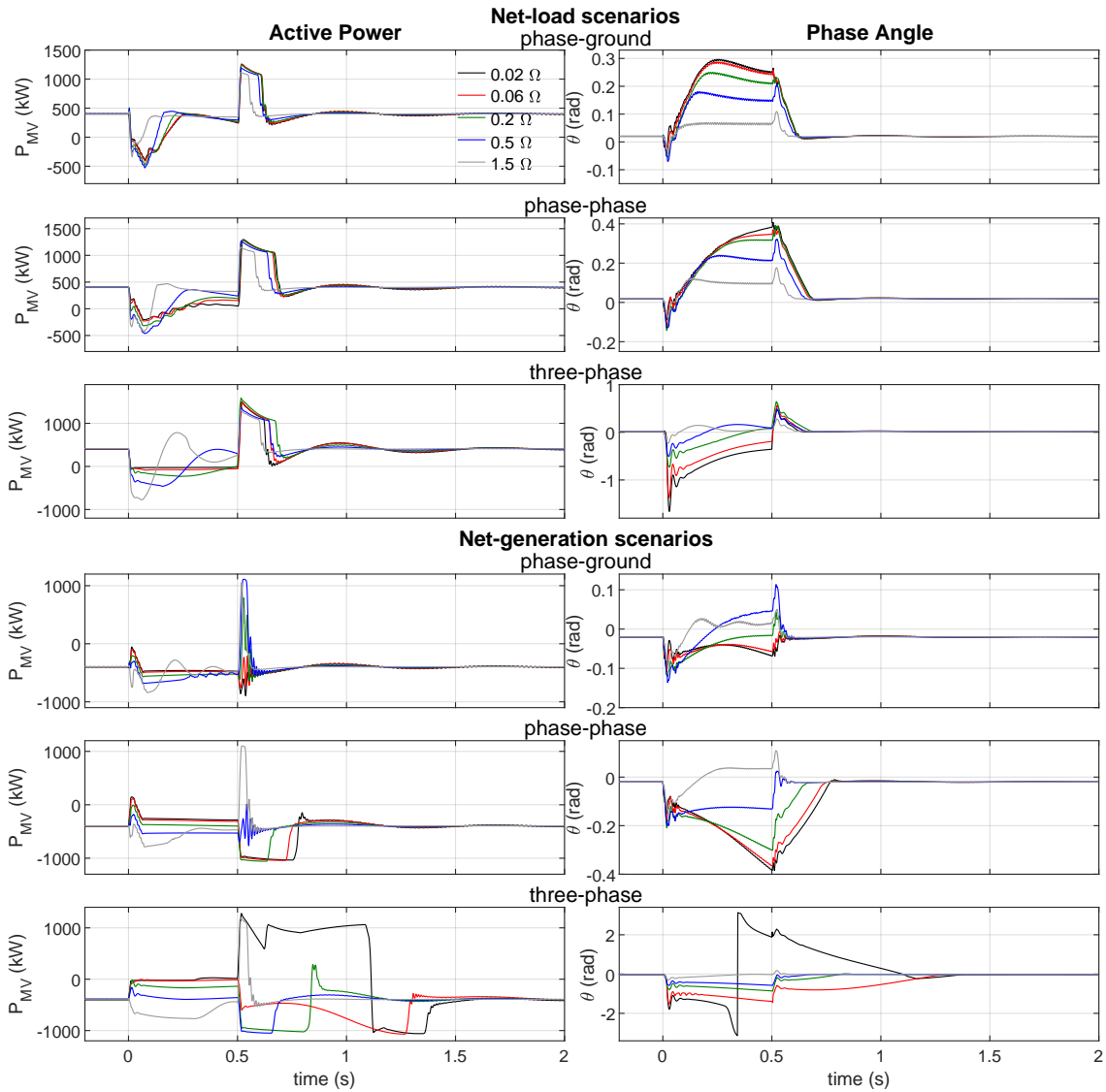


**Figure 6.32:** Active power and phase shift in the output LC filter of the ST's MV inverter, considering  $Z_{eq1}$  and fault impedances with a time duration of 0.5 s.

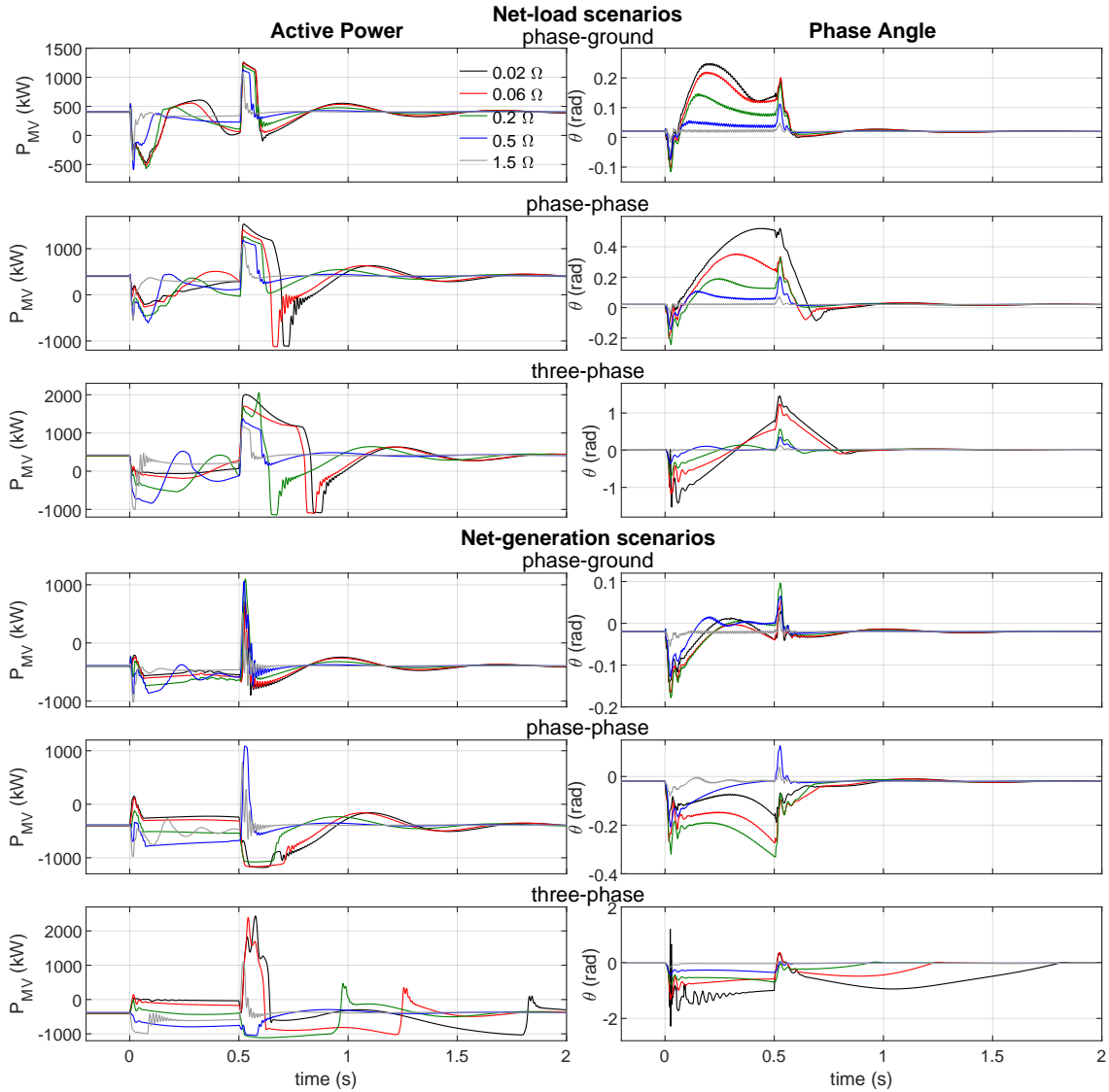


**Figure 6.33:** Active power and phase shift in the output LC filter of the ST's MV inverter, considering  $Z_{eq2}$  and fault impedances with a time duration of 0.5 s.

Another important observation drawn from the presented results is the frequent inversion of the active power flow in the ST's MV inverter during the actuation of the FRT mechanism, when the ST is absorbing power in the upstream AC grid (net-load) comparatively to the homologous scenarios where the ST is injecting power (net-generation). The occurrence of a fault disturbance affecting a ST operating as a load, forces a change in the direction of the power flow in the ST's MV inverter (towards the ST during normal conditions and towards the grid during the fault), which forces (comparatively) a larger phase shift in the ST's MV inverter, except for the most severe simulated symmetrical three-phase fault disturbances, as illustrated in Figures 6.32, 6.33, B.17 and B.18. Among the most severe fault disturbances, phase

"jumps" can be observed, specially visible in Figure 6.32, meaning that the phase reference of the ST's MV inverter "jumped" one or more laps in the trigonometric circle. Still, the ST was able to synchronize with the upstream AC power system after the fault extinction. This is evidence of robustness showed by the proposed FRT mechanism, which was able to assure the successful synchronization of the ST in its effort to limit  $I_{AC_{MV}}$ . The reason behind a possible loss of synchronization during the fault disturbance is the very low voltage at the ST's terminals caused by the fault disturbance, which poses an extremely challenging scenario for the grid-forming ST to attain the synchronism with the upstream AC power system.

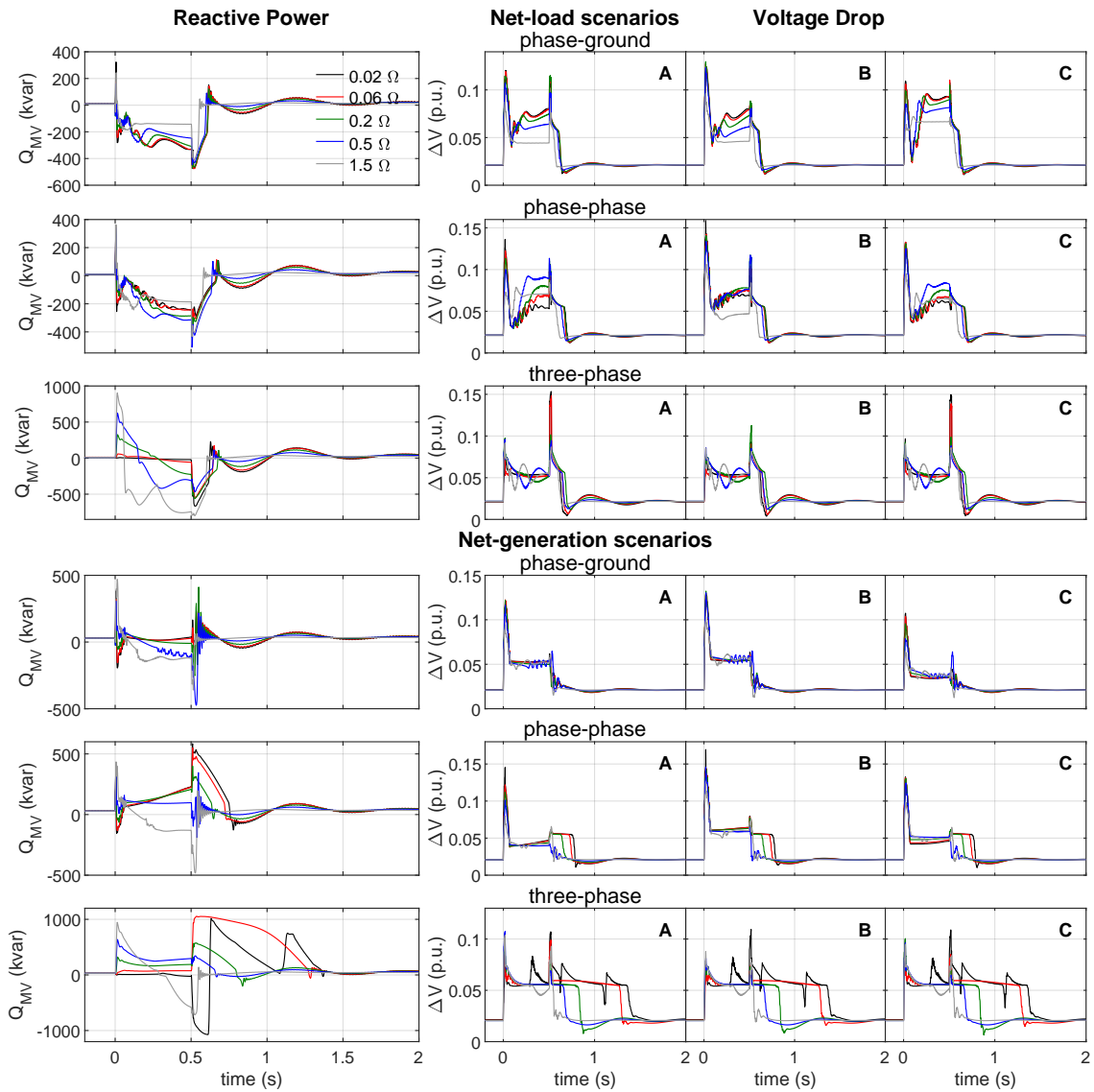


**Figure 6.34:** Reactive power and voltage drops (per phase) in the output LC filter of the ST's MV inverter considering  $Z_{eq1}$  and fault impedances with a time duration of 0.5 s.

In order to further evaluate the effectiveness of the proposed FRT mechanism, the

detailed AC current waveforms in the ST's MV inverter, around the time instants where the surge and extinction of fault disturbances in the upstream AC power system take place, are also presented in Figures 6.36, 6.37, B.21 and B.22. The presented current waveforms are related to symmetric and asymmetric faults considering the lowest fault impedance presented in Table 6.1 ( $0.02\Omega$ ), being considered the respective fault disturbances with time duration of 0.5 and 0.2 seconds for the scenarios considering the equivalent impedances  $Z_{eq1}$  and  $Z_{eq2}$ .

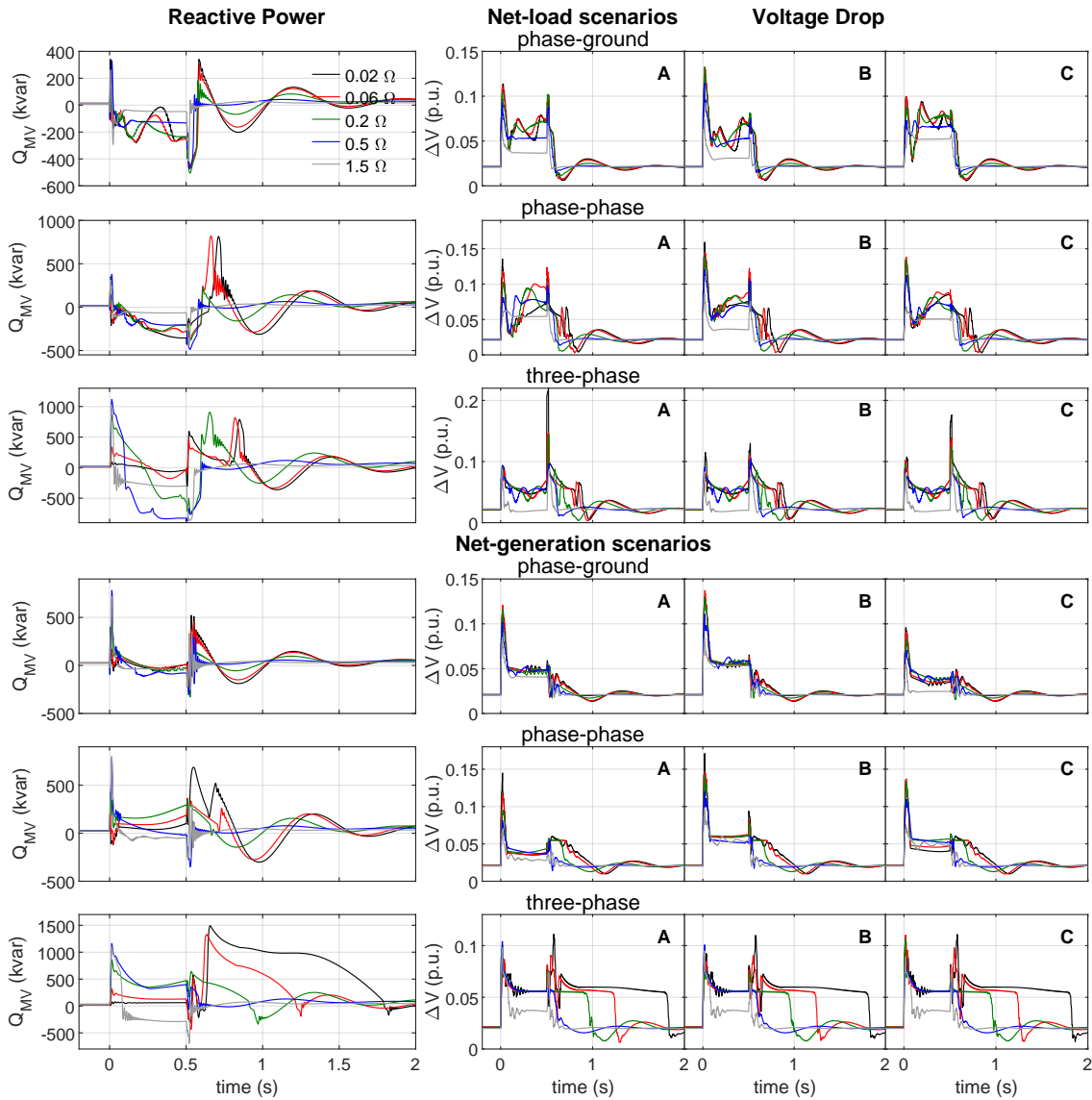


**Figure 6.35:** Reactive power and voltage drops (per phase) in the output LC filter of the ST's MV inverter considering  $Z_{eq2}$  and fault impedances with a time duration of 0.5 s.

In order to not overburden the chapter's reading, the results related to the fault disturbances with time duration of 0.2 seconds are shown in Appendix B, in Figures B.21 and B.22. The results related to the fault disturbances with time duration of

0.5 seconds are presented here since they represent the most extreme scenarios. It is possible to observe the presence of significant current distortions during the actuation of the FRT mechanism. The observed current distortions are more concentrated in the instants immediately after the surge and extinction of fault disturbances, and are more prominent in the scenarios related to asymmetric fault disturbances. In comparison, scenarios related to symmetric fault disturbances present in general a much lower distortions in  $IAC_{MV}$ , which are only significant after a fault extinction in the scenarios considering the equivalent impedance  $Z_{eq2}$  and faults with a time duration of 0.2 seconds.

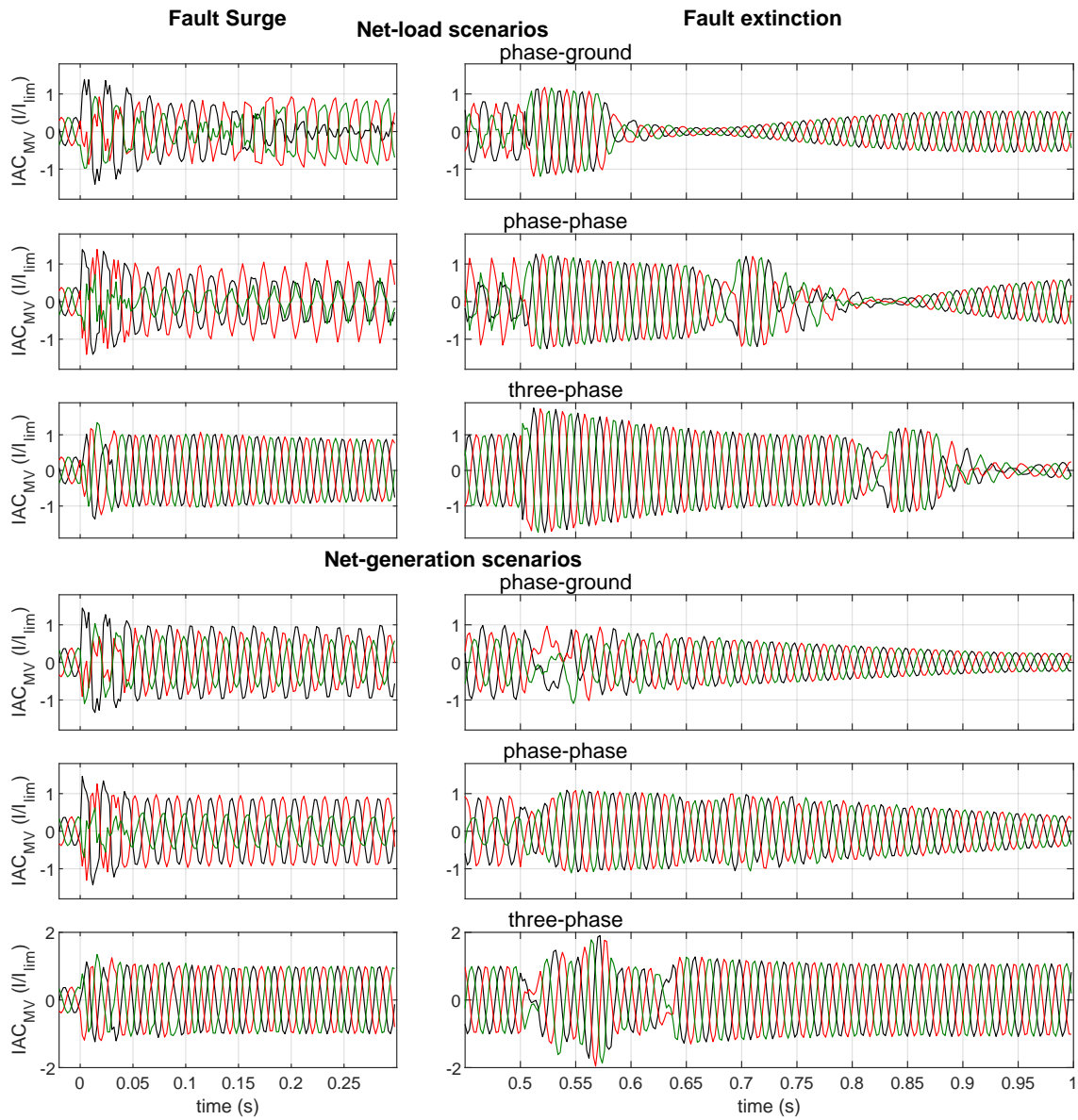


**Figure 6.36:** Three-phase current waveforms in the ST MV inverter for faults with impedance of  $0.02\Omega$  and time duration of 0.5 s, considering  $Z_{eq1}$ . Black: phase A current; Red: phase B current; Green: phase C current.



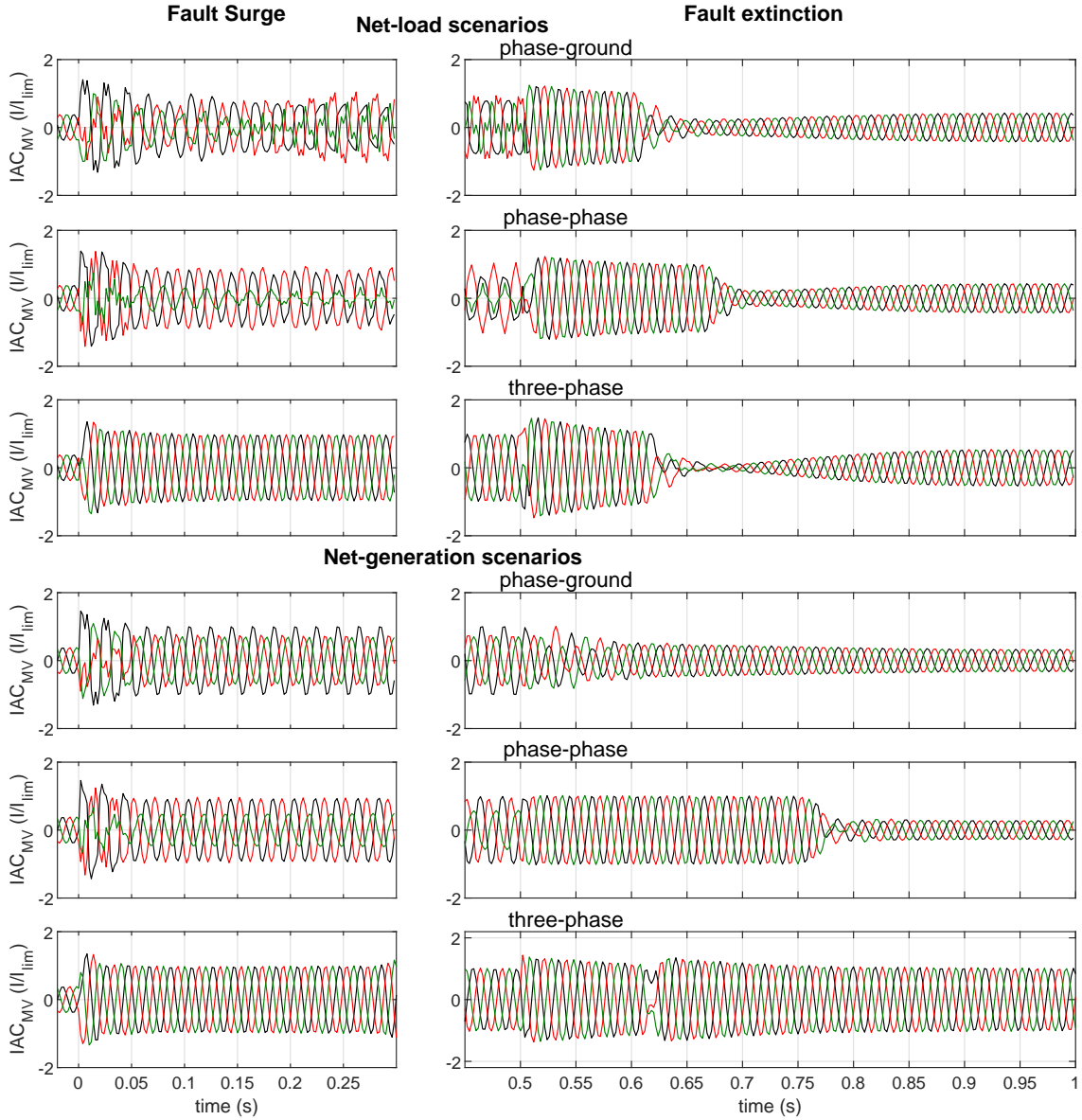


**Figure 6.37:** Three-phase current waveforms in the ST MV inverter for faults with impedance of  $0.02\Omega$  and time duration of 0.5 s, considering  $Z_{eq2}$ . Black: phase A current; Red: phase B current; Green: phase C current.

Besides the current distortions, current unbalances are also observed but only following asymmetric fault disturbances, which is expected given the voltage unbalances resulting from such faults. The predominance of current unbalances could be attenuated through a dedicated control for the negative symmetric component of the voltage. Also,  $IAC_{MV}$  distortions may also be partially attributed to the absence of a control for the negative symmetric component of the voltage, since the unbalanced nature of the voltage following an asymmetric fault disturbance forces a pulsating reaction of the FRT mechanism, whose actuation is partially non-linear in nature. Nevertheless, the inclusion of a control for the negative symmetric component of the voltage was

discarded because the obtained benefits did not overweight the crucial disadvantage of the time response delays it would introduce to the FRT mechanism, which severely compromises its effectiveness.

### 6.2.3 Case Study 4

The results related to the evaluation of the case study 4 are presented in this subsection. Starting with the voltage and frequency profiles in the HMMG side resulting from the fault disturbances described in Table 6.7 and subsequent islanding of the HMMG, the associated results highlighting the time evolution of different electrical quantities are illustrated in Figures 6.38 and 6.39.

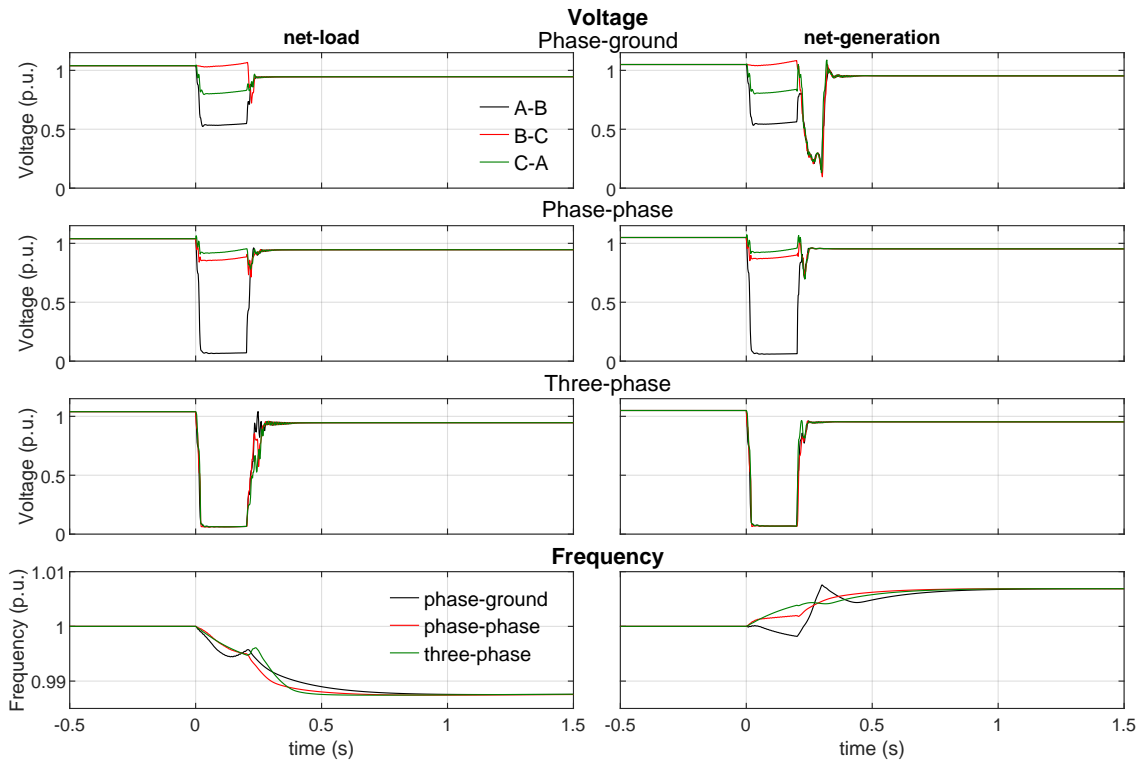


**Figure 6.38:** Voltage and frequency disturbances observed at HMMG side in the connection point with the upstream AC power system, resulting from fault disturbances in the upstream AC power system. HMMG islanding at time = 0.2 s

Similarly to previous case studies, the results presented in p.u. use the nominal voltages and frequency presented in Table 6.3 as base values, and the start of the fault disturbance considered in this case study is assumed to be at  $time (s) = 0$ . It is possible to observe that the islanding of the HMMG was successful for all simulated fault disturbances, as the voltage and frequency in the HMMG did not collapse after the islanding procedure. The islanded HMMG is sustained by the grid-forming ST which is now responsible to preserve the power balance in the HMMG.



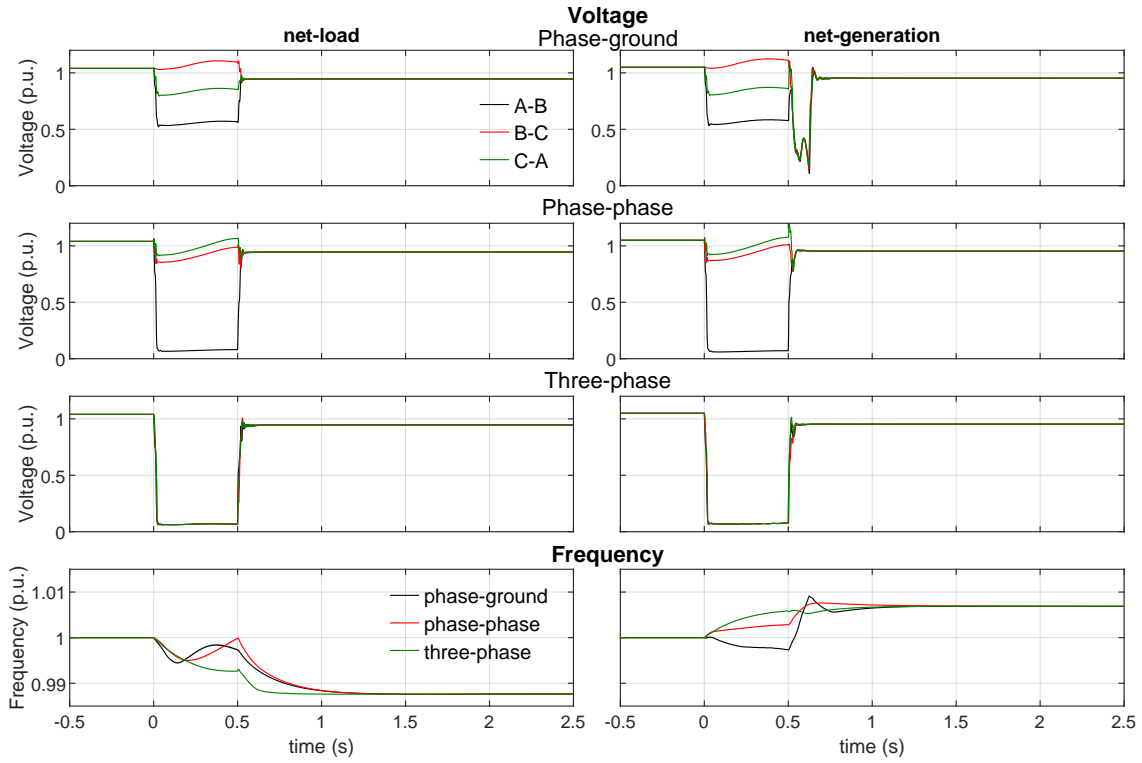


**Figure 6.39:** Voltage and frequency disturbances observed at HMMG side in the connection point with the upstream AC power system, resulting from fault disturbances in the upstream AC power system. HMMG islanding at time = 0.5 s

The grid-forming ST uses the  $f(\Delta P_{MV})$  droop controller embedded in the controller of the ST' MV inverter to perform the power balance in the HMMG, notorious in Figures 6.38 and 6.39 by observing the evolution of the HMMG frequency after the islanding. The frequency in the islanded HMMG stabilizes below the nominal value for net-load scenarios in the HMMG given the excess net-load in the HMMG, and above the nominal value for net-generation scenarios as there is an excess net-generation in the HMMG. This frequency deviation results from the deviation of the active power in the grid-forming ST from its active power set-point defined by the offset in the  $f(\Delta P_{MV})$  droop controller for the nominal frequency.

The active power throughout the HMMG, before the fault disturbance, during the fault disturbance and after the islanding of the HMMG, is illustrated in Figures 6.40 and 6.41, for fault disturbances with time durations of 0.2 and 0.5 seconds respectively. Positive values for the active power correspond to consumed power and negative values correspond to injected/generated active power. Figures 6.40 and 6.41 show the active power in the MV inverters of each ST integrated in the HMMG, as well the remaining load and generation in the HMMG. It is possible to observe that both ST remained in operation following the fault disturbances and subsequent islanding of

the HMMG, for all considered fault scenarios. During net-generation scenarios, the DG unit in bus 3 suffers a transient following the islanding of the HMMG in some of the simulated fault scenarios, but still, the grid-forming ST reacted accordingly and sustained the islanded operation of the HMMG.

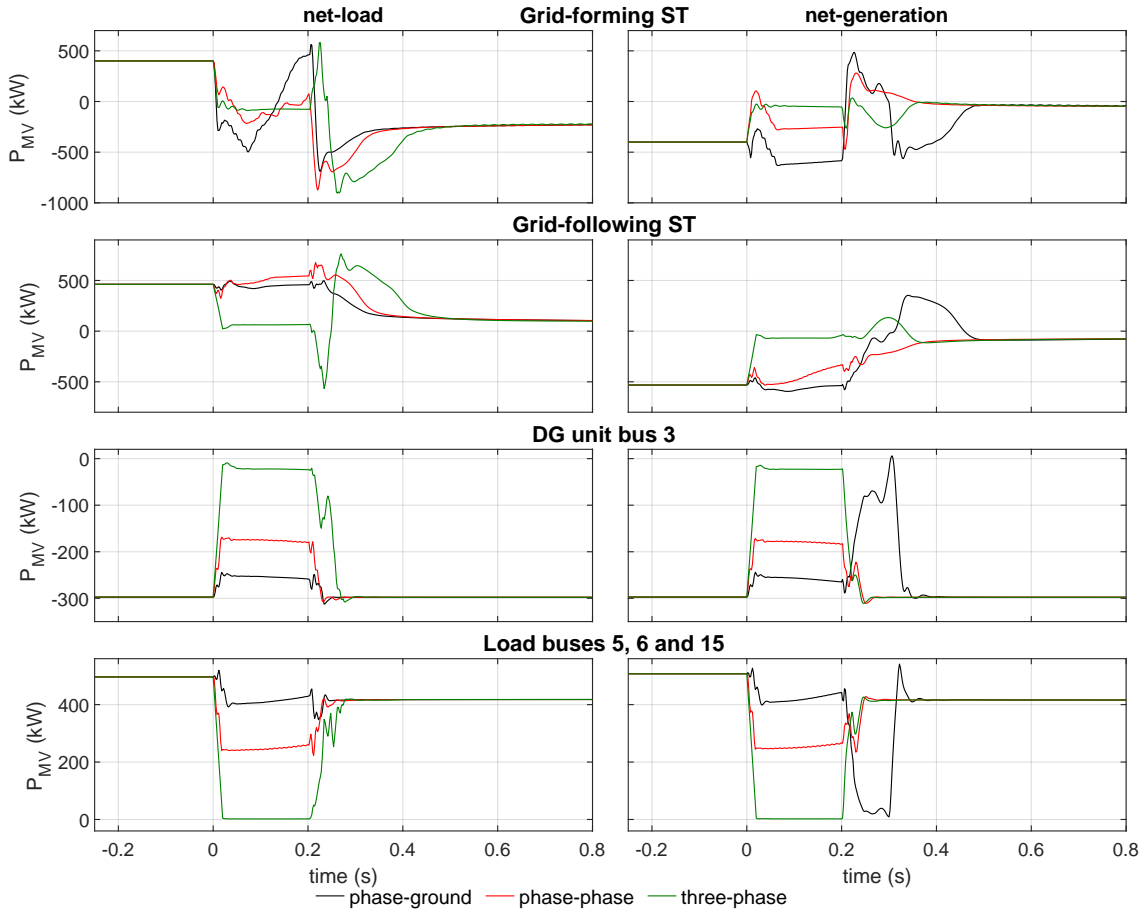


**Figure 6.40:** Active power profiles in the ST and remaining generation and loads integrating the HMMG for all types of fault disturbances. HMMG islanding at time = 0.2 s

The most important observation from the presented results is the redistribution of the active power among the resources in the HMMG after the islanding of the HMMG takes place, with both ST operating in a coordinated manner. For net-generation scenarios, the steady-state active power injected by both grid-forming and grid-following ST reduces considerably, as most of it cannot be consumed in the HMMG. For net-load scenarios, the grid-forming ST inverts its steady-state output power (from load to generator) while the grid-following ST reduces considerably its consumed active power in steady-state operation. This active power redistribution is a consequence of the power-frequency sensitivity of the grid-forming ST, which changes its output frequency (and hence, the frequency of the HMMG) in order to adjust its output power to preserve the power balance in the HMMG (Figures 6.38 and 6.39). By other hand,

the power-frequency sensitivity of the grid-following ST (and its hybrid AC/DC grid) enables it to provide a precious contribution for the power balance in the HMMG. The grid-forming ST achieves such reduction through its  $f(\Delta P_{MV})$  which indirectly commands the ST's local ESS as slack power unit, while the grid-following ST exploits its power-frequency support mechanism to reduce the net-generation in its based hybrid AC/DC grid. These mechanisms were already validated in case studies 1 and 3 (subsections 6.2.1 and 6.2.2), and thus, are not described in detail here. As expected, this outcome is not influenced by the time duration or type of the fault disturbance preceding the islanding of the HMMG. The different types of fault disturbances only influence the settling time of the steady-state operation.

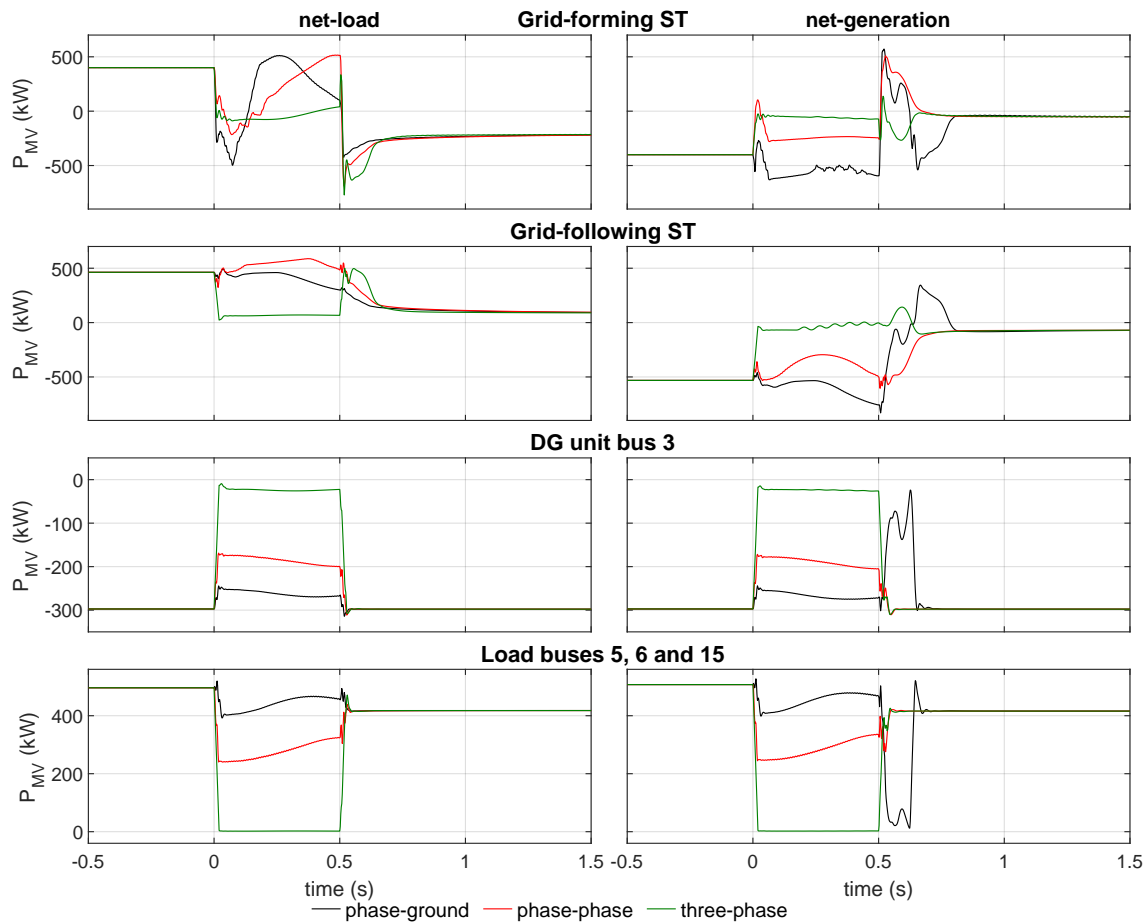


**Figure 6.41:** Active power profiles in the ST and remaining generation and loads integrating the HMMG for all types of fault disturbances. HMMG islanding at time = 0.5 s

The steady state operation of the DG unit remains unchanged (it operates as a constant power source). The active power consumed by the load in buses, 5, 6 and 15 show a reduction because the voltage levels in the islanded HMMG are lower comparatively to those observed with the HMMG operating connected to the upstream AC power system. This results from the fact that the reactive power consumed by

the load in buses, 5, 6 and 15 with the HMMG operating in islanded mode is now provided by the grid-forming ST and not by the upstream AC power system, as evidenced in Figures 6.42 and 6.43. In face of the increased reactive power demand, the  $\Delta VAC_{MV}(Q_{MVg})$  droop controller integrating the MV inverter of the grid-forming ST reduces the magnitude of the voltage generated by the grid-forming ST.

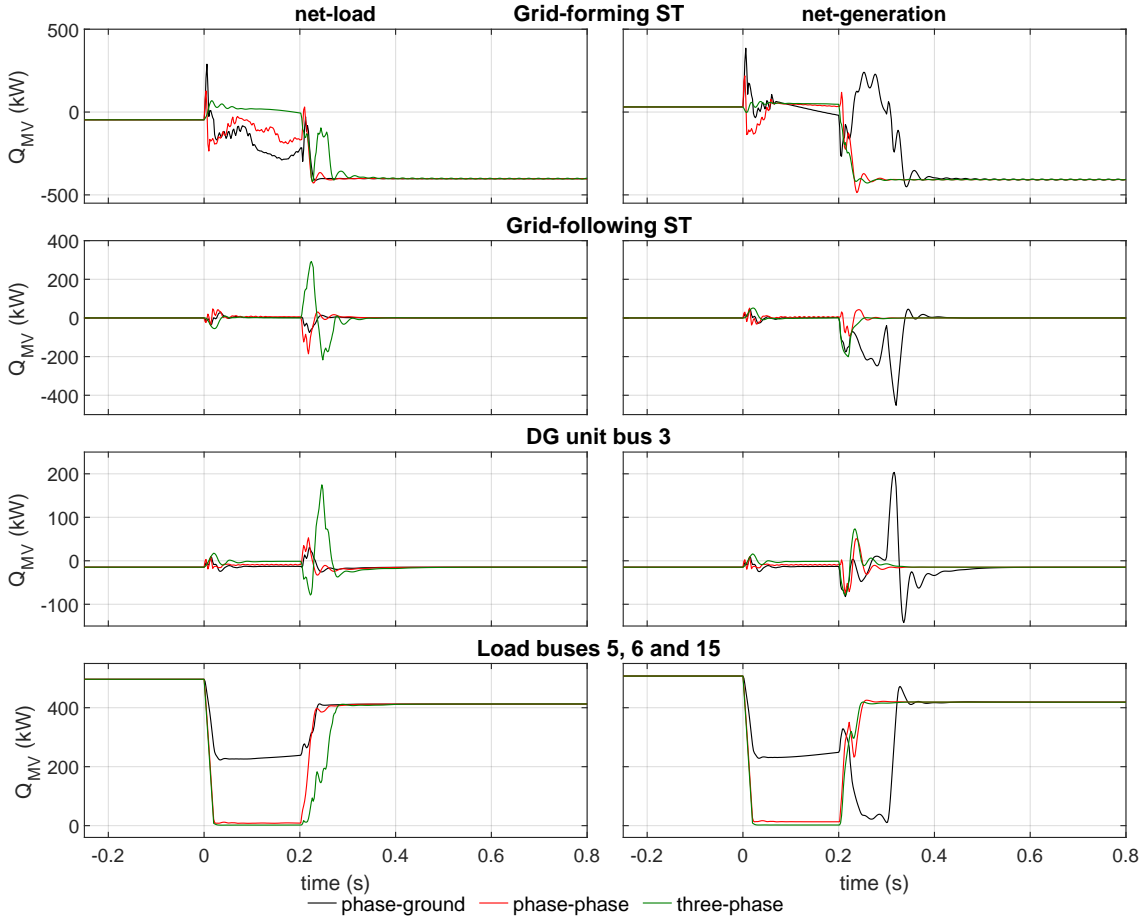


**Figure 6.42:** Reactive power profiles in the ST and remaining generation and loads integrating the HMMG for all types of fault disturbances. HMMG islanding at time = 0.2 s

### 6.2.4 Case Study 5

At last, the evaluation of case study 5 is presented in this subsection. This case study considers that the LV AC grid with feeding points provided by the MV/LV distribution substation in bus 3 (based on a LFT) and by the grid-forming ST (see Figure 6.3) is initially operating in ring configuration. For the sake of simplicity, the MV/LV distribution substation in bus 3 based on a LFT is designated henceforth in this subsection simply by LFT.

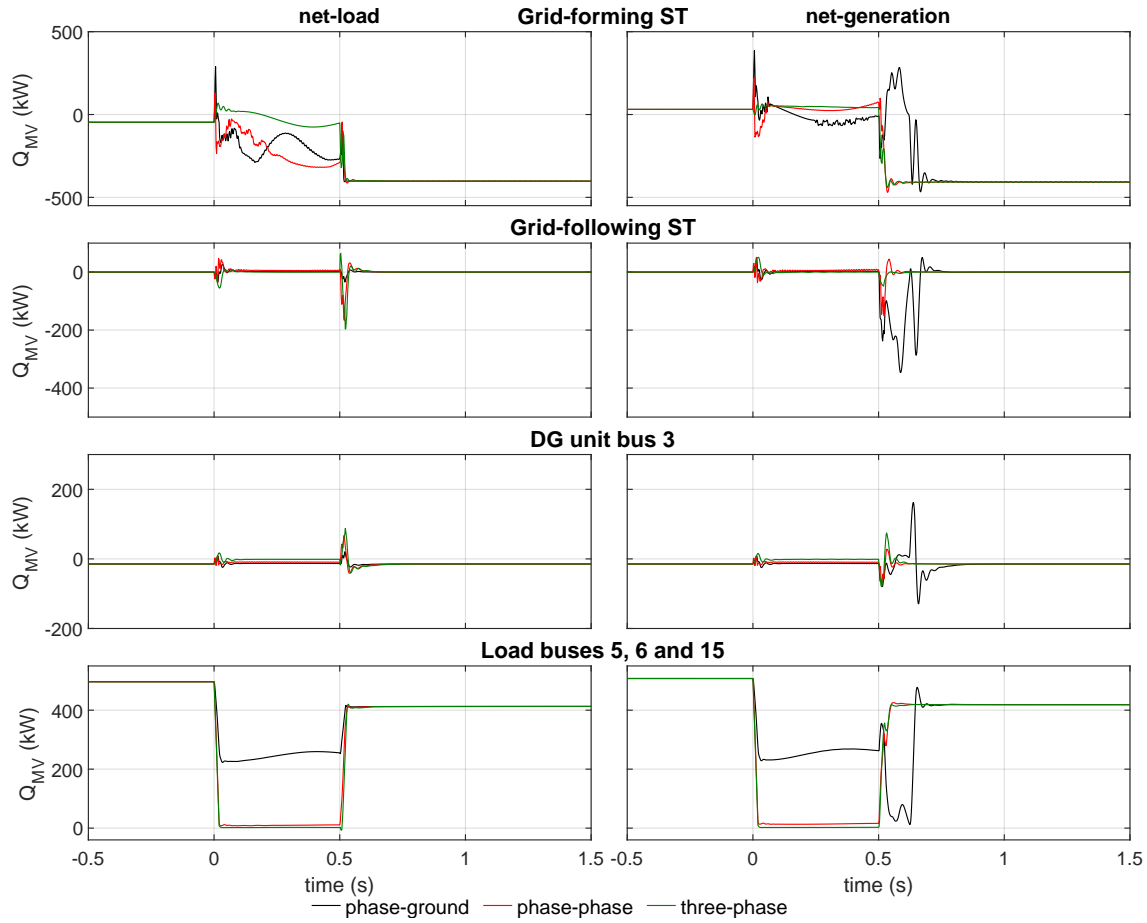


**Figure 6.43:** Reactive power profiles in the ST and remaining generation and loads integrating the HMMG for all types of fault disturbances. HMMG islanding at time = 0.5 s

At a given moment in time, the LFT is disconnected, and the LV AC grid becomes dependent on the grid-forming ST as the remaining feeding connection. This transition is illustrated in Figure 6.44. It can be observed that the ST is capable to assume all the LV AC grid with no noticeable difficulties in case of disconnection of the LFT. The active and reactive power flows previously traveling through the LFT are now assumed by the ST, with positive values for the active power corresponding to consumed power while negative values correspond to injected/generated active power. Figure 6.44 also shows the angular position difference between the voltages in the LV and MV AC grids. It is possible to observe that the angular position difference between the voltages in the LV and MV AC grids starts to increase following the disconnection of the LFR. This results from the fact that the frequency in the LV AC grid is no longer coupled to the frequency in the MV AC grid, and both start to drift apart. It is important to mention that the illustrated angular position difference already have into account the phase shift associated to the vector group of the LFT.

In a posterior moment, the LFT is ready to be connected again, and then, the pre-

synchronization mechanism implemented in the grid-forming ST is initiated, in order to prepare the LV AC grid to be reconfigured in ring configuration. This action is followed by the effective reconnection of the LFR, thus concluding the reconfiguration of the LV AC grid in ring configuration. This transition is illustrated in Figure 6.45. Prior to the start of the pre-synchronization, the evolution of the angular position difference between the voltages in the LV and MV AC grids indicates that the frequencies of both AC grids were not correlated. After the *Instant 1* a coupling process between the two frequencies is initiated. In the *Instant 2*, the phase-shift associated to the vector group of the LFT is introduced. Finally, in *Instant 3*, the LFT is reconnected. After *Instant 3* it is possible to observe a redistribution of the active and reactive power in the LV AC grid among the two feeding points. Besides the influence of the voltage levels in the MV AC grid, the active and reactive power flowing through the LFT can be regulated by adjusting the parameters of the droop controllers integrating the grid reconfiguration mechanism. It is important to mention that the reconnection process does not cause severe transients following the instant the LFT is reconnected, as illustrated in Figure 6.46 (LFT reconnection at time = 0).

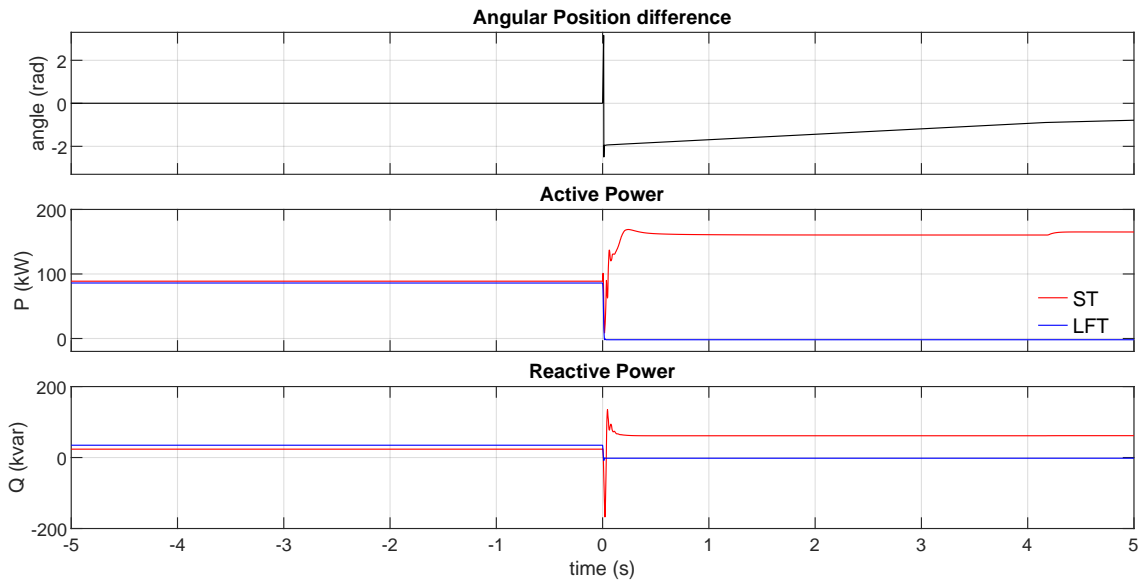


**Figure 6.44:** Active and Reactive power in the LFT and ST's LV inverter, and angular position difference between the voltages in the LV and MV AC grids, following the disconnection of the LFT.

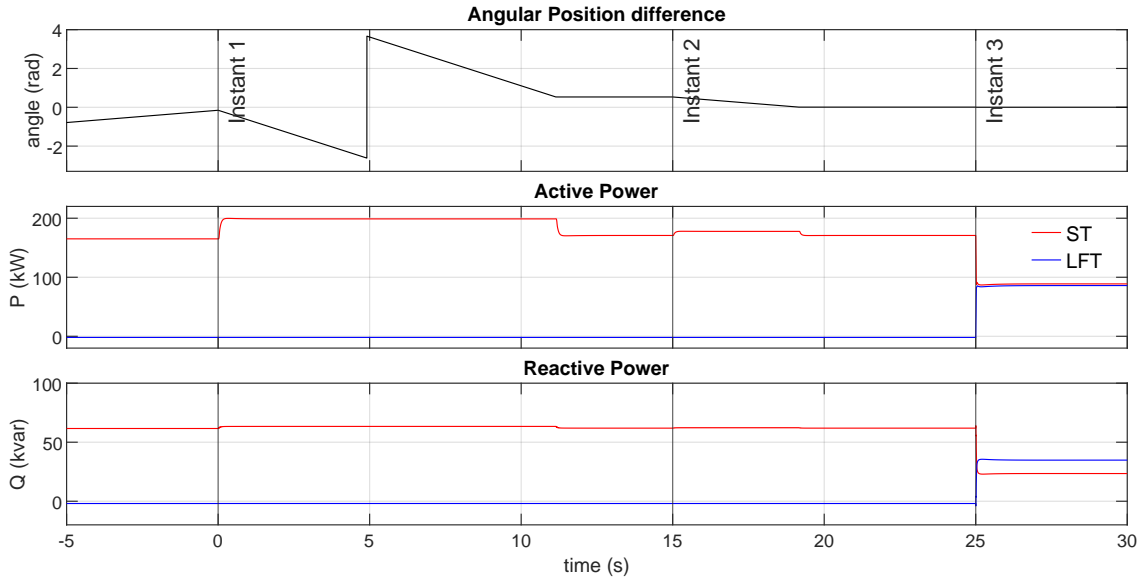


**Figure 6.45:** Active and Reactive power in the LFT and ST's LV inverter, and angular position difference between the voltages in the LV and MV AC grids, following the pre-synchronization process and the effective reconnection of the LFT.

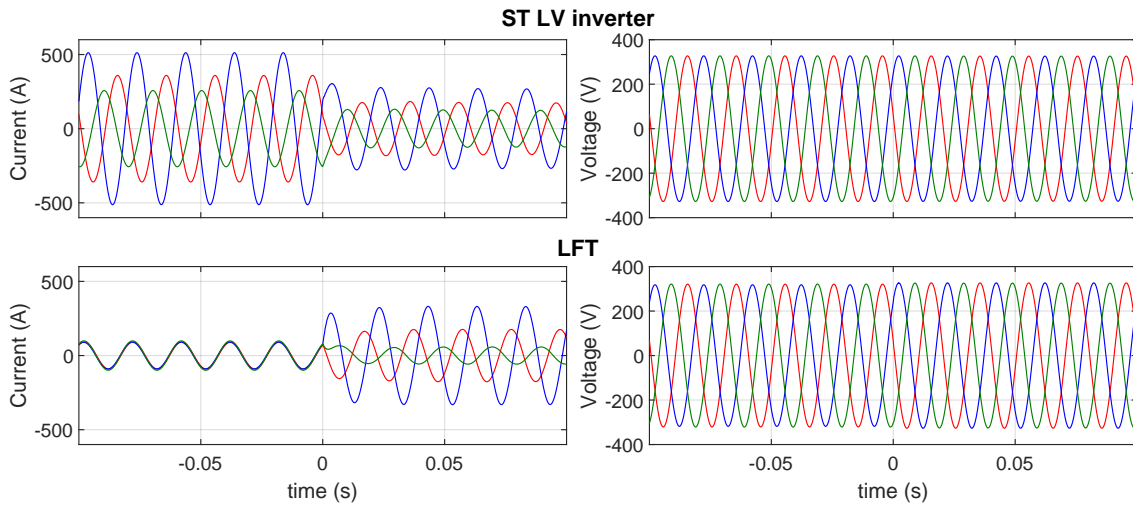


**Figure 6.46:** Three-phase voltage and currents in the LV inverter of the ST and in the LFT (secondary winding) following the reconnection of the LFT to the upstream AC power system.

### 6.3 Final Remarks - Summary

This chapter describes the case studies and the respective results demonstrating the effectiveness of the proposed FRT control and grid reconfiguration strategies, namely:

- The capability of a grid-following ST with no local ESS available to provide FRT by exploiting the flexibility of its hybrid AC/DC grid. It is also demonstrated that the proposed FRT is suitable for simultaneous operation with the aforementioned power-frequency support functionalities demonstrated in chapter 5.

- The capability of the grid-forming ST in provide FRT while operating in grid-forming mode, and sustain the transition of wider HMMG to islanded mode after a fault disturbance. It is also demonstrated that grid-forming and grid-following ST can operate in a coordinated manner regarding the provision of FRT and power–frequency support in an islanded HMMG.
- The incorporation of communication-free grid reconfiguration mechanisms in ST, enabling the formation of meshed distribution grids.

The FRT control strategy for the grid-following ST relies on the exploitation of load-voltage and load-frequency sensitivity on its based hybrid AC/DC grid (comprising resources such as non-controllable load, ESS, EV chargers and PV generation), but also on a dump-load for net-generation scenarios in its hybrid AC/DC grid, to dissipate its net generated power. The FRT control strategy for the grid-forming ST is based on a virtual impedance combined with the exploitation of the voltage drop in the output filter of the ST in order to enhance the current limitation capabilities of the ST. The effectiveness of the proposed FRT strategies is demonstrated for symmetrical and asymmetrical voltage sags, while considering also net load and net generation scenarios in the ST-based hybrid AC/DC distribution grids.

The presented numerical simulation results, illustrated in different operating scenarios showing the effectiveness of the proposed approaches, provide support to the possibility of further exploiting the proposed solution in ST regarding FRT provision and grid reconfiguration capabilities.



# Chapter 7

## Conclusions and Future Research

### 7.1 Conclusions

The work presented in this thesis exploits advanced control functionalities for Smart-Transformers (ST) integrating Hybrid Microgrids (HMG) and Hybrid Multi-Microgrids (HMMG), aiming to enhance and consolidate the controllability of HMG and HMMG concepts in face of the expected increasing penetration ratios of Distributed Generation (DG), Electric Vehicles (EV) and Energy Storage Systems (ESS). After a careful literature review presented in chapter 2, important literature gaps were identified in this regard. Given the wide range of the potentialities offered by the ST, and the impossibility to address all identified literature gaps with the deserved detail in this thesis, the following research topics were selected given its prominence:

- Provision of power–frequency support functionalities to the upstream AC power system by exploiting the flexibility available in a ST-based HMG, namely exploiting the flexibility available in the fleet of distributed resources located in the HMG.
- Provision of Fault-Ride-Through (FRT) capabilities by a ST with its MV inverter operating in grid-following mode, in order to improve immunity to fault disturbances within its hybrid HMG in events where energy storage capacity is insufficient or unavailable.
- Evaluation of the capability of the ST to sustain the islanded operation of a HMMG and sections of the legacy MV AC network following fault disturbances in the upstream power system, by exploiting the operation of the MV inverter of the ST in grid-forming mode and the incorporation of FRT capabilities enabling the ST to remain connected during the fault disturbance and sustain the islanding procedure.

- The provision of on-line grid reconfiguration capabilities for ST-based and non-ST based distribution grids enabling the reconfiguration of radial and meshes grid structures within a HMMG.

The effectiveness of the advanced control functionalities proposed in this thesis (chapter 4) to address the aforementioned research gaps were successfully demonstrated in the work developed in this thesis (chapters 5 and 6).

The effectiveness of the advanced control functionalities to endow a ST and its based HMG with the capability to provide power–frequency support to the upstream AC power system is evaluated in chapter 5. The proposed control strategies rely on a set of droop-based controllers incorporated in the ST power conversion stages that are responsible to modulate its electrical variables (DC grids voltage, LV AC grid voltage and frequency) as well as the local ESS active power. Moreover, droop based controllers are also associated to controllable DER available in the hybrid distribution network, making them responsive to electric variables generated by the ST. The load-voltage sensitivity of AC and DC connected loads is also exploited as a possible contribution within the scope of the active power-frequency regulation. It was demonstrated that a ST with its MV inverter operating in grid-following mode is capable to modulate the active power in its local ESS and in the resources available in its hybrid AC/DC grid in order to obtain the active power contribution required for the provision of power – frequency support. Regarding a ST with its MV inverter operating in grid-forming mode, it is shown that although it relies on its local ESS to provide immediate power – frequency support to the upstream AC grid, the active power sensitivity of its hybrid AC/DC grid can also be exploited in order to reduce the power and energy required to the ST's local ESS to perform such task.

The advanced control functionalities proposed to endow ST with FRT capabilities are evaluated in chapter 6. It was demonstrated that a ST with its MV inverter operating in grid-following mode and without local energy storage capacity available is capable to exploit the flexibility of its hybrid AC/DC grid in order to make the provision of FRT possible. During net generation scenarios, the proposed FRT control strategy relied successfully on a dump-load to dissipate the excessive net generation in the hybrid AC/DC network, but also exploited the load-frequency sensitivity in the LV AC sub-grid. Regarding net load scenarios, the proposed FRT control strategy modulated the electrical quantities in the hybrid AC/DC grid (voltages in DC grids and LV AC grid, and frequency in LV AC grid), thus exploiting its power-voltage and power-frequency sensitivities in order to eliminate its excessive net load. It is also demonstrated that the proposed FRT is suitable for simultaneous operation with the

aforementioned power–frequency support functionalities demonstrated in chapter 5. The effectiveness of the FRT control functionalities for ST with its MV inverter operating in grid-forming mode is also demonstrated in chapter 6. It is demonstrated that a grid-forming ST can withstand fault disturbances without changing its control architecture, and sustain the transition of wider HMMG to islanded mode after a fault disturbance. It is also demonstrated that grid-forming and grid-following ST can operate in a coordinated manner regarding the provision of FRT and power–frequency support in an islanded HMMG. The effectiveness of the proposed strategies are demonstrated against symmetric and asymmetric fault disturbances while considering also net load and net generation scenarios in the ST’s hybrid AC/DC distribution grid.

At last, the incorporation of communication-free grid reconfiguration mechanisms in ST, enabling the formation of meshed distribution grids, is also demonstrated in chapter 6. It is shown that the synchronization of several LV AC grids under the same MV AC grid in a meshed configuration is possible by resorting solely to the angular position and frequency in the MV AC grid, which are easily measured by the ST from the upstream MV AC grid in the point where it is connected.

## 7.2 Future Research

Several interesting research topics related with the presented work, but not limited to, should deserve a proper evaluation in the future. They are enumerated as follows:

- The FRT control approach proposed for grid-following ST successfully exploits all the available resources connected downstream the ST together with complementary solutions at the ST level. However, the parameterization of the FRT controller as a function of the existing resources in the hybrid AC/DC distribution network is not addressed. This topic is relevant since the performance of the proposed FRT control approach is dependent on the characteristics of the hybrid AC/DC grid in question.
- The coordination of several ST incorporating the proposed FRT control approach but taking into account the influence of synthetic inertia in the ST remains to be evaluated. This aspect is of utmost importance regarding transient stability given the interaction not only among ST but also with conventional generation units.
- FRT capabilities for meshed distribution LV AC grids involving several ST also deserves further attention.
- The implementation of black-start capabilities using ST in HMMG requires

further evaluation as well. In this context, DC grids may play a fundamental role in a quick setup of distribution grids following a catastrophic blackout, since DC grids based on ST do not require frequency synchronization and may operate as flexible power buffers among AC grids.

# Appendices



# Appendix A

## Parametrization of Smart-Transformers, Hybrid Microgrids and Hybrid Multi-Microgrids

### A.1 Smart-Transformers

Table A.1: Smart-Transformer: general parameters

Nominal Power	1 MVA
Nominal MV AC Voltage (ph-ph)	15000 V (RMS)
Nominal MV DC link Voltage	27000 V
Nominal LV DC link Voltage	720 V
Nominal LV AC Voltage (ph-n)	230 V (RMS)
Nominal frequency (MV and LV inverters)	50 Hz
Switching frequency (All power converters)	20 kHz
<b>LC filter in the MV inverter</b>	
Capacitance (F) / Resistance capacitor ( $\Omega$ )	$1.6 \times 10^{-7}$ / $1 \times 10^{-3}$
Inductance (H) / Resistance inductor ( $\Omega$ )	$3.95 \times 10^{-2}$ / 1
<b>LC filter in the LV inverter</b>	
Capacitance (F) / Resistance capacitor ( $\Omega$ )	$3.3 \times 10^{-4}$ / $1 \times 10^{-2}$
Inductance (H) / Resistance inductor ( $\Omega$ )	$8.5 \times 10^{-6}$ / $1 \times 10^{-3}$
<b>ST DC buses</b>	
MV bus Capacitance (F) / Resistance capacitor ( $\Omega$ )	$1.008 \times 10^{-5}$ / $1 \times 10^{-3}$
LV bus Capacitance (F) / Resistance capacitor ( $\Omega$ )	$1.42 \times 10^{-2}$ / $1 \times 10^{-3}$

Table A.2: Grid-Following MV inverter: Control parameters

VDC Control / P Control				
PI Control		P = 50; I = 10000		
Current Control				
PI Control for $I_{d_{MV}}$		P = 0.5; I = 800	PI Control for $I_{q_{MV}}$	P = 0.5; I = 400
$P(f_{MV})$ droop controller				
Slope		4000	Dead-band: high / low	50.025 / 49.975
Offset		0	Saturation: min / max	5000 / -5000
$VDC_{MV}(f_{MV})$ droop controller				
Slope		30000	Dead-band: high / low	0.025 / -0.025
Offset		0	Saturation: min / max	$1 \times 10^5$ / $-1 \times 10^5$
FRT Control				
$k_{dl}$	-0.1	$k_{LV}$	0.014	
$k_{MV}$	0.014	$k_f$	-0.028	
$I_{DLmax}$	80	$\Delta f_{max}$	2	
$\Delta f_{min}$	-2			

Table A.3: Grid-Forming MV inverter: Control parameters

<b><math>f(\Delta P_{MV})</math> droop controller</b>	
Slope	$1 \times 10_{-6}$
Offset	see case studies in chapters 5 and 6
Dead-band: high / low	0 / 0
Saturation: min / max	$1 \times 10_6$ / $-1 \times 10_6$
<b>First-order low-pass filter</b>	
Time constant	0.25
<b><math>\Delta VAC_{MV}(Q_{MVg})</math> droop controller</b>	
Slope	0.002
Offset	0
Dead-band: high / low	0 / 0
Saturation: min / max	$1 \times 10_6$ / $-1 \times 10_6$
<b><math>VDC_{MV}(f_{MV})</math> droop controller</b>	
Slope	4000
Offset	0
Dead-band: high / low	50.025 / 49.975
Saturation: min / max	5000 / -5000
<b>FRT control</b>	
Virtual impedance ( $Z_V$ ): $R_d$ / $R_q$ / $R_o$	1000 / 500 / 500
$k_p$	$5 \times 10^5$
<b>miscellaneous</b>	
PI Control for $VDC_{MV}$	P = 0.2; I = 50
$k\theta d$ (damping coefficient)	0.03



**Table A.4:** Hypothetical Supercapacitor Bank (not modeled). An illustrative example of a supercapacitor bank using a commercially available solution as reference [260]. The required capacitance was determined according to Equation (3.29) for the following assumptions: A maximum DC voltage ripple of 0.5% in the ST's MV DC bus due to unbalanced voltage sags in the MV AC grid, and a maximum 90% drop in the LV DC bus voltage during a voltage sag in the MV AC grid.

Pack: Assembling	63 (parallel) $\times$ 4 (series)		
Pack: Nominal voltage	10.8 V	Unit: Nominal voltage	2.7 V
Pack: Capacitance	7.88 kF	Unit: Capacitance	500 F
Pack: Peak power	1.8 MW	Unit: Peak current	400 A

**Table A.5:** Grid-Forming LV inverter: Control parameters

<b><math>V_{AC_{LV}}(P_{AC_{LVg}})</math> droop controller</b>	
Slope	$1.5 \times 10^{-6}$
Offset	0
Dead-band: high / low	50.025 / 49.975
Saturation: min / max	25 / -25
<b><math>f_{LV}(f_{MV})</math> droop controller</b>	
Slope	1.5
Offset	0
Dead-band: high / low	50.025 / 49.975
Saturation: min / max	0.5 / -0.5
<b><math>V_{AC_{LV}}(f_{MV})</math> droop controller</b>	
Slope	80
Offset	0
Dead-band: high / low	50.025 / 49.975
Saturation: min / max	25 / -25
<b>Grid reconfiguration mechanism</b>	
$k_{VP}$	0.5
$k_{VQ}$	0.5
$k_{\theta P}$	0.5
$k_{\theta Q}$	0.5
Slope $\theta(P : Q)$ droop	$8.7 \times 10^{-8}$
Slope $V(P : Q)$ droop	$1.5 \times 10^{-6}$

## A.2 Hybrid Microgrids and Hybrid Multi-Microgrids

Table A.6: Upstream AC power system

<b>Equivalent synchronous machine</b>	
Nominal Power	1 GW
line-to-line voltage	15 kV
Nominal frequency	50 Hz
Inertia coefficient	2 s
Reactances: $X_d$ ; $X_d'$ ; $X_d''$ ; $X_q$ ; $X_q'$ ; $X_q''$ ; $X_l$	1.6; 0.7; 0.35; 1.55; 0.85; 0.35; 0.2 (p.u.)
Time constants: $T_d'$ ; $T_d''$ ; $T_q'$ ; $T_q''$	5; 0.06; 0.2; 0.06 (s)
<b>Equivalent load</b>	
line-to-line voltage	15 kV
Initial active power	600MW
Initial reactive power	200Mvar
Nominal frequency	50 Hz
<b>Equivalent impedance (default)</b>	$0.02 + 0.23\Omega$
<b>Governor TGOV<sub>1</sub></b>	
Droop constant	5%
Remaining parameters as default values according to original model available in MATLAB <sup>®</sup> /Simulink <sup>®</sup> .	
<b>Governor TGOV<sub>1</sub></b>	
Default values from the original model available in MATLAB <sup>®</sup> /Simulink <sup>®</sup> .	
<b>Speed Regulator</b>	
Integral gain	3

Table A.7: Base parameters for the simplified LV AC sub-grid: buses, lines and loads (per phase)

Bus in	Bus out	Cable	Bus	Active Load	Reactive Load
ST	1	$0.019 + j0.003\Omega$	1	[0.9 0.4 0.0] kW	[0.3 0.1 0.0] kvar
1	2	$0.012 + j0.002\Omega$	2	[0.1 2.9 3.1] kW	[0.0 0.9 0.9] kvar
2	3	$0.004 + j0.001\Omega$	3	[0.2 4.5 0.9] kW	[0.0 1.4 0.3] kvar
3	4	$0.01 + j0.003\Omega$	4	[2.7 7.0 0.7] kW	[0.8 2.2 0.2] kvar
4	5	$0.011 + j0.003\Omega$	5	[12.7 14.7 1.3] kW	[4.0 4.7 0.4] kvar
5	6	$0.03 + j0.006\Omega$	6	[0.6 4.0 0.5] kW	[0.2 1.2 0.2] kvar
6	end	$0.029 + j0.004\Omega$			

**Table A.8:** Base parameters for the simplified LV AC sub-grid: DER units (per phase)

Bus	PV	EV charging	Energy Storage
Installed capacity			
1	[2.0 1.0 0.5] kW	[0.0 0.0 2.0] kW	[1.0 0.0 0.0] kW
2	[1.5 1.5 1.5] kW	[2.0 0.0 0.0] kW	[1.0 0.0 0.0] kW
3	[0.0 3.0 0.0] kW	[0.0 2.0 0.0] kW	[0.0 2.0 0.0] kW
4	[1.0 2.0 1.0] kW	[4.0 0.0 2.0] kW	[2.0 0.0 1.0] kW
5	[5.0 5.0 5.0] kW	[6.0 6.0 0.0] kW	[2.0 2.0 2.0] kW
6	[1.0 2.0 1.0] kW	[0.0 0.0 2.0] kW	[0.0 1.0 0.0] kW
Current consumption/injection			
1	[-2.0 -1.0 -0.5] kW	[0.0 0.0 1.5] kW	[0.0 0.0 0.0] kW
2	[-1.5 -1.5 -1.5] kW	[1.5 0.0 0.0] kW	[0.5 0.0 0.0] kW
3	[0.0 -3.0 0.0] kW	[0.0 1.0 0.0] kW	[0.0 1.0 0.0] kW
4	[-1.0 -2.0 -1.0] kW	[0.0 0.0 1.5] kW	[0.0 0.0 0.0] kW
5	[-5.0 -5.0 -5.0] kW	[0.0 0.0 1.5] kW	[1.0 1.0 1.0] kW
6	[-1.0 -2.0 -1.0] kW	[0.0 0.0 1.0] kW	[0.0 1.0 0.0] kW

**Table A.9:** Base Simplified LV AC sub-grid: load-voltage and load-frequency sensitivity coefficients (per phase)

Coefficient	Phase A	Phase B	Phase C
$k_{pv}$	0.62	0.42	0.31
$k_{qv}$	0.29	0.21	0.15
$k_{pf}$	2.5	5	0
$k_{qf}$	1.2	4	-2.5

**Table A.10:** Base Simplified LV AC sub-grid: droop controllers in DER units

Variable	PV	EV chargers	Energy storage
$P(VAC_{LVg})$ droop controller			
Slope (p.u)	-2.5	-2.5	-2.5
Offset (p.u)	-1	-1	-1
Dead-band: high / low	na	na	na
Saturation: min / max	0 / mpp *	-Pmax / Pmax **	-Pmax / Pmax **
$P(f_{LV})$ droop controller			
Slope (p.u)	-50	-50	-50
Offset (p.u)	-1	-1	-1
Dead-band: high / low	na	na	na
Saturation: min / max	0 / mpp *	-Pmax / Pmax **	-Pmax / Pmax **

\* maximum power point available

\*\* nominal power

**Table A.11:** Base parameters for the LV DC sub-grid: buses, lines and loads

Bus in	Bus out	Cable	Bus	Non-controllable load
ST	1	0.03Ω	1	10 kW
1	2	0.03Ω	2	15 kW
2	3	0.03Ω	3	5 kW

**Table A.12:** Base parameters for the LV DC sub-grid: DER units

Bus	PV	EV charging	Energy Storage
Installed capacity			
1	25 kW	6 kW	10 kW
2	10 kW	20 kW	4 kW
3	25 kW	14 kW	10 kW
Current consumption/injection			
1	-25 kW	4 kW	3.5 kW
2	-10 kW	16 kW	2 kW
3	-25 kW	10 kW	5 kW

**Table A.13:** Base Simplified LV DC sub-grid: droop controllers in DER units

Variable	PV	EV chargers	Energy storage
$P(VDC_{LVg})$ droop controller			
Slope (p.u)	-2.5	-2.5	-2.5
Offset (p.u)	-1	-1	-1
Dead-band: high / low	na	na	na
Saturation: min / max	0 / mpp *	-0.25*Psp / 0.25*Psp **	Psp / Psp **

\* maximum power point available

\*\* power set-point

**Table A.14:** Base parameters for the MV DC sub-grid: buses, lines, loads and DER

Bus in	Bus out	Cable	Bus	load	PV (installed)	EV charging (installed)
ST	1	0.5Ω	1	0 kW	0	150 (150) kW
1	2	0.5Ω	2	50 kW	0	0
2	3	0.5Ω	3	0 kW	-200 (200) kW	0

**Table A.15:** Base Simplified MV DC sub-grid: droop controllers in DER units

Variable	PV	EV chargers
$P(VDC_{MVg})$ droop controller		
Slope (p.u)	-2.5	-2.5
Offset (p.u)	-1	-1
Dead-band: high / low	na	na
Saturation: min / max	0 / mpp *	-0.25*Psp / 0.25*Psp **

\* maximum power point available

\*\* power set-point

**Table A.16:** Parameters for the HMMG

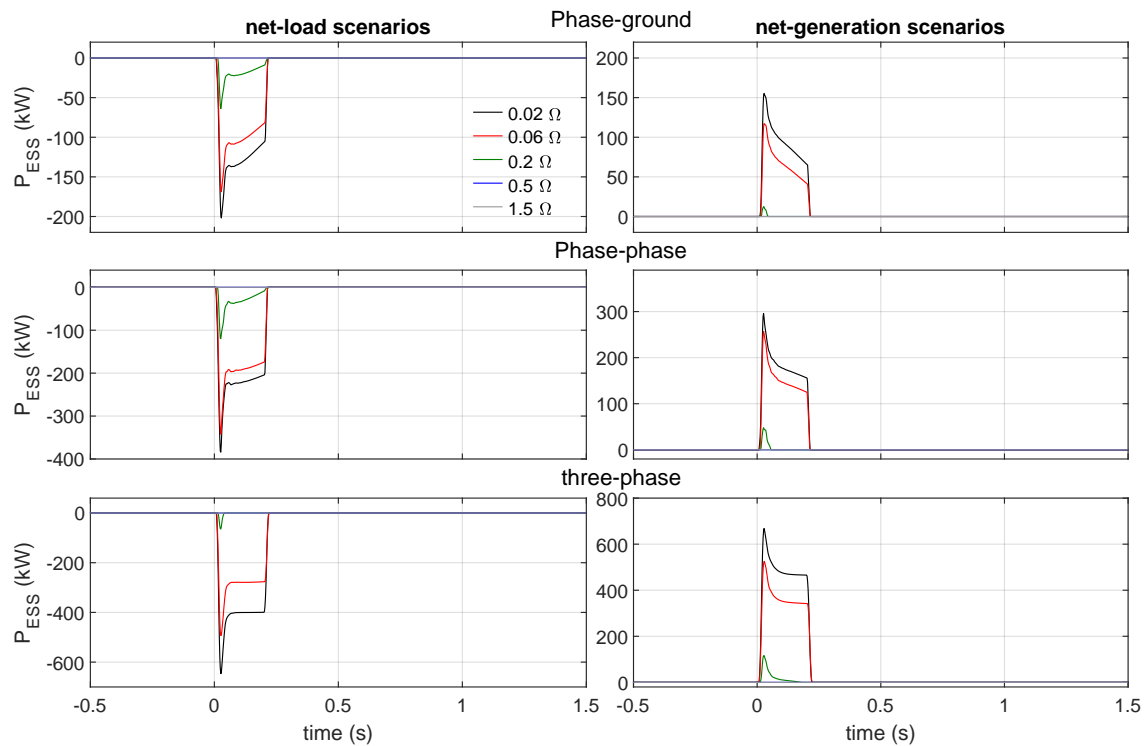
Buses		Lines		
Bus number	Load	Bus in	Bus out	Line Z
6	$350 + j355$ kVA	1	2	$1.35 + j1.1 \Omega$
DG	$-300 + j10$ kVA	2	6	$2.55 + j1.43 \Omega$
15	$70 + j71$ kVA	2	3	$1.17 + j0.95 \Omega$
5	$44 + j45$ kVA	3	4	$0.84 + j0.69 \Omega$
3 (LFT)	0 kVA	4	15	$1.19 + j0.67 \Omega$
<b>Net-load scenario</b>		4	14	$2.23 + j1.25 \Omega$
2 (ST)	462 kVA	4	5	$1.53 + j0.85 \Omega$
14 (ST)	$400 - j25$ kVA			
<b>Net-generation scenario</b>				
2 (ST)	-533 kVA			
14 (ST)	$-400 + j60$ kVA			



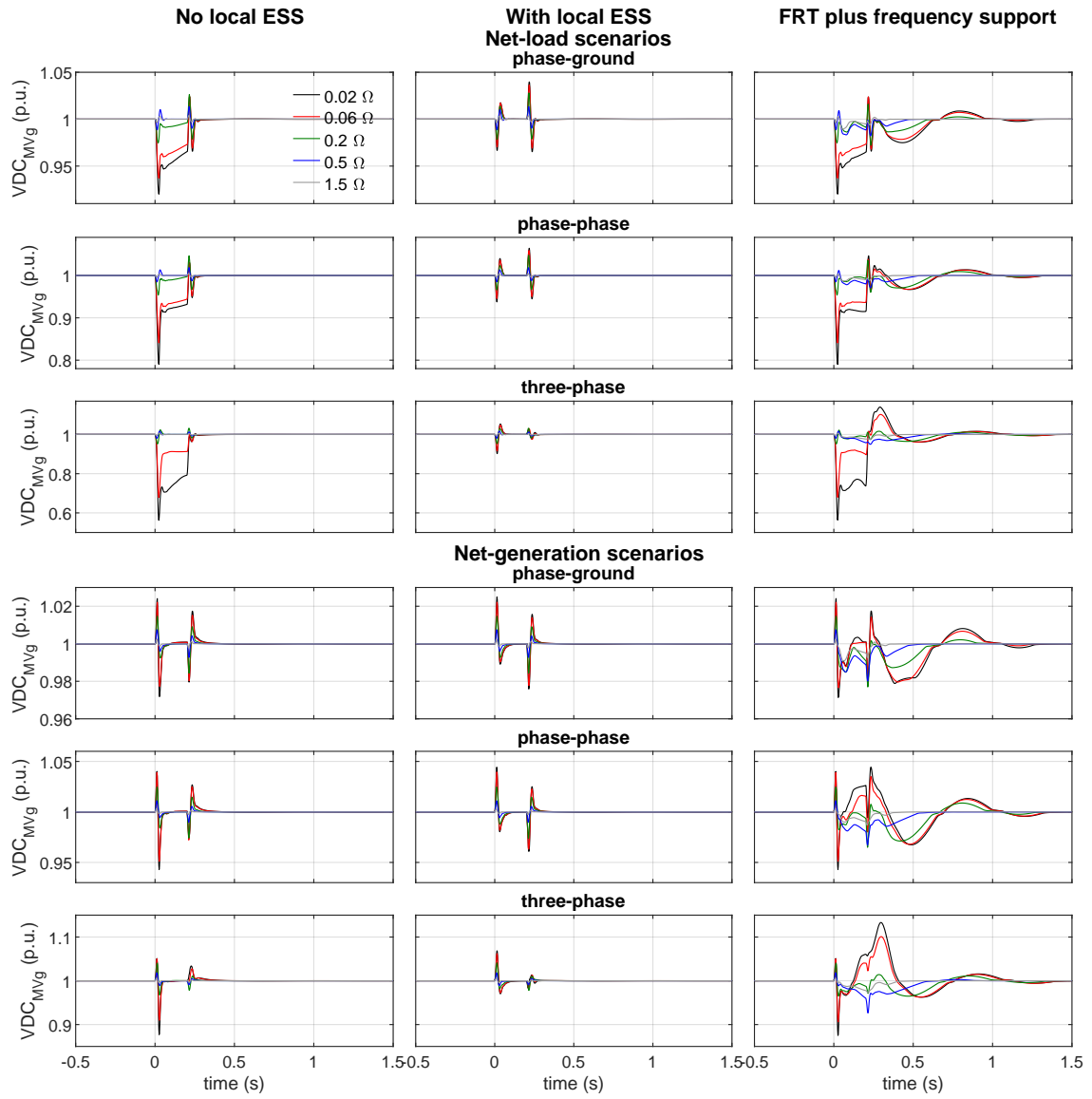
# Appendix B

## Additional Results for Case Studies 1, 2 and 3 - Chapter 6

### B.1 Case Studies 1 and 2

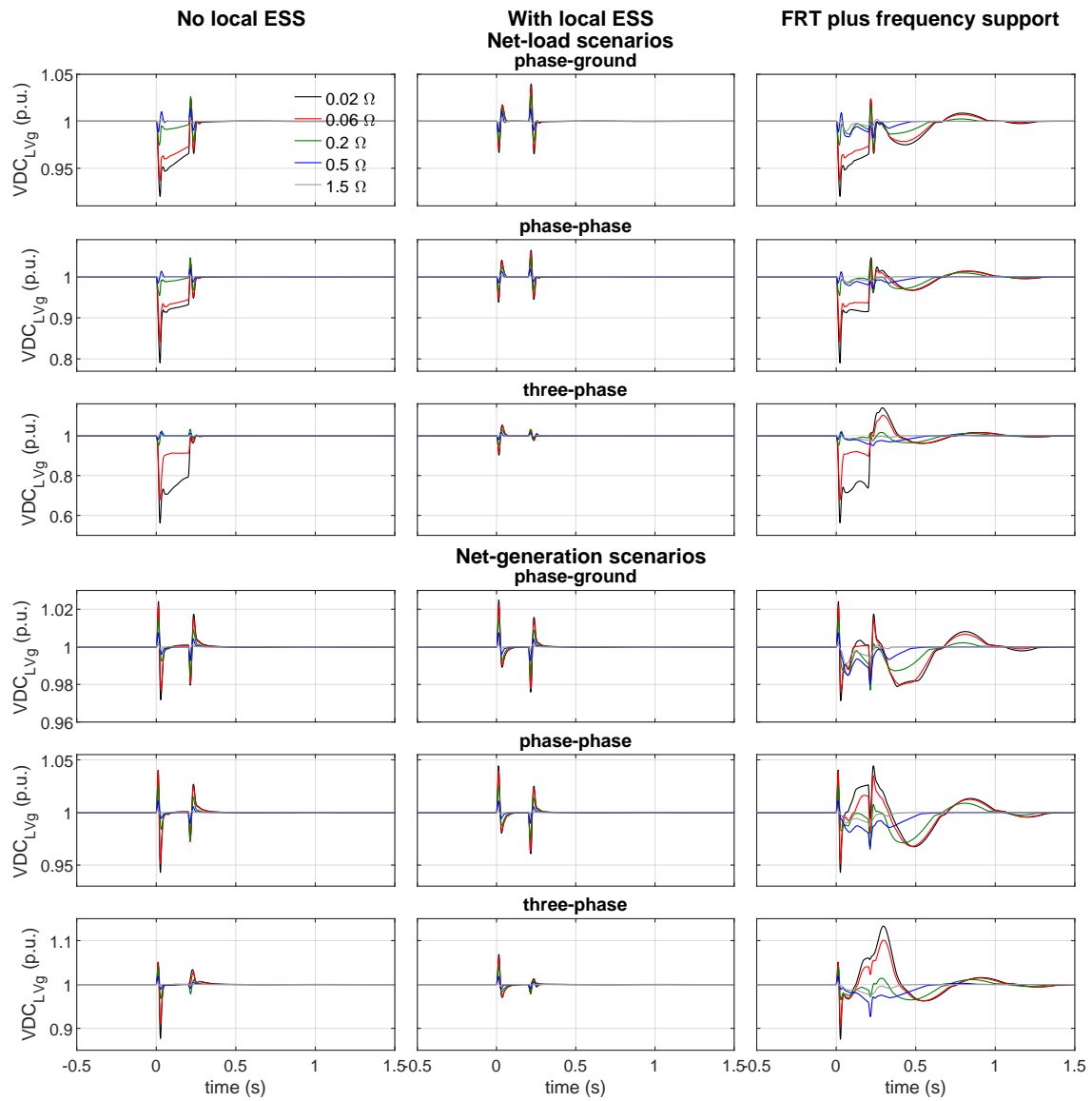


**Figure B.1:** Case study 2 - Active power in the local ESS of the ST for several fault impedances with a time duration of 0.2 s.

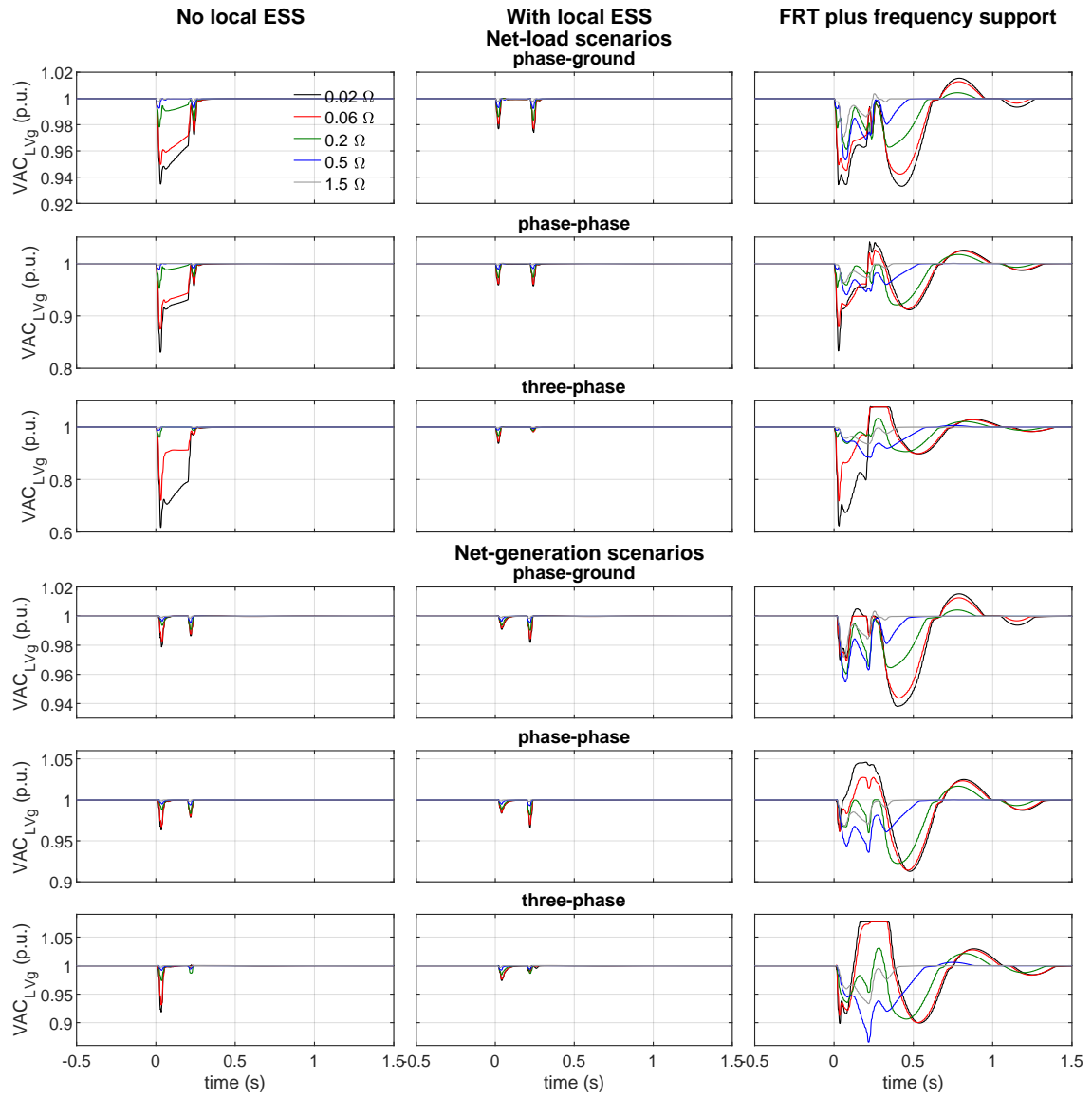


**Figure B.2:** DC voltage in the ST-based MV DC grid for several fault impedances with a time duration of 0.2 s.

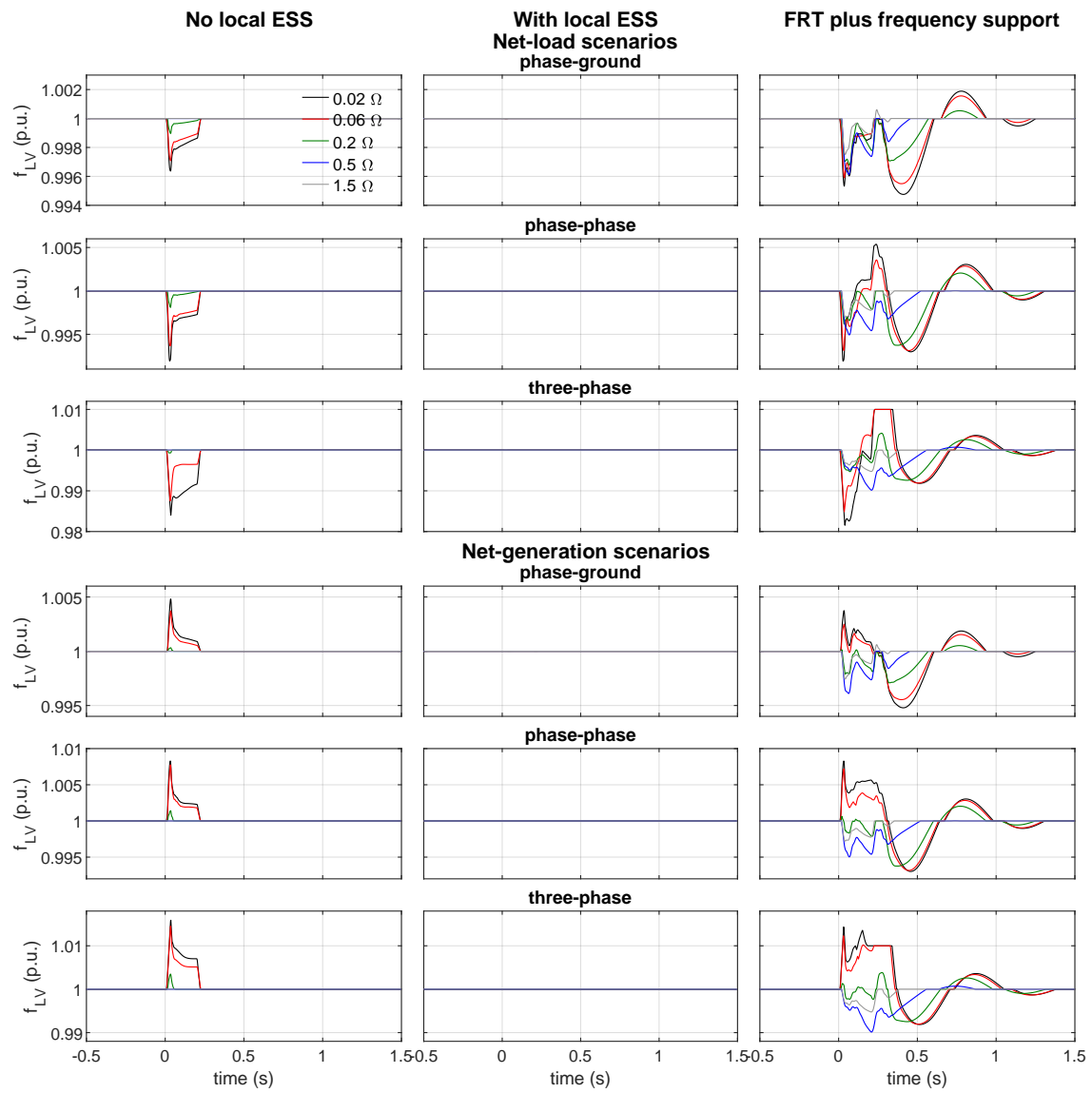




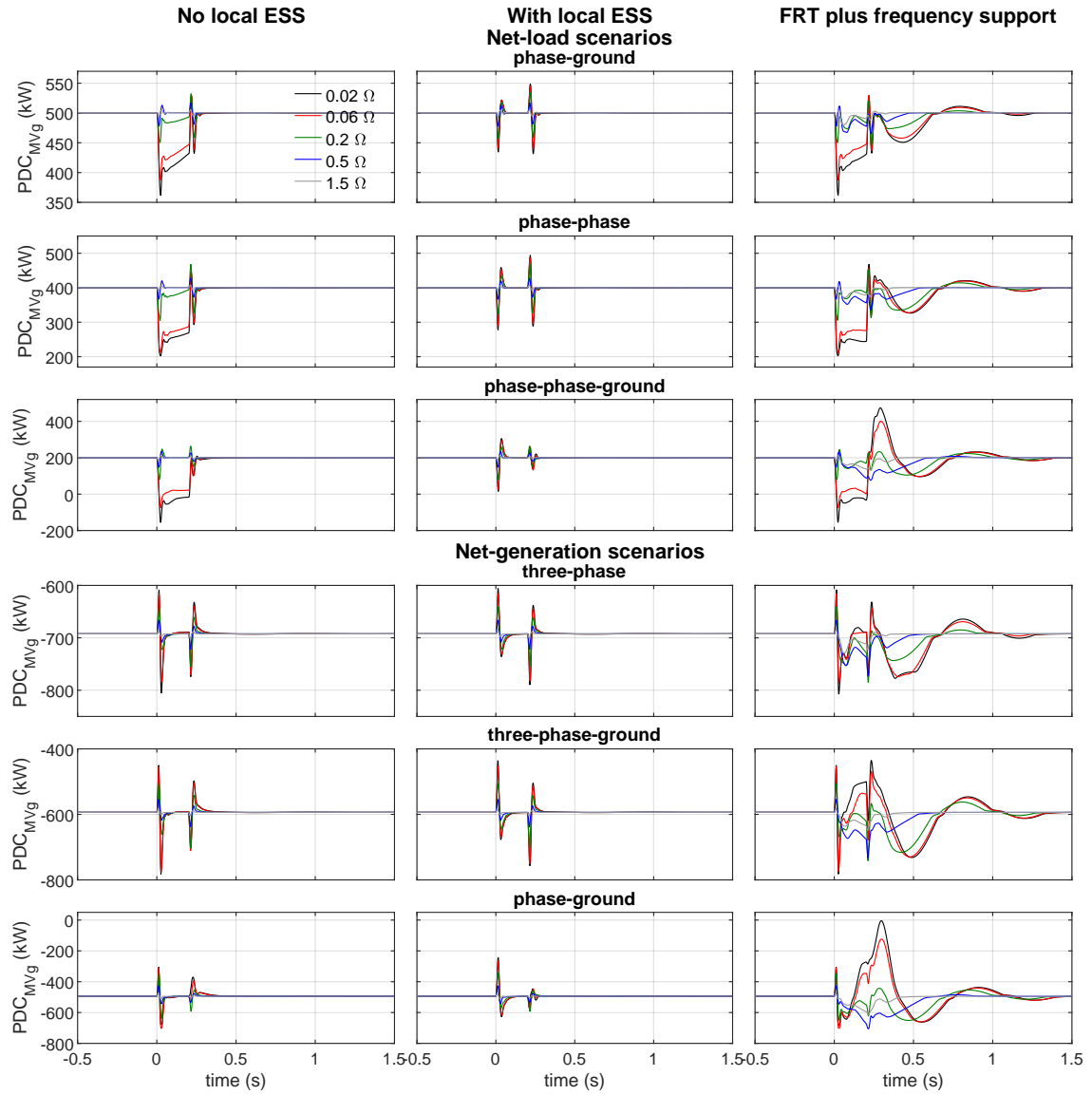
**Figure B.3:** DC voltage in the ST-based LV DC grid for several fault impedances with a time duration of 0.2 s.



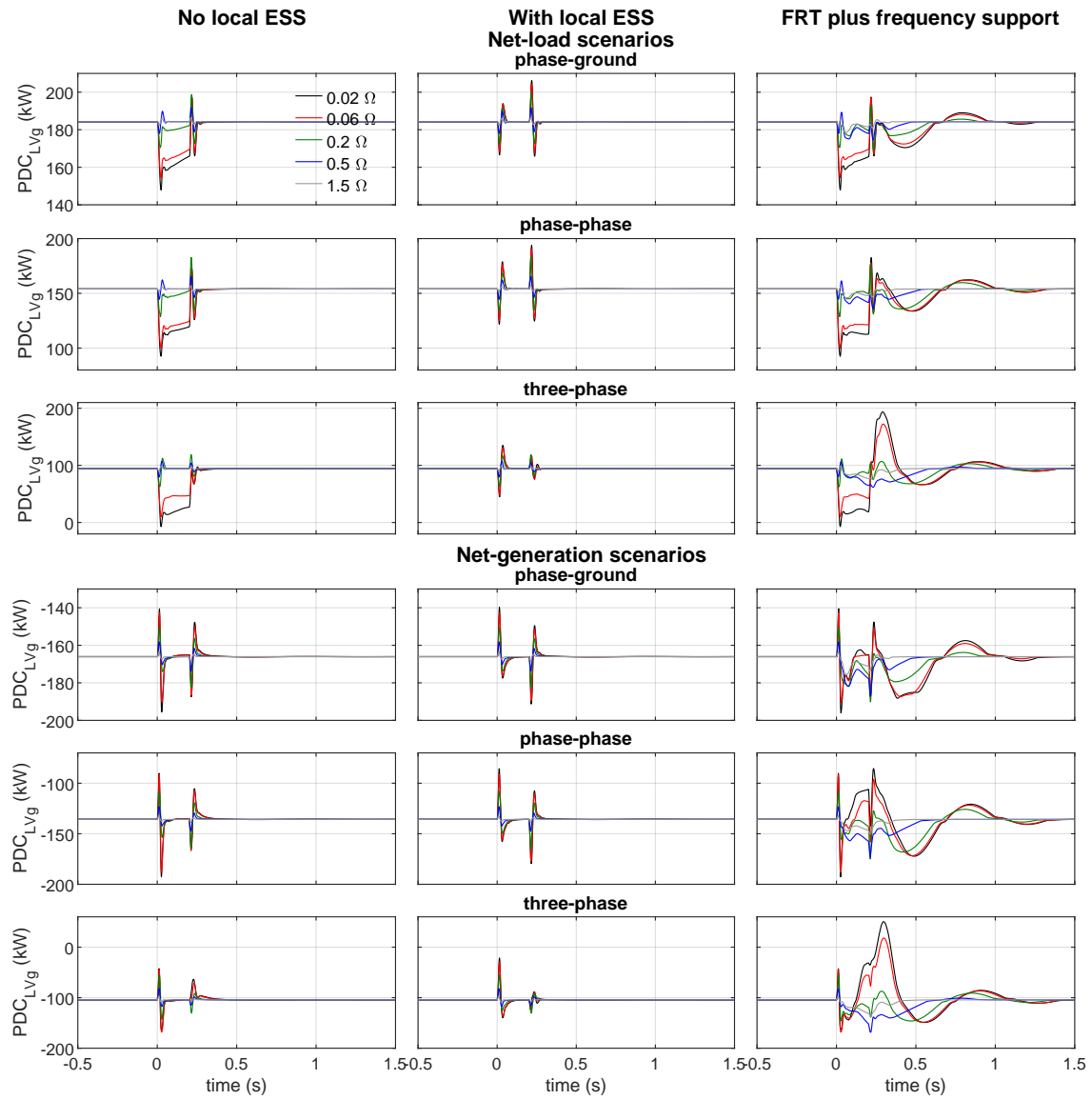
**Figure B.4:** AC voltage in the ST-based LV AC grid for several fault impedances with a time duration of 0.2 s.



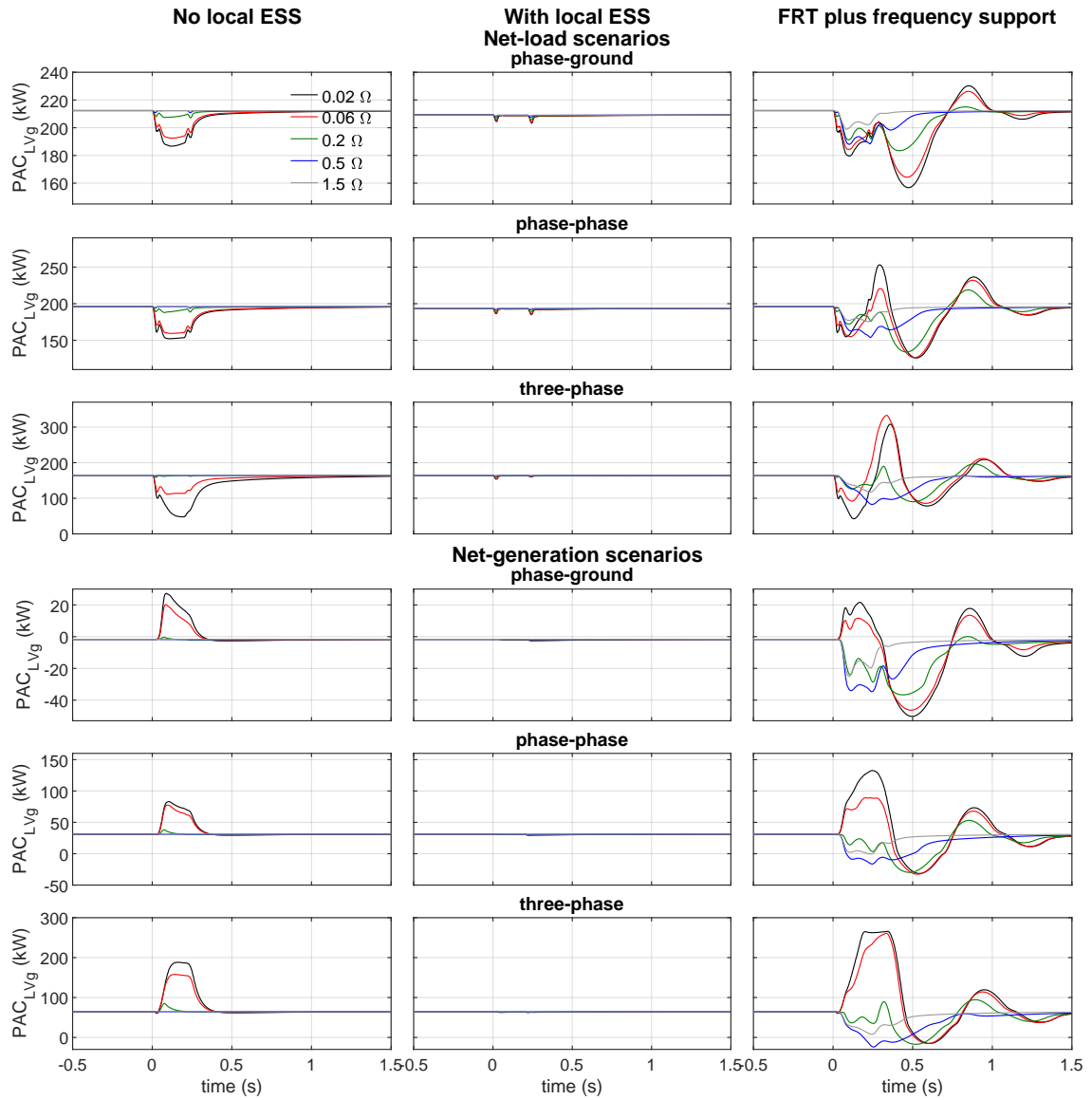
**Figure B.5:** Frequency in the ST-based LV AC grid for several fault impedances with a time duration of 0.2 s.



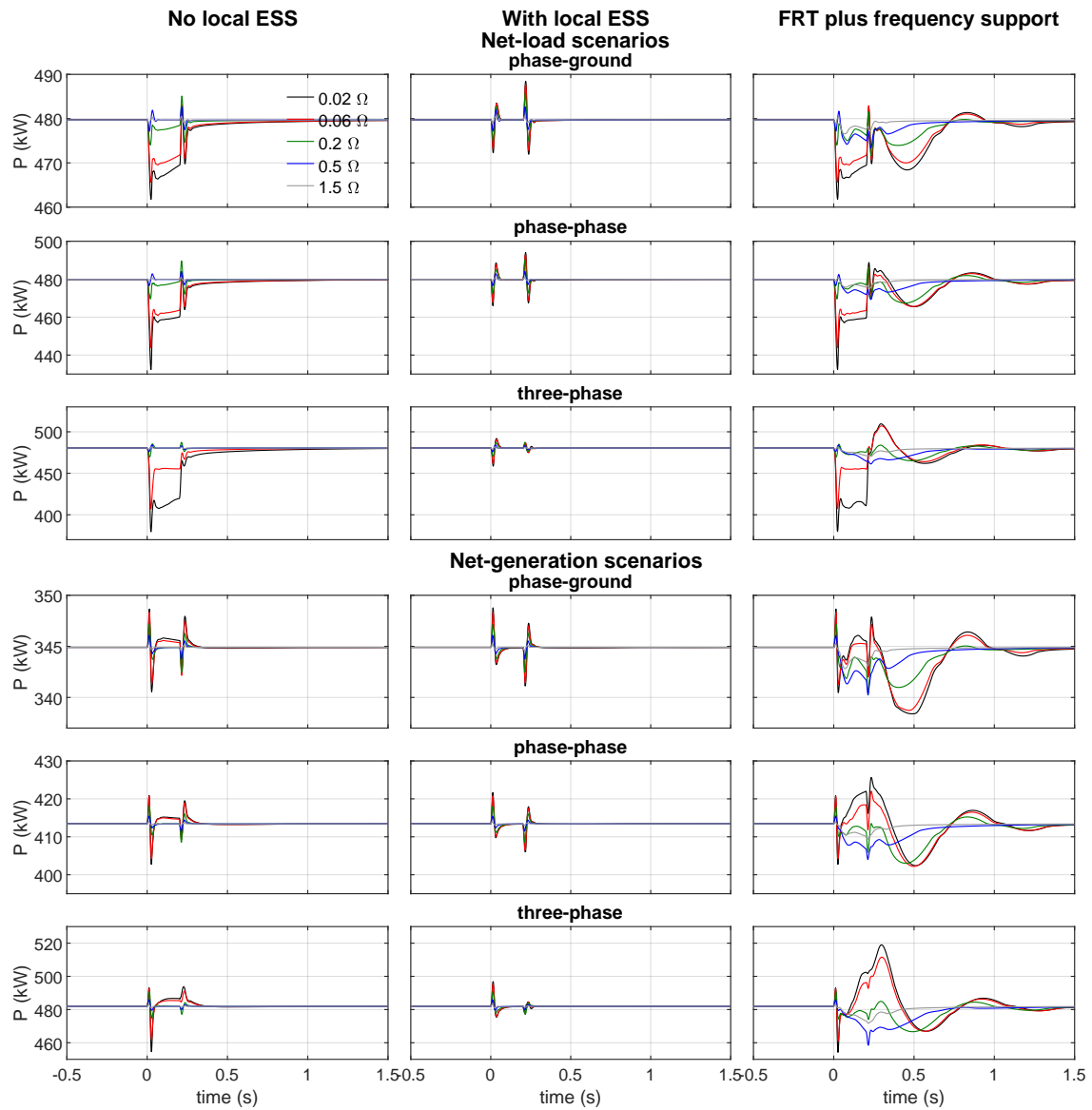
**Figure B.6:** Active power in the ST-based MV DC grid for several fault impedances with a time duration of 0.2 s.



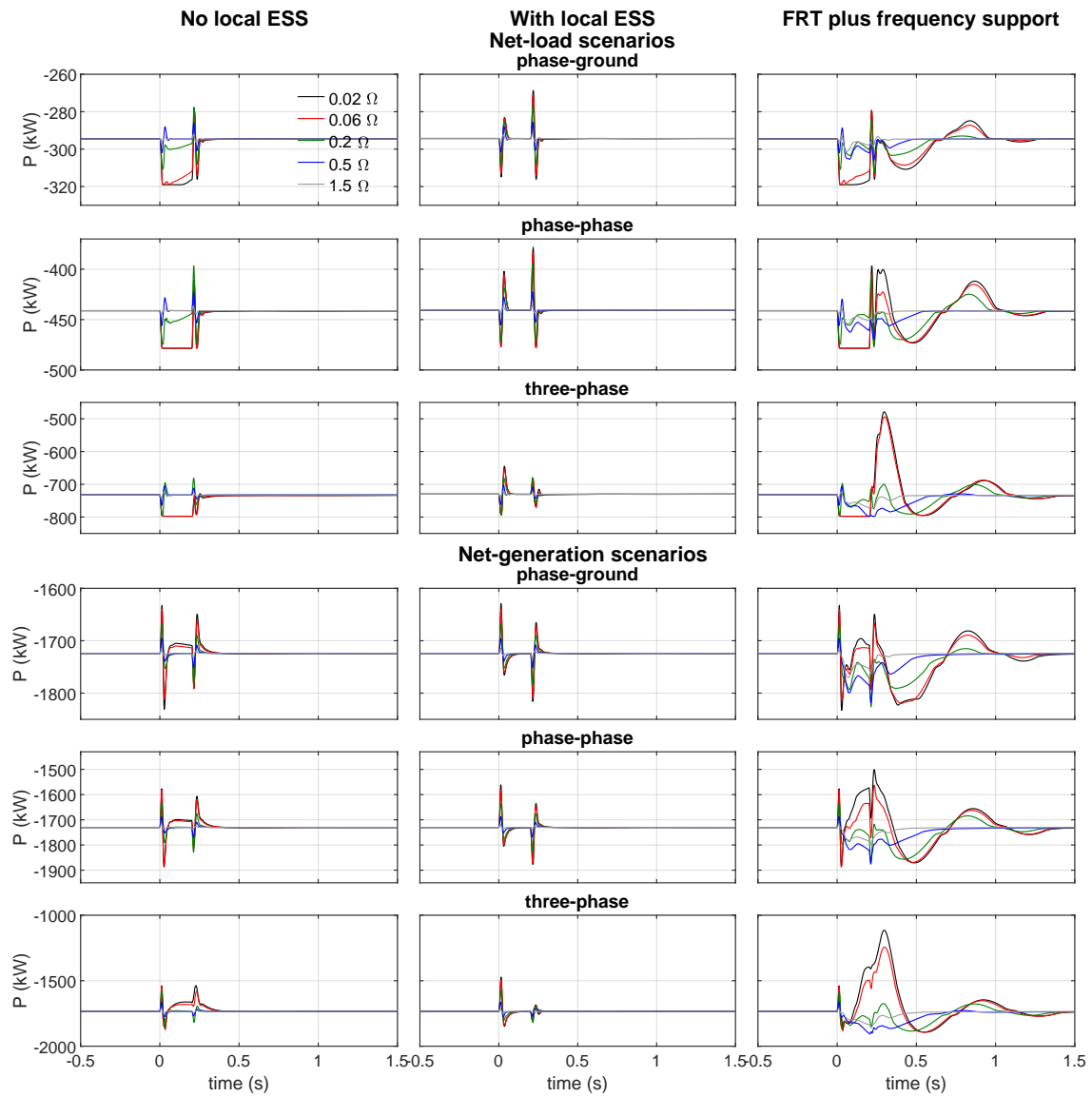
**Figure B.7:** Active power in the ST-based LV DC grid for several fault impedances with a time duration of 0.2 s.



**Figure B.8:** Active power in the ST-based LV AC grid for several fault impedances with a time duration of 0.2 s.



**Figure B.9:** Active power in total non-controllable load in the ST-based hybrid grid for several fault impedances with a time duration of 0.2 s.





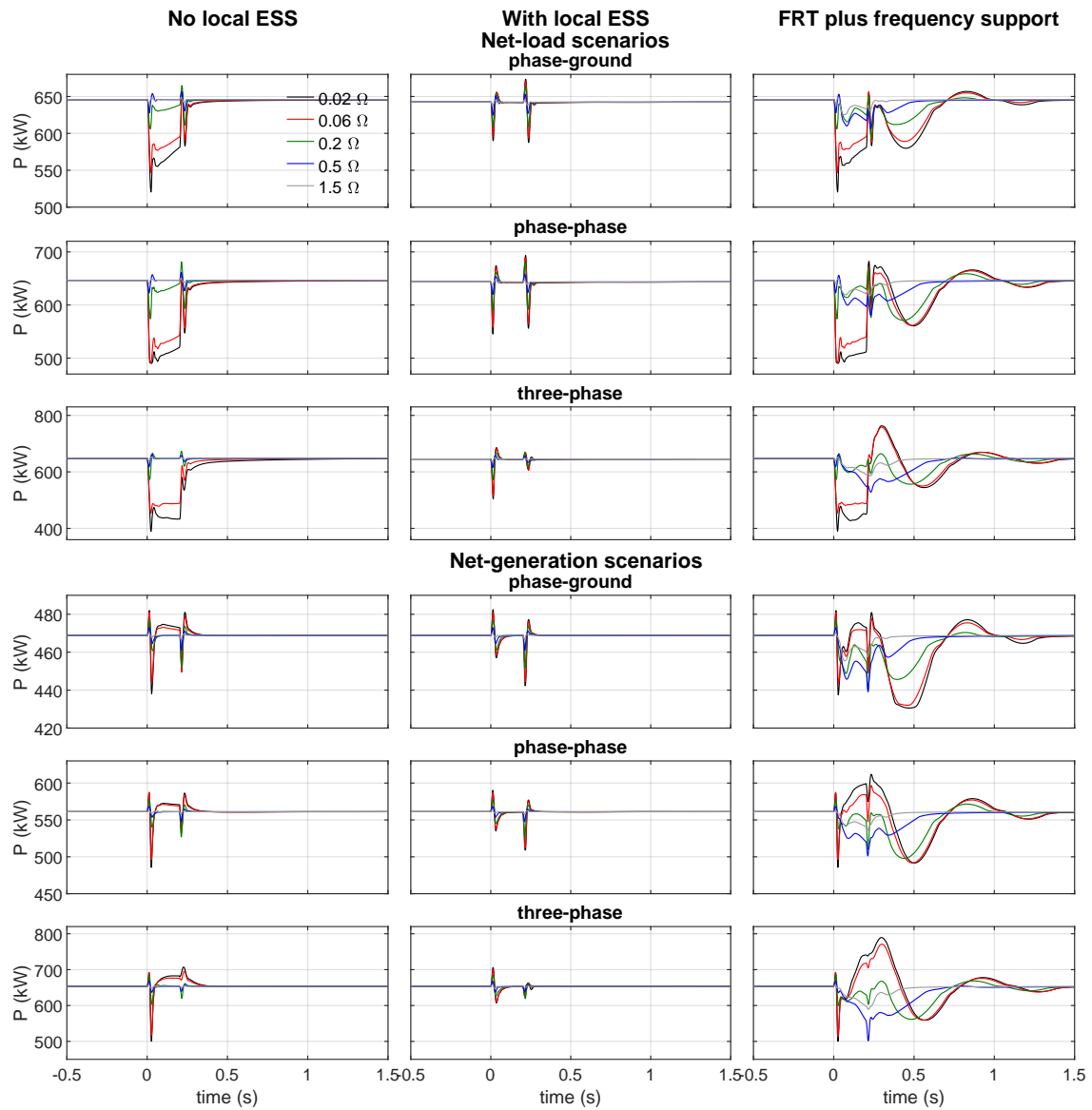


**Figure B.11:** Active power in total EV chargers in the ST-based hybrid grid for several fault impedances with a time duration of 0.2 s.

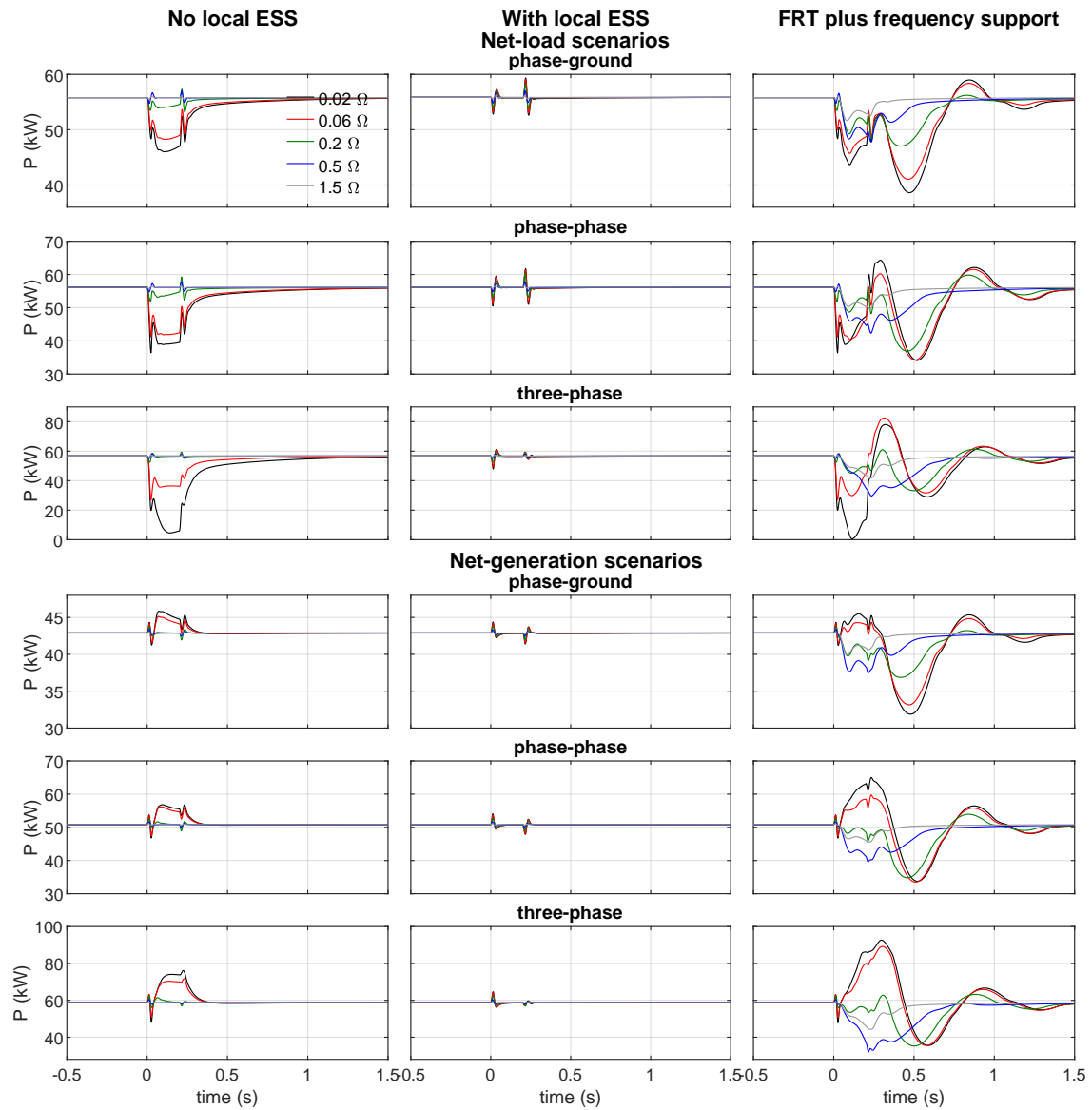


**Figure B.12:** Active power in total energy storage capacity available in the ST-based hybrid grid for several fault impedances with a time duration of 0.2 s.

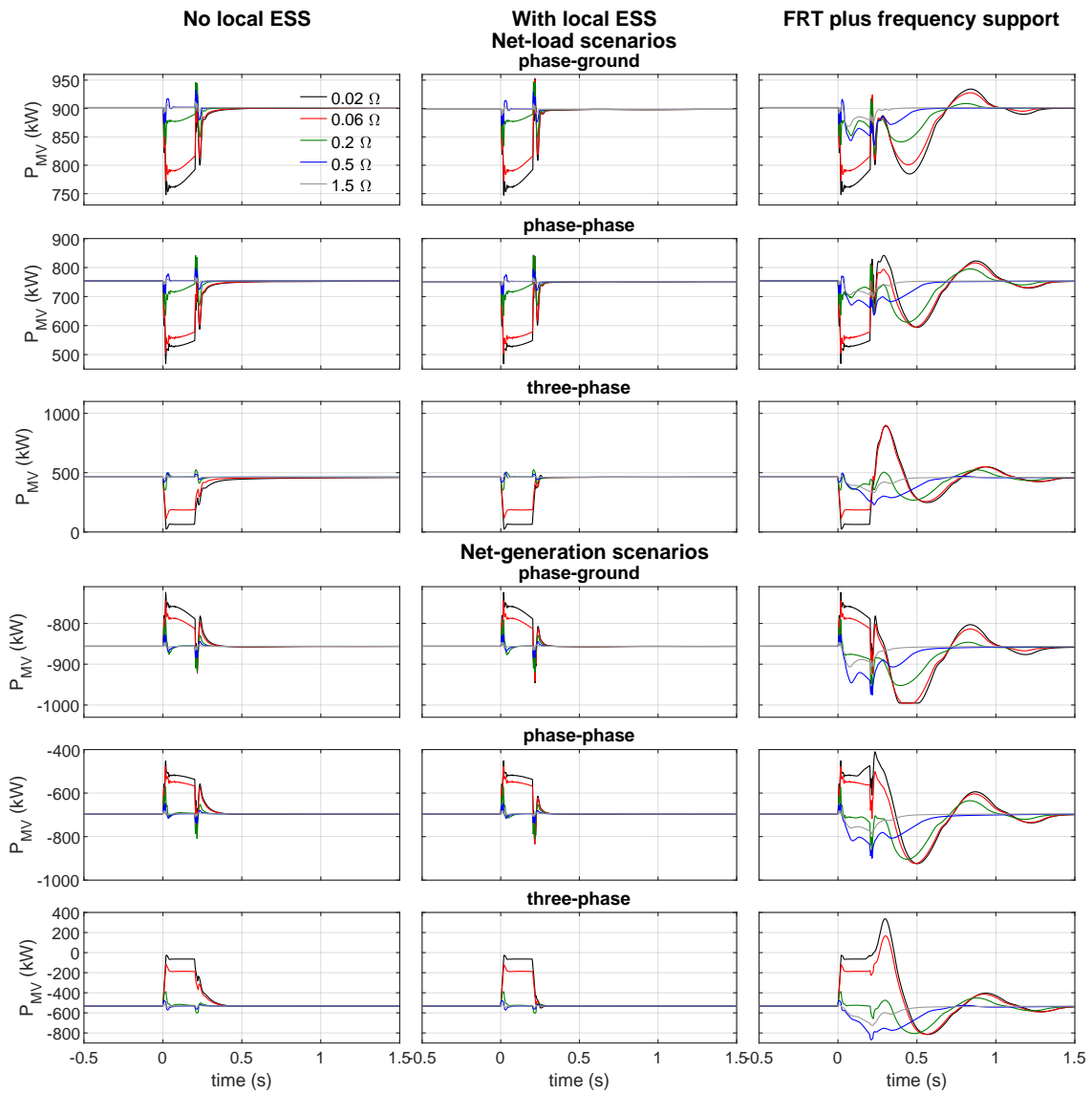


**Figure B.13:** Active power in the ST's MV inverter for several fault impedances with a time duration of 0.2 s.

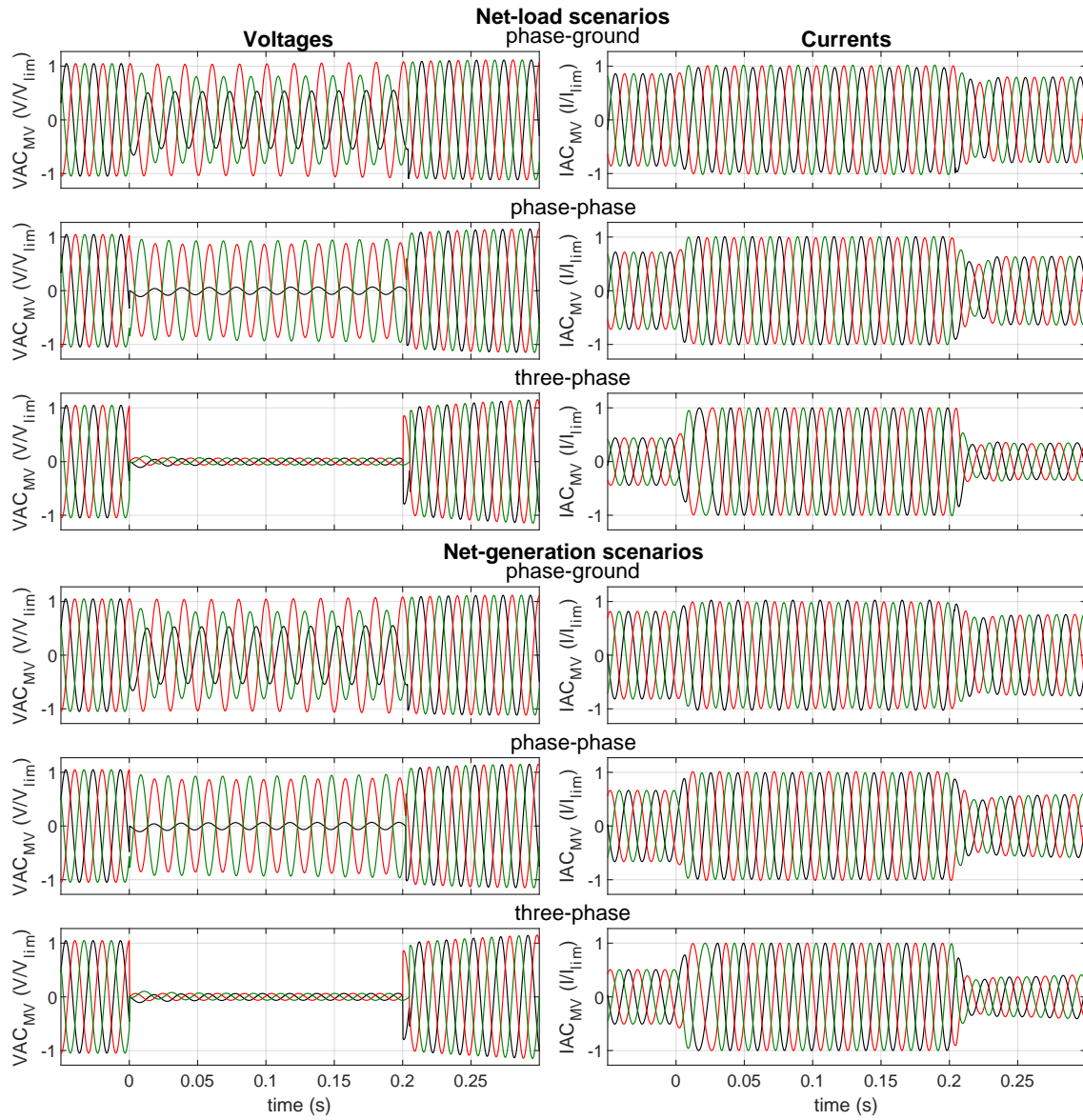


**Figure B.14:** Three-phase voltage and current waveforms in the ST MV inverter for faults with impedance of  $0.02\Omega$  and time duration of 0.2 s. Black: phase-phase A-B voltage and phase A current; Red: phase-phase B-C voltage and phase B current; Green: phase-phase C-A voltage and phase C current.

## B.2 Case Study 3

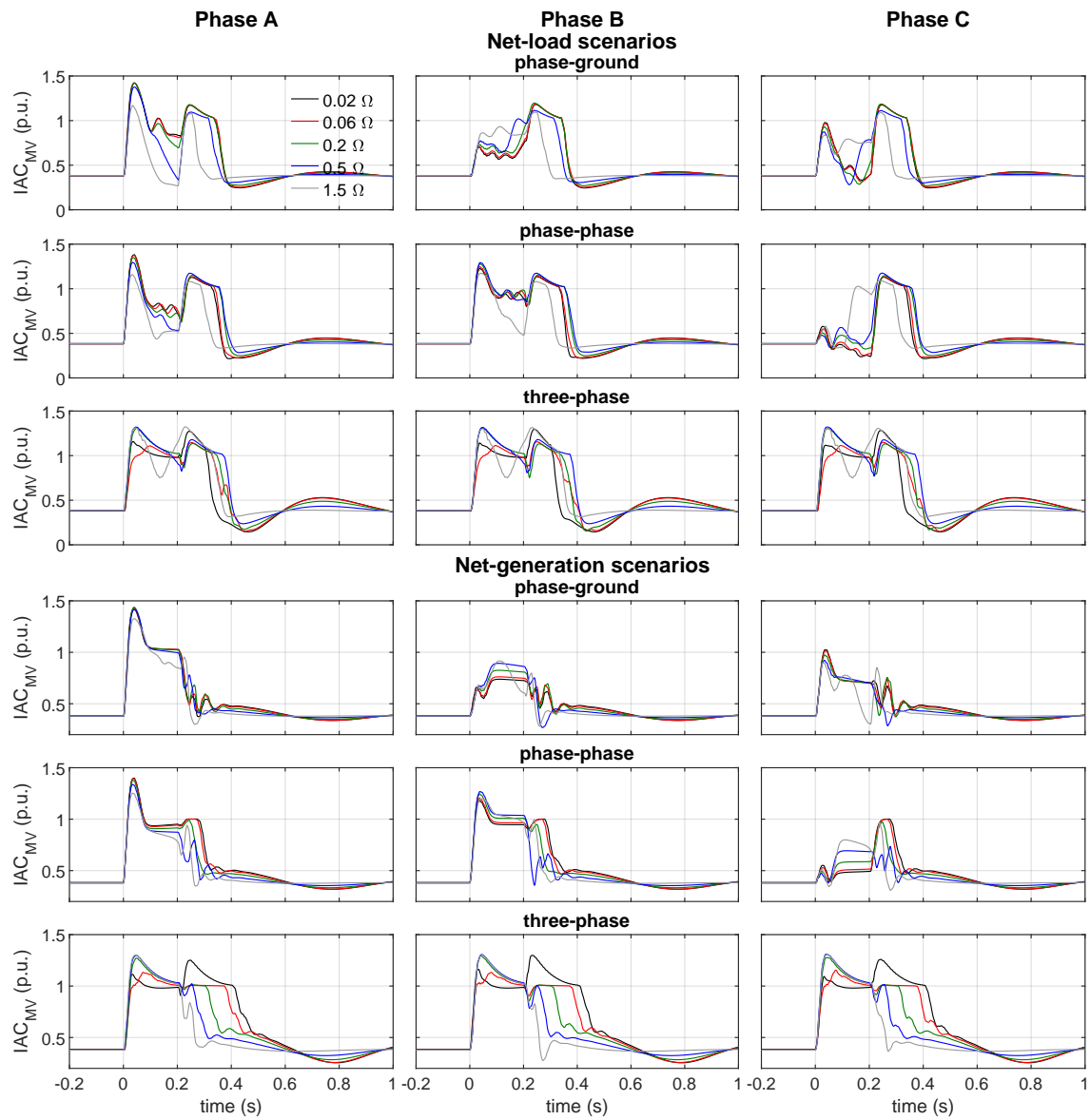


**Figure B.15:** RMS current in the ST's MV inverter considering  $Z_{eq1}$  and fault impedances with a time duration of 0.2 s.

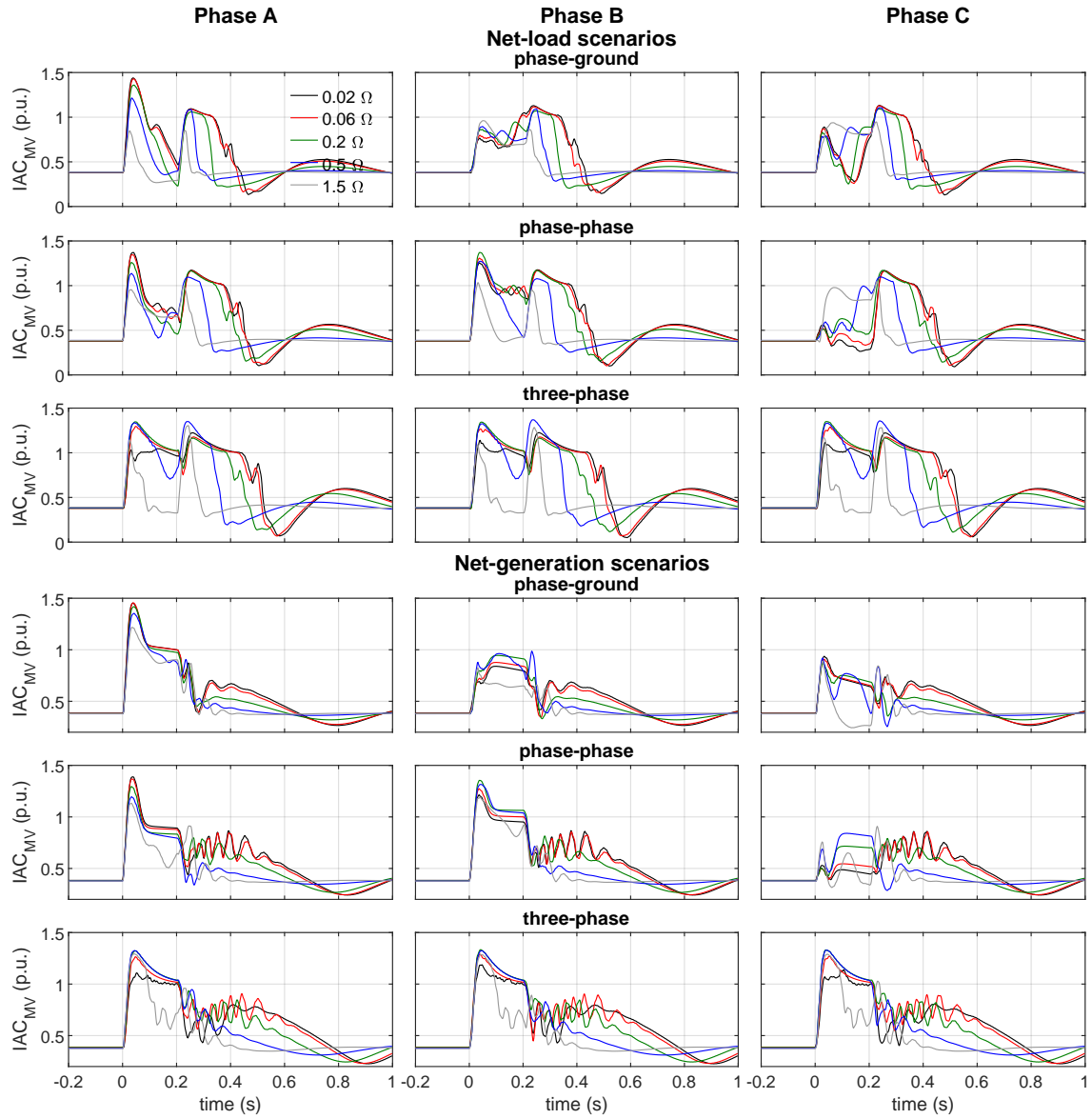


**Figure B.16:** RMS current in the ST's MV inverter considering  $Z_{eq2}$  and fault impedances with a time duration of 0.2 s.

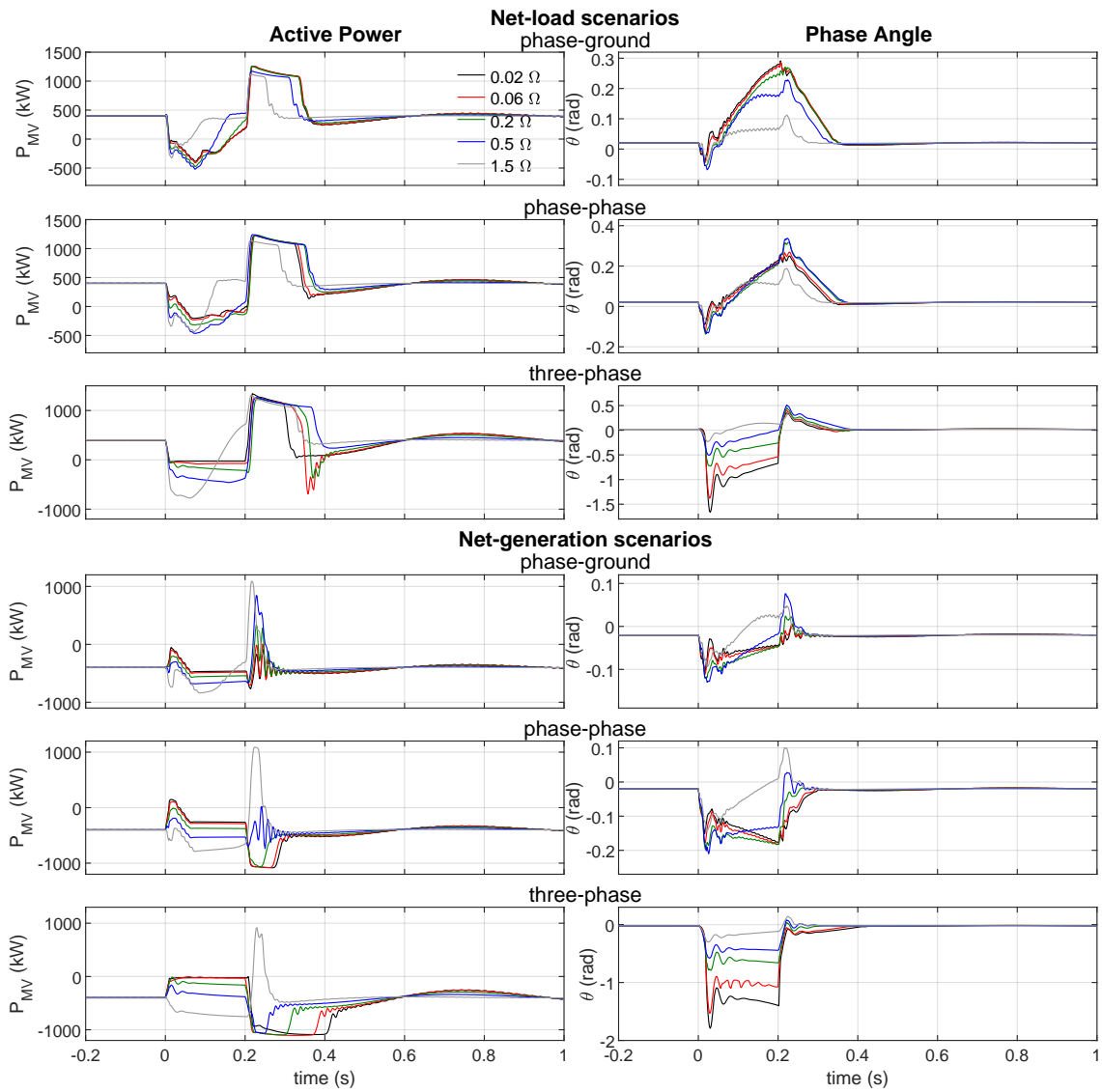


**Figure B.17:** Active power and phase shift in the output LC filter of the ST's MV inverter, considering  $Z_{eq1}$  and fault impedances with a time duration of 0.2 s.

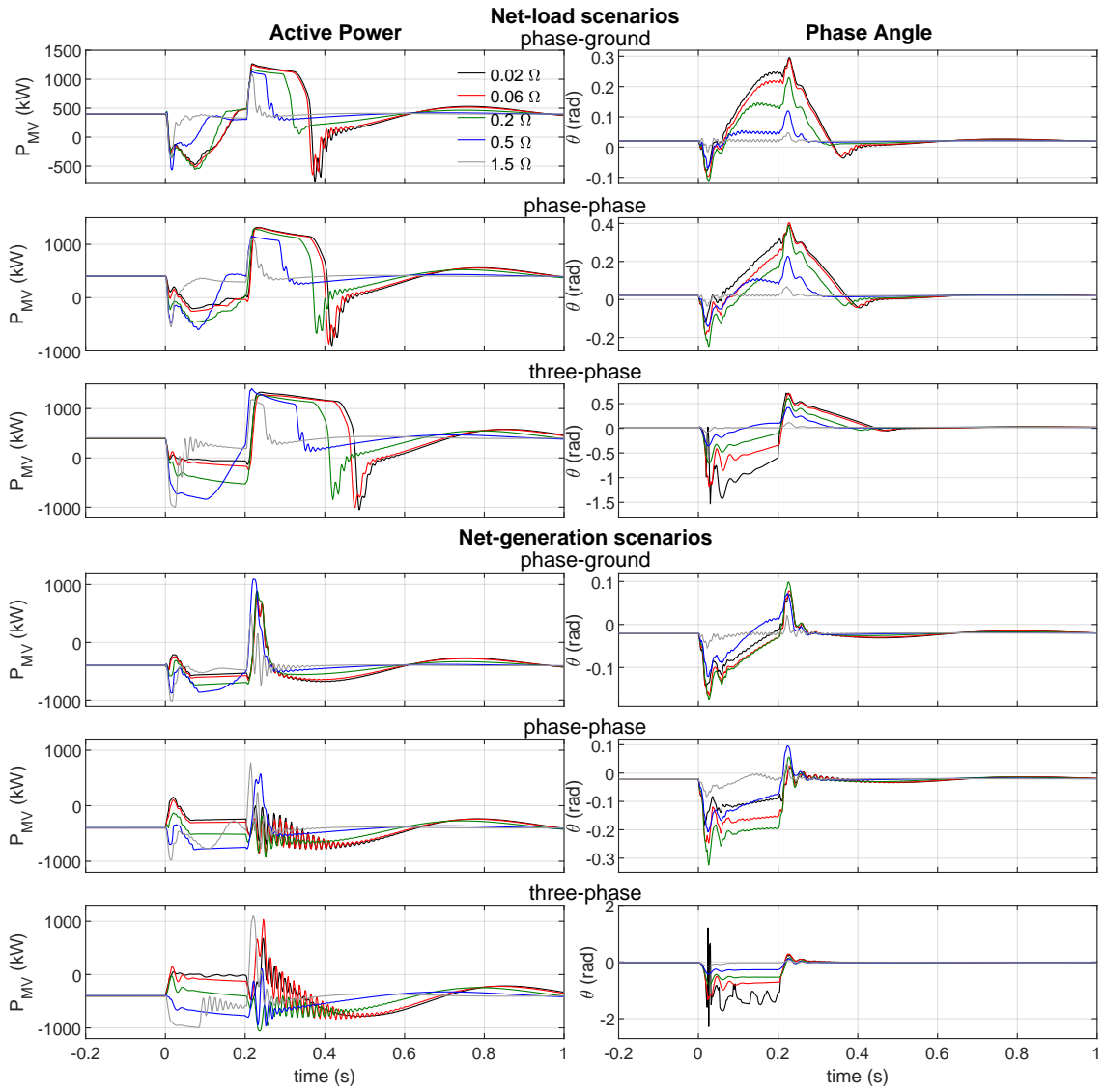


**Figure B.18:** Active power and phase shift in the output LC filter of the ST's MV inverter, considering  $Z_{eq2}$  and fault impedances with a time duration of 0.2 s.



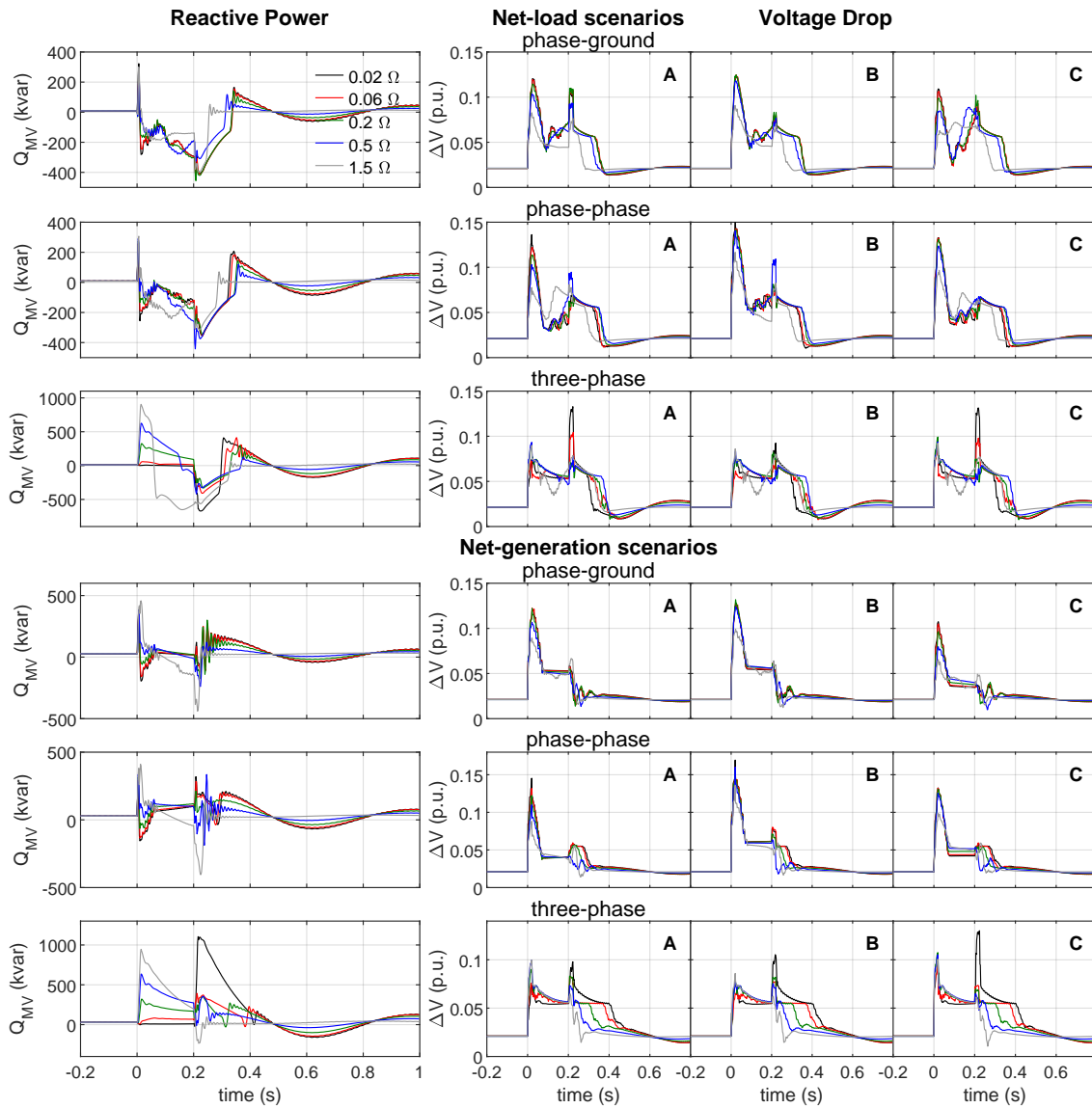


**Figure B.19:** Reactive power and voltage drops (per phase) in the output LC filter of the ST's MV inverter considering  $Z_{eq1}$  and fault impedances with a time duration of 0.2 s.

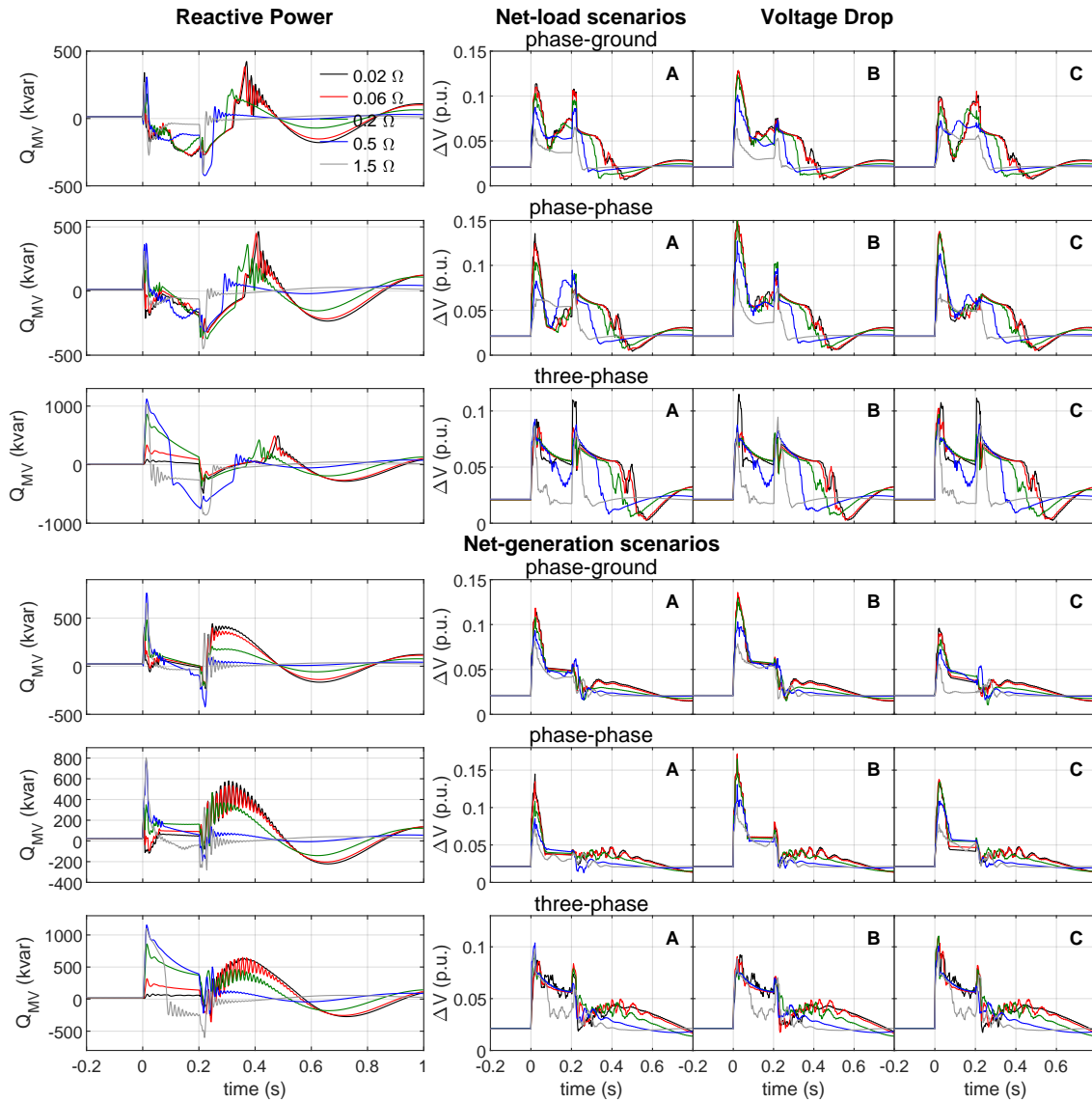
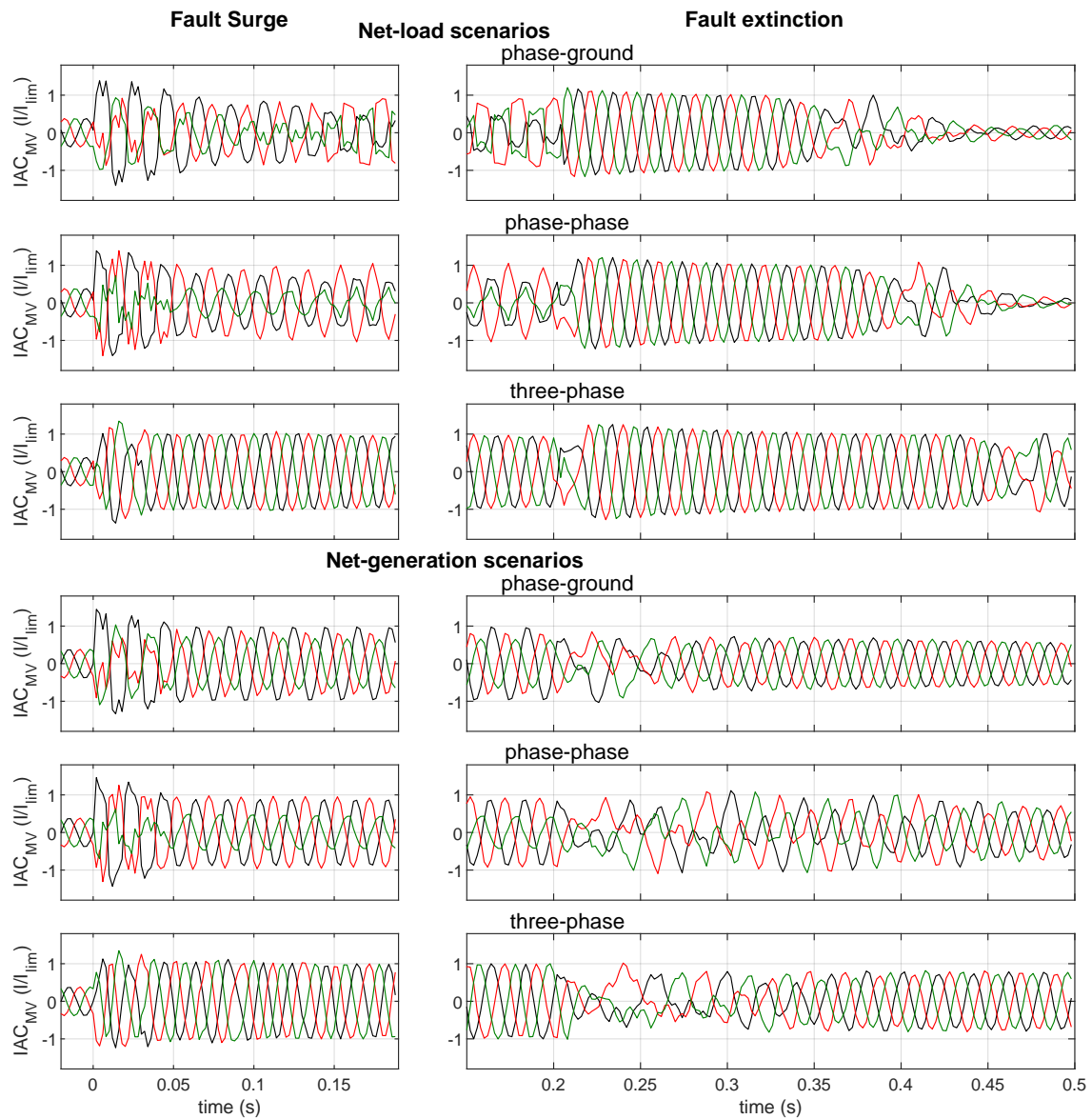
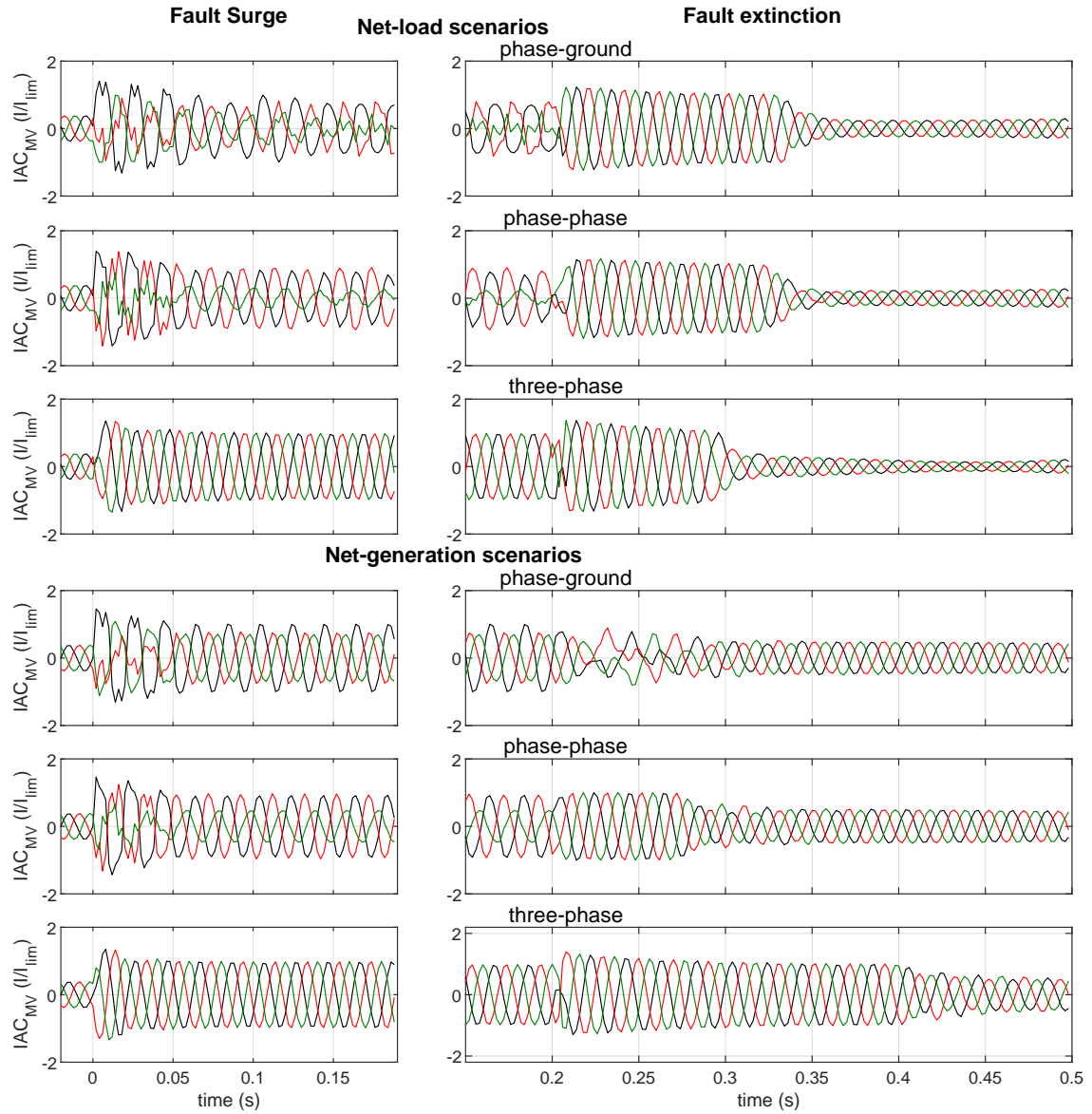


Figure B.20: Reactive power and voltage drops (per phase) in the output LC filter of the ST's MV inverter considering  $Z_{eq2}$  and fault impedances with a time duration of 0.2 s.



**Figure B.21:** Three-phase current waveforms in the ST MV inverter for faults with impedance of  $0.02\Omega$  and time duration of 0.2 s, considering  $Z_{eq1}$ . Black: phase A current; Red: phase B current; Green: phase C current.



**Figure B.22:** Three-phase current waveforms in the ST MV inverter for faults with impedance of  $0.02\Omega$  and time duration of 0.2 s, considering  $Z_{eq2}$ . Black: phase A current; Red: phase B current; Green: phase C current.

# Publications

Many of the materials in this thesis have appeared in the following publications.

## Peer-reviewed Conference Papers

- Justino Rodrigues, Carlos Moreira, and João Peças Lopes. Smart transformers - enabling power-frequency regulation services for hybrid ac/dc networks. In *2019 IEEE Milan PowerTech*, pages 1–6, 2019. doi: 10.1109/PTC.2019.8810773

## Peer-reviewed Journal Papers

- Justino Rodrigues, Carlos Moreira, and João Peças Lopes. Smart transformers as active interfaces enabling the provision of power-frequency regulation services from distributed resources in hybrid ac/dc grids. *Applied Sciences*, 10(4), 2020. ISSN 2076-3417. doi: 10.3390/app10041434. URL <https://www.mdpi.com/2076-3417/10/4/1434>
- Justino Rodrigues, Carlos Moreira, and João Peças Lopes. Fault-ride-through strategies for grid-tied and grid-forming smart-transformers suited for islanding and interconnected operation. *Electric Power Systems Research*, 189:106616, 2020. ISSN 0378-7796. doi: <https://doi.org/10.1016/j.epsr.2020.106616>. URL <https://www.sciencedirect.com/science/article/pii/S037877962030420X>.
- Rongwu Zhu, Markus Andresen, Marius Langwasser, Marco Liserre, Joao Pecas Lopes, Carlos Moreira, Justino Rodrigues, and Mario Couto. Smart transformer/large flexible transformer. *CES Transactions on Electrical Machines and Systems*, 4(4):264–274, 2020. doi: 10.30941/CESTEMS.2020.00033.
- Justino Rodrigues, Carlos Moreira, and João Peças Lopes. Fault-ride-through approach for grid-tied smart transformers without local energy storage. *Energies*, 14(18), 2021. ISSN 1996-1073. doi: 10.3390/en14185622. URL <https://www.mdpi.com/1996-1073/14/18/5622>



# References

- [1] IRENA (2021). Renewable energy statistics 2021 (2021 edition). Technical report, International Renewable Energy Agency, Abu Dhabi, 2021. Cited on p. 1.
- [2] British Petroleum Company (2021). Bp statistical review of world energy 2021 - 70th edition. Technical report, British Petroleum Co, London, 2021. Cited on p. 1.
- [3] SolarPower Europe (2021). Global market outlook for solar power 2021-2025. Technical report, 2021. Cited on pp. 1 and 2.
- [4] IEA (2021). Net zero by 2050. Technical report, IEA, Paris, 2021. Cited on p. 1.
- [5] IRENA (2020). Global renewables outlook: Energy transformation 2050. Technical report, International Renewable Energy Agency, Abu Dhabi, 2020. Cited on p. 1.
- [6] IEA (2021). Renewable energy market update 2021. Technical report, IEA, Paris, 2021. Cited on p. 2.
- [7] IEA (2018). World energy investment 2018. Technical report, IEA, Paris, 2018. Cited on p. 2.
- [8] U.S. Energy Information Administration. Preliminary monthly electric generator inventory (based on form eia-860m as a supplement to form eia-860), 2021. URL <https://www.eia.gov/electricity/data/eia860m/>. Cited on p. 2.
- [9] REN21 (2021). Renewables 2021: Global status report. Technical report, REN21, Paris, 2021. Cited on p. 2.
- [10] IEA (2019). Renewables 2019. Technical report, IEA, Paris, 2019. Cited on p. 2.
- [11] IEA (2020). Renewables 2020. Technical report, IEA, Paris, 2020. Cited on p. 2.
- [12] IEA (2021). Global ev outlook 2021. Technical report, IEA, Paris, 2021. Cited on pp. 2 and 3.
- [13] C. A. Hill, M. C. Such, D. Chen, J. Gonzalez, and W. M. Grady. Battery energy storage for enabling integration of distributed solar power generation. *IEEE Transactions on Smart Grid*, 3(2):850–857, June 2012. Cited on p. 3.
- [14] PV Magazine. Strong growth ahead for battery storage, 2021. URL <https://www.pv-magazine.com/2021/04/13/strong-growth-ahead-for-battery-storage/>. Cited on p. 3.
- [15] Wood Mackenzie (2021). Global energy storage outlook: H2 2021. Technical report, Wood Mackenzie, Edinburgh, 2021. Cited on p. 3.
- [16] SolarPower Europe (2020). European market outlook for residential battery storage 2020-2024. Technical report, 2020. Cited on p. 3.
- [17] European Comission. Commission welcomes european parliament adoption of key files of the clean energy for all europeans package. [http://europa.eu/rapid/press-release\\_IP-18-6383\\_en.htm](http://europa.eu/rapid/press-release_IP-18-6383_en.htm), 2018. Cited on p. 3.

- [18] European Commission. Proposal for a directive of the European Parliament and of the Council amending Directive (EU) 2018/2001 of the European Parliament and of the Council, Regulation (EU) 2018/1999 of the European Parliament and of the Council and Directive 98/70/EC of the European Parliament and of the Council as regards the promotion of energy from renewable sources, and repealing Council Directive (EU) 2015/652. <https://eur-lex.europa.eu/legal-content/EN/TXT/?uri=CELEX:52021PC0557>, 2021. Cited on p. 4.
- [19] República Portuguesa - Presidência do Conselho de Ministros. Resolução do Conselho de Ministros n.º 107/2019 de 1 de julho, roteiro para a neutralidade carbónica 2050 (RNC 2050) - estratégia de longo prazo para a neutralidade carbónica da economia portuguesa em 2050, Diário da República, 1.ª série — n.º 123 — 1 de julho de 2019. <https://dre.pt/application/conteudo/122777644>, 2019. Cited on p. 4.
- [20] Molly F. Sherlock. The value of energy tax incentives for different types of energy resources. Technical report, Congressional Research Service, Washington DC, USA, 2019. Cited on p. 4.
- [21] U.S. Energy Information Administration. Summary of legislation and regulations included in the annual energy outlook 2021, 2021. URL <https://www.eia.gov/outlooks/aeo/assumptions/pdf/summary.pdf>. Cited on p. 4.
- [22] People's Republic of China. 14th five-year plan. [englishversion:https://cset.georgetown.edu/wp-content/uploads/t0284\\_14th\\_Five-Year\\_Plan\\_EN.pdf](https://cset.georgetown.edu/wp-content/uploads/t0284_14th_Five-Year_Plan_EN.pdf), 2021. Cited on p. 4.
- [23] M. Gavrilas, B. C. Neagu, R. D. Pentiuc, and E. Hopulele. Overview on distributed generation integration in distribution systems. In *2018 International Conference and Exposition on Electrical and Power Engineering (EPE)*, pages 1063–1069, Oct 2018. Cited on p. 4.
- [24] R. J. Bravo, R. Salas, T. Bialek, and C. Sun. Distributed energy resources challenges for utilities. In *2015 IEEE 42nd Photovoltaic Specialist Conference (PVSC)*, pages 1–5, June 2015. Cited on p. 4.
- [25] J. Driesen and R. Belmans. Distributed generation: challenges and possible solutions. In *2006 IEEE Power Engineering Society General Meeting*, pages 8 pp.–, 2006. Cited on pp. 4 and 41.
- [26] N. Hatziargyriou, H. Asano, R. Iravani, and C. Marnay. Microgrids. *IEEE Power and Energy Magazine*, 5(4):78–94, July 2007. Cited on p. 4.
- [27] J. M. Guerrero, M. Chandorkar, T. Lee, and P. C. Loh. Advanced control architectures for intelligent microgrids—part i: Decentralized and hierarchical control. *IEEE Transactions on Industrial Electronics*, 60(4):1254–1262, April 2013. Cited on p. 4.
- [28] T. L. Vandoorn, J. C. Vasquez, J. De Kooning, J. M. Guerrero, and L. Vandevelde. Microgrids: Hierarchical control and an overview of the control and reserve management strategies. *IEEE Industrial Electronics Magazine*, 7(4):42–55, Dec 2013. Cited on p. 4.
- [29] Fahad Saleh Al-Ismael. Dc microgrid planning, operation, and control: A comprehensive review. *IEEE Access*, 9:36154–36172, 2021. doi: 10.1109/ACCESS.2021.3062840. Cited on pp. 4 and 11.
- [30] T. Morstyn, B. Hredzak, and V. G. Agelidis. Control strategies for microgrids with distributed energy storage systems: An overview. *IEEE Transactions on Smart Grid*, 9(4):3652–3666, July 2018. Cited on p. 4.
- [31] J. M. Guerrero, P. C. Loh, T. Lee, and M. Chandorkar. Advanced control architectures for intelligent microgrids—part ii: Power quality, energy storage, and ac/dc microgrids. *IEEE Transactions on Industrial Electronics*, 60(4):1263–1270, April 2013. Cited on p. 4.
- [32] F. Nejabatkhah and Y. W. Li. Overview of power management strategies of hybrid ac/dc microgrid. *IEEE Transactions on Power Electronics*, 30(12):7072–7089, Dec 2015. Cited on pp. 4, 12, 31, 32, and 43.



- [33] F. Nejabatkhah, Y. W. Li, and H. Tian. Power quality control of smart hybrid ac/dc microgrids: An overview. *IEEE Access*, 7:52295–52318, 2019. Cited on pp. 4 and 31.
- [34] S. M. Malik, X. Ai, Y. Sun, C. Zhengqi, and Z. Shupeng. Voltage and frequency control strategies of hybrid ac/dc microgrid: a review. *IET Generation, Transmission Distribution*, 11(2):303–313, 2017. Cited on pp. 4, 31, 32, 43, and 44.
- [35] Zhuoli Zhao, Zhirong Xu, Juntao Guo, Ping Yang, and Loi Lei Lai. Multi-time scale regional autonomous operation strategy for multi-microgrids with three-phase/single-phase hybrid structure. *IEEE Access*, 8:85923–85938, 2020. doi: 10.1109/ACCESS.2020.2991984. Cited on p. 4.
- [36] Dan Zhou, Shangren Chen, Hanyun Wang, Minyuan Guan, Lihua Zhou, Jian Wu, and Yaojie Hu. Autonomous cooperative control for hybrid ac/dc microgrids considering multi-energy complementarity. *Frontiers in Energy Research*, 9:397, 2021. ISSN 2296-598X. doi: 10.3389/fenrg.2021.692026. URL <https://www.frontiersin.org/article/10.3389/fenrg.2021.692026>. Cited on p. 4.
- [37] Hasan Mehrjerdi. Resilience improvement with zero load curtailment by multi-microgrid based on system of systems. *IEEE Access*, 8:198494–198502, 2020. doi: 10.1109/ACCESS.2020.3035251. Cited on p. 4.
- [38] B. K. Bose. Power electronics, smart grid, and renewable energy systems. *Proceedings of the IEEE*, 105(11):2011–2018, Nov 2017. Cited on p. 5.
- [39] Juan Manuel Carrasco, Leopoldo Garcia Franquelo, Jan T Bialasiewicz, Eduardo Galván, Ramón Carlos PortilloGuisado, MA Martin Prats, José Ignacio León, and Narciso Moreno-Alfonso. Power-electronic systems for the grid integration of renewable energy sources: A survey. *IEEE Transactions on industrial electronics*, 53(4):1002–1016, 2006. Cited on p. 5.
- [40] Frede Blaabjerg, Zhe Chen, and Soeren Baekhoej Kjaer. Power electronics as efficient interface in dispersed power generation systems. *IEEE transactions on power electronics*, 19(5):1184–1194, 2004. Cited on p. 5.
- [41] L. Ferreira Costa, G. De Carne, G. Buticchi, and M. Liserre. The smart transformer: A solid-state transformer tailored to provide ancillary services to the distribution grid. *IEEE Power Electronics Magazine*, 4(2):56–67, June 2017. Cited on pp. 5, 10, 13, 14, 24, 25, 32, 54, and 64.
- [42] A. Chakraborty. Infusing autonomy in power distribution networks using smart transformers. In *2017 IEEE Conference on Control Technology and Applications (CCTA)*, pages 1110–1116, Aug 2017. Cited on p. 6.
- [43] E. McMurray. Power converter circuits having a high frequency link, 1968. U.S. Patent US3517300. Cited on p. 9.
- [44] W. McMurray. The thyristor electronic transformer: a power converter using a high-frequency link. *IEEE Transactions on Industry and General Applications*, IGA-7(4):451–457, July 1971. Cited on p. 9.
- [45] J. E. Huber and J. W. Kolar. Applicability of solid-state transformers in today’s and future distribution grids. *IEEE Transactions on Smart Grid*, 10(1):317–326, Jan 2019. Cited on pp. 9, 48, 49, and 50.
- [46] C. Zhao, D. Dujic, A. Mester, J. K. Steinke, M. Weiss, S. Lewdeni-Schmid, T. Chaudhuri, and P. Stefanutti. Power electronic traction transformer; medium voltage prototype. *IEEE Transactions on Industrial Electronics*, 61(7):3257–3268, July 2014. Cited on pp. 9 and 10.
- [47] M. Liserre, G. Buticchi, M. Andresen, G. De Carne, L. F. Costa, and Z. X. Zou. The smart transformer: Impact on the electric grid and technology challenges. *IEEE Industrial Electronics Magazine*, 10(2):46–58, June 2016. Cited on pp. 10, 13, 14, 15, 16, 24, 25, 38, 44, and 64.

- [48] Dan Wang, Chengxiong Mao, Jiming Lu, Shu Fan, and Fangzheng Peng. Theory and application of distribution electronic power transformer. *Electric Power Systems Research*, 77("3"):219 – 226, 2007. ISSN 0378-7796. Cited on p. 10.
- [49] Ankan De, Sudhin Roy, and Subhashish Bhattacharya. Efficiency comparison of ac-link and tips (sst) topologies based on accurate device models. In *2012 IEEE Energy Conversion Congress and Exposition (ECCE)*, pages 3862–3868, 2012. doi: 10.1109/ECCE.2012.6342282. Cited on p. 10.
- [50] Sachin Madhusoodhanan, Subhashish Bhattacharya, and Kamalesh Hatua. Control technique for 15 kv sic igbt based active front end converter of a 13.8 kv grid tied 100 kva transformerless intelligent power substation. In *2013 IEEE Energy Conversion Congress and Exposition*, pages 4697–4704, 2013. doi: 10.1109/ECCE.2013.6647331. Cited on p. 10.
- [51] Jih-Sheng Lai, Wei-Han Lai, Seung-Ryul Moon, Lanhua Zhang, and Arindam Maitra. A 15-kv class intelligent universal transformer for utility applications. In *2016 IEEE Applied Power Electronics Conference and Exposition (APEC)*, pages 1974–1981, 2016. doi: 10.1109/APEC.2016.7468139. Cited on p. 10.
- [52] Dan Wang, Jie Tian, Chengxiong Mao, Jiming Lu, Yuping Duan, Jun Qiu, and Huihong Cai. A 10-kv/400-v 500-kva electronic power transformer. *IEEE Transactions on Industrial Electronics*, 63(11):6653–6663, 2016. doi: 10.1109/TIE.2016.2586440. Cited on p. 10.
- [53] D. Wang, Y. Yang, J. Tian, C. Mao, and J. Zhang. Design and implementation of 10-kv mw-level electronic power transformer (ept). In *2018 IEEE Industry Applications Society Annual Meeting (IAS)*, pages 1–10, Sep. 2018. Cited on p. 10.
- [54] Lv engine - a smarter electricity network (project code: Spmeno2). <https://www.ofgem.gov.uk/publications/electricity-nic-submission-sp-energy-networks-lv-engine>, 2018 - 2022. Cited on p. 10.
- [55] Athanasios Vasilakis, Igyso Zafeiratou, Dimitris T. Lagos, and Nikos D. Hatziargyriou. The evolution of research in microgrids control. *IEEE Open Access Journal of Power and Energy*, 7: 331–343, 2020. doi: 10.1109/OAJPE.2020.3030348. Cited on p. 10.
- [56] B. Lasseter. Microgrids [distributed power generation]. In *2001 IEEE Power Engineering Society Winter Meeting. Conference Proceedings (Cat. No.01CH37194)*, volume 1, pages 146–149 vol.1, 2001. doi: 10.1109/PESW.2001.917020. Cited on pp. 10 and 11.
- [57] R. Lasseter et al. Integration of distributed energy resources. the certs microgrid concept. Technical report, Consortium Electr. Rel. Technol. Solutions, Berkeley, CA, USA, Tech. Rep. LBNL–50829, Apr. 2002. Cited on pp. 10 and 11.
- [58] European project microgrids - large scale integration of micro-generation to low voltage grids (grant agreement id: Enk5-ct-2002-00610). <https://cordis.europa.eu/project/id/ENK5-CT-2002-00610>, 2003 - 2005. Cited on p. 11.
- [59] European project more-microgrids - advanced architectures and control concepts for more microgrids (grant agreement id: 19864). <https://cordis.europa.eu/project/id/19864>, 2006 -2009. Cited on pp. 11 and 13.
- [60] Mike Barnes, Junji Kondoh, Hiroshi Asano, Jose Oyarzabal, Giri Ventakaramanan, Robert Lasseter, Nikos Hatziargyriou, and Tim Green. Real-world microgrids-an overview. In *2007 IEEE International Conference on System of Systems Engineering*, pages 1–8, 2007. doi: 10.1109/SYSOSE.2007.4304255. Cited on pp. 11 and 27.
- [61] Luis Eduardo Zubieta. Are microgrids the future of energy?: Dc microgrids from concept to demonstration to deployment. *IEEE Electrification Magazine*, 4(2):37–44, 2016. doi: 10.1109/MELE.2016.2544238. Cited on p. 11.

- [62] Y. Ito, Y. Zhongqing, and H. Akagi. Dc microgrid based distribution power generation system. In *The 4th International Power Electronics and Motion Control Conference, 2004. IPEMC 2004.*, volume 3, pages 1740–1745 Vol.3, 2004. Cited on p. 11.
- [63] M. Brenna, E. Tironi, and G. Ubezio. Proposal of a local dc distribution network with distributed energy resources. In *2004 11th International Conference on Harmonics and Quality of Power (IEEE Cat. No.04EX951)*, pages 397–402, 2004. doi: 10.1109/ICHQP.2004.1409388. Cited on p. 11.
- [64] Jackson John Justo, Francis Mwasilu, Ju Lee, and Jin-Woo Jung. Ac-microgrids versus dc-microgrids with distributed energy resources: A review. *Renewable and Sustainable Energy Reviews*, 24:387 – 405, 2013. ISSN 1364-0321. doi: <https://doi.org/10.1016/j.rser.2013.03.067>. URL <http://www.sciencedirect.com/science/article/pii/S1364032113002268>. Cited on pp. 11 and 26.
- [65] Ahmed T. Ghareeb, Ahmed A. Mohamed, and Osama A. Mohammed. Dc microgrids and distribution systems: An overview. In *2013 IEEE Power Energy Society General Meeting*, pages 1–5, 2013. doi: 10.1109/PESMG.2013.6672624. Cited on p. 11.
- [66] Jintae Cho, Hongjoo Kim, Youngpyo Cho, Hyunmin Kim, and Juyong Kim. Demonstration of a dc microgrid with central operation strategies on an island. In *2019 IEEE Third International Conference on DC Microgrids (ICDCM)*, pages 1–5, 2019. doi: 10.1109/ICDCM45535.2019.9232893. Cited on pp. 11 and 12.
- [67] Yoshio Izui, Daisuke Natsuume, Masashi Saito, Hirokazu Tabata, and Masanori Fujimoto. Dc microgrid experimental system at kit hakusan-roku campus for regional areas. In *2019 IEEE Third International Conference on DC Microgrids (ICDCM)*, pages 1–7, 2019. doi: 10.1109/ICDCM45535.2019.9232869. Cited on p. 11.
- [68] European project tigon - towards intelligent dc-based hybrid grids optimizing the network performance (grant agreement id: 957769). <https://cordis.europa.eu/project/id/957769>, 2020 - 2024. Cited on p. 11.
- [69] Z. Jiang and X. Yu. Hybrid dc- and ac-linked microgrids: Towards integration of distributed energy resources. In *2008 IEEE Energy 2030 Conference*, pages 1–8, Nov 2008. Cited on pp. 11 and 12.
- [70] Z. Jiang and Xunwei Yu. Power electronics interfaces for hybrid dc and ac-linked microgrids. In *2009 IEEE 6th International Power Electronics and Motion Control Conference*, pages 730–736, May 2009. Cited on pp. 11 and 12.
- [71] Eneko Unamuno and Jon Andoni Barrena. Hybrid ac/dc microgrids—part i: Review and classification of topologies. *Renewable and Sustainable Energy Reviews*, 52:1251 – 1259, 2015. ISSN 1364-0321. doi: <https://doi.org/10.1016/j.rser.2015.07.194>. URL <http://www.sciencedirect.com/science/article/pii/S1364032115008412>. Cited on pp. 12, 31, and 32.
- [72] Poh Chiang Loh, Ding Li, Yi Kang Chai, and Frede Blaabjerg. Autonomous operation of hybrid ac-dc microgrids with progressive energy flow tuning. In *2012 Twenty-Seventh Annual IEEE Applied Power Electronics Conference and Exposition (APEC)*, pages 1056–1060, 2012. doi: 10.1109/APEC.2012.6165949. Cited on p. 12.
- [73] Guangqian Ding, Feng Gao, Song Zhang, Poh Chiang Loh, and Frede Blaabjerg. Control of hybrid ac/dc microgrid under islanding operational conditions. *Journal of Modern Power Systems and Clean Energy*, 2(3):223–232, 2014. doi: 10.1007/s40565-014-0065-z. Cited on p. 12.
- [74] Abdulkarim Karabiber, Cemal Keles, Asim Kaygusuz, and B. Baykant Alagoz. An approach for the integration of renewable distributed generation in hybrid dc/ac microgrids. *Renewable Energy*, 52:251–259, 2013. ISSN 0960-1481. doi: <https://doi.org/10.1016/j.renene.2012.10.041>. URL <https://www.sciencedirect.com/science/article/pii/S0960148112006866>. Cited on p. 12.

- [75] Xu She, Srdjan Lukic, Alex. Q. Huang, Subhashishi Bhattacharya, and Mesut Baran. Performance evaluation of solid state transformer based microgrid in freedom systems. In *2011 Twenty-Sixth Annual IEEE Applied Power Electronics Conference and Exposition (APEC)*, pages 182–188, 2011. doi: 10.1109/APEC.2011.5744594. Cited on pp. 12 and 13.
- [76] Jianhua Zhang, Wenye Wang, and Subhashish Bhattacharya. Architecture of solid state transformer-based energy router and models of energy traffic. In *2012 IEEE PES Innovative Smart Grid Technologies (ISGT)*, pages 1–8, 2012. doi: 10.1109/ISGT.2012.6175637. Cited on pp. 12 and 13.
- [77] W. A. Rodrigues, L. M. F. Morais, T. R. Oliveira, R. A. S. Santana, A. P. L. Cota, and W. W. A. G. Silva. Analysis of solid state transformer based microgrid system. In *2016 12th IEEE International Conference on Industry Applications (INDUSCON)*, pages 1–6, 2016. doi: 10.1109/INDUSCON.2016.7874543. Cited on p. 13.
- [78] Xu She, Alex Q. Huang, Srdjan Lukic, and Mesut E. Baran. On integration of solid-state transformer with zonal dc microgrid. *IEEE Transactions on Smart Grid*, 3(2):975–985, 2012. doi: 10.1109/TSG.2012.2187317. Cited on p. 13.
- [79] Xunwei Yu, Xu She, Xiaohu Zhou, and Alex. Q. Huang. Power management for dc microgrid enabled by solid-state transformer. *IEEE Transactions on Smart Grid*, 5(2):954–965, 2014. doi: 10.1109/TSG.2013.2277977. Cited on p. 13.
- [80] Enrique Espina, Claudio Burgos-Mellado, Juan S. Gomez, Jacqueline Llanos, Erwin Rute, Alex Navas F., Manuel Martínez-Gómez, Roberto Cárdenas, and Doris Sácz. Experimental hybrid ac/dc-microgrid prototype for laboratory research. In *2020 22nd European Conference on Power Electronics and Applications (EPE'20 ECCE Europe)*, pages 1–9, 2020. doi: 10.23919/EPE20ECCEurope43536.2020.9215751. Cited on p. 13.
- [81] Nuno Jose Gil and J. A. Peças Lopes. Hierarchical frequency control scheme for islanded multi-microgrids operation. In *2007 IEEE Lausanne Power Tech*, pages 473–478, 2007. doi: 10.1109/PCT.2007.4538363. Cited on pp. 13, 26, 34, and 35.
- [82] Cherry Yuen and Alexandre Oudalov. The feasibility and profitability of ancillary services provision from multi-microgrids. In *2007 IEEE Lausanne Power Tech*, pages 598–603, 2007. doi: 10.1109/PCT.2007.4538384. Cited on p. 13.
- [83] Julija Vasiljevska, Joao A. Peças Lopes, and Manuel A. Matos. Multi-microgrid impact assessment using multi criteria decision aid methods. In *2009 IEEE Bucharest PowerTech*, pages 1–8, 2009. doi: 10.1109/PTC.2009.5282054. Cited on p. 13.
- [84] M. Couto, J.A. Peças Lopes, and C.L. Moreira. Control strategies for multi-microgrids islanding operation through smart transformers. *Electric Power Systems Research*, 174:105866, 2019. ISSN 0378-7796. doi: <https://doi.org/10.1016/j.epsr.2019.105866>. URL <http://www.sciencedirect.com/science/article/pii/S0378779619301798>. Cited on pp. 13, 16, 34, 40, 42, and 52.
- [85] M. Couto, J. Peças Lopes, and Carlos Moreira. Developing black start strategies in multi-microgrids exploiting smart transformers. In *2020 International Conference on Smart Energy Systems and Technologies (SEST)*, pages 1–6, 2020. doi: 10.1109/SEST48500.2020.9203285. Cited on pp. 13, 16, 34, and 47.
- [86] Yang Fu, Zhiqian Zhang, Yang Mi, Zhenkun Li, and Fangxing Li. Droop control for dc multi-microgrids based on local adaptive fuzzy approach and global power allocation correction. *IEEE Transactions on Smart Grid*, 10(5):5468–5478, 2019. doi: 10.1109/TSG.2018.2883559. Cited on pp. 13 and 35.

- [87] Ali Abdali, Reza Noroozian, and Kazem Mazlumi. Simultaneous control and protection schemes for dc multi microgrids systems. *International Journal of Electrical Power & Energy Systems*, 104: 230–245, 2019. ISSN 0142-0615. doi: <https://doi.org/10.1016/j.ijepes.2018.06.054>. URL <https://www.sciencedirect.com/science/article/pii/S0142061517314242>. Cited on pp. 13 and 35.
- [88] Mohamed Zaery, Panbao Wang, Wei Wang, and Dianguo Xu. A novel fully distributed fixed-time optimal dispatch of dc multi-microgrids. *International Journal of Electrical Power & Energy Systems*, 129:106792, 2021. ISSN 0142-0615. doi: <https://doi.org/10.1016/j.ijepes.2021.106792>. URL <https://www.sciencedirect.com/science/article/pii/S0142061521000326>. Cited on pp. 13 and 35.
- [89] Hui Guo, Fei Wang, Jian Luo, and Lijun Zhang. Review of energy routers applied for the energy internet integrating renewable energy. In *2016 IEEE 8th International Power Electronics and Motion Control Conference (IPEMC-ECCE Asia)*, pages 1997–2003, 2016. doi: 10.1109/IPEMC.2016.7512602. Cited on pp. 13 and 36.
- [90] Haifeng Qiu, Bo Zhao, Wei Gu, and Rui Bo. Bi-level two-stage robust optimal scheduling for ac/dc hybrid multi-microgrids. *IEEE Transactions on Smart Grid*, 9(5):5455–5466, 2018. doi: 10.1109/TSG.2018.2806973. Cited on pp. 13 and 36.
- [91] Hrishikesan V M and Chandan Kumar. Operation of meshed hybrid microgrid during adverse grid conditions with storage integrated smart transformer. *IEEE Open Journal of the Industrial Electronics Society*, 2:315–325, 2021. doi: 10.1109/OJIES.2021.3073142. Cited on pp. 13 and 36.
- [92] Hrishikesan V M, Chandan Kumar, and Marco Liserre. An mvdc based meshed hybrid microgrid enabled using smart transformers. *IEEE Transactions on Industrial Electronics*, pages 1–1, 2021. doi: 10.1109/TIE.2021.3071683. Cited on pp. 13 and 36.
- [93] G. Messinis, V. Kleftakis, I. Kouveliotis-Lysikatos, A. Rigas, A. Vassilakis, P. Kotsampopoulos, and N. Hatziaargyriou. A multi-microgrid laboratory infrastructure for smart grid applications. In *MedPower 2014*, pages 1–6, 2014. doi: 10.1049/cp.2014.1670. Cited on p. 13.
- [94] L. F. Costa, G. Buticchi, and M. Liserre. Highly efficient and reliable sic-based dc–dc converter for smart transformer. *IEEE Transactions on Industrial Electronics*, 64(10):8383–8392, Oct 2017. Cited on p. 14.
- [95] A. Q. Huang, Q. Zhu, L. Wang, and L. Zhang. 15 kv sic mosfet: An enabling technology for medium voltage solid state transformers. *CPSS Transactions on Power Electronics and Applications*, 2(2):118–130, 2017. Cited on pp. 14 and 15.
- [96] G. Zhang, J. Chen, B. Zhang, and Y. Zhang. A critical topology review of power electronic transformers: In view of efficiency. *Chinese Journal of Electrical Engineering*, 4(2):90–95, June 2018. Cited on p. 14.
- [97] Alex Q. Huang. 2 - solid state transformers, the energy router and the energy internet. In Wencong Su and Alex Q. Huang, editors, *The Energy Internet*, pages 21 – 44. Woodhead Publishing, 2019. ISBN 978-0-08-102207-8. doi: <https://doi.org/10.1016/B978-0-08-102207-8.00002-3>. URL <http://www.sciencedirect.com/science/article/pii/B9780081022078000023>. Cited on p. 14.
- [98] S. Falcones, X. Mao, and R. Ayyanar. Topology comparison for solid state transformer implementation. In *IEEE PES General Meeting*, pages 1–8, July 2010. Cited on p. 14.
- [99] S. Madhusoodhanan, K. Mainali, A. Tripathi, A. Kadavelugu, K. Vechalapu, D. Patel, and S. Bhattacharya. Comparative evaluation of 15 kv sic igbt and 15 kv sic mosfet for 3-phase medium voltage high power grid connected converter applications. In *2016 IEEE Energy Conversion Congress and Exposition (ECCE)*, pages 1–8, Sep. 2016. Cited on p. 15.



- [100] Satish Belkhode, Poornachandra Rao, Anshuman Shukla, and Suryanarayana Doolla. Comparative evaluation of silicon and silicon-carbide devices-based mmc and npc converter for medium voltage applications. *IEEE Journal of Emerging and Selected Topics in Power Electronics*, pages 1–1, 2021. doi: 10.1109/JESTPE.2021.3103075. Cited on p. 15.
- [101] Peter Unruh, Maria Nuschke, Philipp Strauß, and Friedrich Welck. Overview on grid-forming inverter control methods. *Energies*, 13(10), 2020. ISSN 1996-1073. URL <https://www.mdpi.com/1996-1073/13/10/2589>. Cited on pp. 15, 16, 17, 18, 19, 20, and 23.
- [102] Roberto Rosso, Xiongfei Wang, Marco Liserre, Xiaonan Lu, and Soenke Engelken. Grid-forming converters: an overview of control approaches and future trends. In *2020 IEEE Energy Conversion Congress and Exposition (ECCE)*, pages 4292–4299, 2020. doi: 10.1109/ECCE44975.2020.9236211. Cited on pp. 15 and 16.
- [103] Xiongfei Wang, Josep Guerrero, F. Blaabjerg, and Z. Chen. A review of power electronics based microgrids. *Journal of power electronics*, 12:181–192, 01 2012. doi: 10.6113/JPE.2012.12.1.181. Cited on pp. 15, 21, 22, and 23.
- [104] F. Blaabjerg, R. Teodorescu, M. Liserre, and A.V. Timbus. Overview of control and grid synchronization for distributed power generation systems. *IEEE Transactions on Industrial Electronics*, 53(5): 1398–1409, 2006. doi: 10.1109/TIE.2006.881997. Cited on pp. 15 and 21.
- [105] S. Dutta, V. Ramachandaran, and S. Bhattacharya. Black start operation for the solid state transformer created micro-grid under islanding with storage. In *2014 IEEE Energy Conversion Congress and Exposition (ECCE)*, pages 3934–3941, Sep. 2014. Cited on p. 16.
- [106] Lidong Zhang, Lennart Harnefors, and Hans-Peter Nee. Power-synchronization control of grid-connected voltage-source converters. *IEEE Transactions on Power Systems*, 25(2):809–820, 2010. doi: 10.1109/TPWRS.2009.2032231. Cited on pp. 17 and 18.
- [107] Stefan Laudahn, Julia Seidel, Bernd Engel, Thorsten Bülo, and Daniel Premm. Substitution of synchronous generator based instantaneous frequency control utilizing inverter-coupled der. In *2016 IEEE 7th International Symposium on Power Electronics for Distributed Generation Systems (PEDG)*, pages 1–8, 2016. doi: 10.1109/PEDG.2016.7527020. Cited on p. 18.
- [108] Hans-Peter Beck and Ralf Hesse. Virtual synchronous machine. In *2007 9th International Conference on Electrical Power Quality and Utilisation*, pages 1–6, 2007. doi: 10.1109/EPQU.2007.4424220. Cited on p. 18.
- [109] Linbin Huang, Huanhai Xin, Zhen Wang, Kuayu Wu, Haijiao Wang, Jiabing Hu, and Cencen Lu. A virtual synchronous control for voltage-source converters utilizing dynamics of dc-link capacitor to realize self-synchronization. *IEEE Journal of Emerging and Selected Topics in Power Electronics*, 5(4):1565–1577, 2017. doi: 10.1109/JESTPE.2017.2740424. Cited on pp. 18 and 19.
- [110] Mohit Sinha, Florian Dörfler, Brian B. Johnson, and Sairaj V. Dhople. Uncovering droop control laws embedded within the nonlinear dynamics of van der pol oscillators. *IEEE Transactions on Control of Network Systems*, 4(2):347–358, 2017. doi: 10.1109/TCNS.2015.2503558. Cited on p. 19.
- [111] Puspall Hazra, Ramtin Hadidi, and Elham Makram. Dynamic study of virtual oscillator controlled inverter based distributed energy source. In *2015 North American Power Symposium (NAPS)*, pages 1–6, 2015. doi: 10.1109/NAPS.2015.7335221. Cited on p. 19.
- [112] M. A. Awal and Iqbal Husain. Unified virtual oscillator control for grid-forming and grid-following converters. *IEEE Journal of Emerging and Selected Topics in Power Electronics*, 9(4):4573–4586, 2021. doi: 10.1109/JESTPE.2020.3025748. Cited on pp. 19 and 20.

- [113] Gab-Su Seo, Marcello Colombino, Irina Subotic, Brian Johnson, Dominic Groß, and Florian Dörfler. Dispatchable virtual oscillator control for decentralized inverter-dominated power systems: Analysis and experiments. In *2019 IEEE Applied Power Electronics Conference and Exposition (APEC)*, pages 561–566, 2019. doi: 10.1109/APEC.2019.8722028. Cited on p. 20.
- [114] Mario Ndreko, Sven Rüberg, and Wilhelm Winter. Grid forming control for stable power systems with up to 100 % inverter based generation: A paradigm scenario using the ieee 118-bus system. 10 2018. Cited on p. 20.
- [115] Yonghao Gui, Xiongfei Wang, Frede Blaabjerg, and Donghua Pan. Control of grid-connected voltage-source converters: The relationship between direct-power control and vector-current control. *IEEE Industrial Electronics Magazine*, 13(2):31–40, 2019. doi: 10.1109/MIE.2019.2898012. Cited on pp. 20 and 21.
- [116] Ebrahim Rokrok, Taoufik Qoria, Antoine Bruyere, Bruno Francois, and Xavier Guillaud. Effect of using pll-based grid-forming control on active power dynamics under various scr. In *IECON 2019 - 45th Annual Conference of the IEEE Industrial Electronics Society*, volume 1, pages 4799–4804, 2019. doi: 10.1109/IECON.2019.8927648. Cited on p. 21.
- [117] Peter J. van Duijsen and Diëgo C. Zuidervliet. Teaching field oriented control using animation. In *2021 17th Conference on Electrical Machines, Drives and Power Systems (ELMA)*, pages 1–6, 2021. doi: 10.1109/ELMA52514.2021.9502966. Cited on p. 22.
- [118] Andrés Peña Asensio, Francisco Gonzalez-Longatt, Santiago Arnaltes, and Jose Luis Rodríguez-Amenedo. Analysis of the converter synchronizing method for the contribution of battery energy storage systems to inertia emulation. *Energies*, 13(6), 2020. ISSN 1996-1073. URL <https://www.mdpi.com/1996-1073/13/6/1478>. Cited on p. 22.
- [119] Mariusz Malinowski, M.P. Kazmierkowski, and Andrzej M Trzynadlowski. A comparative study of control techniques for pwm rectifiers in ac adjustable speed drives. *Power Electronics, IEEE Transactions on*, 18:1390 – 1396, 12 2003. doi: 10.1109/TPEL.2003.818871. Cited on p. 22.
- [120] Adel Aberbour and Kassa Idjdarene. Study on sliding mode virtual flux oriented control for three-phase pwm rectifiers. 2016. Cited on pp. 22 and 23.
- [121] Daniel Duckwitz. *Power System Inertia*. PhD thesis, Kassel, Universität Kassel, Fachbereich Elektrotechnik/Informatik, 2019. Cited on pp. 23 and 24.
- [122] I. Erlich, A. Korai, and F. Shewarega. Study on the minimum share of conventional generation units required for stable operation of future converter-dominated grids. In *2018 IEEE Power Energy Society General Meeting (PESGM)*, pages 1–5, 2018. doi: 10.1109/PESGM.2018.8585943. Cited on p. 23.
- [123] Stefano Giacomuzzi, Giovanni De Carne, Sante Pugliese, Giuseppe Buja, Marco Liserre, and Ali Kazerooni. Synchronization of low voltage grids fed by smart and conventional transformers. *IEEE Transactions on Smart Grid*, 12(4):2941–2951, 2021. doi: 10.1109/TSG.2021.3054478. Cited on pp. 25, 46, and 117.
- [124] R. J. G. Montoya, A. Mallela, and J. C. Balda. An evaluation of selected solid-state transformer topologies for electric distribution systems. In *2015 IEEE Applied Power Electronics Conference and Exposition (APEC)*, pages 1022–1029, March 2015. Cited on p. 25.
- [125] Yeliz Yoldaş, Ahmet Önen, S.M. Muyeen, Athanasios V. Vasilakos, and İrfan Alan. Enhancing smart grid with microgrids: Challenges and opportunities. *Renewable and Sustainable Energy Reviews*, 72:205 – 214, 2017. ISSN 1364-0321. doi: <https://doi.org/10.1016/j.rser.2017.01.064>. URL <http://www.sciencedirect.com/science/article/pii/S1364032117300746>. Cited on p. 26.

- [126] A. Bidram and A. Davoudi. Hierarchical structure of microgrids control system. *IEEE Transactions on Smart Grid*, 3(4):1963–1976, Dec 2012. Cited on p. 26.
- [127] H. Han, X. Hou, J. Yang, J. Wu, M. Su, and J. M. Guerrero. Review of power sharing control strategies for islanding operation of ac microgrids. *IEEE Transactions on Smart Grid*, 7(1):200–215, Jan 2016. Cited on p. 26.
- [128] S. Mirsaeidi, X. Dong, S. Shi, and D. Tzelepis. Challenges, advances and future directions in protection of hybrid ac/dc microgrids. *IET Renewable Power Generation*, 11(12):1495–1502, 2017. Cited on pp. 26 and 31.
- [129] C. Gouveia, J. Moreira, C. L. Moreira, and J. A. Peças Lopes. Coordinating storage and demand response for microgrid emergency operation. *IEEE Transactions on Smart Grid*, 4(4):1898–1908, 2013. doi: 10.1109/TSG.2013.2257895. Cited on pp. 26 and 78.
- [130] Brevann Nun, Muhammad Farooq Umar, Anas Karaki, Mohammad B Shadmand, Sertac Bayhan, and Haitham Abu-Rub. Rank-based predictive control for community microgrids with dynamic topology and multiple points of common coupling. *IEEE Journal of Emerging and Selected Topics in Industrial Electronics*, pages 1–1, 2021. doi: 10.1109/JESTIE.2021.3110746. Cited on p. 27.
- [131] Ashutosh Trivedi and Mukhtiar Singh.  $I_1$  adaptive droop control for ac microgrid with small mesh network. *IEEE Transactions on Industrial Electronics*, 65(6):4781–4789, 2018. doi: 10.1109/TIE.2017.2772211. Cited on p. 27.
- [132] K.S. Rajesh, S.S. Dash, Ragam Rajagopal, and R. Sridhar. A review on control of ac microgrid. *Renewable and Sustainable Energy Reviews*, 71:814–819, 2017. ISSN 1364-0321. doi: <https://doi.org/10.1016/j.rser.2016.12.106>. URL <https://www.sciencedirect.com/science/article/pii/S1364032116311613>. Cited on pp. 27 and 28.
- [133] Amira Mohammed, Shady S. Refaat, Sertac Bayhan, and Haithem Abu-Rub. Ac microgrid control and management strategies: Evaluation and review. *IEEE Power Electronics Magazine*, 6(2):18–31, 2019. doi: 10.1109/MPEL.2019.2910292. Cited on pp. 27 and 28.
- [134] Enrique Espina, Jacqueline Llanos, Claudio Burgos-Mellado, Roberto Cárdenas-Dobson, Manuel Martínez-Gómez, and Doris Sáez. Distributed control strategies for microgrids: An overview. *IEEE Access*, 8:193412–193448, 2020. doi: 10.1109/ACCESS.2020.3032378. Cited on pp. 27, 29, and 30.
- [135] Josep M. Guerrero, Juan C. Vasquez, José Matas, Luis García de Vicuna, and Miguel Castilla. Hierarchical control of droop-controlled ac and dc microgrids—a general approach toward standardization. *IEEE Transactions on Industrial Electronics*, 58(1):158–172, 2011. doi: 10.1109/TIE.2010.2066534. Cited on pp. 27 and 29.
- [136] T. Dragičević, X. Lu, J. C. Vasquez, and J. M. Guerrero. Dc microgrids—part i: A review of control strategies and stabilization techniques. *IEEE Transactions on Power Electronics*, 31(7):4876–4891, July 2016. Cited on pp. 29 and 30.
- [137] T. Dragičević, X. Lu, J. C. Vasquez, and J. M. Guerrero. Dc microgrids—part ii: A review of power architectures, applications, and standardization issues. *IEEE Transactions on Power Electronics*, 31(5):3528–3549, May 2016. Cited on p. 29.
- [138] I. Zafeiratou, I. Prodan, L. Lefèvre, and L. Piétrac. Meshed dc microgrid hierarchical control: A differential flatness approach. *Electric Power Systems Research*, 180:106133, 2020. ISSN 0378-7796. doi: <https://doi.org/10.1016/j.epsr.2019.106133>. URL <https://www.sciencedirect.com/science/article/pii/S0378779619304523>. Cited on p. 29.
- [139] Fei Gao, Ren Kang, Jun Cao, and Tao Yang. Primary and secondary control in dc microgrids: a review. *Journal of Modern Power Systems and Clean Energy*, 7(2):227–242, 2019. doi: 10.1007/s40565-018-0466-5. Cited on pp. 29 and 30.



- [140] X. Liu, P. Wang, and P. C. Loh. A hybrid ac/dc microgrid and its coordination control. *IEEE Transactions on Smart Grid*, 2(2):278–286, June 2011. Cited on p. 31.
- [141] Saroja Kanti Sahoo, Avinash Kumar Sinha, and N. K. Kishore. Control techniques in ac, dc, and hybrid ac–dc microgrid: A review. *IEEE Journal of Emerging and Selected Topics in Power Electronics*, 6(2):738–759, 2018. doi: 10.1109/JESTPE.2017.2786588. Cited on p. 32.
- [142] Eneko Unamuno and Jon Andoni Barrena. Hybrid ac/dc microgrids—part ii: Review and classification of control strategies. *Renewable and Sustainable Energy Reviews*, 52:1123 – 1134, 2015. ISSN 1364-0321. doi: <https://doi.org/10.1016/j.rser.2015.07.186>. URL <http://www.sciencedirect.com/science/article/pii/S1364032115008333>. Cited on p. 32.
- [143] Dwijasish Das, V. M. Hrishikesan, Chandan Kumar, and Marco Liserre. Smart transformer-enabled meshed hybrid distribution grid. *IEEE Transactions on Industrial Electronics*, 68(1):282–292, 2021. doi: 10.1109/TIE.2020.2965489. Cited on pp. 33, 40, and 46.
- [144] Dwijasish Das, Rampelli Manojkumar, Chandan Kumar, and Sanjib Ganguly. Optimal power management for islanded operation of st-based meshed hybrid lv microgrid. In *2021 IEEE 12th Energy Conversion Congress Exposition - Asia (ECCE-Asia)*, pages 183–188, 2021. doi: 10.1109/ECCE-Asia49820.2021.9479110. Cited on p. 33.
- [145] Dwijasish Das and Chandan Kumar. Partial start-up scheme for smart transformer in meshed hybrid islanded grid operation. *IEEE Transactions on Industry Applications*, pages 1–1, 2021. doi: 10.1109/TIA.2021.3124862. Cited on pp. 33 and 46.
- [146] Rongwu Zhu, Marco Liserre, Marius Langwasser, and Chandan Kumar. Operation and control of the smart transformer in meshed and hybrid grids: Choosing the appropriate smart transformer control and operation scheme. *IEEE Industrial Electronics Magazine*, 15(1):43–57, 2021. doi: 10.1109/MIE.2020.3005357. Cited on pp. 33 and 46.
- [147] Rongwu Zhu and Marco Liserre. Operation and supervision control in smart transformer-based meshed and hybrid grids. In *2020 6th IEEE International Energy Conference (ENERGYCon)*, pages 1019–1023, 2020. doi: 10.1109/ENERGYCon48941.2020.9236572. Cited on pp. 33 and 46.
- [148] Nikos Hatziargyriou. *Operation of Multi-Microgrids*, pages 165–205. 2014. doi: 10.1002/9781118720677.ch05. Cited on p. 34.
- [149] Ming Ding, Kai Ma, Rui Bi, Meiqin Mao, and Liuchen Chang. A hierarchical control scheme based on multi-agent system for islanded multi-microgrids. In *2013 4th IEEE International Symposium on Power Electronics for Distributed Generation Systems (PEDG)*, pages 1–5, 2013. doi: 10.1109/PEDG.2013.6785639. Cited on p. 34.
- [150] Xiaoyu Wu, Xiangyu Wu, Yin Xu, and Jinghan He. A hierarchical control framework for islanded multi-microgrid systems. In *2018 IEEE Power Energy Society General Meeting (PESGM)*, pages 1–5, 2018. doi: 10.1109/PESGM.2018.8586235. Cited on p. 34.
- [151] Rohit R. Deshmukh and Makarand S. Ballal. Hierarchical control for effective power management and to improve voltage regulation in dc multi-microgrid system. In *2020 IEEE International Conference on Power Electronics, Drives and Energy Systems (PEDES)*, pages 1–6, 2020. doi: 10.1109/PEDES49360.2020.9379359. Cited on p. 35.
- [152] Moossa Khodadadi Arpanahi, Abolfazl Nateghi, and Miadreza Shafie-khah. A coordinated decentralized loss minimization scheme for hybrid ac/dc distribution system with multiple microgrids. In *2021 International Conference on Smart Energy Systems and Technologies (SEST)*, pages 1–6, 2021. doi: 10.1109/SEST50973.2021.9543199. Cited on p. 36.

- [153] Minh-Cong Pham, Quoc-Tuan Tran, Ahmad Hably, and Seddik Bacha. Application of energy routers for frequency support in an ac/dc multi-microgrid system. In *2021 IEEE International Conference on Environment and Electrical Engineering and 2021 IEEE Industrial and Commercial Power Systems Europe (EEEIC / I CPS Europe)*, pages 1–6, 2021. doi: 10.1109/EEEIC/ICPSEurope51590.2021.9584708. Cited on p. 36.
- [154] M. Yang, D. Xie, H. Zhu, and Y. Lou. Architectures and control for multi-terminal dc (mtdc) distribution network-a review. In *11th IET International Conference on AC and DC Power Transmission*, pages 1–7, Feb 2015. Cited on p. 37.
- [155] J. P. Olvera, T. Green, and A. Junyent-Ferre. Using multi-terminal dc networks to improve the hosting capacity of distribution networks. In *2018 IEEE PES Innovative Smart Grid Technologies Conference Europe (ISGT-Europe)*, pages 1–6, Oct 2018. Cited on p. 37.
- [156] C. Liang, J. Mengmeng, H. Qiang, Y. Xiaodong, C. Gu, and L. Fei. Research on power information hybrid simulation technology of dc distribution network based on multi-terminal flexible dc. In *2018 2nd IEEE Conference on Energy Internet and Energy System Integration (EI2)*, pages 1–6, Oct 2018. Cited on p. 37.
- [157] P. Chen, R. Salcedo, Q. Zhu, F. de Leon, D. Czarkowski, Z. Jiang, V. Spitsa, Z. Zabar, and R. E. Uosef. Analysis of voltage profile problems due to the penetration of distributed generation in low-voltage secondary distribution networks. *IEEE Transactions on Power Delivery*, 27(4):2020–2028, Oct 2012. Cited on p. 38.
- [158] Z. Li, Q. Guo, H. Sun, J. Wang, Y. Xu, and M. Fan. A distributed transmission-distribution-coupled static voltage stability assessment method considering distributed generation. *IEEE Transactions on Power Systems*, 33(3):2621–2632, May 2018. Cited on p. 38.
- [159] A. Dubey and S. Santoso. Electric vehicle charging on residential distribution systems: Impacts and mitigations. *IEEE Access*, 3:1871–1893, 2015. Cited on p. 38.
- [160] W. Li, Y. Gu, H. Luo, W. Cui, X. He, and C. Xia. Topology review and derivation methodology of single-phase transformerless photovoltaic inverters for leakage current suppression. *IEEE Transactions on Industrial Electronics*, 62(7):4537–4551, July 2015. Cited on pp. 38 and 41.
- [161] S. Mokkapaty, J. Weiss, F. Schallow, and J. Declercq. New generation voltage regulation distribution transformer with an on load tap changer for power quality improvement in the electrical distribution systems. *CIREN - Open Access Proceedings Journal*, 2017(1):784–787, 2017. Cited on p. 39.
- [162] M. Sojer and W. Hofer. Beyond grid integration of renewables – voltage regulation distribution transformers (vrtds) in public grids, at industrial sites, and as part of generation units. *CIREN - Open Access Proceedings Journal*, 2017(1):50–53, 2017. Cited on p. 39.
- [163] H. Sagha, G. Mokhtari, A. Arefi, G. Nourbakhsh, G. Ledwich, and A. Ghosh. A new approach to improve pv power injection in lv electrical systems using dvr. *IEEE Systems Journal*, 12(4):3324–3333, Dec 2018. Cited on p. 39.
- [164] P. T. Ogunboyo, R. Tiako, and I. E. Davidson. Effectiveness of dynamic voltage restorer for unbalance voltage mitigation and voltage profile improvement in secondary distribution system. *Canadian Journal of Electrical and Computer Engineering*, 41(2):105–115, Spring 2018. Cited on p. 39.
- [165] S. Kincic, X. T. Wan, D. T. McGillis, A. Chandra, Boon-Teck Ooi, F. D. Galiana, and G. Joos. Voltage support by distributed static var systems (svs). *IEEE Transactions on Power Delivery*, 20(2):1541–1549, April 2005. Cited on p. 39.
- [166] P. S. Sensarma, K. R. Padiyar, and V. Ramanarayanan. Analysis and performance evaluation of a distribution statcom for compensating voltage fluctuations. *IEEE Transactions on Power Delivery*, 16(2):259–264, April 2001. Cited on p. 39.

- [167] N. Takahashi and Y. Hayashi. Centralized voltage control method using plural d-statcom with controllable dead band in distribution system with renewable energy. In *2012 3rd IEEE PES Innovative Smart Grid Technologies Europe (ISGT Europe)*, pages 1–5, Oct 2012. Cited on p. 39.
- [168] K. E. Antoniadou-Plytaria, I. N. Kouveliotis-Lysikatos, P. S. Georgilakis, and N. D. Hatziargyriou. Distributed and decentralized voltage control of smart distribution networks: Models, methods, and future research. *IEEE Transactions on Smart Grid*, 8(6):2999–3008, Nov 2017. Cited on p. 39.
- [169] A. T. Al-Awami, E. Sortomme, G. M. Asim Akhtar, and S. Faddel. A voltage-based controller for an electric-vehicle charger. *IEEE Transactions on Vehicular Technology*, 65(6):4185–4196, June 2016. Cited on p. 39.
- [170] S. Martinenas, K. Knezović, and M. Marinelli. Management of power quality issues in low voltage networks using electric vehicles: Experimental validation. *IEEE Transactions on Power Delivery*, 32(2):971–979, April 2017. Cited on p. 39.
- [171] J. Quirós-Tortós, L. F. Ochoa, S. W. Alnaser, and T. Butler. Control of ev charging points for thermal and voltage management of lv networks. *IEEE Transactions on Power Systems*, 31(4):3028–3039, July 2016. Cited on p. 39.
- [172] S. Jupe, S. Hoda, A. Park, M. Wright, and S. Hodgson. Active management of generation in low-voltage networks. *CIREN - Open Access Proceedings Journal*, 2017(1):916–919, 2017. Cited on p. 39.
- [173] F. Nejabatkhah, Y. W. Li, and B. Wu. Control strategies of three-phase distributed generation inverters for grid unbalanced voltage compensation. *IEEE Transactions on Power Electronics*, 31(7):5228–5241, July 2016. Cited on p. 39.
- [174] S. Weckx and J. Driesen. Load balancing with ev chargers and pv inverters in unbalanced distribution grids. *IEEE Transactions on Sustainable Energy*, 6(2):635–643, April 2015. Cited on p. 39.
- [175] J. Rodrigues, A. Lopes, L. Miranda, C. Gouveia, C. Moreira, and J. Peças Lopes. The role of low-voltage-ride-through capability of distributed energy resources for the mitigation of voltage sags in low voltage distribution grids. In *2018 Power Systems Computation Conference (PSCC)*, pages 1–7, June 2018. Cited on pp. 39 and 78.
- [176] C. Gouveia, D. Rua, F. Ribeiro, C. L. Moreira, and J. A. P. Lopes. Inesc porto experimental smart grid: Enabling the deployment of ev and der. In *2013 IEEE Grenoble Conference*, pages 1–6, June 2013. Cited on p. 39.
- [177] Ali Q. Al-Shetwi and Muhamad Zahim Sujod. Grid-connected photovoltaic power plants: A review of the recent integration requirements in modern grid codes. *International Journal of Energy Research*, 42(5):1849–1865, 2018. doi: <https://doi.org/10.1002/er.3983>. URL <https://onlinelibrary.wiley.com/doi/abs/10.1002/er.3983>. Cited on pp. 39 and 41.
- [178] H. V. M, D. Das, and C. Kumar. A flexible and coordinated voltage control strategy for smart transformer. In *2018 IEEE International Conference on Power Electronics, Drives and Energy Systems (PEDES)*, pages 1–6, Dec 2018. Cited on p. 40.
- [179] D. Shah and M. L. Crow. Online volt-var control for distribution systems with solid-state transformers. *IEEE Transactions on Power Delivery*, 31(1):343–350, Feb 2016. Cited on p. 40.
- [180] X. Gao, G. De Carne, M. Liserre, and C. Vournas. Voltage control by means of smart transformer in medium voltage feeder with distribution generation. In *2017 IEEE Manchester PowerTech*, pages 1–6, June 2017. Cited on p. 40.

- [181] J. Chen, R. Zhu, M. Liu, G. De Carne, M. Liserre, F. Milano, and T. O'Donnell. Smart transformer for the provision of coordinated voltage and frequency support in the grid. In *IECON 2018 - 44th Annual Conference of the IEEE Industrial Electronics Society*, pages 5574–5579, Oct 2018. Cited on pp. 40 and 43.
- [182] Stefano Giacomuzzi, Marius Langwasser, Giovanni De Carne, Giuseppe Buja, and Marco Liserre. Smart transformer-based medium voltage grid support by means of active power control. *CES Transactions on Electrical Machines and Systems*, 4(4):285–294, 2020. doi: 10.30941/CESTEMS.2020.00035. Cited on p. 40.
- [183] D. Das and C. Kumar. Operation and control of smart transformer based distribution grid in a microgrid system. In *2017 National Power Electronics Conference (NPEC)*, pages 135–140, Dec 2017. Cited on p. 40.
- [184] L. Wang, D. Zhang, Y. Wang, B. Wu, and H. S. Athab. Power and voltage balance control of a novel three-phase solid-state transformer using multilevel cascaded h-bridge inverters for microgrid applications. *IEEE Transactions on Power Electronics*, 31(4):3289–3301, April 2016. Cited on p. 40.
- [185] Mário Couto, João A. Peças Lopes, and Carlos L. Moreira. Smart transformer control strategies for multi-microgrid islanding operation. In *Mediterranean Conference on Power Generation, Transmission, Distribution and Energy Conversion (MEDPOWER 2018)*, pages 1–6, 2018. doi: 10.1049/cp.2018.1847. Cited on pp. 40 and 42.
- [186] S. Winternheimer, M. Ames, and M. Igel. The challenge to replace synchronous generators by inverter based distributed generation systems. In *2015 IEEE 6th International Symposium on Power Electronics for Distributed Generation Systems (PEDG)*, pages 1–6, June 2015. Cited on p. 41.
- [187] E. Serban, M. Ordonez, and C. Pondiche. Voltage and frequency grid support strategies beyond standards. *IEEE Transactions on Power Electronics*, 32(1):298–309, Jan 2017. Cited on p. 41.
- [188] European Commission. Establishing a network code on requirements for grid connection of generators, no 2016/631, 14 April 2016. Cited on p. 41.
- [189] S. S. Guggilam, C. Zhao, E. Dall'Anese, Y. C. Chen, and S. V. Dhople. Optimizing power–frequency droop characteristics of distributed energy resources. *IEEE Transactions on Power Systems*, 33(3): 3076–3086, May 2018. Cited on p. 41.
- [190] K. Kaur, N. Kumar, and M. Singh. Coordinated power control of electric vehicles for grid frequency support: Milp-based hierarchical control design. *IEEE Transactions on Smart Grid*, 10(3): 3364–3373, May 2019. Cited on p. 41.
- [191] X. Lyu, Z. Xu, J. Zhao, and K. P. Wong. Advanced frequency support strategy of photovoltaic system considering changing working conditions. *IET Generation, Transmission Distribution*, 12(2): 363–370, 2018. Cited on p. 41.
- [192] J. W. Shim, G. Verbič, N. Zhang, and K. Hur. Harmonious integration of faster-acting energy storage systems into frequency control reserves in power grid with high renewable generation. *IEEE Transactions on Power Systems*, 33(6):6193–6205, Nov 2018. Cited on p. 41.
- [193] L. Miao, J. Wen, H. Xie, C. Yue, and W. Lee. Coordinated control strategy of wind turbine generator and energy storage equipment for frequency support. *IEEE Transactions on Industry Applications*, 51(4):2732–2742, July 2015. Cited on p. 41.
- [194] G. Delille, B. Francois, and G. Malarange. Dynamic frequency control support by energy storage to reduce the impact of wind and solar generation on isolated power system's inertia. *IEEE Transactions on Sustainable Energy*, 3(4):931–939, Oct 2012. Cited on p. 41.

- [195] G. De Carne, G. Buticchi, M. Liserre, P. Marinakis, and C. Vournas. Coordinated frequency and voltage overload control of smart transformers. In *2015 IEEE Eindhoven PowerTech*, pages 1–5, June 2015. Cited on p. 42.
- [196] G. De Carne, G. Buticchi, M. Liserre, and C. Vournas. Frequency-based overload control of smart transformers. In *2015 IEEE Eindhoven PowerTech*, pages 1–5, June 2015. Cited on p. 42.
- [197] Z. X. Zou, G. De Carne, G. Buticchi, and M. Liserre. Frequency-adaptive control of smart transformer-fed distribution grid. *IEEE Transactions on Industrial Electronics*, PP(99):1–1, 2017. Cited on p. 42.
- [198] G. De Carne, G. Buticchi, M. Liserre, and C. Vournas. Real-time primary frequency regulation using load power control by smart transformers. *IEEE Transactions on Smart Grid*, 10(5):5630–5639, Sep. 2019. Cited on p. 43.
- [199] S. Eftekharnajad, V. Vittal, G. T. Heydt, B. Keel, and J. Loehr. Impact of increased penetration of photovoltaic generation on power systems. *IEEE Transactions on Power Systems*, 28(2):893–901, May 2013. Cited on p. 44.
- [200] J. Alipoor, Y. Miura, and T. Ise. Distributed generation grid integration using virtual synchronous generator with adoptive virtual inertia. In *2013 IEEE Energy Conversion Congress and Exposition*, pages 4546–4552, Sept 2013. Cited on p. 44.
- [201] Salvatore D’Arco and Jon Are Suul. Equivalence of virtual synchronous machines and frequency-droops for converter-based microgrids. *IEEE Transactions on Smart Grid*, 5(1):394–395, 2014. Cited on pp. 44 and 61.
- [202] G. Legudi and M. Datta. Transient stability of a hybrid micro-grid with multivariable droop and virtual synchronous generator. In *2016 IEEE Innovative Smart Grid Technologies - Asia (ISGT-Asia)*, pages 171–176, Nov 2016. Cited on p. 44.
- [203] S. Debbarma and R. Shrivastwa. Grid frequency support from v2g aggregators and hvdc links in presence of nonsynchronous units. *IEEE Systems Journal*, 13(2):1757–1766, June 2019. Cited on p. 44.
- [204] M. Langwasser, G. De Carne, and M. Liserre. Smart transformer-based frequency support in variable inertia conditions. In *2019 IEEE 13th International Conference on Compatibility, Power Electronics and Power Engineering (CPE-POWERENG)*, pages 1–6, April 2019. Cited on p. 44.
- [205] Junru Chen, Muyang Liu, Giovanni De Carne, Rongwu Zhu, Marco Liserre, Federico Milano, and Terence O’Donnell. Impact of smart transformer voltage and frequency support in a high renewable penetration system. *Electric Power Systems Research*, 190:106836, 2021. ISSN 0378-7796. doi: <https://doi.org/10.1016/j.epsr.2020.106836>. URL <https://www.sciencedirect.com/science/article/pii/S0378779620306362>. Cited on p. 44.
- [206] X. Liang and J. Hofman. Trip curves and ride-through evaluation for power electronic devices in power system dynamic studies. *IEEE Transactions on Industry Applications*, 52(2):1290–1296, March 2016. Cited on p. 45.
- [207] A. Mojallal and S. Lotfifard. Enhancement of grid connected pv arrays fault ride through and post fault recovery performance. *IEEE Transactions on Smart Grid*, 10(1):546–555, Jan 2019. Cited on p. 45.
- [208] M. E. Elshiekh, D. A. Mansour, and A. M. Azmy. Improving fault ride-through capability of dfig-based wind turbine using superconducting fault current limiter. *IEEE Transactions on Applied Superconductivity*, 23(3):5601204–5601204, June 2013. Cited on p. 45.



- [209] R. Zeng and M. S. Chinthavali. Fault ride-through control strategy for single-phase virtual synchronous generator. In *2019 IEEE Power Energy Society Innovative Smart Grid Technologies Conference (ISGT)*, pages 1–5, Feb 2019. Cited on p. 45.
- [210] S. F. Zarei, H. Mokhtari, M. A. Ghasemi, and F. Blaabjerg. Reinforcing fault ride through capability of grid forming voltage source converters using an enhanced voltage control scheme. *IEEE Transactions on Power Delivery*, pages 1–1, 2018. Cited on p. 45.
- [211] Kangle Ren, Xing Zhang, Fusheng Wang, LeiLei Guo, Zhijie Wang, and Lingxiang Wang. Grid fault ride through of a medium-voltage three-level full power wind power converter. In *2016 IEEE 8th International Power Electronics and Motion Control Conference (IPEMC-ECCE Asia)*, pages 1509–1514, May 2016. Cited on p. 45.
- [212] H. Dehghani Tafti, A. I. Maswood, Z. Lim, G. H. P. Ooi, and P. H. Raj. Npc photovoltaic grid-connected inverter with ride-through capability under grid faults. In *2015 IEEE 11th International Conference on Power Electronics and Drive Systems*, pages 518–523, June 2015. Cited on p. 45.
- [213] A. Gkountaras, S. Dieckerhoff, and T. Sezi. Evaluation of current limiting methods for grid forming inverters in medium voltage microgrids. In *2015 IEEE Energy Conversion Congress and Exposition (ECCE)*, pages 1223–1230, Sep. 2015. Cited on p. 45.
- [214] Changhee Cho, Jin-Hong Jeon, Jong-Yul Kim, Soonman Kwon, Kyongyop Park, and Sungshin Kim. Active synchronizing control of a microgrid. *IEEE Transactions on Power Electronics*, 26(12): 3707–3719, 2011. doi: 10.1109/TPEL.2011.2162532. Cited on p. 45.
- [215] Tatiana Mariano Lessa Assis and Glauco Nery Taranto. Automatic reconnection from intentional islanding based on remote sensing of voltage and frequency signals. *IEEE Transactions on Smart Grid*, 3(4):1877–1884, 2012. doi: 10.1109/TSG.2012.2191579. Cited on pp. 45 and 46.
- [216] Fen Tang, Josep M. Guerrero, Juan C. Vasquez, Dan Wu, and Lexuan Meng. Distributed active synchronization strategy for microgrid seamless reconnection to the grid under unbalance and harmonic distortion. *IEEE Transactions on Smart Grid*, 6(6):2757–2769, 2015. doi: 10.1109/TSG.2015.2406668. Cited on pp. 45 and 46.
- [217] Carter Lassetter, Eduardo Cotilla-Sanchez, and Jinsub Kim. A learning scheme for microgrid reconnection. *IEEE Transactions on Power Systems*, 33(1):691–700, 2018. doi: 10.1109/TPWRS.2017.2709741. Cited on p. 45.
- [218] G. Celli, F. Pilo, G. Pisano, V. Allegranza, R. Cicoria, and A. Iaria. Meshed vs. radial mv distribution network in presence of large amount of dg. In *IEEE PES Power Systems Conference and Exposition, 2004.*, pages 709–714 vol.2, 2004. doi: 10.1109/PSCE.2004.1397664. Cited on p. 46.
- [219] H. H. Zeineldin, Hebatallah M. Sharaf, Doaa K. Ibrahim, and Essam El-Din Abou El-Zahab. Optimal protection coordination for meshed distribution systems with dg using dual setting directional over-current relays. *IEEE Transactions on Smart Grid*, 6(1):115–123, 2015. doi: 10.1109/TSG.2014.2357813. Cited on p. 46.
- [220] Stefano Rivero, Fabio Sarzo, and Giancarlo Ferrari-Trecate. Plug-and-play voltage and frequency control of islanded microgrids with meshed topology. *IEEE Transactions on Smart Grid*, 6(3): 1176–1184, 2015. doi: 10.1109/TSG.2014.2381093. Cited on p. 46.
- [221] D. I. Brandao, J. A. Pomilio, T. Caldognetto, S. Buso, and P. Tenti. Coordinated control of distributed generators in meshed low-voltage microgrids: Power flow control and voltage regulation. In *2016 17th International Conference on Harmonics and Quality of Power (ICHQP)*, pages 249–254, 2016. doi: 10.1109/ICHQP.2016.7783458. Cited on p. 46.

- [222] Youssef Hennane, Abdelmajid Berdai, Serge Pierfederici, Farid Meibody-Tabar, Jean-Philippe Martin, and Milad Bahrami. Accurate power sharing and synchronization strategies in mesh islanded or grid-connected microgrids. In *2021 10th International Conference on Power Science and Engineering (ICPSE)*, pages 28–33, 2021. doi: 10.1109/ICPSE53473.2021.9656859. Cited on p. 46.
- [223] F. Belloni, R. Chiumeo, C. Gandolfi, and M. Brenna. Application of back-to-back converters in closed-loop and meshed mv distribution grid. In *2014 AEIT Annual Conference - From Research to Industry: The Need for a More Effective Technology Transfer (AEIT)*, pages 1–6, 2014. doi: 10.1109/AEIT.2014.7002023. Cited on p. 46.
- [224] Shafiuzzaman K. Khadem, Malabika Basu, and Michael F. Conlon. Intelligent islanding and seamless reconnection technique for microgrid with upqc. *IEEE Journal of Emerging and Selected Topics in Power Electronics*, 3(2):483–492, 2015. doi: 10.1109/JESTPE.2014.2326983. Cited on p. 46.
- [225] Zhi-Xiang Zou, Xingqi Liu, Jian Tang, Giovanni De Carne, Marco Liserre, Zheng Wang, and Ming Cheng. Power synchronization of smart transformers allowing universal operation in radial and meshed grids. *CSEE Journal of Power and Energy Systems*, pages 1–9, 2022. doi: 10.17775/CSEEJPES.2021.02350. Cited on pp. 46 and 117.
- [226] G. De Carne, M. Liserre, and C. Vournas. On-line load sensitivity identification in lv distribution grids. *IEEE Transactions on Power Systems*, 32(2):1570–1571, March 2017. ISSN 0885-8950. Cited on p. 47.
- [227] G. De Carne, G. Buticchi, M. Liserre, and C. Vournas. Load control using sensitivity identification by means of smart transformer. In *2017 IEEE Manchester PowerTech*, pages 1–1, June 2017. Cited on pp. 47 and 81.
- [228] E. Pournaras and J. Espejo-Urbe. Self-repairable smart grids via online coordination of smart transformers. *IEEE Transactions on Industrial Informatics*, 13(4):1783–1793, Aug 2017. Cited on p. 47.
- [229] Nicholas Parks, Sumit Dutta, Vivek Ramachandram, Kamalesh Hatua, and Subhashish Bhattacharya. Black start control of a solid state transformer for emergency power restoration. In *2012 IEEE Energy Conversion Congress and Exposition (ECCE)*, pages 188–195, 2012. doi: 10.1109/ECCE.2012.6342824. Cited on pp. 47 and 48.
- [230] S. A. Saleh, E. Ozkop, B. Alsayid, C. Richard, X. F. S. Onge, K. McDonald, and L. Chang. Solid-state transformers for distribution systems—part ii: Deployment challenges. *IEEE Transactions on Industry Applications*, pages 1–1, 2019. doi: 10.1109/TIA.2019.2938143. Cited on p. 48.
- [231] J. A. P. Lopes, C. L. Moreira, and A. G. Madureira. Defining control strategies for microgrids islanded operation. *IEEE Transactions on Power Systems*, 21(2):916–924, May 2006. Cited on p. 52.
- [232] N. Eghtedarpour and E. Farjah. Power control and management in a hybrid ac/dc microgrid. *IEEE Transactions on Smart Grid*, 5(3):1494–1505, May 2014. Cited on p. 52.
- [233] Abraham Rojas Tarango and Gregory J. Kish. Dynamic phasor modeling and analysis of three-phase dc/dc/ac mmcs for hybrid ac/dc grids. *IEEE Canadian Journal of Electrical and Computer Engineering*, 44(4):391–401, 2021. doi: 10.1109/ICJECE.2021.3094119. Cited on p. 53.
- [234] Dewu Shu, Xiaorong Xie, Zheng Yan, Venkata Dinavahi, and Kai Strunz. A multi-domain co-simulation method for comprehensive shifted-frequency phasor dc-grid models and emt ac-grid models. *IEEE Transactions on Power Electronics*, 34(11):10557–10574, 2019. doi: 10.1109/TPEL.2019.2899651. Cited on p. 53.
- [235] S. Chiniforoosh, J. Jatskevich, A. Yazdani, V. Sood, V. Dinavahi, J. A. Martinez, and A. Ramirez. Definitions and applications of dynamic average models for analysis of power systems. *IEEE Transactions on Power Delivery*, 25(4):2655–2669, 2010. doi: 10.1109/TPWRD.2010.2043859. Cited on p. 53.

- [236] Juan A. Martinez-Velasco, Salvador Alepuz, Francisco González-Molina, and Jacinto Martin-Arnedo. Dynamic average modeling of a bidirectional solid state transformer for feasibility studies and real-time implementation. *Electric Power Systems Research*, 117:143 – 153, 2014. Cited on pp. 53, 58, and 65.
- [237] J. M. Ramirez, R. A. Barrios, and B. J. Salome. Details and implementation of a sic-based solid state transformer prototype. In *2017 IEEE PES Innovative Smart Grid Technologies Conference - Latin America (ISGT Latin America)*, pages 1–6, Sep. 2017. Cited on p. 54.
- [238] T. Lagier, L. Chédot, F. W. L. Ghossein, B. Lefebvre, P. Dworakowski, M. Mermet-Guyennet, and C. Buttay. A 100 kw 1.2 kv 20 khz dc-dc converter prototype based on the dual active bridge topology. In *2018 IEEE International Conference on Industrial Technology (ICIT)*, pages 559–564, Feb 2018. Cited on p. 54.
- [239] Amirnaser Yazdani. Electromagnetic transients of grid-tied photovoltaic systems based on detailed and averaged models of the voltage-sourced converter. In *2011 IEEE Power and Energy Society General Meeting*, pages 1–8, 2011. doi: 10.1109/PES.2011.6039185. Cited on p. 58.
- [240] W. Zhang and X. Yan. Equivalence analysis of virtual synchronous machines and frequency-droops for inertia emulation in power systems with converter-interfaced renewables. *J. Electr. Eng. Technol.*, 15:1167–1175, 2020. Cited on p. 61.
- [241] M. N. Kheraluwala, R. W. Gascoigne, D. M. Divan, and E. D. Baumann. Performance characterization of a high-power dual active bridge dc-to-dc converter. *IEEE Transactions on Industry Applications*, 28(6):1294–1301, Nov 1992. Cited on pp. 64 and 65.
- [242] Martin Kasperek. Analysis of voltage quality parameters in mv distribution grid. *CIREN - Open Access Proceedings Journal*, 2017:517–521(4), October 2017. URL <https://digital-library.theiet.org/content/journals/10.1049/oap-cired.2017.0148>. Cited on p. 67.
- [243] Xuejun Pei, Wu Zhou, and Yong Kang. Analysis and calculation of dc-link current and voltage ripples for three-phase inverter with unbalanced load. *IEEE Transactions on Power Electronics*, 30(10):5401–5412, 2015. doi: 10.1109/TPEL.2014.2375353. Cited on pp. 68 and 69.
- [244] Task Force on Turbine-Governor Modeling. Dynamic Models for Turbine-Governors in Power System Studies. Technical report, IEEE Power & Energy Society, 01 2013. Cited on p. 74.
- [245] Ieee recommended practice for excitation system models for power system stability studies. *IEEE Std 421.5-1992*, pages 1–56, 1992. doi: 10.1109/IEEESTD.1992.106975. Cited on p. 74.
- [246] Ieee pes test feeder. <https://cmte.ieee.org/pes-testfeeders/resources/>. Accessed: 2022-03-05. Cited on pp. 75 and 76.
- [247] L. M. Korunović, J. V. Milanović, S. Z. Djokic, K. Yamashita, S. M. Villanueva, and S. Sterpu. Recommended parameter values and ranges of most frequently used static load models. *IEEE Transactions on Power Systems*, 33(6):5923–5934, Nov 2018. Cited on pp. 76 and 77.
- [248] Raphael Bleilevens, Jens Priebe, Niklas Wehbring, and Albert Moser. Reliability analysis of dc distribution grids. In *2019 54th International Universities Power Engineering Conference (UPEC)*, pages 1–6, 2019. doi: 10.1109/UPEC.2019.8893614. Cited on p. 80.
- [249] Julian Saat, Raphael Bleilevens, Dominik Mildt, Jens Priebe, Niklas Wehbring, and Albert Moser. Design aspects of medium and low voltage dc distribution grids - an overview. In *2020 5th IEEE Workshop on the Electronic Grid (eGRID)*, pages 1–6, 2020. doi: 10.1109/eGRID48559.2020.9330652. Cited on p. 80.



- [250] K. E. Lucas-Marcillo, D. A. Plaza Guingla, W. Barra, R. L. P. De Medeiros, E. Melo Rocha, D. A. Vaca-Benavides, S. J. Ríos Orellana, and E. V. Herrera Muentes. Novel robust methodology for controller design aiming to ensure dc microgrid stability under cpl power variation. *IEEE Access*, 7:64206–64222, 2019. Cited on p. 80.
- [251] X. Lu, K. Sun, J. M. Guerrero, J. C. Vasquez, L. Huang, and J. Wang. Stability enhancement based on virtual impedance for dc microgrids with constant power loads. *IEEE Transactions on Smart Grid*, 6(6):2770–2783, Nov 2015. Cited on p. 80.
- [252] A. Gopi and P. Ajay-D-Vimal Raj. Distributed generation for line loss reduction in radial distribution system. In *2012 International Conference on Emerging Trends in Electrical Engineering and Energy Management (ICETEEEM)*, pages 29–32, 2012. doi: 10.1109/ICETEEEM.2012.6494439. Cited on pp. 84 and 85.
- [253] Vinod Kumar Naik and Anamika Yadav. High impedance fault detection and classification on ieee-15 bus radial distribution system by using fuzzy inference system. In *2018 2nd International Conference on Power, Energy and Environment: Towards Smart Technology (ICEPE)*, pages 1–6, 2018. doi: 10.1109/EPETSG.2018.8658778. Cited on pp. 84 and 85.
- [254] E-redes: Rede nacional de distribuição - alta tensão e subestações. <https://e-redes-rede.wntech.com>. Accessed: 2022-03-15. Cited on p. 84.
- [255] Saman A. Gorji, Hosein G. Sahebi, Mehran Ektesabi, and Ahmad B. Rad. Topologies and control schemes of bidirectional dc–dc power converters: An overview. *IEEE Access*, 7:117997–118019, 2019. doi: 10.1109/ACCESS.2019.2937239. Cited on p. 99.
- [256] Hirofumi Matsuo and Fujio Kurokawa. New solar cell power supply system using a boost type bidirectional dc-dc converter. *IEEE Transactions on Industrial Electronics*, IE-31(1):51–55, 1984. doi: 10.1109/TIE.1984.350020. Cited on p. 99.
- [257] Taoufik Qoria, François Gruson, Frédéric Colas, Guillaume Denis, Thibault Prevost, and Xavier Guillaud. Critical clearing time determination and enhancement of grid-forming converters embedding virtual impedance as current limitation algorithm. *IEEE Journal of Emerging and Selected Topics in Power Electronics*, 8(2):1050–1061, 2020. doi: 10.1109/JESTPE.2019.2959085. Cited on p. 110.
- [258] Zheming Jin and Xiongfei Wang. A DQ-frame asymmetrical virtual impedance control for enhancing transient stability of grid-forming inverters. *IEEE Transactions on Power Electronics*, 37(4):4535–4544, 2022. doi: 10.1109/TPEL.2021.3124286. Cited on p. 110.
- [259] Rongwu Zhu, Vivek Raveendran, and Marco Liserre. Overload operation of lv-side inverter in smart transformer. In *2019 IEEE Energy Conversion Congress and Exposition (ECCE)*, pages 5997–6004, 2019. doi: 10.1109/ECCE.2019.8912607. Cited on p. 176.
- [260] AVX Corporation scc le series-low ers cylindrical supercapacitors. <https://datasheets.avx.com/AVX-SCC-LE.pdf>. Accessed: 2020-09-30. Cited on p. 199.



